HIGH-RESOLUTION STUDIES OF AQUEOUS ENVIRONMENTS ON ANCIENT MARS

A Dissertation

Presented to the Faculty of the Graduate School

of Cornell University

In Partial Fulfillment of the Requirements for the Degree of

Doctor of Philosophy

by

James Joseph Wray

January 2011

HIGH-RESOLUTION STUDIES OF AQUEOUS ENVIRONMENTS ON ANCIENT MARS

James Joseph Wray, Ph.D.

Cornell University 2011

Hydrated minerals on the surface of Mars record past aqueous conditions and permit assessment of whether, where, and when the planet may have been habitable. Both phyllosilicates (e.g., clays) and hydrated sulfate minerals were recently identified via orbital near-infrared spectroscopy. This work uses the Compact Reconnaissance Imaging Spectrometer for Mars (CRISM) and High Resolution Imaging Science Experiment (HiRISE) to characterize these and other aqueous mineral deposits, determining their composition, stratigraphy, and morphology. These properties and observations from other Mars-orbiting instruments allow formulation and testing of hypotheses on how Martian environments varied across space and time.

The Mawrth Vallis region hosts the largest areal exposure of phyllosilicates, and CRISM spectral maps show these are compositionally stratified, with Al-clays overlying Fe/Mg-clays throughout the region. Geometric measurements reveal that the Al-clay horizon traces the Mawrth Vallis topography, implying that the Al-clays postdate this channel and may have formed via surface weathering. CRISM data further reveal the Ca-sulfate bassanite in outcrops underlying Fe/Mg-clays. Each hydrated unit exhibits ubiquitous meter-scale polygons or other fracture patterns, which correlate with composition.

A CRISM-based survey of Mars' ancient southern highlands uncovers numerous aqueous deposits undetected at lower resolution. Fe/Mg-phyllosilicates are

widespread, in some cases exposed by craters and elsewhere spanning the intercrater plains. Sulfates occur at higher latitudes than those observed previously, and are associated with phyllosilicates in some locations. Elsewhere, phyllosilicates co-occur with other hydrated silicates or putative chlorides. Fe/Ca-carbonate is also identified for the first time. These diverse mineral assemblages likely reflect diverse aqueous conditions.

Columbus crater and others in Terra Sirenum contain layered deposits with diverse clays and sulfates. Digital elevation models, crater counts, thermal emission spectra, and hydrologic modeling results are added to CRISM and HiRISE image analyses to test several different hypotheses for these deposits, including their possible formation in a deep lake within Columbus crater during the Late Noachian Epoch.

CRISM analysis of Endeavour crater in Meridiani Planum reveals Fe/Mg-smectite clays in its rim and hydrated sulfates on the adjacent plains. Opportunity is currently driving toward these locations, which may provide the first ground truth of hydrated minerals detected from Mars orbit.

BIOGRAPHICAL SKETCH

James Joseph Wray was born January 10, 1984 in New York, NY, but grew up in Princeton Junction, NJ. He was fortunate to attend the West Windsor-Plainsboro public school system in grades K-12. As a high school senior, he fell in love with Princeton University while taking math courses there, and in 2006 graduated *summa cum laude* with an A.B. in Astrophysical Sciences and a Certificate in Engineering Physics. For his undergraduate thesis, he collected and analyzed spectra of the icy moons Europa and Enceladus.

Science was always James' favorite school subject, and hindsight reveals early hints at an affinity for planetary exploration. Around the age of five, his grandmother subscribed him to the nature magazine "Ranger Rick," of which his favorite issue by far was a special edition on Madagascar—to youthful eyes, a land of "alien" life here on Earth. Years later, in Kathy Mora's middle school science class, each student wrote a report on a solar system object; James was fascinated by Titan, at the time known only as a mysterious moon with organic-rich hazes completely concealing its surface. The film "Contact," a dramatization of the search for life beyond Earth, has been James' favorite movie since he first saw it in the theater. And although he had planned to major in Aerospace Engineering, a week in summer 2002 spent under the exquisitely dark skies of the Outer Banks, NC sparked an overriding passion for astronomy that was subsequently nurtured by many excellent professors at Princeton. Still, some of his favorite college classes were electives in geology, ecology, and molecular biology. James discovered that astrobiology and planetary science are ideal pursuits for those who struggle to choose just one of the traditional science disciplines.

After completing the Ph.D., James will continue Mars and Europa research at Cornell until August 2011, when he will begin an Assistant Professorship in Earth and Atmospheric Sciences at the Georgia Institute of Technology.

This thesis is dedicated to Patricia, David, Jeff, and Maggie Wray, all of whom helped make me the person I am today. And to my grandfathers: James, whom I never knew, was once Professor and Chair of Orthopedics in nearby Syracuse; I imagine I inherited my scientific mindset from him. Joe, who died in the past year, always encouraged me to pursue a career that brings me happiness. I am proud to carry both their names.

ACKNOWLEDGMENTS

I am probably too young to name accurately the most important decisions of my life, but I expect that doing my Ph.D. with Steve Squyres will always be in the top five. I came to Cornell to work with Steve, and from day one he treated me more like a colleague than a student. He provided exactly as much guidance as I asked for—no less, and no more. This challenged me, of course. I remember when Steve told me in fall 2006 that OMEGA had found "phyllosilicates" on Mars. Steve was excited, but I was confused—what were phyllosilicates again?? As the text below will show, I soon learned the answer. This episode exemplifies Steve's gentle touch, steering me toward scientifically compelling topics but allowing me to ask the specific questions and find the answers myself. As I begin advising students of my own, Steve will be my role model for effective mentoring. Graduate school may be over, but I know I am not finished learning from Steve (and he should take this as fair warning that I will continue to seek his advice throughout my career).

I also feel a great debt of gratitude to Carl Sagan, whom I never met, but who did three specific things for me: (1) he built Cornell Astronomy into a premiere department for planetary studies; (2) he, more than any other single person, made the search for life beyond Earth a respectable and popular field of scientific inquiry; and (3) he wrote the novel Contact, and pursued its eventual release as a major motion picture. I saw this film in middle school, and it strongly influenced my direction as a young scientist. I have no idea what I would be doing with my life if not for Carl. His former student Chris Chyba also provided crucial guidance when I was choosing a graduate school.

I have received help at Cornell from many more people than I can list here, but at the very least I want to thank my other Special Committee members. Jim Bell

taught me the importance of testing specific hypotheses and evaluating alternative explanations for one's results, among very many other things. Jamie Lloyd challenged me to improve my knowledge of optics, and his comments on the benefits of teaching strongly influenced my decision to enter the professoriate. Bryan Isacks showed me the value of a quantitative approach to understanding geologic processes. Bob Kay gave me a crucial petrological foundation for studying the composition of rocks on other worlds. And I have always thought of Jean-Luc Margot as an "unofficial" Committee member; he has continued to provide guidance even after leaving Cornell in 2009.

Significant mentors outside Cornell include Alfred McEwen, whose HiRISE investigation has not only provided key data and funded my frequent travel, but also has shown me how rewarding and fun it is to participate in early science analysis from a spaceflight investigation; I look forward to providing similar experiences for my own students. Scott Murchie graciously welcomed me to CRISM team meetings and telecons, and provided access to unreleased data and analysis tools without which this dissertation—every chapter—would have been impossible. I have been extremely fortunate to have such positive role models for planetary science investigation leadership.

Discussions with my research collaborators improved each chapter of this dissertation; in alphabetical order, they include Jeff Andrews-Hanna (chapter 4), Ray Arvidson (5), Alice Baldridge (4), Janice Bishop (2, 4), Matt Chojnacki (4), Roger Clark (4), Colin Dundas (4), Bethany Ehlmann (2, 3, 4), Randy Kirk (2), Alfred McEwen (5), Ralph Milliken (4), Scott Murchie (3, 4, 5), Jack Mustard (2, 5), Eldar Noe Dobrea (2), Leah Roach (2), Frank Seelos (3, 4), Steve Squyres (all), Gregg Swayze (4), Livio Tornabene (3, 4), and Sandra Wiseman (5).

I would also like to thank the National Science Foundation and the Fannie and

John Hertz Foundation, who provided my tuition and stipend funds, freeing me to pursue research full-time, but also allowed me to teach when I requested to do so in spring 2008.

Finally, but most importantly, I thank my family for their constant support. My path to where I am today began with my mother's devotion to raising her children and with my father's commitment to reading to me every night as a toddler. Their countless gifts to me can never be repaid, only (hopefully) someday paid forward. My brother was my best friend growing up and now inspires me with his own accomplishments. And my wife, with whom I have shared every step of my education after high school, is my sounding board, my social life, and so much more; none of this would be worthwhile without her. Because of the people with whom I share it, Earth will always be my favorite planet.

TABLE OF CONTENTS

LIST OF FIGURES

CHAPTER 1

INTRODUCTION

The Milky Way galaxy contains at least 500 known planets (and probably orders of magnitude more), but as of this writing the most "Earth-like" of these is Mars. The Red Planet is the easiest beyond Earth for humans and their robotic emissaries to land on, explore, and eventually colonize, and appears the most likely place in our solar system to have harbored and preserved evidence of extraterrestrial life at or near its surface. Robotic spacecraft have returned scientific data from Mars since 1965, and continuously since 1997, with no planned hiatus on the horizon.

Mars, although only ~$1/10^{th}$ the mass of Earth, contains approximately the same terrestrial land area. Like Earth, its surface morphology provides evidence for impact, volcanic, tectonic, and gradational processes, the latter including erosion and deposition driven by gravity, wind, and water. Unlike Earth, Mars lacks compelling evidence for plate tectonics, and in the absence of this process has been able to retain rocks from the first billion years of solar system history at or near its modern surface [e.g., *Carr and Head*, 2010]. It should therefore come as no surprise that the Martian surface documents a great diversity of physical and geochemical processes and environments.

Whether any of these environments have hosted life remains unknown. For most of the spacecraft era, Mars' astrobiological appeal has derived chiefly from its morphologic evidence for surface liquid water. The modern surface of Mars is frigid and desiccated at low latitudes, but valley networks attest to a former era of more active hydrology [e.g., *Baker*, 1982; *Carr*, 1995; *Fassett and Head*, 2008a]. Although in some cases surface water may have been ephemeral [*Segura et al.*, 2002], there is also evidence for standing bodies of water that may have persisted for hundreds to

thousands of years or longer [e.g., *Malin and Edgett*, 2003; *Moore et al.*, 2003; *Fassett and Head*, 2005; *Grant et al.*, 2008]. Isotopic evidence suggests early escape of a thicker atmosphere [*Jakosky and Phillips*, 2001] that might have contained greenhouse gases capable of warming the surface above the freezing point of water [e.g., *Pollack et al.*, 1987; *Kasting*, 1997; *Sagan and Chyba*, 1997; *Johnson et al.*, 2008]. Even a continuously cold climate would allow at least ephemeral liquid brines [e.g., *Rennó et al.*, 2009] or water heated by magma [e.g., *Squyres et al.*, 1987] or impacts [e.g., *Newsom et al.*, 1996; *Williams and Malin*, 2008], possibly creating temporary habitable niches with both liquid water and available energy.

Whether via surface weathering or hydrothermal alteration, water-rock interactions on Mars should have affected not only its geomorphology but also its mineralogy. Secondary minerals including phyllosilicates, sulfates, and carbonates were tentatively identified in regional-to-global soils or dust via spectra from ground-based telescopes [*McCord et al.*, 1982; *Bell and Crisp*, 1993; *Blaney and McCord*, 1995], the Kuiper Airborne Observatory [*Pollack et al.*, 1990], the Earth-orbiting Infrared Space Observatory [*Lellouch et al.*, 2000; *Fedorova et al.*, 2002], the Infrared Spectrometers on Mariner 6 and 7 [*Calvin et al.*, 1994], and the Imaging Spectrometer for Mars (ISM) on Phobos 2 [*Murchie et al.*, 1993, 2000]. Although these investigations correctly identified surface hydration, most of their specific secondary mineral detections were viewed as equivocal (see review by *Calvin and Bell* [2008]). Meteorites from Mars contain minor (<1% by volume) clays, sulfates, halides, and carbonates [*Bridges et al.*, 2001], and chemical analyses from the Viking and Mars Pathfinder landing sites suggested these minerals may be widely distributed in Martian soils [*Clark and Van Hart*, 1981; *Wänke et al.*, 2001]; however, their origin was poorly constrained, and the lander chemistry data allow a range of mineralogic interpretations [*Clark*, 1993]. To search for localized deposits enriched in secondary

minerals, spectral data with the high spatial resolution possible from a Mars-orbiting platform were long anticipated [e.g., *Bell and McCord*, 1989].

The Thermal Emission Spectrometer (TES) on board Mars Observer [*Christensen et al.*, 1992] would have provided the first global infrared mapping at high spatial and spectral resolution, but Mars Observer failed prior to orbit insertion. Another TES instrument was flown on Mars Global Surveyor (MGS) four years later [*Christensen et al.*, 2001a], and was followed by the Thermal Emission Imaging System (THEMIS) on the 2001 Mars Odyssey mission, which provided higher spatial but lower spectral resolution [*Christensen et al.*, 2004a]. TES identified regional concentrations of crystalline gray hematite [*Christensen et al.*, 2000; 2001b], one of which (Meridiani Planum) was chosen as the landing site for the Mars Exploration Rover (MER) Opportunity, whose *in situ* investigations revealed an aqueous environment for hematite formation [*Squyres et al.*, 2004]. Yet other secondary minerals such as clays, carbonates and sulfates were not found by TES, suggesting that these minerals are not present at the surface in abundances >10–15% at the scales (a few kilometers or wider) to which TES was sensitive. TES confirmed minor carbonate (~2–5 weight %) in global Martian dust [*Bandfield et al.*, 2003], but the apparent ubiquity of primary minerals (feldspars, pyroxene, and minor or locally abundant olivine) was viewed as evidence for "a geologic history dominated by a cold, dry climate" with minimal aqueous alteration [*Christensen et al.*, 2001a].

Relative to these thermal emission data, visible to near-infrared (NIR) reflectance spectroscopy provides distinct constraints on the alteration mineralogy. Multiple scattering dominates the visible/NIR light reflected from particulate and textured surfaces, so absorption band strengths often are not linearly proportional to mineral abundances [e.g., *Clark*, 1999]. This nonlinearity can allow minor mineralogic components to be detected, including many hydrated and hydroxylated

minerals as well as carbonates, all of which have vibrational overtone and combination bands in the 1–4 μm spectral range [*Clark*, 1999]. A Visible and (Near-)Infrared Mapping Spectrometer was originally planned for the Mars Observer mission, but was descoped due to cost constraints [*Albee et al.*, 1992]. Several years earlier, ISM mapped a subset of equatorial Mars at ~22 km/pixel from orbit, revealing crustal primary mineralogy [*Mustard et al.*, 1993, 1997; *Mustard and Sunshine*, 1995] and variable hydration [*Bibring et al.*, 1989; *Murchie et al.*, 1993, 2000]. It was over a decade later that another such spectrometer began observing Mars with higher spatial resolution and wider coverage.

The Observatoire pour la Minéralogie, l'Eau, les Glaces et l'Activité (OMEGA) was developed for the Russian Mars-96 mission but—like the first TES on Mars Observer—it never reached Mars. A spare model with redesigned electronics was flown on Mars Express [*Bibring et al.*, 2004]. Within its first year of observation, OMEGA identified a great diversity of surface mineralogy [*Bibring et al.*, 2005], including not only several different primary compositions [*Mustard et al.*, 2005] but also gypsum in the north polar region [*Langevin et al.*, 2005], other sulfates in equatorial layered deposits [*Gendrin et al.*, 2005], and various phyllosilicates including Fe-, Mg-, and Al-rich smectite clays [*Poulet et al.*, 2005]. Meanwhile, Opportunity was identifying sedimentary rocks with abundant sulfates including the acid sulfate jarosite [*Klingelhöfer et al.*, 2004]. The different chemistries required to form these minerals [*Chevrier et al.*, 2007] and their apparent segregation into terrains of different ages prompted a model positing a period of neutral-to-alkaline phyllosilicate formation in the Early to Mid Noachian (prior to ~3.8 Ga according to *Hartmann and Neukum* [2001]), followed by a more acidic aqueous period of sulfate formation from the Late Noachian into the Late Hesperian (~3.8–3.5 Ga), with only minor alteration forming anhydrous iron oxides since then [*Bibring et al.*, 2006a,b].

OMEGA and MER validated decades of searches for aqueous alteration products on Mars and provided a new framework for the planet's history of water and habitability. Nevertheless, many questions remained, some old and some new: where are the carbonates long predicted from aqueous weathering under a CO_2-rich atmosphere [e.g., *Kahn*, 1985]? Did phyllosilicates form at the surface or beneath it? Do all sulfates reflect acidic conditions? How long-lasting were the aqueous conditions that formed each of these mineral types? Were they globally widespread or only local to regional? What are the full alteration—and primary—mineral assemblages? How diverse are the clay and sulfate minerals, and do certain types occur preferentially in specific geologic settings? Finally, which mineralogies and geologic contexts appear most likely to record habitable environments in which evidence for ancient life might be preserved?

The OMEGA investigation is ongoing, but another near-infrared spectrometer has now arrived at Mars. The Mars Reconnaissance Orbiter (MRO) launched in August 2005, entered Mars orbit in March 2006, and began its primary science phase in November 2006. It carries the Compact Reconnaissance Imaging Spectrometer for Mars (CRISM), with similar spectral range to OMEGA but >2x finer spectral resolution beyond 1 μm and ~10–100x finer spatial resolution [*Murchie et al.*, 2007]. CRISM set out to map all of Mars at ~100 or 200 m/pixel and reduced spectral resolution (72 channels from 0.36 to 3.9 μm), with higher-resolution sampling of key locations (544 channels, ~18 or 36 m/pixel) [*Murchie et al.*, 2009c]. MRO also carries the High Resolution Imaging Science Experiment (HiRISE) for 3-color imaging of key targets at the unprecedented scale of ~30 cm/pixel [*McEwen et al.*, 2007] and the Context Camera (CTX) for covering broader areas panchromatically at ~6 m/pixel [*Malin et al.*, 2007]. Together these instruments can probe the detailed mineralogy, morphology, and stratigraphy of aqueous deposits on Mars, enabling us to begin

addressing questions such as those posed in the preceding paragraph. Such is the goal of this dissertation.

The CRISM science team and the broader Mars science community includes dozens to hundreds of individuals using the voluminous MRO dataset to unravel the aqueous history of Mars, so this dissertation focuses on a subset of the surface. I begin with a detailed analysis of the largest areal exposure of phyllosilicates identified by OMEGA, surrounding the outflow channel Mawrth Vallis. This region contains multiple phyllosilicate minerals with distinct spatial distributions, and CRISM data overlain on HiRISE images allow localization of each mineral to particular layers in the stratigraphy. Meter-scale textures in these clay-bearing rocks attest to their complex geologic history, and strike/dip measurements from a HiRISE-scale digital elevation model (DEM) provide some insight into depositional processes. A lower-resolution DEM from the High Resolution Stereo Camera (HRSC) on Mars Express [*Neukum and Jaumann*, 2004] reveals the regional geometry of major stratigraphic units and constrains when and how the various clays might have formed. Finally, several outcrops with a newly identified hydrated sulfate (bassanite) are found underlying the clay-bearing layers in Mawrth Vallis, permitting assessment of hypotheses for the timing of clay vs. sulfate formation. These findings are described in chapter 2.

Chapter 3 uses the ever-growing CRISM dataset to identify aqueous mineral exposures across a large fraction of Mars independent from previous OMEGA detections. All available CRISM data were surveyed across portions of the Noachian southern highlands in which OMEGA had found few hydrated minerals, and many new exposures are reported. Fe/Mg-phyllosilicates are frequently exposed by impact craters and are inferred to be present in the shallow subsurface across most Noachian terrains. These are variably accompanied by Al-phyllosilicates, zeolites, hydrated

sulfates, carbonates, or chlorides inferred from thermal emission spectroscopy. Their geologic settings, as inferred from images spanning a range of resolutions, are also diverse, including Noachian crater floor deposits, intercrater basin fill, and possible ancient volcanoes.

Chapter 4 explores in greater detail one of the new aqueous mineral settings identified in chapter 3: layered clays and sulfates within large craters in northwest Terra Sirenum. In Columbus crater, CRISM spectra reveal gypsum and other sulfates interbedded with the Al-clay kaolinite in a discrete ring around the crater walls. These minerals are also found on the crater floor, along with montmorillonite, Fe/Mg-phyllosilicates, jarosite, alunite, and crystalline ferric oxide or hydroxide. Thermal emission spectra suggest abundances of these minerals in the tens of percent range. Nearby large craters also contain layered deposits and Al/Fe/Mg-phyllosilicates, and one other crater (Cross) also hosts sulfates. The region's intercrater plains contain scattered exposures of Al-phyllosilicates and an isolated mound with opaline silica, in addition to more common Fe/Mg-phyllosilicates with chlorides. Crater counts are used to estimate a Late Noachian age for the aqueous deposits in Columbus. Using spectral and imaging data supplemented by insights from DEMs, thermal inertia, and hydrologic modeling, several hypotheses for the origin of these deposits are evaluated, including the possibility of a deep, groundwater-fed paleolake in Columbus crater.

Chapter 5 discusses an upcoming chance to obtain the first ground truth on phyllosilicates and hydrated sulfates identified in orbital data. CRISM data are used to identify Fe/Mg-smectite clays in the rim of Endeavour crater, toward which Opportunity is currently driving. Rim textures provide further insights into the age and distribution of these materials. Other CRISM spectra reveal polyhydrated sulfate in the younger light-toned rocks immediately surrounding Endeavour's rim, and monohydrated sulfate exposed by the fresh crater Ada ~140 km from Opportunity.

Ways in which the rover's Athena science payload could improve understanding of these remotely sensed aqueous deposits are discussed.

Finally, chapter 6 summarizes the results of the preceding chapters and significant discoveries by other Mars researchers that have unfolded concurrently with this dissertation research. Collectively, these findings suggest many possible avenues for further CRISM analysis and future missions to Mars, which are outlined.

CHAPTER 2

COMPOSITIONAL STRATIGRAPHY AT MAWRTH VALLIS[*]

2.1 Introduction

Phyllosilicate-bearing outcrops on Mars were first definitively identified by the OMEGA infrared spectrometer [*Bibring et al.*, 2005]. Subsequent studies have detected phyllosilicates in a variety of settings scattered across the planet, usually in materials of Noachian age [e.g., *Poulet et al*., 2005; *Bibring et al.*, 2006a; *Mustard et al*., 2008]. Phyllosilicates are intriguing from the perspective of habitability because they are inferred to have formed through alteration at neutral to alkaline pH [*Chevrier et al*., 2007], and terrestrial analogs suggest that their formation may have required aqueous conditions persisting for at least thousands of years [e.g., *Eberl*, 1984; *Price et al.*, 2005].

The region surrounding Mawrth Vallis contains one of the largest exposures of phyllosilicates on the Martian surface [*Poulet et al*., 2005; *Bibring et al.*, 2006a]. This region had previously been identified as one of the few large regional exposures of light-toned layered outcrop on Mars [*Malin and Edgett*, 2000], and the phyllosilicates indeed occur within these layered deposits [*Poulet et al.*, 2005; *Loizeau et al*., 2007; *Michalski and Noe Dobrea*, 2007]. Mawrth Vallis is an outflow channel that cuts Noachian cratered terrain in Western Arabia before debouching into Chryse Planitia at 26°N, 340°E [*Scott and Tanaka*, 1986]. It is inferred to be the oldest of the circum-Chryse outflow channels, with a Mid-to-Late Noachian age estimated from crater counts [*Ivanov and Head*, 2001]. Most authors to date have interpreted the region's clay-bearing layered deposits as ancient sedimentary and/or altered pyroclastic

[*] Much of the work described herein was originally published by Wray, J. J., et al. (2008), Compositional stratigraphy of clay-bearing layered deposits at Mawrth Vallis, Mars, *Geophys. Res. Lett., 35*, L12202, doi:10.1029/2008GL034385; or by Wray, J. J., et al. (2010), Identification of the Ca-sulfate bassanite in Mawrth Vallis, Mars, *Icarus, 209*, 416–421, doi:10.1016/j.icarus.2010.06.001.

deposits predating the Mawrth Vallis outflow(s) [*Poulet et al.*, 2005; *Loizeau et al.*, 2007; *Michalski and Noe Dobrea*, 2007]. Alternatively, *Howard and Moore* [2007] have suggested that these layered deposits may drape and therefore postdate the outflow channel. There is similar ambiguity in the relative timing of clay formation vs. the impact that formed the largest crater in the region, Oyama (Fig. 2.1), as clay-bearing layered deposits are found both exposed in its rim and filling its interior [*Loizeau et al.*, 2007]. Resolving these chronologies would constrain not only the age of the layered materials, but also their depositional process(es)—e.g., marine/lacustrine deposition in an ancient enclosed basin vs. aeolian airfall draping the modern topography.

OMEGA spectra have been used to identify two distinct phyllosilicate minerals in layered outcrops in and around Mawrth Vallis: Fe/Mg-rich smectite and the Al-rich smectite montmorillonite [*Poulet et al*., 2005; *Loizeau et al*., 2007]. These clays are found in different outcrops, but the relationship between them is unknown: do the different clays occur in different layers, or do they reflect lateral variations oblique to layering from paleo-gradients in primary mineralogy, sediment source, and/or conditions of alteration? In addition, the morphologies of the two clay-bearing rock types were indistinguishable at the several meter/pixel scale of MGS Mars Orbiter Camera (MOC) [*Malin et al.*, 1992; *Malin and Edgett*, 2001] images [*Poulet et al.*, 2005, *Loizeau et al.*, 2007]. The higher resolution of HiRISE may reveal informative differences.

The full mineral assemblages in the clay-bearing rocks of Mawrth Vallis are also unknown. Olivine appears absent from this region, and pyroxene is found only in a distinct dark deposit that overlies the clay-bearing rocks [*Loizeau et al.*, 2007]. As *Milliken et al.* [2009] have recently emphasized, clay mineral formation via alteration of basalt would have released excess cations that should have been accommodated in

complementary salts (e.g., carbonates, sulfates, halides) and/or oxides. OMEGA-based studies of the Mawrth Vallis region have not yet identified such phases.

In this study, HiRISE and CRISM data are used to refine the mineralogy and stratigraphy of the Mawrth Vallis layered materials. The stratigraphy at multiple sites, along with topographic data from HRSC and HiRISE, provides insight into the geometries of the clay-bearing layers at regional and outcrop scales, constraining their age and mode of deposition.

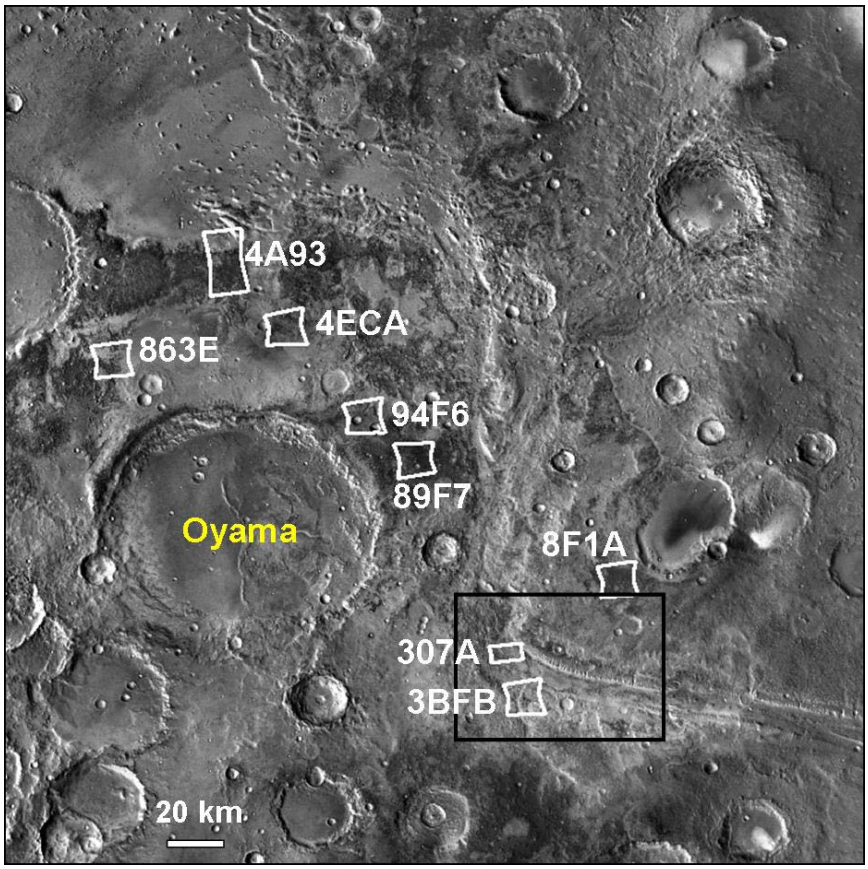

Figure 2.1: THEMIS daytime IR mosaic of Mawrth Vallis region. CRISM footprints and image identifiers are shown for images used to determine compositional stratigraphy; 307A and 4A93 are half-resolution (~36 m/pixel), while others are full resolution. Black box outlines area of Fig. 2.16a. Here and subsequently, north is up unless indicated otherwise.

2.2 Spectral Processing Methods

Due to the strong phyllosilicate signatures surrounding Mawrth Vallis, this

~300x400 km region has been heavily targeted with CRISM: dozens of full or half-resolution (~18 or 36 m/pixel) observations have been acquired to date, supplemented by lower-resolution multispectral data [*Murchie et al.*, 2007, 2009c]. To resolve compositional stratigraphy, this work focuses on the co-located HiRISE-CRISM hyperspectral observation pairs available as of spring 2008 (Fig. 2.1). These have three different formats: full-resolution targeted (FRT; 18 m/pixel, covering ~10x10 km), half-resolution long (HRL; 36 m/pixel, 10x20 km) and half-resolution short (HRS; 36 m/pixel, 10x10 km).

CRISM I/F data are processed as described by *Murchie et al.* [2009c], including division by the cosine of the solar incidence angle to minimize photometric effects and atmospheric removal via division by a scaled transmission spectrum derived from observations over Olympus Mons; this "volcano-scan" algorithm does not account for atmospheric aerosols or variable CO and H_2O mixing ratios, but is an effective and widely used approach to remove CO_2 gas absorptions from Mars orbital spectra from ISM to OMEGA to CRISM [e.g., *Bibring et al.*, 1989; *Mustard et al.*, 2005, 2008]. Spectra from many pixels are averaged to improve the signal-to-noise ratio (SNR), and the resulting average spectra are divided by a spectral average from a dusty or otherwise spectrally "neutral" region in the same CRISM scene. This spectral ratio method suppresses residual artifacts of instrument calibration and atmospheric removal [e.g., *Mustard et al.*, 2008] while accentuating spectral signatures in the numerator spectrum that are unique relative to the denominator. Known artifacts that remain in some ratio spectra include a discontinuity near 1.65 μm due to a detector filter boundary and small features near 2.0 μm resulting from imperfect removal of atmospheric CO_2 bands [*Murchie et al.*, 2009c]; where these artifacts were egregious, they have been masked in the spectra plotted here.

CRISM has a VNIR detector spanning ~0.4–1.0 μm and an IR detector

spanning ~1.0–4.0 μm. In subsequent chapters, VNIR detector data are used sparingly because this wavelength range is affected by ferric minerals in rock coatings and surficial dust that can mask the bulk mineralogy [*Swayze*, 2004; *Cloutis et al.*, 2006]; however, the Mawrth Vallis region exhibits meaningful variations in the VNIR, as described below. Beyond 2.6 μm, CRISM IR data have lower SNR and several known instrument artifacts [*Murchie et al.*, 2009c]. In addition, wavelengths longer than 3 μm typically include a contribution from thermal emission that reduces absorption band strengths; no standard correction for these thermal effects has yet been developed for CRISM. I therefore devote the most attention herein to the spectral range from 1.0 to 2.6 μm, which includes diagnostic absorptions for mafic minerals (Fe^{2+} crystal field absorptions) and vibrational overtone and combination bands for carbonates and hydrated or hydroxylated minerals including sulfates and phyllosilicates [e.g., *Clark*, 1999; *Ehlmann et al.*, 2009].

CRISM data are used to identify geologic units of distinct composition, and then compared with HiRISE images to reveal stratigraphic relationships among units. CRISM pixels having spectral absorptions characteristic of particular minerals can be mapped using spectral summary (i.e., mineral indicator) parameters [*Pelkey et al.*, 2007]. The intensity of each parameter at a given pixel corresponds to an absorption band depth (or, in some cases, the steepness of a spectral slope), which reflects a combination of mineral abundance within the pixel as well as textural effects such as grain size. Parameter maps are manually overlain on HiRISE RED images by translating and/or warping the geometrically projected CRISM data to align them with HiRISE, a necessary step at this time due to subtle differences in the way each dataset is projected [*S. L. Murchie*, personal communication].

The key spectral parameters for mapping phyllosilicates track bands at ~1.9 μm (H_2O bend + asymmetric stretch combination band, due to H_2O in hydrated

minerals), ~2.2 μm (Al-OH bend + OH stretch combination, observed in Al-rich phyllosilicates), and ~2.3 μm (Fe/Mg-OH bend + OH stretch combination, observed in Fe/Mg-rich phyllosilicates) [*Clark et al.*, 1990]. For Fe/Mg-smectites, the ~2.3 μm band center ranges from 2.28 μm in Fe^{3+}-rich dioctahedral nontronite to 2.31–2.32 μm in Mg-rich trioctahedral saponite [*Swayze et al*., 2002]. Smectites have additional, slightly weaker absorptions at ~1.4 and ~2.4 μm that can also be diagnostic of composition [e.g., *Bishop et al.*, 2002b]. In this and subsequent chapters, these and other spectral features are used for mineral identification through visual comparison of CRISM data with library mineral spectra [e.g., *R. Clark et al*., 2007].

2.3 Compositional Diversity

Aside from small impact craters, the southern wall of the Mawrth Vallis channel provides some of the best continuous stratigraphic exposures in the region. CRISM spectral parameter maps overlain on a HiRISE image from this area (Fig. 2.2a) reveal mineralogical stratification, with Mg/Fe-phyllosilicate-bearing layers (1) overlying Al-clay-bearing layers (2), which overlie another Fe/Mg-clay-bearing unit (4). Between stratigraphic units 2 and 4 is a layer exhibiting a hydration band, but comparatively weak metal-OH bands (3), possibly a mixture of units 2 and 4. Corresponding CRISM ratio spectra (Fig. 2.2b) show that unit 4 has a band centered at 2.29 μm and a strong 1.9 μm H_2O band, while unit 1 has a band centered at 2.31 μm and a negligible 1.9 μm H_2O band. Unit 4 therefore likely contains an Fe-rich smectite clay such as nontronite (with minor Mg substituting for Fe, to shift the band center from 2.28 to 2.29 μm), whereas unit 1 is more consistent with an Mg-rich phyllosilicate with negligible interlayer water. As discussed below, the spectral character of unit 4 is much more commonly observed across Mawrth Vallis than that of unit 1.

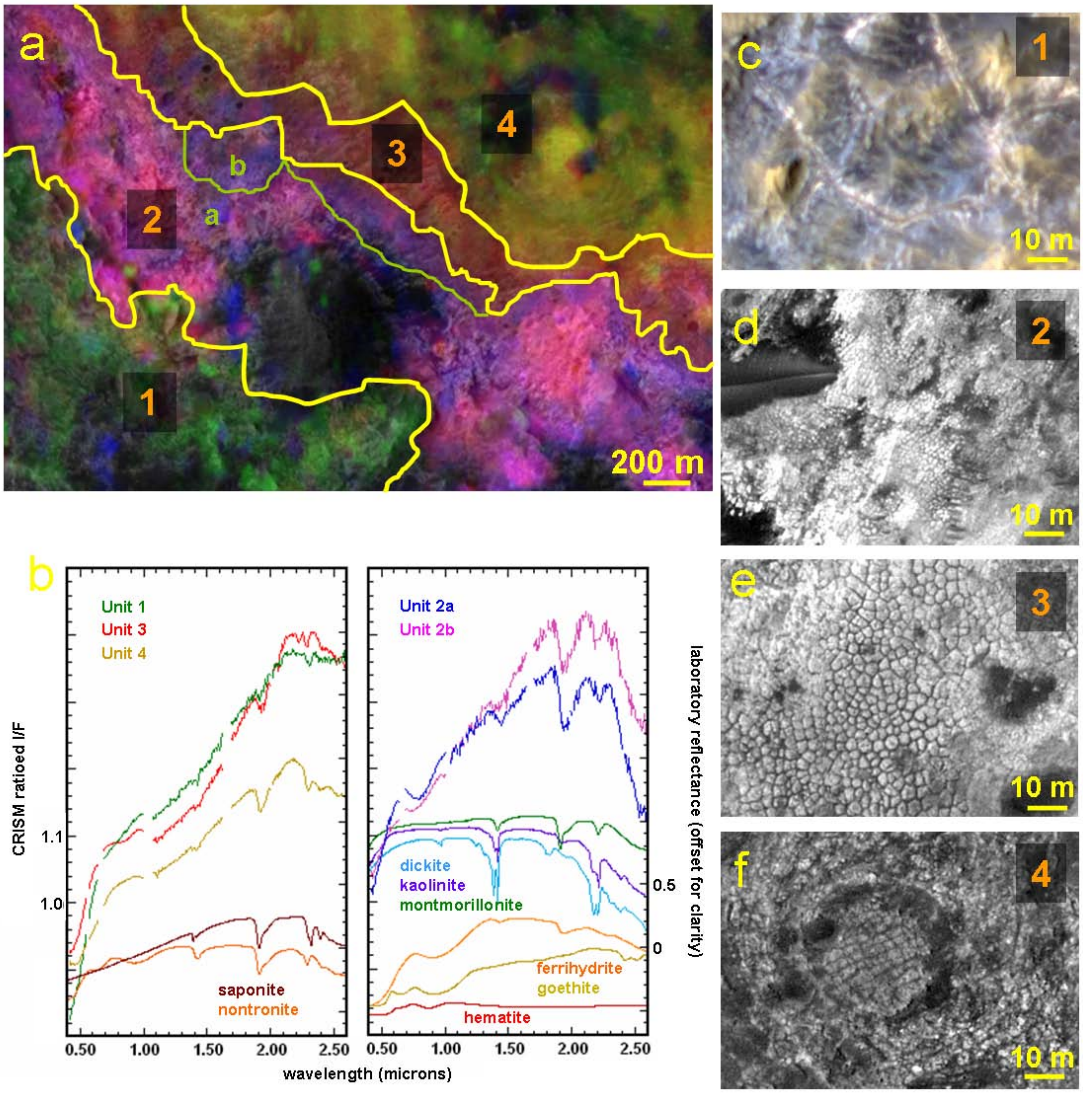

Figure 2.2: (a) Maps of band depth at 1.9 μm (red), 2.3 μm (green), and 2.2 μm (blue) indicative of hydration, Fe/Mg-phyllosilicates, and Al-phyllosilicates, respectively. Band maps from a portion of CRISM FRT 3BFB overlain on HiRISE PSP_002140_2025. Area slopes down toward upper right. (b) CRISM ratio spectra of compositional units in (a) compared to library spectra. Units 2a and 2b are subunits within unit 2 with distinct spectral shapes shortward of 1 μm, indicating ferric oxide variation. Morphology of (c) unit 1, showing bright-rimmed fractures; (d) unit 2, with meter-scale polygonal fractures; (e) unit 3, which has larger polygons; and (f) unit 4.

Unit 2 has bands at 1.9 and 2.2 μm, diagnostic of hydrated Al-bearing phyllosilicates. Unit 2a's slight doublet at 2.2 μm—even more evident in the spectra

shown in Fig. 2.3—indicates a kaolin group ($Al_2Si_2O_5[OH]_4$) mineral such as kaolinite or dickite, probably in a mixture with the Al-smectite montmorillonite previously identified in the region by OMEGA. In addition to these H_2O and OH-related bands, the shape of the CRISM ratio spectra shortward of 1 μm is consistent with the presence of crystalline ferric oxide minerals [e.g., *Morris et al.*, 2000]. In particular, a broad absorption centered near 0.82–0.86 μm is consistent with crystalline hematite. Variation of an iron oxide component absorbing between 0.8 and 0.9 μm is especially evident in unit 2 and suggests subunits of distinct ferric oxide + Al-phyllosilicate composition (e.g., units 2a/b in Fig. 2.2b).

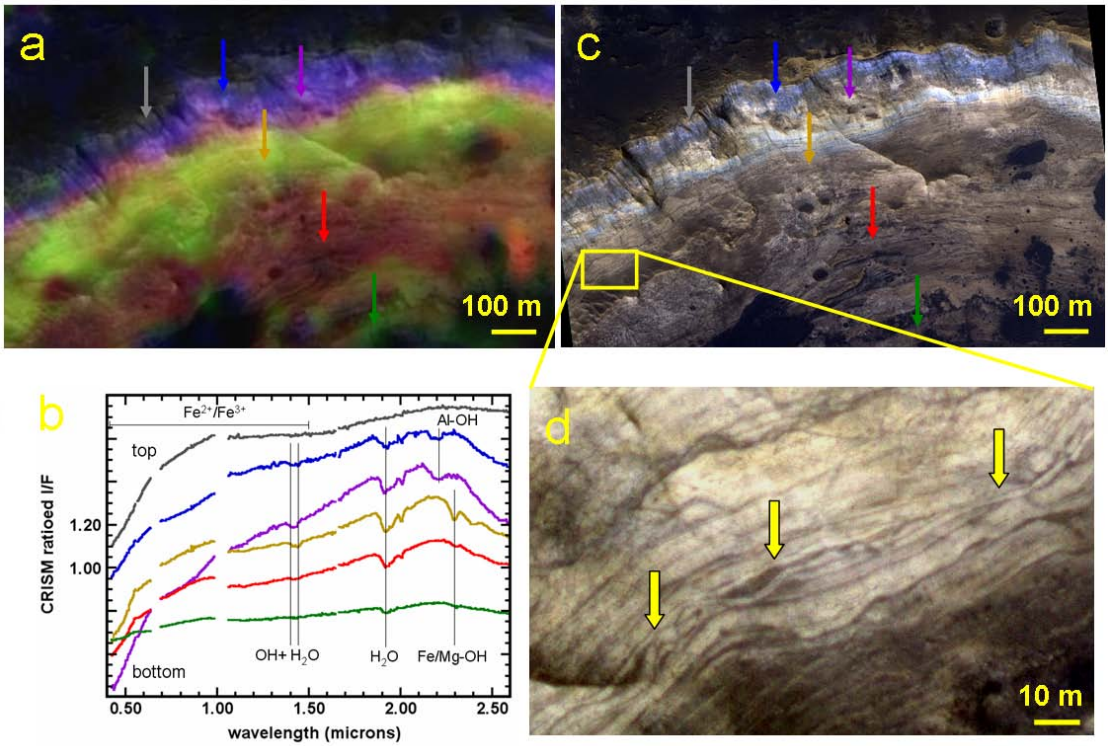

Figure 2.3: (a) Compositional stratigraphy exposed in the northern wall of a 4-km diameter crater. CRISM FRT 94F6 band depth overlain on HiRISE PSP_004052_2045 with colors as in Fig. 2.2. (b) CRISM ratio spectra of six distinct layers in (a). (c) Color HiRISE image of the crater wall, with IR/Red/Blue-green bands (~875/700/500 nm) mapped to R/G/B. (d) Some Fe/Mg-clay-bearing layers appear folded (e.g., arrows).

Despite this variability in visible/NIR spectral properties, some consistent trends are observed, with each of the four compositional units in Fig. 2.2 having a distinct color in HiRISE IRB images (Fig. 2.4); these display HiRISE IR (~875 nm), RED (~700 nm), and BG filter (~500 nm) images in the red, green, and blue channels, respectively [*McEwen et al.*, 2007, 2010]. In the default image stretch, unit 1 appears yellow, unit 2 blue-white, unit 3 tan, and unit 4 brown. Other CRISM-HiRISE image pairs across the region confirm that the Al-clay-bearing surfaces are generally bluer than Fe/Mg-clay-bearing surfaces. *Loizeau et al.* [2010] have confirmed a similar correlation between HRSC image color and phyllosilicate mineralogy derived from OMEGA.

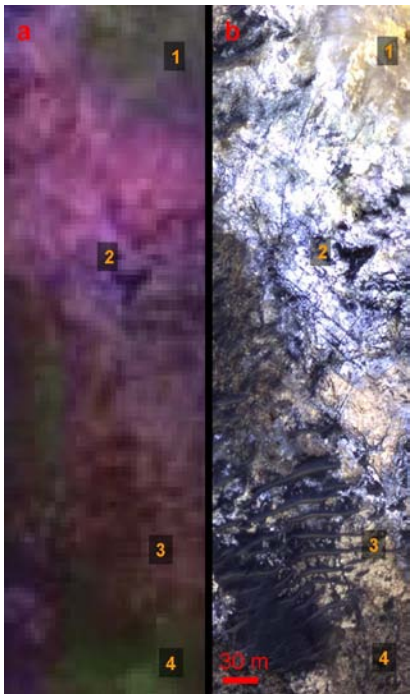

Figure 2.4: Compositional units (1–4) identified in Fig. 2.2 each have distinct color in HiRISE IRB images; (a) is from CRISM FRT 3BFB and (b) from HiRISE PSP_002140_2025.

The detailed mineralogy of the clay-bearing deposits at Mawrth Vallis is not the primary focus of this work, and several other studies concurrent or subsequent to

ours have explored this topic in depth [*Bishop et al*., 2008b; *Poulet et al.*, 2008b; *McKeown et al.*, 2009; *Noe Dobrea et al.*, 2010]. These studies confirm the above identifications of kaolinite and ferric oxides/hydroxides, and demonstrate that although nontronite is the most widespread clay mineral detected from orbit in this region, other Fe/Mg-phyllosilicates are also seen in some locations. *Bishop et al.* [2008b] also infer the presence of hydrated silica within the Al-clay-bearing deposits, and interpret the strong positive slope and/or concave-up curvature from 1 to 2 μm in some Mawrth spectra (e.g., units 2b and 3 in Fig. 2.2b, and the purple spectrum in Fig. 2.3b) as evidence for an unknown ferrous mineral. As these are the same spectra in which a crystalline ferric oxide component is inferred, a mixture of redox states may be represented in the mineralogy of these layers.

In summary, although subsequent sections emphasize the major dichotomy between Al-clay-bearing and Fe/Mg-clay-bearing materials at Mawrth Vallis, the mineralogy within each of these major units appears complex and variable.

2.4 Morphological Diversity

Although the four stratigraphic units in Fig. 2.2 were identified on the basis of mineralogy, each also has a distinctive morphology. Unit 1 (Fig. 2.2c) is cut by sparse fractures bounded by bright "halos;" similar features elsewhere on Mars have been interpreted as zones of localized alteration by subsurface fluids [*Okubo and McEwen*, 2007]. The brightness of the halos could reflect intrinsic higher albedo due to mineralogic alteration ("bleaching" or precipitation of secondary phases) and/or lesser cover by dark surficial fines; the latter scenario could result from a textural difference, or the "halos" may be high-standing due to erosional resistance provided by cements precipitated from fracture fluids. Dark halos are observed in some other locations (Fig. 2.5), and in some cases visible shadows indicate that the fracture-filling materials

are indeed now relatively high-standing (Fig. 2.6).

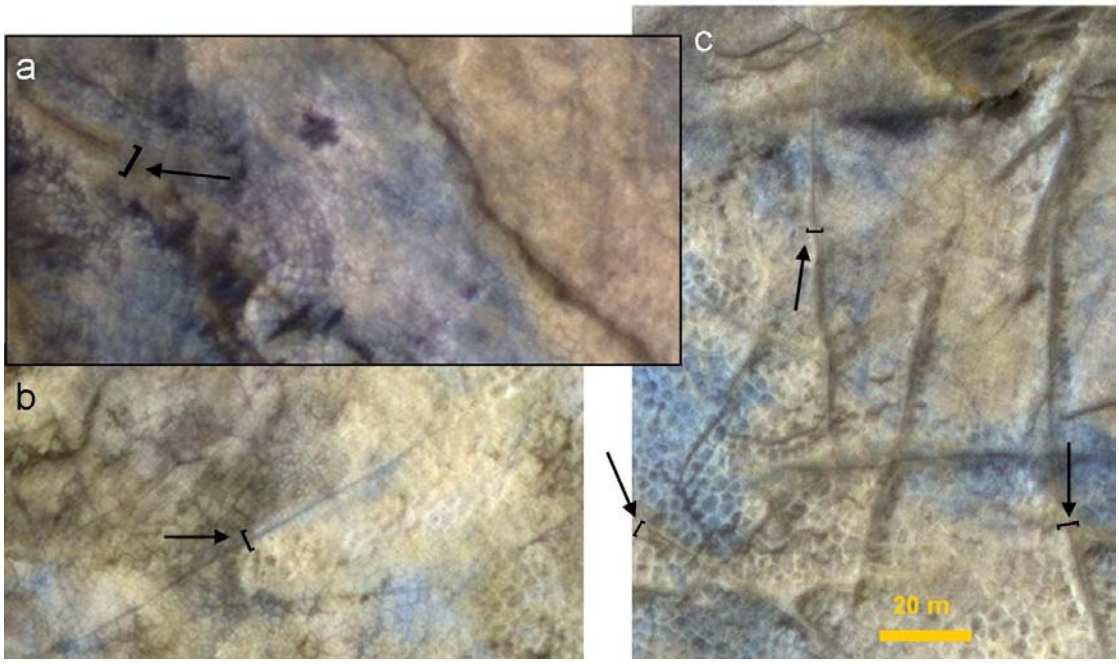

Figure 2.5: Sample dark (a) or bright (b, c) halos (arrows) surrounding fractures in light-toned rocks west of Mawrth Vallis (HiRISE PSP_008825_2040).

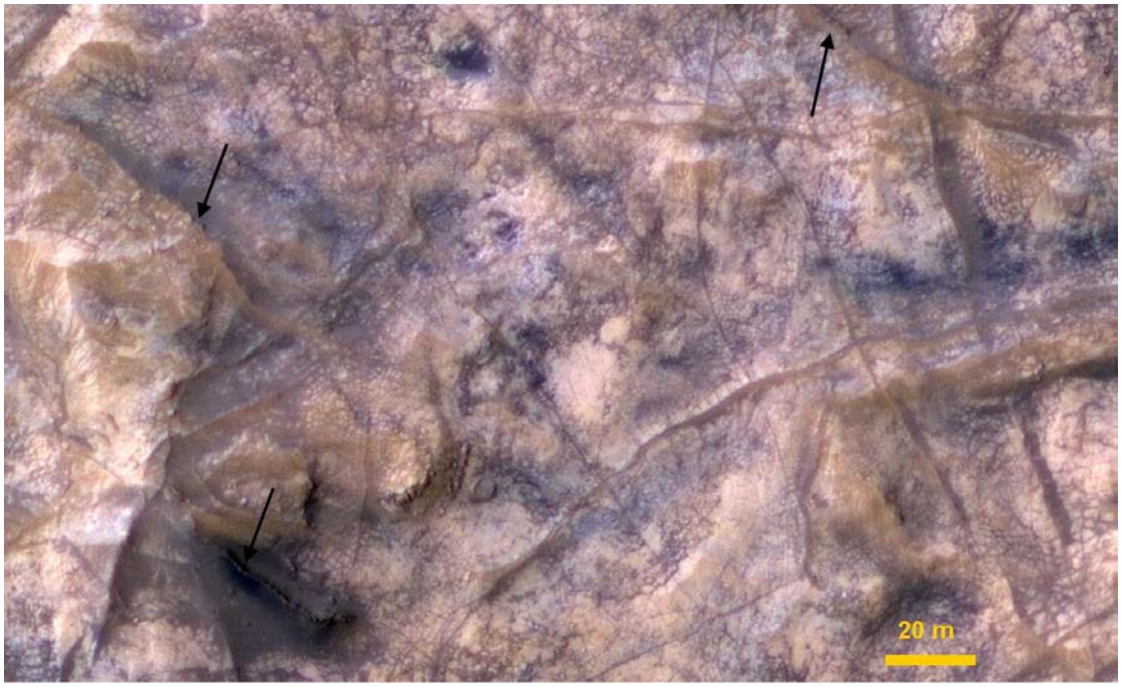

Figure 2.6: Dark fracture-filling materials in the Mawrth Vallis region (HiRISE PSP_008390_2050). Shadows indicate positive relief in some locations (arrows).

Units 2 and 3 (Figs. 2.2d and 2.2e) are fractured into polygons ranging in diameter from under a meter (unit 2) to 5–10 meters (unit 3). In some locations these have relatively dark rims (Fig. 2.2) and elsewhere relatively bright rims (Fig. 2.5c). Again, these could be intrinsic albedo differences or textural/topographic effects related to variable surficial cover; in some cases the bright rims appear relatively high-standing (Fig. 2.7a) while elsewhere their distinct colors (Fig. 2.7b) suggest the rims may differ mineralogically from the polygon interiors. Larger-scale polygons exceeding 100 m in diameter are found exclusively on the Mawrth Vallis floor where the channel bends northward (near CRISM HRS 307A in Fig. 2.1) [*Loizeau et al.*, 2007]. Elsewhere on Mars, formation of polygons within this broad size range has been attributed to freeze-thaw [e.g., *Seibert and Kargel*, 2001], thermal contraction in permafrost [*Mellon et al.*, 2008], desiccation of water-rich sediments [*El Maarry et al.*, 2010], or a range of rock weathering processes [*Chan et al.*, 2008]. Some of the polygons at Mawrth Vallis cut across layers (Fig. 2.8), favoring formation via rock weathering rather than processes penecontemporaneous with sedimentation.

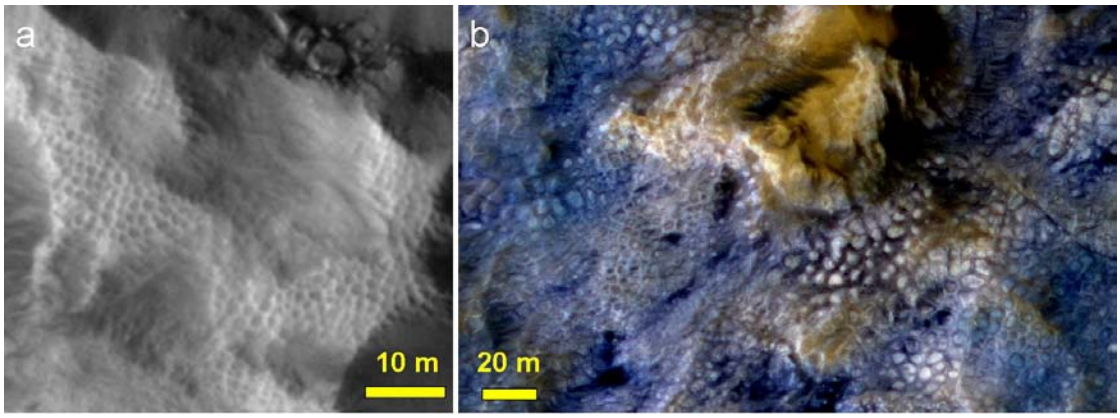

Figure 2.7: Bright-rimmed polygons near Mawrth Vallis. (a) Al-clay-bearing surface with polygon rims standing in positive relief (HiRISE PSP_002641_2025). (b) Polygons rims that differ in color from polygon interiors.

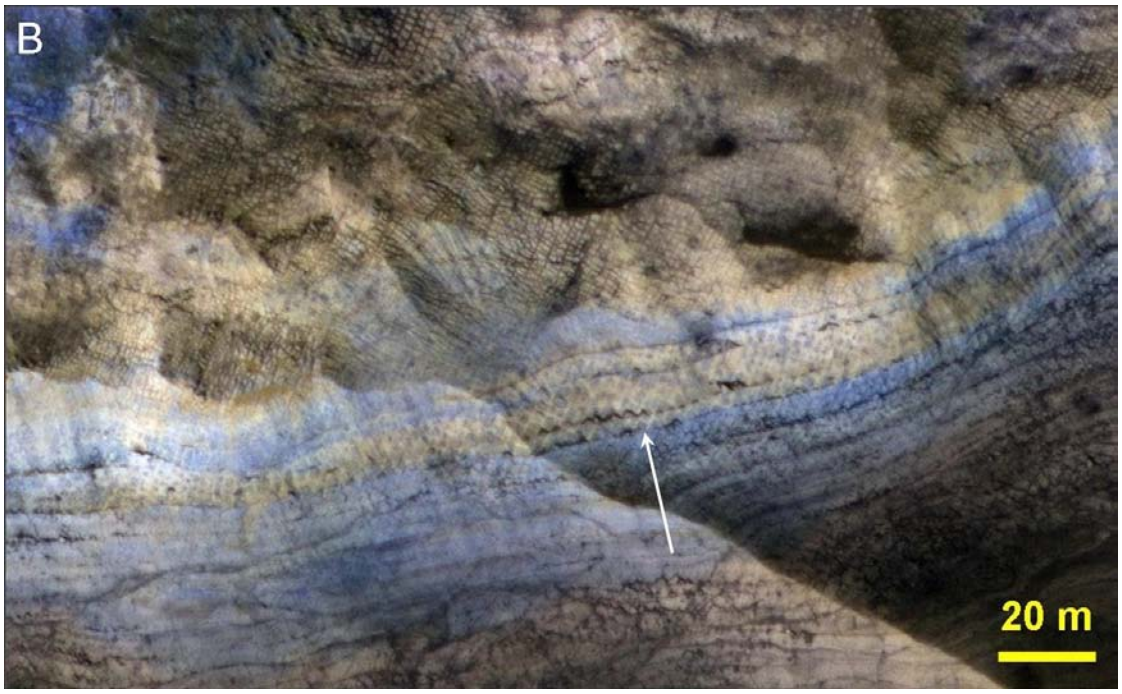

Figure 2.8: Polygons cutting across layers (e.g., arrow) exposed in the crater wall shown in Fig. 2.3c (HiRISE PSP_004052_2045).

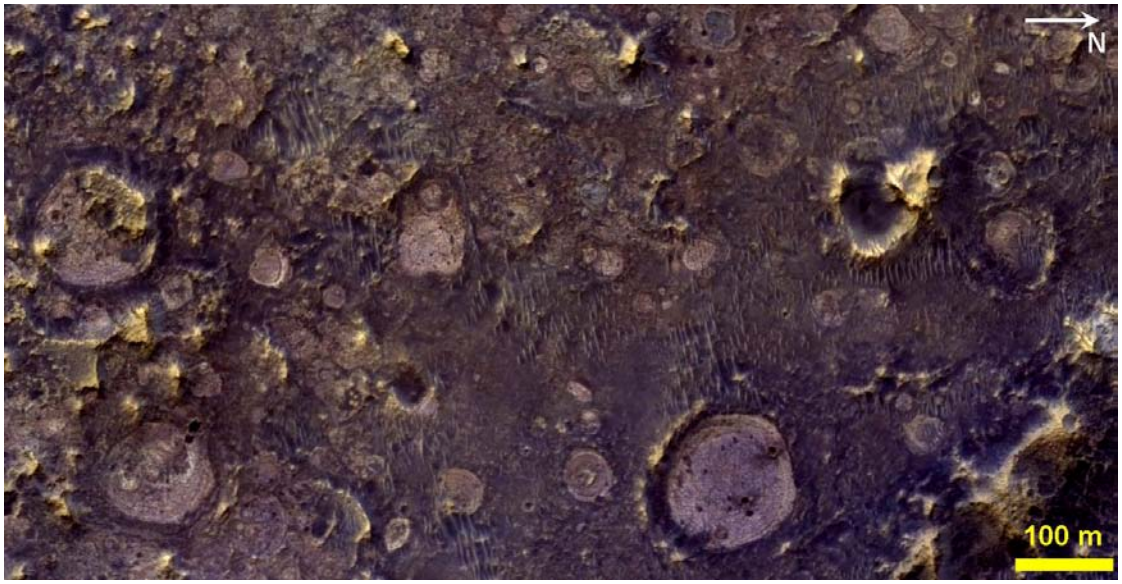

Figure 2.9: Quasi-circular features interpreted as degraded impact craters in Fe/Mg-phyllosilicate-bearing materials (HiRISE PSP_002641_2025).

Unit 4 (Fig. 2.2f) is densely fractured and has quasi-circular albedo features that may be degraded remnants of impact craters. In some cases their floors have the

colors of the overlying layers seen in adjacent mesas (Fig. 2.9), suggesting that the craters may have been buried by these layers and more recently exhumed by erosion. *Loizeau et al.* [2010] note that these quasi-circular features are typically observed at a high density as in Fig. 2.9 and suggest that these are ancient paleo-surfaces predating the clay-bearing layered deposits. However, *Michalski and Noe Dobrea* [2007] have noted that some buried craters—such as that shown in Fig. 2.10a—appear to occur within the layered deposits, implying deposition over an extended period of time.

Non-planar bedding structures are also resolved in a few locations. In one example west of the outflow channel, a ~4-km diameter crater exposes Fe/Mg-smectite-bearing layers, some of which appear deformed while adjacent layers are undeformed (Fig. 2.3d). A similar phenomenon is observed in some Fe-smectite-bearing layers on the outflow channel floor (Fig. 2.10b). The folded layers may have undergone syndepositional (e.g., soft sediment) deformation; alternatively, later tectonics could have preferentially affected these layers due to strain partitioning within weaker multilayers (e.g., where the bedding is thinner). For comparison, soft sediment deformation has been hypothesized to explain the larger-scale folds observed from orbit in some layered deposits of Valles Marineris [*Metz et al.*, 2010]. Alternatively, cross-beds deposited on a complex surface might explain the geometries observed in Fig. 2.3d. Relatively unambiguous cross-beds—and possible folds—are observed in layers on the floor of Oyama crater (Fig. 2.11).

All clay-bearing units in the Mawrth Vallis region are unconformably overlain by a darker, heavily cratered mantle deposit (e.g., Figs. 2.3 and 2.10a). *Loizeau et al.* [2007] report pyroxene in this mantle, whereas hydrated minerals are not observed. Although *Noe Dobrea et al.* [2010] describe this mantle's texture as "massive," it does exhibit internal bedding in places (Fig. 2.12).

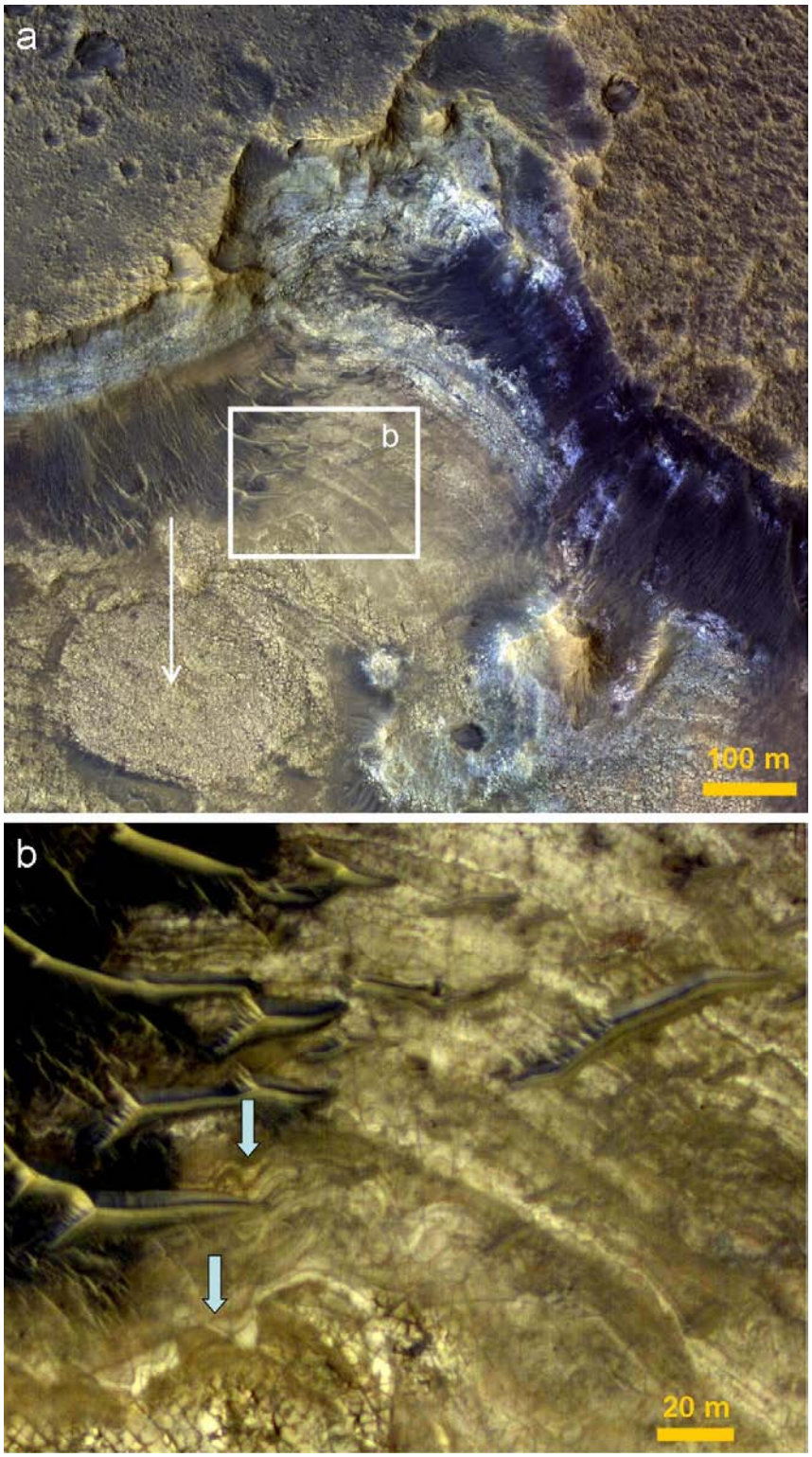

Figure 2.10: (a) Bluer layers overlying redder layers on the Mawrth Vallis channel floor (HiRISE PSP_001784_2030). The redder layers contain Fe/Mg-clays and a quasi-circular feature interpreted as an exhumed crater (arrow). (b) Deformed layers (arrows).

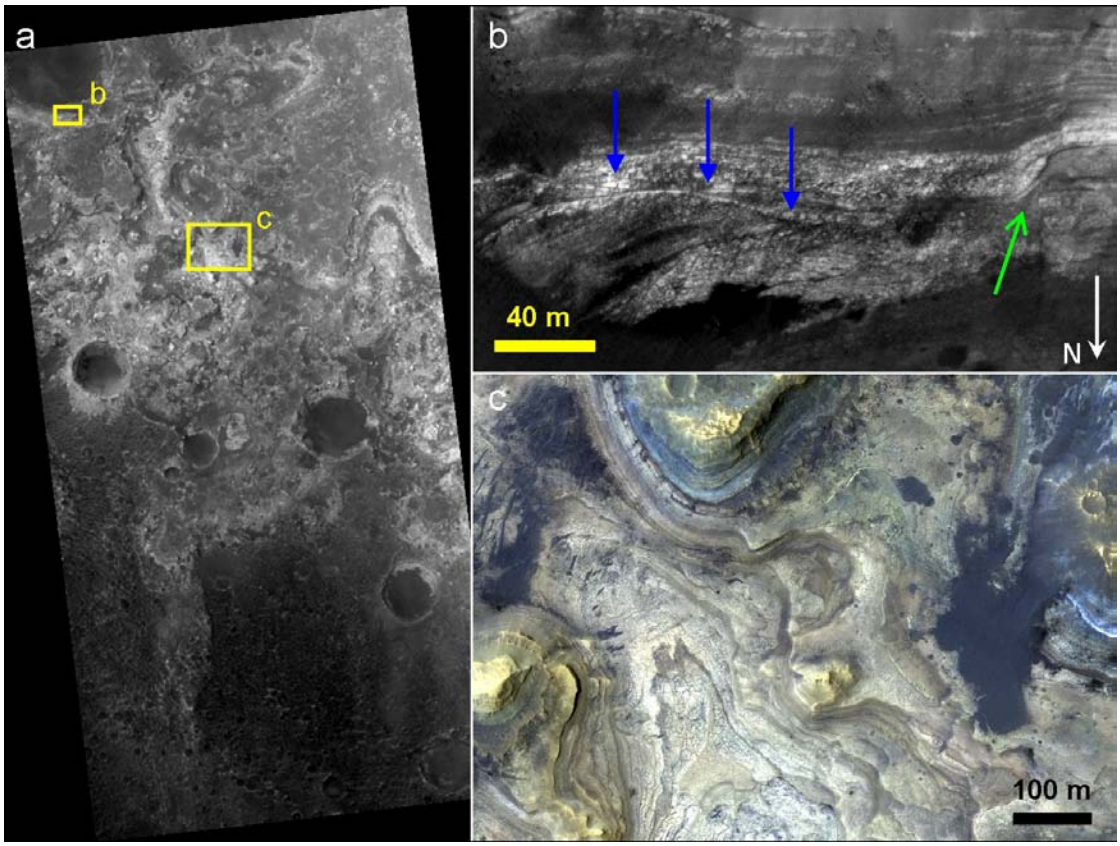

Figure 2.11: (a) HiRISE ESP_017963_2035 covering part of the southern floor of Oyama crater (see Fig. 2.1). (b) Non-parallel bedding (blue arrows) and possible fold (green arrow) in layers exposed in wall of small crater on Oyama floor. (c) Dozens of layers are exposed on Oyama's floor, with bluer layers overlying redder layers as elsewhere in the Mawrth region.

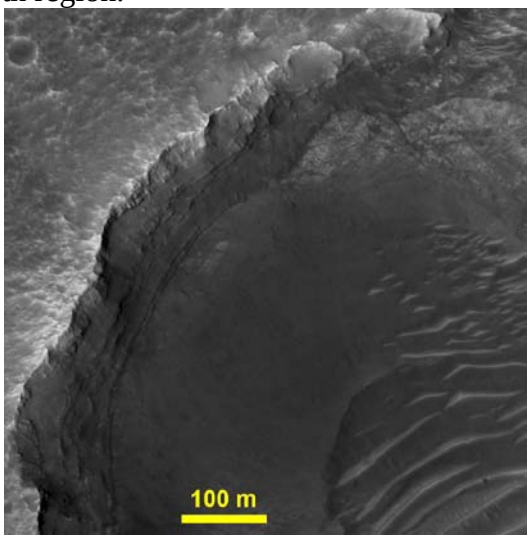

Figure 2.12: Layers within the dark mantling unit overlying lighter-toned Fe/Mg-clay-bearing materials, here exposed in a crater wall (HiRISE PSP_002140_2025).

In summary, diverse morphologies in the layered deposits at Mawrth Vallis suggest a range of depositional and post-depositional processes were active here.

2.5 Similarity of Layer Sequences

I have used coordinated HiRISE-CRISM observations to determine the compositional stratigraphy at each of the locations shown in Fig. 2.1. These include observations on both sides of the outflow channel and on its floor (HRS 307A). Both Al-clays and Fe/Mg-phyllosilicates are observed in every scene, and the Al-clays nearly always overlie the Fe/Mg-clays. An intervening hydrated unit analogous to unit 3 in Fig. 2.2 is seen in some cases, but not all.

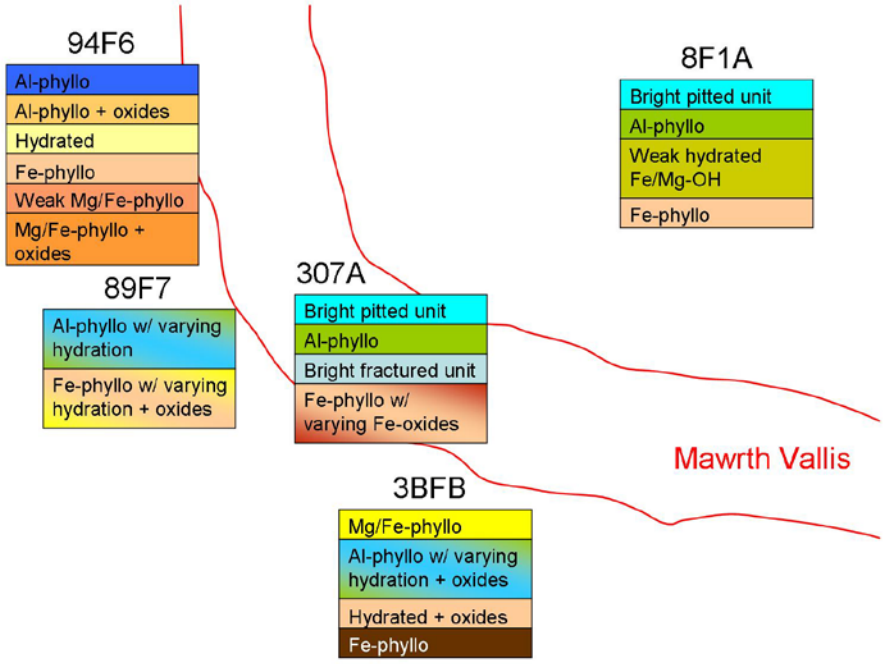

Figure 2.13: Color and compositional stratigraphy of light-toned deposits in those CRISM-HiRISE paired observations (Fig. 2.1) nearest the outflow channel. Al-phyllosilicates generally overlie Fe/Mg-phyllosilicates on both sides of the channel and on its floor.

Relatively blue layers (in HiRISE and HRSC color images) also typically overlie relatively red layers. The color stratification may be related to the

compositional stratification, but the two are not perfectly correlated: some relatively blue layers have no Al-clay spectral signature (e.g., those in Fig. 2.10a), and not all Al-clay-bearing layers are relatively blue (e.g., purple arrow in Fig. 2.3). Fig. 2.13 shows the geographic distribution of inferred stratigraphic columns (color and composition) for a subset of the locations in Fig. 2.1. At still other locations that lack CRISM data, HiRISE images can nevertheless be used to infer a stratigraphy analogous to that in Fig. 2.2 (Figs. 2.14, 2.15). Meter-scale layers exhibit diverse colors and suggest a mineralogically and/or texturally diverse sequence in detail, but the overarching trend is clear: relatively blue/Al-clay-bearing layers overlying redder/Fe-clay-bearing layers. This mineral stratigraphy is inverted in some impact crater ejecta, but the only other exception found to date is at the location shown in Fig. 2.2, where the Mg/Fe-phyllosilicate-bearing unit 1 overlies the Al-clay-bearing unit 2; however, unit 1 is spectrally distinct from typical Fe/Mg-smectites in Mawrth Vallis and may have formed through a different process. No observations to date show multiple Al-clay-bearing units separated stratigraphically by Fe/Mg-clay-bearing materials.

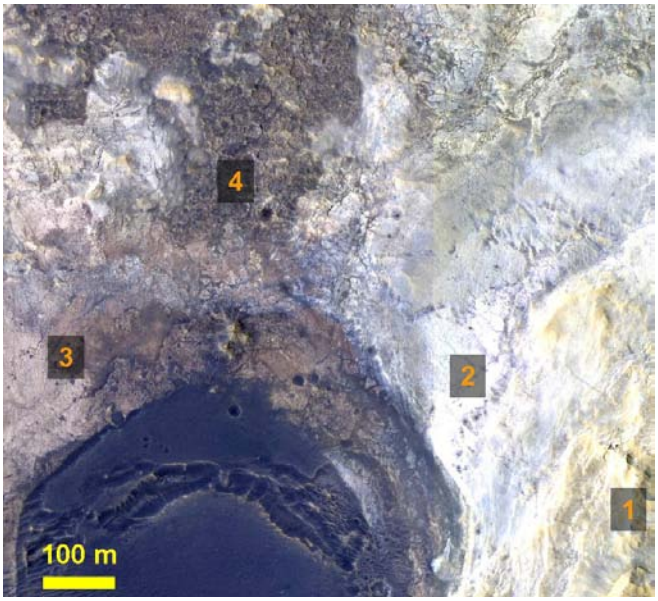

Figure 2.14: Color/morphological stratigraphy analogous to that in Figs. 2.2 and 2.4 is also observed ~50 km to the east (HiRISE PSP_002641_2025).

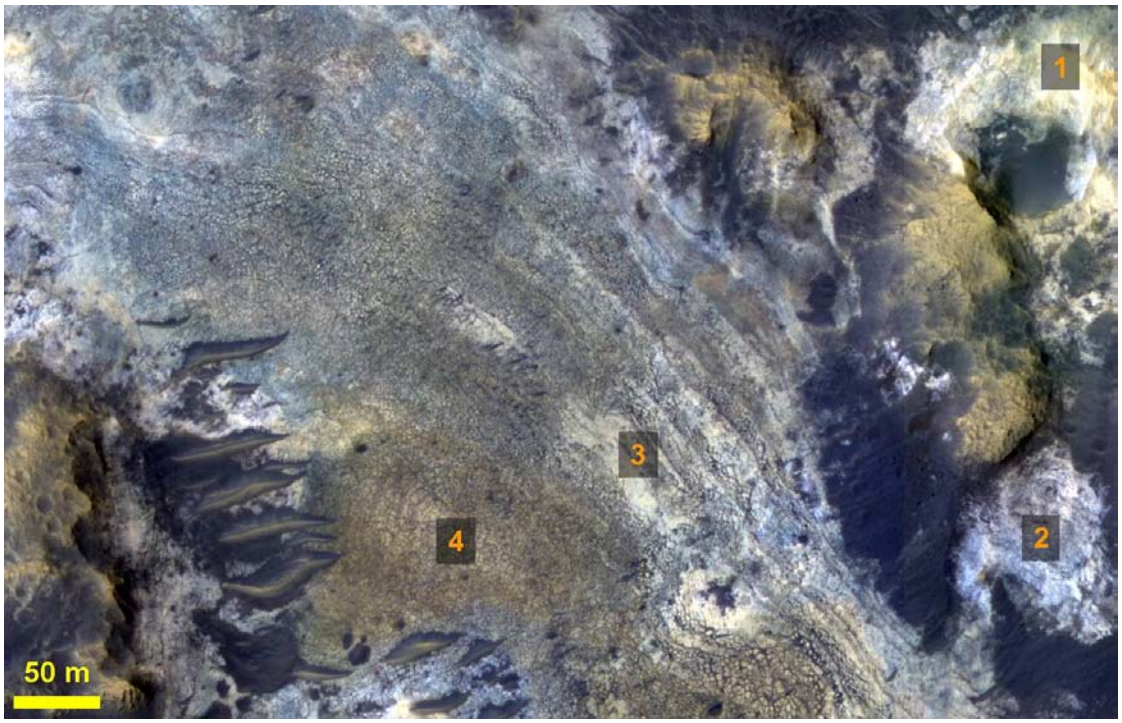

Figure 2.15: Color/morphological stratigraphy analogous to that found on the channel flank (Figs. 2.2, 2.4, 2.14) is also observed on its floor (HiRISE PSP_002140_2025).

These observations suggest the hypothesis that many or all of the Al-clay exposures in this region may be stratigraphically correlated in a single unit. This hypothesis can be tested with topographic data.

2.6 Topography

2.6.1 Regional geometry of compositional units

To probe the regional geometry of the clay-bearing layers, I use a digital elevation model (DEM) derived from an HRSC image by Alexander Dumke, according to methods outlined by *Dumke et al.* [2008]. The HRSC observation h1293_0000 (Fig. 2.16a) covers most of the Mawrth Vallis channel at ~50 m/pixel in the color bands. This does not resolve the fine-scale layering seen in HiRISE images (e.g., Fig. 2.3d), but the thicker color "horizons" depicted in Fig. 2.13 are resolved.

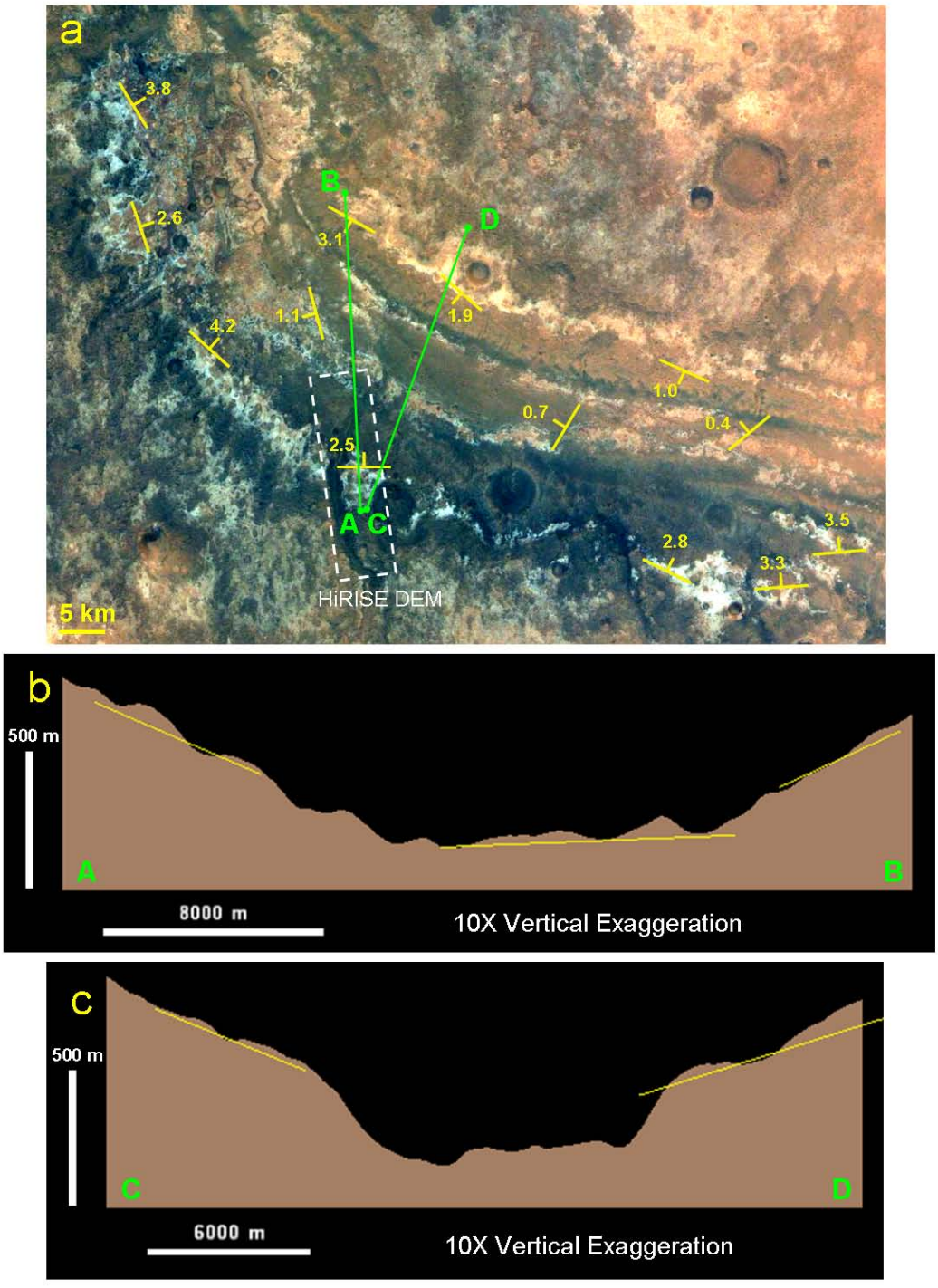

Figure 2.16: (a) A portion of the HRSC color image h1293_0000, showing southeast Mawrth Vallis. Strike and dip measurements (degrees) from the HRSC DEM are superposed. (b) HRSC elevation profile across channel walls and floor; measured contact orientations (yellow line segments) conform to channel topography. (c) Elevation profile displaying break in wall slope ~400 m above the channel floor, as discussed in the text.

The DEM from h1293_0000 has 50 m grid spacing. Strike and dip angles of contacts between units of different color in the HRSC color composite are measured using multi-linear regression to find the best-fit plane through a set of points. At least six points along a contact are used for each measurement shown here. All measured contacts are between relatively blue or white layers and underlying redder layers, interpreted to correspond (in most cases) to occurrences of Al-clays and Fe/Mg-phyllosilicates, respectively. These contacts may be equivalent to those between units 2/3 or 3/4 in Fig. 2.2, or 2/4 in cases where unit 3 is not observed; the relatively thin unit 3 cannot be clearly distinguished with HRSC data alone.

As Fig. 2.16 shows, the contacts exposed in both channel walls dip toward the channel floor, with typical dip angles ~3º. Dips range from 1.0º to 4.2º, with typical uncertainties of ~1.0º (95% confidence level). These dips are consistent with the average slopes of the unmantled upper channel walls (Fig. 2.16b); the measured contacts are exposed on locally steeper slopes. Contacts on the channel floor have measured dip angles <1º, dipping generally downstream.

The eastern half of the channel segment shown in Fig. 2.16a has a break in wall slope ~400 meters above the channel floor (Fig. 2.16c), below which both walls are steeper (~10º). However, the lower walls are completely obscured by the dark mantle deposit, so it is unknown whether the contacts dip more steeply here (as expected if they extend downslope to join similar contacts on the channel floor), or instead are cut by the lower channel walls. The possibility of repeating stratigraphic sequences that are cut by the channel yet hidden beneath the dark mantle cannot be ruled out, but such repeating sequences are not observed in CTX or HRSC images of the unmantled channel wall on the western side of Fig. 2.16a. The overall conformity of the exposed contacts to the topography of the channel walls and floor supports the hypothesis that the bluer, typically Al-clay-bearing outcrops occupy a single unit that

drapes over the outflow channel.

No contact between the redder, Fe/Mg-clay-bearing materials and any underlying units is observed consistently across the Mawrth Vallis region. The regional geometry of this unit therefore cannot be constrained, and its clays—and/or the layers containing them—may predate the outflow channel. This possibility is illustrated in the right panel of Fig. 2.17.

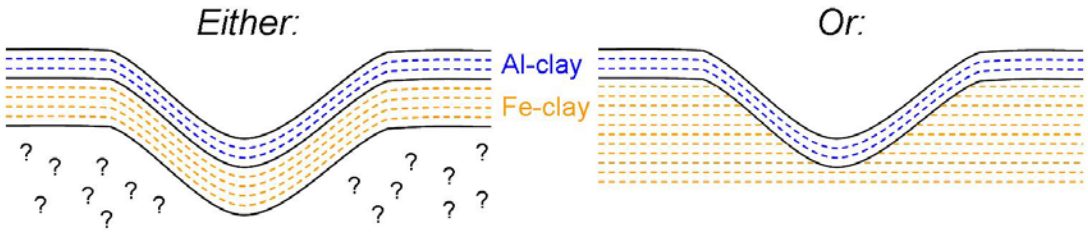

Figure 2.17: Stratigraphy and DEM measurements reveal that the Al-clays at Mawrth Vallis trace the topography of the outflow channel (shown here in cross section), but the base of the Fe/Mg-clay unit is rarely observed, permitting either of the two scenarios depicted.

2.6.2 Geometry of meter-scale layers

To verify the above HRSC measurements and to measure the geometries of individual layers of meter-to-decameter thickness, I now use a DEM derived from HiRISE images. The HiRISE DEM has 1 m grid spacing, and was derived by Mark Rosiek from images PSP_002074_2025 and PSP_002140_2025 via techniques described by *Kirk et al.* [2008]. This DEM covers an area of ~6x20 km on the southern channel wall (outlined in Fig. 2.16a), including the area of Fig. 2.2a.

By fitting planes to the unit 1/2 and unit 2/3 contacts, the true thickness of the Al-clay-bearing unit 2 has been measured at several points along the section shown in Fig. 2.2a, yielding a mean value of 41±14 m. The unit 2/3 contact has 3.2±0.6º dip, 24.8±12.1º dip direction (clockwise from North); the HRSC DEM measurement of the same contact yields a dip of 2.5±0.5º and dip direction of 0.5±13.9º. Similarly, the unit 3/4 contact has 2.9±0.7º dip and 12.9±14.1º dip direction in the HiRISE DEM.

These compositional unit geometries measured in the HiRISE DEM confirm the HRSC DEM measurement at this location.

From 14 individual layers within unit 2 spread across the HiRISE DEM, the average dip is 8.5º and the average dip direction 40º, notably steeper and slightly more easterly than the unit 2/3 contact. Measured layer dips range from 3.6º to 15.6º, with typical uncertainties ~2º (95% confidence level); dip directions range from 334º to 99º, with typical uncertainties ~17º. Examples of these measurements are shown in Fig. 2.18. Unfortunately, the other units—including the Fe/Mg-clay-bearing materials—exhibit few well-defined layers within the DEM, so their orientations cannot be compared to those of the layers in unit 2. Nevertheless, it is noteworthy that the compositional unit boundaries do not appear exactly parallel to the surfaces of individual meter-scale layers.

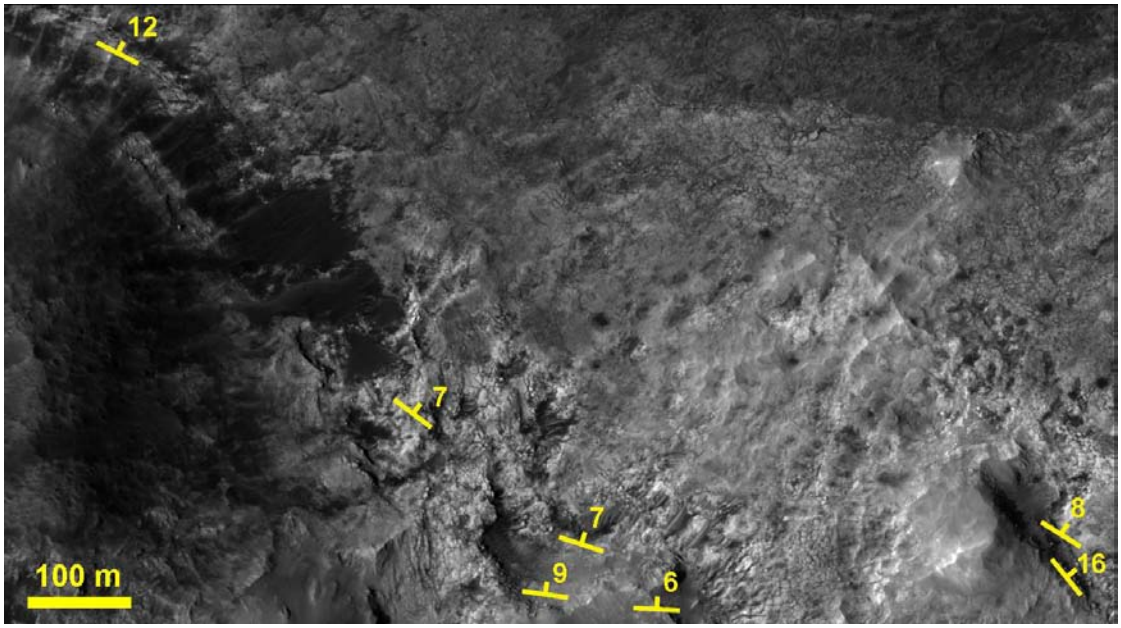

Figure 2.18: Portion of HiRISE PSP_002140_2025 showing a subset of strike and dip measurements (in degrees) made on Al-clay-bearing layers using HiRISE DEM.

2.7 Hydrated Sulfates

As mentioned in section 2.1, salt minerals might reasonably be expected to

accompany the phyllosilicates of Mawrth Vallis [e.g., *Milliken et al.*, 2009], but these have not been previously identified. *Bishop et al*. [2009b] recently reported weak absorptions at ~2.4–2.5 µm in phyllosilicate-dominated spectra from Mawrth Vallis that may be consistent with other secondary minerals as a lesser constituent of these rocks, but these spectral features could not be assigned to specific minerals. I therefore searched for locations in the Mawrth Vallis region in which hydrated salts are the spectrally dominant component.

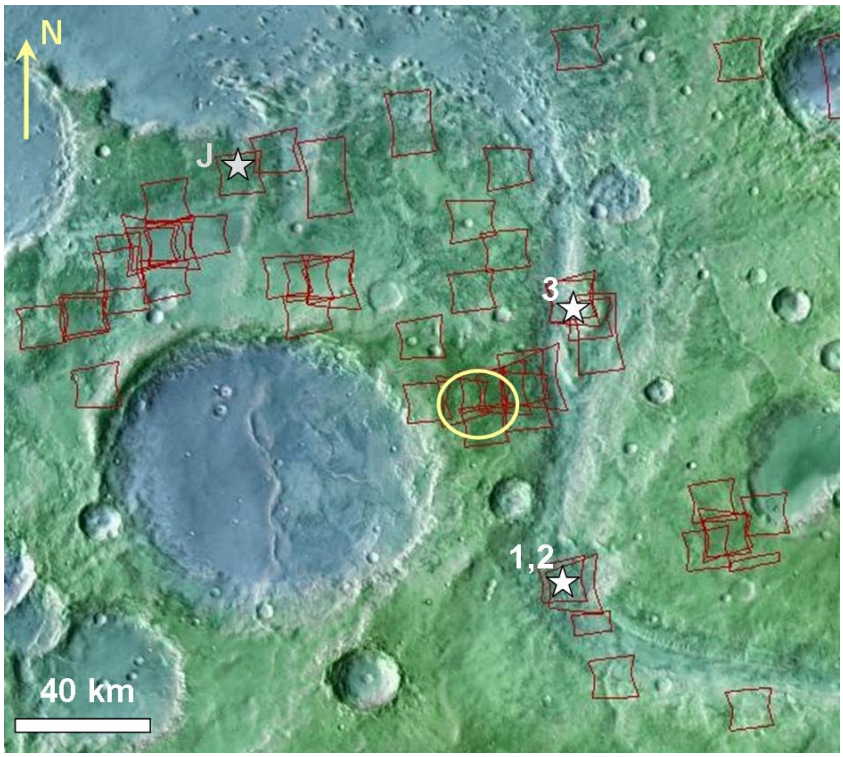

Figure 2.19: The region surrounding Mawrth Vallis (24°N, 341°E). CRISM targeted images acquired to date are outlined in red. Background is THEMIS daytime IR mosaic colorized with Mars Orbiter Laser Altimeter (MOLA) digital elevation model [*Smith et al.*, 1999]. Candidate Mars Science Laboratory landing ellipse (yellow, near center) is 25 by 20 km. The three locations with probable hydrated sulfate are numbered, while the location at which jarosite was identified by *Farrand et al.* [2009] is marked with a "J."

To identify promising CRISM observations, I examined browse products [*Seelos et al.*, 2008] for hyperspectral images widely distributed across the region (Fig. 2.19). Of particular interest were observations with spatially contiguous areas

highlighted by the BD1900 parameter, which tracks hydrated minerals, but not highlighted by the BD2210 or D2300 parameters that track Al- or Fe/Mg-phyllosilicates, respectively [*Pelkey et al.*, 2007]. Of greatest interest were those locations highlighted by the SINDEX parameter used to map hydrated sulfates [*Roach et al.*, 2009]. For these observations, CRISM data were processed as described in section 2.2, but using an updated atmospheric correction [*McGuire et al*., 2009] and a spatial and spectral noise filtering procedure developed by *Parente* [2008].

Three locations have spectra dominated by a non-phyllosilicate hydrated phase, all on the floor of Mawrth Vallis (Fig. 2.19). Spectra from these sites share strong bands at 1.91 and 2.48 μm (Fig. 2.20a), and they do not have the distinct absorptions at 2.2 or 2.3 μm characteristic of phyllosilicates (e.g., nontronite). The overall slope of these spectra from 1 to 2.5 μm is influenced by the choice of spectral denominator, but the positions of the 1.91 and 2.48 μm bands are independent of this choice. The same band positions are also observed in overlapping CRISM observations at each site (FRTs 9326, 10424, and 13E49 for sites 1 and 2; FRTs C872, 12D3C, and 12E72 for site 3).

Several different hydrated salts and zeolites have absorptions near 1.9 and 2.4–2.5 μm (Fig. 2.20a); however, Ca-sulfates provide the best match to the CRISM spectra. The spectrum from site 1 exhibits the strongest absorptions at 1.91 and 2.48 μm and has additional features including a doublet at 1.43 and 1.47 μm and weaker features at 1.77, 2.10, and 2.26 um. Together these spectral features are most consistent with bassanite ($CaSO_4 \cdot ½H_2O$). For comparison, gypsum ($CaSO_4 \cdot 2H_2O$) has a similar suite of absorptions at different wavelengths: 1.74, 1.94, 2.21, and 2.41 μm, with a broader triplet at 1.4–1.5 μm and a 1.2 μm band not observed in the spectrum from site 1. Some hydrated chlorides such as carnallite also have similar spectral features, but again their exact wavelengths are distinct from those observed

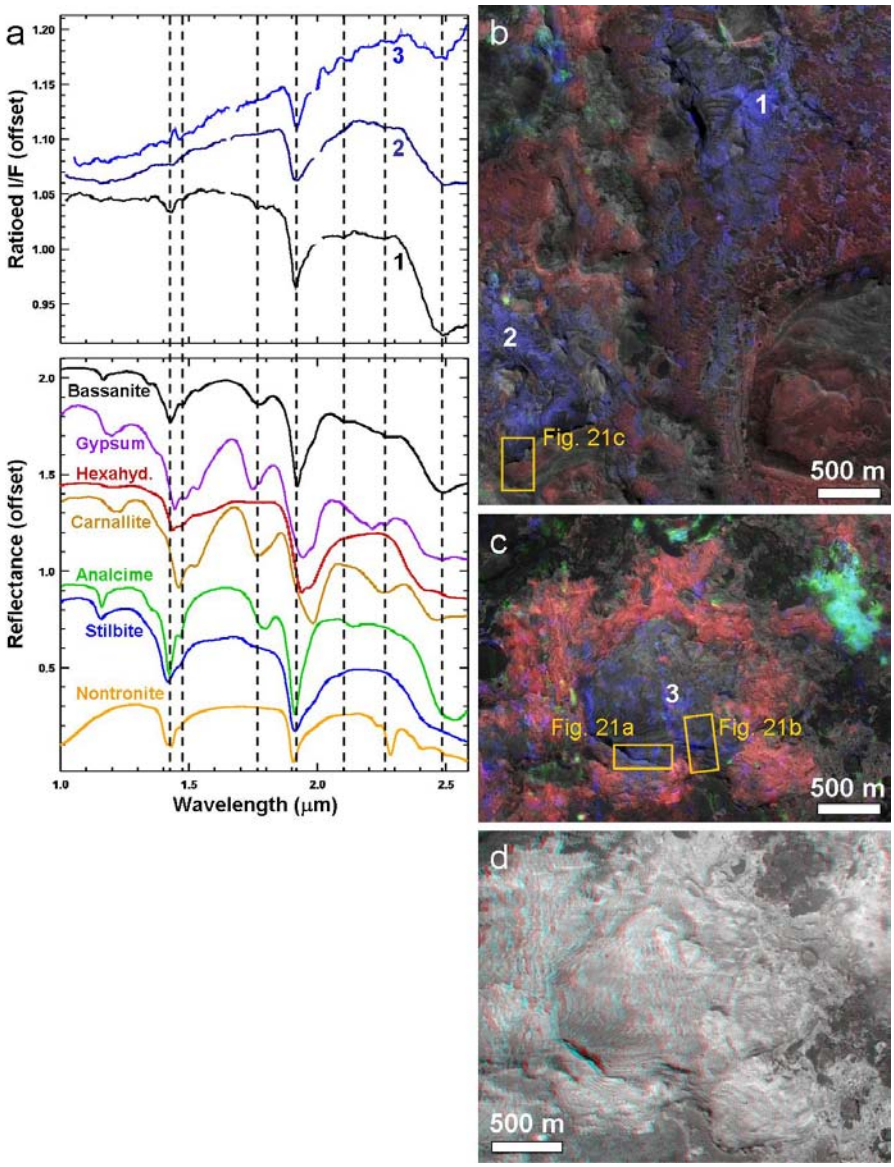

Figure 2.20: Spectra and locations of newly identified hydrated phase in Mawrth Vallis. (a) CRISM spectra (median-filtered) from Mawrth Vallis (top) and lab spectra of hydrated minerals (bottom). CRISM spectra correspond to numbered locations in (b and c). Spectrum 1 (FRT00009326) is most consistent with bassanite, while 2 (FRT00009326) and 3 (FRT00012E72) are less definitive and may be consistent with other hydrated salts or zeolites. Bassanite ($CaSO_4 \cdot ½H_2O$) is sample GDS145, gypsum ($CaSO_4 \cdot 2H_2O$) is HS333.3B, carnallite ($KMgCl_3 \cdot 6H_2O$) is NMNH98011, analcime (Na-zeolite) is GDS1, and stilbite (Na/Ca-zeolite) is GDS8 from *R. Clark et al.* [2007]; hexahydrite ($MgSO_4 \cdot 6H_2O$) is LASF57A and nontronite (Fe-smectite) is NBJB26 from CRISM spectral library. (b) CRISM FRT00009326 parameter maps overlain on HiRISE ESP_014007_2030; red is Fe/Mg-phyllosilicate, green Al-phyllosilicate, and blue a hydrated mineral with strong 2.5 μm band. See Fig. 2.19 for location. (c) CRISM FRT00012D3C on HiRISE ESP_013229_2050, colors same as in (b). (d) Stereo anaglyph covering same area as (c), from HiRISE ESP_013229_2050 and ESP_013295_2050.

here (Fig. 2.20a). Polyhydrated Mg-sulfates lack absorptions at 2.5 or 1.75–1.8 μm and are an even poorer match. Indeed, to my knowledge no measured hydrated salts share the narrow 1.91 μm and strong 2.48 μm absorptions of bassanite [e.g., *Crowley*, 1991].

Zeolites are also characterized by strong absorptions at ~1.4, 1.9, and 2.4–2.5 μm [*Cloutis et al.*, 2002], and their presence in the Mawrth Vallis region has been suggested on the basis of thermal infrared spectral analysis [*Michalski and Fergason*, 2009]. However, near-IR spectra of most zeolites have no distinct minimum longward of 2.4 μm nor a band in the 1.75–1.8 μm range [*Cloutis et al.*, 2002]. A counterexample is analcime, which has these two characteristics and has been identified elsewhere on Mars [*Ehlmann et al.*, 2009; see also chapter 3], but its band centers at 1.79 μm and 2.52 μm are distinct from those in the site 1 spectrum (Fig. 2.20a). No other mineral or combination of minerals in the CRISM or USGS spectral libraries has all the features in the observed spectrum; therefore, I conclude that the spectrum of site 1 indicates bassanite as the spectrally dominant component, although additional minerals that are featureless in this spectral range (e.g., anhydrous sulfates) could also be present. Spectra from site 2 and the noisier observations of site 3 are also consistent with—though less diagnostic of—bassanite, possibly in mixtures with Fe-bearing phases that could be responsible for the spectral curvature from 1 to 1.5 μm and the obscuration of the 1.4 μm absorption (Fig. 2.20a).

The BD2500 spectral parameter defined by *Ehlmann et al.* [2009] is well suited for mapping the bassanite at Mawrth Vallis. Comparing its mapped distribution to imaging and topographic data reveals that it is found in topographic depressions (e.g., Fig. 2.20d) that are surrounded by exposures of Fe/Mg-smectite (Fig. 2.20b,c). Although some of the bassanite could be erosional debris accumulating in these depressions, HiRISE images show that it also occurs in distinct layers (Fig. 2.21a) that

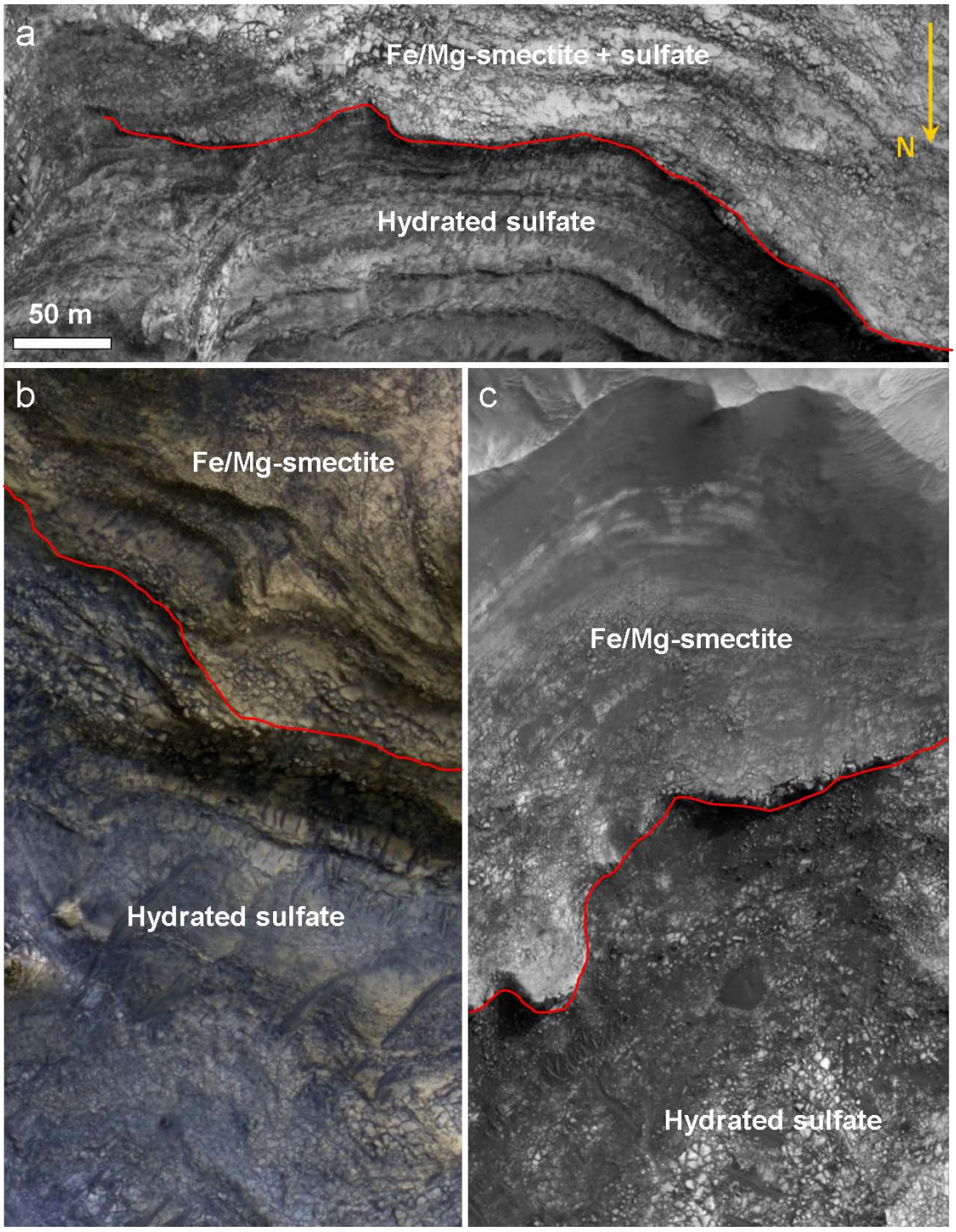

Figure 2.21: Meter-scale textures of probable sulfate-bearing layers and overlying smectite-bearing layers. (a) and (b) are from site 3 (see Fig. 2.20c for context); (c) is from site 2 (context in Fig. 2.20b). All panels have the same scale and have been rotated ~180º so that the downslope direction is toward the bottom. Red lines mark approximate mineralogic boundaries inferred from CRISM maps in Fig. 2.20b-c. (a,b) are from HiRISE ESP_013229_2050, (c) from ESP_014007_2030.

stratigraphically underlie the adjacent Fe/Mg-smectites (Fig. 2.21b,c). Stratigraphic boundaries between the smectite and sulfate range from gradual (Fig. 2.21a) to sharp (Fig. 2.21c) relative to CRISM resolution. Color images show that the areas with the strongest sulfate signatures are bluer than adjacent Fe/Mg-smectite-bearing materials (e.g., Fig. 2.21b), consistent with a lower Fe^{3+} content in the spectrally dominant mineral. The sulfate-bearing materials exhibit varying fracture patterns at scales of a few meters (Fig. 2.21a-c), and appear texturally distinct from the overlying smectite-bearing materials, suggesting different physical or chemical properties and/or a different modification history. The base of the sulfate-bearing strata is not observed, but exposures such as that in Fig. 2.21a suggest a thickness of at least a few meters, based on the scarp geometry and assuming the beds are approximately horizontal. Whether additional clay-bearing layers exist beneath the sulfates identified to date remains unclear.

2.8 Discussion

As the above results demonstrate, the spatial and spectral resolution of MRO instruments is well suited for studying compositional stratigraphy on Mars.

2.8.1 Clay stratigraphy

Our use of HRSC topography and the high-resolution stratigraphic analysis possible with CRISM and HiRISE leads us to different stratigraphic conclusions from most previous studies of the Mawrth Vallis region. Specifically, the result that the Al-rich clays at Mawrth Vallis may occupy a single unit (unit 2) that drapes the outflow channel differs from prior inferences that this region's clays predate the channel [*Poulet et al.*, 2005; *Loizeau et al*., 2007; *Michalski and Noe Dobrea*, 2007]. *Howard and Moore* [2007] reached a conclusion similar to ours, but they did not distinguish between units of different clay composition. The fact that blue, Al-clay-bearing layers

overlie redder Fe/Mg-clay-bearing layers on the floor of Oyama crater (Fig. 2.11c) suggests that the Al-clays also postdate Oyama's formation.

Mawrth Vallis is the oldest of the circum-Chryse outflow channels, with a Mid-to-Late Noachian age estimated from crater counts [*Ivanov and Head*, 2001]. Therefore, Al-clay formation or deposition here may still have occurred as early as the Late Noachian or Early Hesperian, consistent with the presence of the heavily cratered mantle overlying the clay-bearing units. Furthermore, if the Al-clay unit is sedimentary, then the clay-forming alteration event(s) may have occurred even earlier at another location, with subsequent erosion and transport carrying the clays to Mawrth Vallis. In this scenario, the subunits of distinct ferric oxide and Al-clay composition within unit 2 may reflect a changing sediment source. The Al-clay unit could alternatively be a pyroclastic deposit draping the outflow channel; volcanic glasses in such a deposit could be relatively easily altered into clays. However, the fact that individual layers within this unit do not conform to its base (the unit 2/3 contact) argues against airfall emplacement of these layers.

If the Al-clay-bearing layers postdate Mawrth Vallis and are superposed on the modern topography, then deposition in an ancient marine basin at this location is ruled out, as the modern topography preserves no evidence for such a basin. Marine deposition could only have occurred in a hemispheric ocean as described by *Edgett and Parker* [1997]; such an ocean would have needed to extend even farther south (to higher elevations) than Mawrth Vallis to explain the similar clay exposures recently identified in western Arabia Terra by *Noe Dobrea et al.* [2010]. There is little evidence for such an extensive ocean during the Late Noachian. Another hypothesis for the Mawrth layered deposits—that they are ejecta from the impact that formed the Chryse basin [*Tornabene et al.*, 2007]—is also ruled out if the layers postdate Mawrth Vallis, as Mawrth flows into Chryse and thus must postdate it.

An alternative hypothesis is that the Al-clay-bearing unit formed through *in situ* alteration—confined to the upper few decameters—of compositionally homogeneous materials during the Late Noachian. The layers could then be older than Mawrth Vallis, and the contact between the Al-clay-bearing unit and Fe/Mg-clay-bearing unit would represent an alteration front. *Noe Dobrea et al*. [2008b] were the first to hypothesize that the stratigraphy at Mawrth Vallis might record an alteration front, but they proposed a bottom-up process with Fe/Mg-smectite as an end product and the Al-clay-bearing horizons (inferred by them to be predominantly hydrated silica/glass) representing partial alteration of the dark-toned rocks capping the sequence. The detailed mineralogy and stratigraphy are inconsistent with this scenario, but a plausible alternative would be top-down alteration of preexisting Fe/Mg-rich rocks. Greater throughflow of water in the upper decameters could have leached Mg, Fe, and Ca cations, yielding a more Al-rich clay composition. This scenario would predict that the compositional horizons should crosscut the sedimentary layers; unfortunately, this is difficult to test definitively from orbit due to CRISM's low resolution compared to the thickness of the layers. Color variations are occasionally observed to crosscut layers (Fig. 2.22) but, as observed above, the colors do not always correlate perfectly with the clay mineralogy.

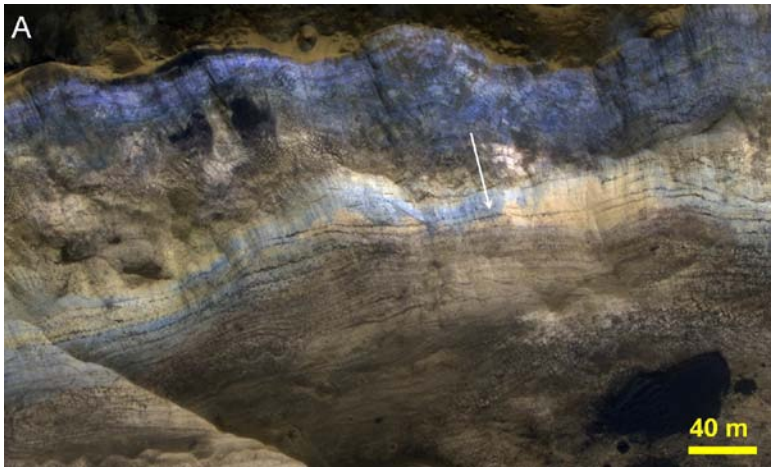

Figure 2.22: Color variations cutting across layers (e.g., arrow) exposed in the crater wall shown in Fig. 2.3c (HiRISE PSP_004052_2045).

2.8.2 Hydrated sulfates

On the basis of their distribution across terrains of different ages, *Bibring et al.* [2006a] proposed that Martian sulfates generally formed later than phyllosilicates. This hypothesis can be tested by observations of places where these two minerals are found in contact. Section 2.7 demonstrated that sulfate-bearing beds in Mawrth Vallis underlie the Fe/Mg-smectite-bearing beds, which had previously been identified as the lowest stratigraphic unit exposed in the region. Although the timing and location of smectite formation are unknown, the principle of superposition implies that the beds hosting the sulfates predate those hosting the phyllosilicates. These results and others discussed in subsequent chapters suggest that the alteration history of at least several regions on Mars may have been different or more complex than portrayed by the model of *Bibring et al.* [2006a].

However, an alternative explanation at Mawrth Vallis could be that sulfates formed in the subsurface coevally with (or after) phyllosilicates. Specifically, if at least some of the region's phyllosilicates formed via top-down weathering that leached mono- and divalent cations from the upper horizons, then these should have precipitated elsewhere in salts or oxides. Especially on Mars, Ca-sulfate is the least soluble of the expected salts [*Tosca et al.*, 2008a] and therefore could have precipitated in the lower horizons at Mawrth Vallis while more soluble salts—including the Mg/Fe sulfates that appear to dominate many equatorial layered deposits [e.g., *Gendrin et al.*, 2005]—were transported elsewhere either initially or after subsequent dissolution [*Milliken et al.*, 2009]. Even if bassanite in Mawrth Vallis formed only from the Ca liberated from smectite interlayer sites, leaching of the uppermost ~50 m of layered deposits ~50% nontronite by volume [*Poulet et al.*, 2008b] could have formed a ~meter-thick layer of pure bassanite. If additional Ca was leached from primary silicates and/or other minerals are present in the bassanite-

bearing unit (both likely), then its thickness could be greater. This hypothesis could be tested by future *in situ* observations of the Al-clay, Fe/Mg-clay, and sulfate-bearing layers; in particular, major element chemistry and microscopic textures would constrain whether the Al-clay horizons could have been the source of cations that combined with sulfate in solution to form the observed salts.

The detection of bassanite ($CaSO_4 \cdot \frac{1}{2}H_2O$) in Mawrth Vallis (23°N) is of interest to global studies of Ca-sulfates on Mars. Gypsum ($CaSO_4 \cdot 2H_2O$) has been found in circumpolar dunes at ~80°N [*Langevin et al.*, 2005] and in Columbus crater at 29°S (chapter 4); preliminary reports of gypsum in equatorial layered deposits [e.g., *Gendrin et al.*, 2005] have been refuted by subsequent analyses [*Noe Dobrea et al.*, 2008a; *Kuzmin et al.*, 2009; *Bishop et al.*, 2009a], although Ca-sulfates may be present in one portion of Noctis Labyrinthus [*Mangold et al.*, 2010]. Both Mars Exploration Rovers have also found evidence for Ca-sulfates, for which the orbital and surface remote sensing data are most consistent with anhydrite ($CaSO_4$) in both the rocks of Meridiani Planum at 2°S [*Clark et al.*, 2005; *Glotch et al.*, 2006] and the bright soils of the Columbia Hills at 15°S [*Johnson et al.*, 2007; *Lane et al.*, 2008]. Collectively, these observations suggest a general trend of increasing Ca-sulfate hydration with latitude, as might be expected if relative humidity and/or surface temperature are controlling the hydration state. However, the slow kinetics of Ca-sulfate hydration state changes under Mars-like conditions may prevent equilibration with the atmosphere [e.g., *Vaniman et al.*, 2008, 2009], as appears to be the case for Martian Mg-sulfates [*Roach et al.*, 2009].

Bassanite could instead have formed via dehydration from gypsum under a warmer paleoclimate [*Vaniman et al.*, 2009]. Other alternatives proposed by *Vaniman et al*. [2008] include bassanite formation under hydrothermal conditions, via burial diagenesis of gypsum, or from acid-sulfate alteration of preexisting calcium

carbonates. The range of hydration states observed across the planet may therefore reflect differences in precursor mineralogy and/or conditions of sulfate formation or diagenetic history. For example, Ca-sulfates were likely buried to hundreds of meters depth at Meridiani Planum [*Hynek et al.*, 2002] and Mawrth Vallis [*Loizeau et al.*, 2007, 2010; *Noe Dobrea et al.*, 2010], which may not have occurred in Columbus crater or the polar sand sea. *In situ* study of the minerals accompanying bassanite at Mawrth Vallis would help to distinguish between the diagenetic, hydrothermal, and acid alteration hypotheses for its origin. Once formed, bassanite may persist longer at the surface of Mars than it does on Earth because of the colder, more arid Martian conditions [*Vaniman et al.*, 2009].

Together with the jarosite recently identified by *Farrand et al.* [2009], bassanite adds to considerable mineralogic diversity of the Mawrth Vallis region as inferred from the spectra of its clay-bearing deposits. Mawrth Vallis is one of the final candidate landing sites for the Mars Science Laboratory (MSL) mission [*Grant et al.*, in press], for which it has been argued that an ideal site would provide access to both phyllosilicates and sulfates [*Grotzinger*, 2009]. Relative to the currently favored landing ellipse, *Farrand et al.*'s [2009] jarosite lies ~95 km from its northwest edge, whereas the hydrated sulfate site 3 discussed above is ~30 km to the northeast (Fig. 2.19). Additional CRISM coverage of the channel floor should be acquired to search for other sulfate exposures even nearer the ellipse. Intriguingly, a crater near the ellipse center exposes Fe/Mg-smectites underlain by a thin, relatively blue layer (Fig. 2.23); CRISM cannot resolve the mineralogy of this layer, but its color and stratigraphic position are consistent with the hydrated sulfates found elsewhere.

If the way is trafficable, driving MSL eastward and down into Mawrth Vallis would allow access to the more definitive sulfate exposures and would also enable a direct test of whether some or all of the region's phyllosilicates and layered deposits

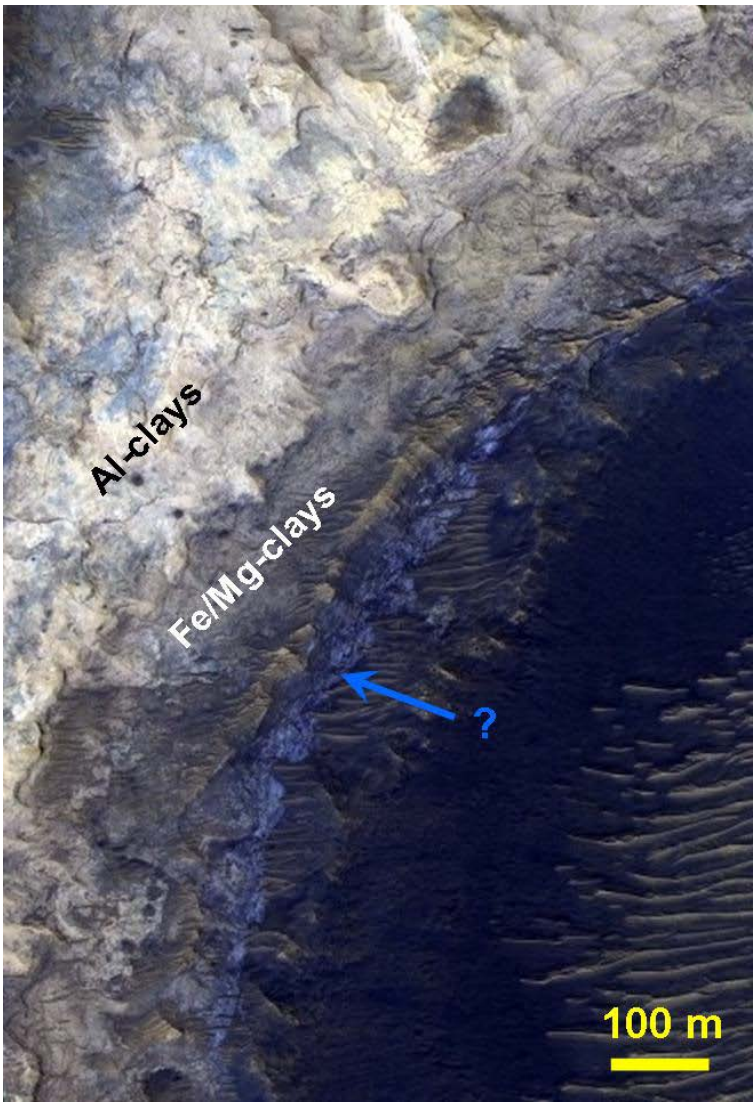

Figure 2.23: A ~2 km diameter crater near the center of the proposed MSL landing ellipse at Mawrth Vallis exposes layers of distinct color and composition along its northwest wall (HiRISE PSP_005964_2045).

predate the outflow channel or instead constitute a younger drape deposit, with significant implications for when and how these deposits formed. Regardless, the presence of diverse minerals in a clear stratigraphic sequence suggests that the layered materials at Mawrth Vallis record a time series of environmental change. This fact, in addition to the role of water in forming the mineralogies and morphologies visible at the surface today, is one of the best arguments for future exploration of Mawrth Vallis by surface missions seeking evidence for habitable environments on ancient Mars.

CHAPTER 3

DIVERSE HYDRATED MINERALS IN THE SOUTHERN HIGHLANDS[*]

3.1 Introduction

As discussed in previous chapters, OMEGA provided the first definitive orbital detections of hydrated minerals on Mars, including both phyllosilicates and hydrated sulfates [*Bibring et al.*, 2005]. At the scales to which OMEGA is sensitive (several kilometers and larger), phyllosilicate exposures are widespread but number only in the dozens, while outside the north polar region sulfates are detected only in a narrow band surrounding the equator east of Tharsis [*Bibring et al.*, 2006a; *Poulet et al.*, 2007]. To date, these two classes of hydrated minerals have rarely been found in close association; phyllosilicates are found in Noachian-aged terrains, and sulfates in younger terrains, leading to the inference that these mineral classes reflect distinct environmental conditions characteristic of different periods in Martian history.

More recently, the higher resolution of CRISM has enabled further discoveries including several new phyllosilicate minerals and a large number of new exposures, particularly in the Noachian southern highlands [*Mustard et al.*, 2008], although a few large craters scattered across the northern lowlands also expose hydrated silicates [*Carter et al.*, 2010]. Carbonate has also been identified, though so far only adjacent to the Isidis basin (e.g., near the Nili Fossae) [*Ehlmann et al.*, 2008b]. At even smaller scales, landed missions have identified diverse alteration minerals including sulfates far from the sulfate regions mapped by OMEGA [e.g., *Yen et al.*, 2008]. CRISM data now enable a re-evaluation of the planetary-scale distribution of hydrated minerals, at higher resolution than was previously possible.

[*] Much of the work described herein was originally published by Wray, J. J., et al. (2009), Diverse aqueous environments on ancient Mars revealed in the southern highlands, *Geology, 37*(11), 1043–1046, doi:10.1130/G30331A.1; or by Wray, J. J., and B. L. Ehlmann, Geology of possible Martian methane source regions, *Planet. Space Sci.*, doi:10.1016/j.pss.2010.05.006, in press.

This chapter describes a survey of CRISM observations in the southern highlands, a largely Noachian terrain [*Scott and Carr*, 1978] on which the surface morphology provides evidence for past liquid water in the form of abundant valley networks [e.g., *Carr*, 1995]. Other authors have previously or concurrently studied hydrated minerals in Terra Tyrrhena [*Mustard et al.*, 2008], Eridania basin [*Noe Dobrea et al.*, 2008c], Argyre basin [*Buczkowski et al.*, in press], and Holden crater and connected basins [*Milliken and Bish*, 2010]. This chapter focuses on new detections elsewhere in the Noachian southern highlands, particularly in Noachis Terra and from Icaria Fossae westward through Sirenum, Cimmeria, and northern Promethei Terrae (Fig. 3.1). Very few detections of hydrated minerals have previously been reported across these vast Noachian terrains [*Bibring et al.*, 2006a; *Poulet et al.*, 2007], even in more recent OMEGA studies concurrent with this work [*Carter et al.*, 2009]. This CRISM-based survey will determine whether these regions truly lack phyllosilicates or merely expose them at smaller scales, and whether hydrated sulfates or carbonates occur in these regions distinct from where they were initially identified.

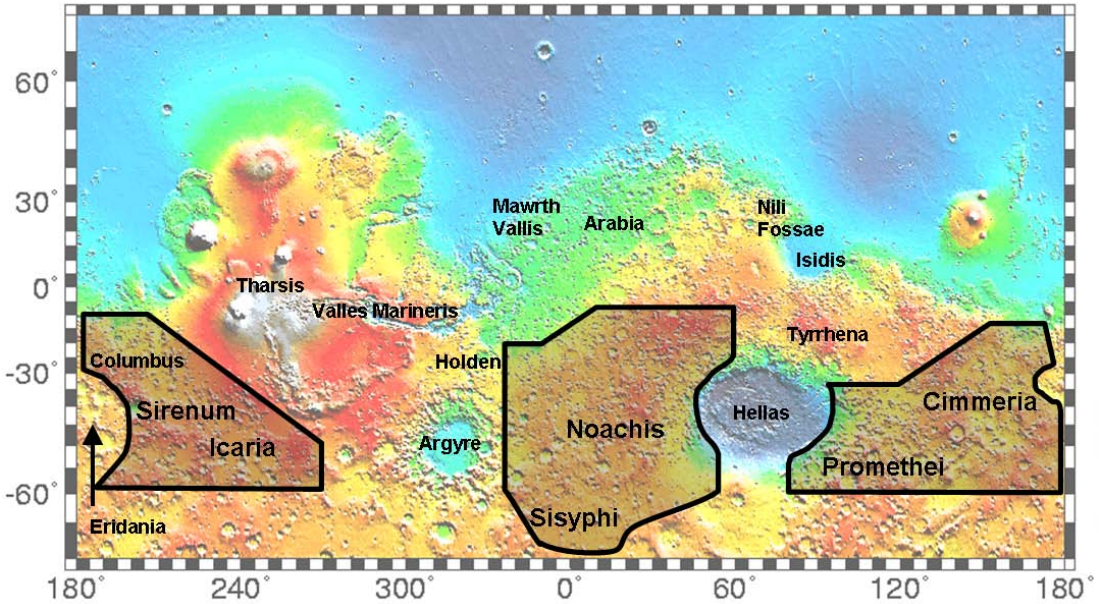

Figure 3.1: Regions surveyed with CRISM (shaded) and other locations mentioned in the chapter. Background is MOLA shaded relief topography [*Smith et al.*, 1999].

3.2 Survey Description

I examined browse products [*Seelos et al.*, 2008] for all CRISM targeted observations in the regions of interest (Fig. 3.1) that were released to the PDS through June 2008, searching for spatially contiguous areas with absorptions characteristic of H_2O- or OH-bearing minerals. These absorptions were subsequently confirmed by plotting CRISM spectra processed as described in section 2.2. Strong, narrow spikes in the spectra have been interpolated over to remove obvious artifacts. In addition, a subset of the parameter maps and spectra shown in the figures have been processed using the spatial and spectral noise-filtering algorithm of *Parente* [2008]. For regional context, I have also surveyed all multispectral map tiles in the regions of interest released through September 2008, and have examined newer hyperspectral observations in areas where hydrated minerals were found by the initial survey. Where available, images from CTX and HiRISE have been used to interpret the morphology, stratigraphy, and possible geologic settings of hydrated mineral exposures.

In a few locations analyzed, the spectra do not allow identification of specific hydrated minerals. For example, Alga crater in southern Margaritifer Terra exposes megabreccia (Fig. 3.2A) with strong olivine and pyroxene signatures, but in some cases these mafic-rich blocks show evidence for alteration (Fig. 3.2B). By itself, the 1.9 μm H_2O band is not diagnostic of a particular hydrated mineral. Fortunately, most hydrated materials found in the southern highlands display additional spectral features allowing their classification as hydrated silicates (mostly phyllosilicates), hydrated sulfates, or carbonates. Each of these classes is discussed in a separate section below.

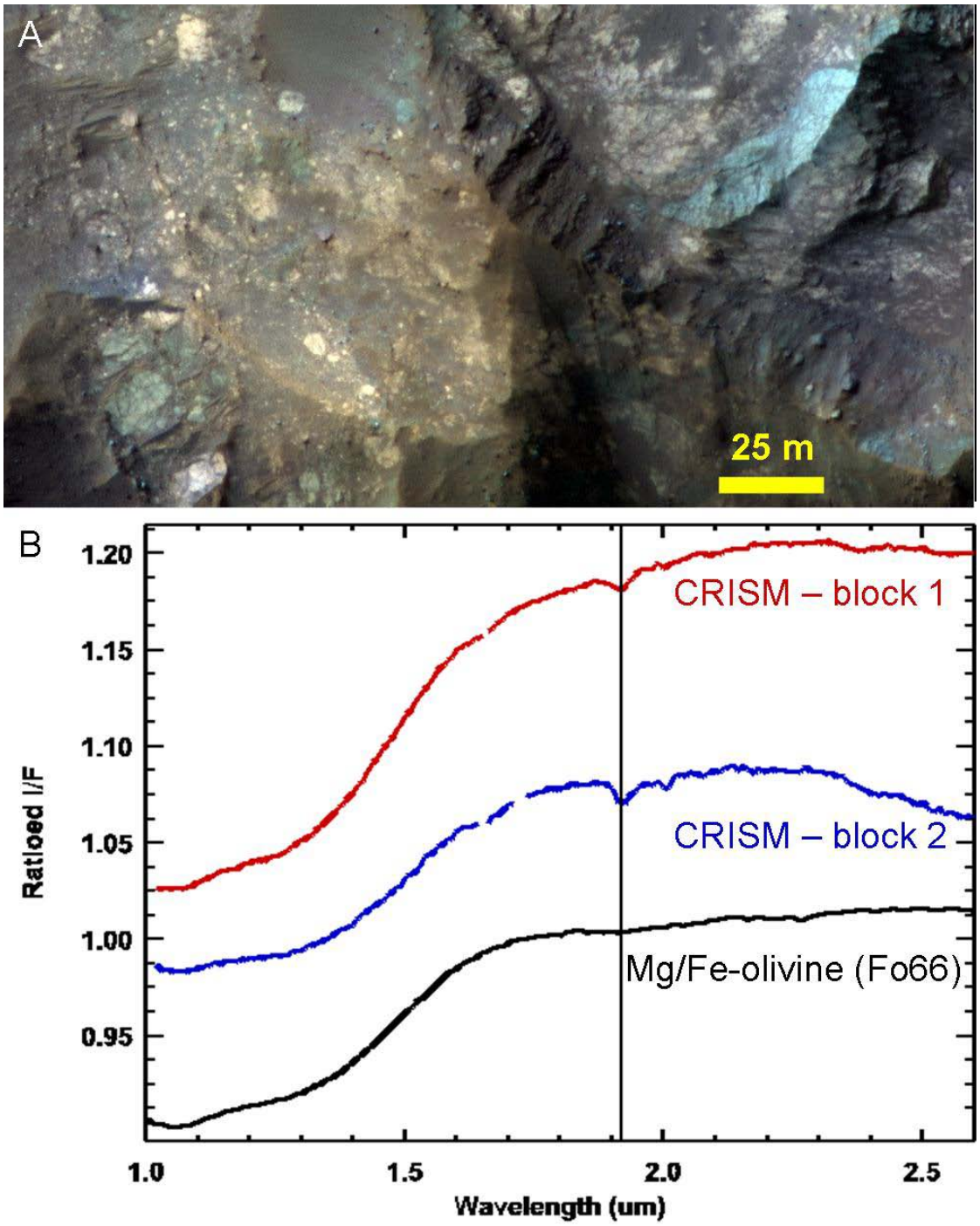

Figure 3.2: Alga crater central uplift exposes (A) megabreccia (HiRISE PSP_007573_1555), including blocks with (B) olivine spectral signature overprinted by minor hydration, as indicated by 1.92 µm absorption (CRISM FRT00006415), which is not present in the lab spectrum of olivine (KI3054 from *R. Clark et al.* [2007]).

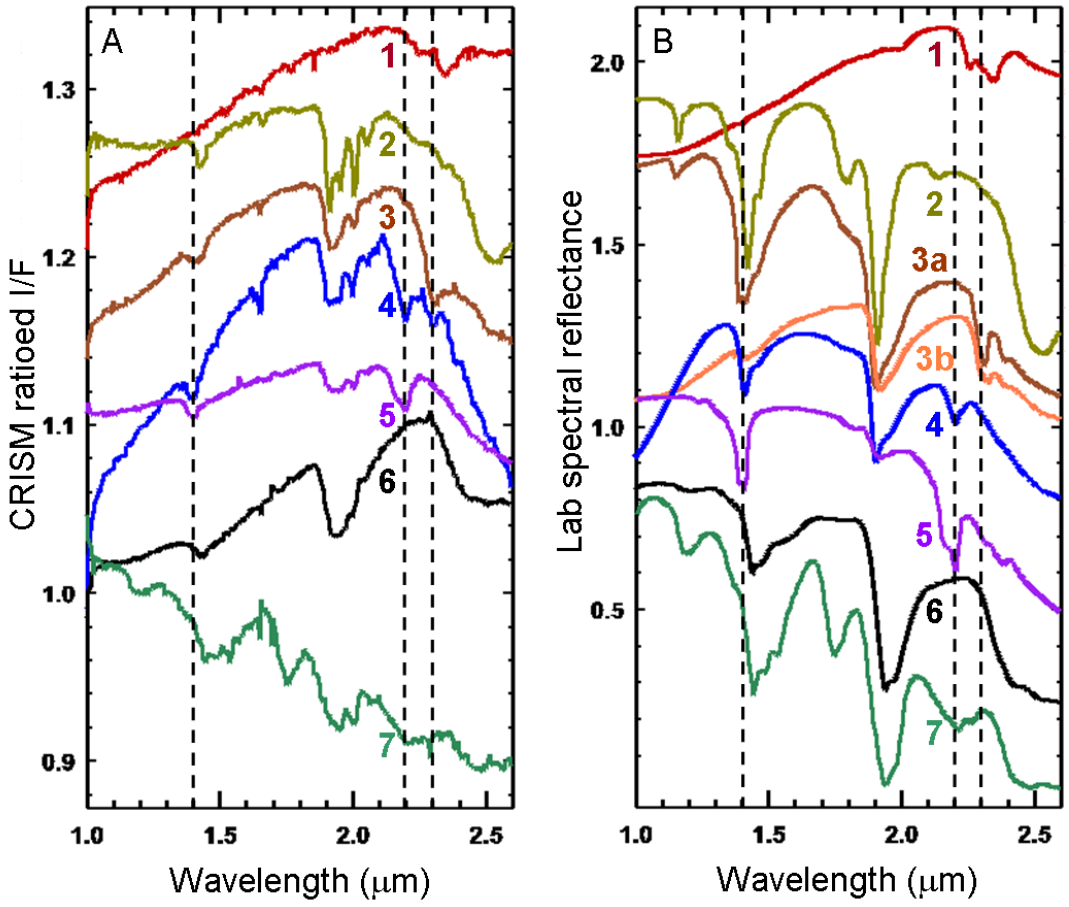

Figure 3.3: Hydrated mineral spectral diversity. (A) CRISM ratio spectra, offset for clarity: (1) Crater in northwest Cimmeria (FRT00008573); (2) Crater in southeast Cimmeria (FRT00009824); (3) Sirenum intercrater plains (FRT00009AAA); (4) Northeast Noachis (FRT0000A2B8); (5–7) Columbus crater (FRT00007D87). Spectrum 3 multiplied by 0.5, and spectrum 7 by 3, for ease of comparison. Spectrum 6 was used as the ratio denominator for spectrum 7, in order to isolate the signature consistent with gypsum in 7. (B) Library mineral spectra with similar absorptions, offset for clarity: (1) Fe-rich clinochlore (chlorite); (2) analcime (zeolite); (3a) saponite; (3b) vermiculite; (4) montmorillonite; (5) kaolinite; (6) hexahydrite (Mg-sulfate); (7) gypsum.

3.3 Phyllosilicates

Among the hydrated silicates observed, Fe/Mg-phyllosilicate is most common overall, consistent with previous OMEGA and CRISM findings [*Bibring et al.*, 2006a; *Mustard et al.*, 2008]. This class is distinguished by spectral absorptions at 2.28–2.35

μm. Absorptions longward of 2.32 μm, coupled with a band at 2.25 μm and a weak to absent hydration band at ~1.9 μm (Fig. 3.3), are consistent with library spectra of chlorites [e.g., *Bishop et al.*, 2008a]. Much more common on Mars are bands at 2.28–2.31 μm in combination with a 1.9-μm band, consistent with an Fe or Mg-smectite such as nontronite or saponite; however, these smectites typically cannot be definitively distinguished by CRISM from the Mg-clay sepiolite [e.g., *Milliken*, 2008]. In addition, an asymmetry in the 2.3-μm band common in CRISM spectra (Fig. 3.3A) is not well-matched by smectite library spectra, and it may indicate a smectite-chlorite mixed-layer clay [*Milliken and Bish*, 2010], the Fe/Mg-mica vermiculite (Fig. 3.3B), and/or the Fe-phyllosilicate hisingerite [*Milliken*, 2008]. Less common Al-phyllosilicates are identified by absorptions at 1.4 and 2.2 μm that appear as doublets in kaolinite group clays and singlets in montmorillonite [*Bishop et al.*, 2008a].

Chlorite is found almost exclusively in the ejecta, walls/terraces, and central uplifts of large (tens of kilometers in diameter), complex impact craters in Noachis and Cimmeria Terrae (Fig. 3.4A). One exception is a sedimentary crater floor deposit north of Hellespontes Montes (38.3°S, 42.1°E) that contains chlorite along with Fe/Mg-smectite and hydrated silica, the latter identified by a broad absorption centered near 2.2 μm that extends past 2.3 μm [e.g., *Milliken et al.*, 2008]. Chlorite has also been reported in association with large impact craters in Terra Tyrrhena and west of Nili Fossae [*Ehlmann et al.*, 2009]. As in Nili Fossae, several large craters in my survey regions contain a distinct hydrated phase in addition to chlorite; strong absorptions at 1.4 μm, 1.9 μm, and particularly a broad band at ~2.5 μm (Fig. 3.3) are most consistent with the Na-zeolite analcime [*Clark et al.*, 1990], while weak bands at 2.25 and 2.35 μm suggest sub-pixel mixing with chlorite. Chlorite and zeolite may have formed in impact-generated hydrothermal systems, or via diagenetic/metamorphic alteration at depth, subsequently exposed by the impact

process [*Ehlmann et al.*, 2009]. While these minerals are most commonly observed in areas of the highlands bordering the Isidis and/or Hellas basins, several examples far from large impact basins are found in eastern Terra Cimmeria (e.g., CRISM image FRT00009824 at 38.1°S, 171.2°E).

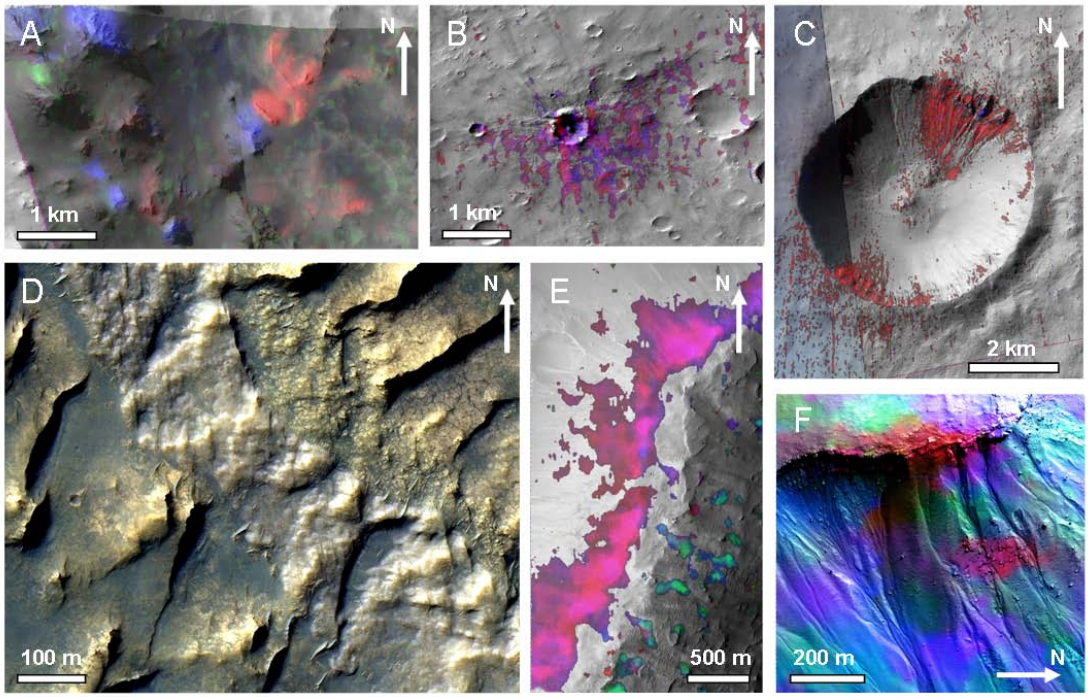

Figure 3.4: Clays in the southern highlands. (A) Chlorite (red), Al-clay or hydrated silica (green) and pyroxene (blue) exposed in crater central uplift, Cimmeria (FRT00008573 on HiRISE PSP_007857_1475 and PSP_005787_1475; 32.0°S, 140.7°E). (B) Fe/Mg-clay (purple) in ejecta of small, fresh crater (note dark radial rays), northeast Noachis (FRT0000B26C on PSP_008889_1640; 16.0°S, 36.9°E). (C) Fe/Mg-clay (red) transported by gullies in Icaria Fossae (FRT000040DB on PSP_006706_1390; 40.8°S, 110.2°W). (D) Chloride (white) filling a valley cut through clay-bearing deposits (yellow, with polygonal fractures) in Sirenum intercrater basin (PSP_007050_1465; 33.4°S, 143.8°W). (E) Al-clay (green) exposed at top of northwest-facing graben wall in northeast Noachis, with Fe/Mg-clay (red) exposed lower on the wall (FRT00009100 on ESP_011592_1595; 20.4°S, 40.3°E). (F) Gullies initiating at an Fe/Mg-phyllosilicate-bearing layer (red) in the interior of a southern Noachis crater (FRT00008431 on PSP_005739_1305; 49.4°S, 14.5°E). This layer exhibits a stronger phyllosilicate signature ~1 km to the west (Fig. 3.10C). Blue colors indicate a weak hydration signature.

The more common Fe/Mg-phyllosilicates consistent with smectite are observed in a range of settings across the highlands, with ~10^2 discrete exposures identified by this study. Exposures in Promethei and southern or northeast Cimmeria are rare, possibly due to their high dust cover relative to other parts of the study regions [*Ruff and Christensen,* 2002]. In Noachis and Sirenum, phyllosilicates are not observed predominantly in association with large impact craters as they are in Tyrrhena [*Mustard et al.*, 2008]. Small impacts, however, can expose clays in their crater walls or ejecta. Fig. 3.4B shows a fresh *D*~400 m crater in northeast Noachis that has ejected—and/or scoured dust from the surrounding surface to reveal—Fe/Mg-smectite. Fig. 3.4C shows a *D*~5 km crater on a hill in Icaria Fossae in which gullies have exposed and transported Fe/Mg-phyllosilicate downslope; phyllosilicate is also present in this crater's ejecta (most visibly to the northeast and southwest) and its non-gullied eastern wall, suggesting that alteration predated the impact and the gully activity. Fig. 3.5 provides additional examples. These and tens of other D<1 km craters with phyllosilicate-bearing ejecta observed in CRISM multispectral data are likely too small to have initiated long-lived hydrothermal activity that would have led to alteration [*Rathbun and Squyres*, 2002]. Instead, these craters likely provide isolated windows into possibly widespread, buried layers of clay-bearing materials.

Fe/Mg-clays are also observed in sedimentary basins. CRISM multispectral data show several ring-shaped clay exposures in Sirenum, which apparently resulted from light-toned, clay-bearing materials filling a crater and being subsequently buried by a more resistant capping deposit—and later exhumed by erosion (Fig. 3.6). Fe/Mg-clays are also observed in dozens of intercrater basins in Sirenum and in northern Noachis, often immediately adjacent to deposits interpreted to contain chlorides based on THEMIS data [*Osterloo et al.*, 2008, 2010]. In most cases the chloride deposits appear relatively low-standing, implying that they either underlie the clay-bearing

materials or embay them; the latter would be more consistent with a single cycle of siliciclastic deposition (or *in situ* formation of sepiolite, common in alkaline saline lakes on Earth [*Milliken*, 2008]) followed by evaporation. Indeed, in one basin at 33.3°S, 143.8°W, chloride fills a small valley cutting through clay-bearing terrain (Figs. 3.4D and 3.7).

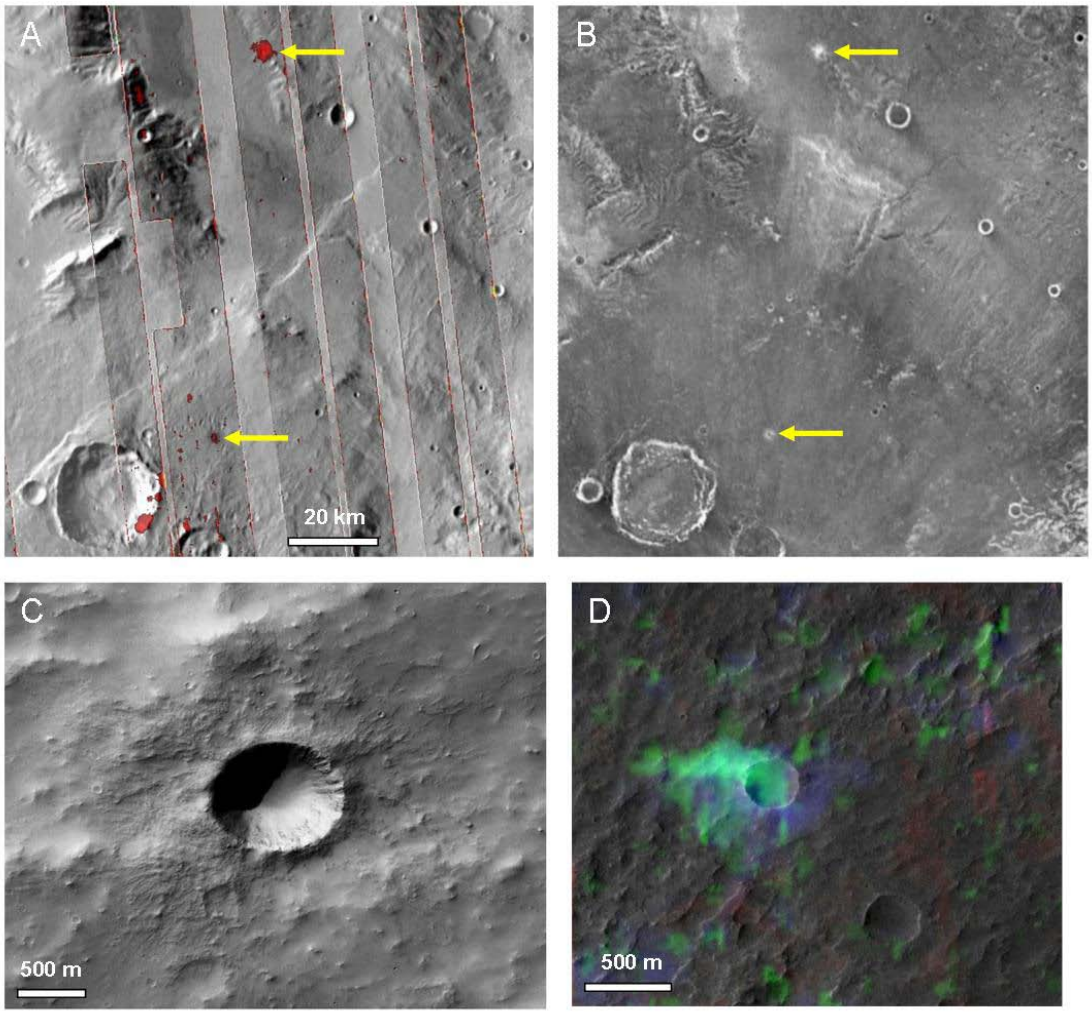

Figure 3.5: Clays exposed by small craters in Noachis. (A) CRISM multispectral data strips with Fe/Mg-phyllosilicate (red) overlain on THEMIS daytime IR mosaic. A large crater in the southwest corner exposes phyllosilicate in its eastern wall, while smaller craters have phyllosilicate-bearing ejecta (arrows). These craters have bright halos in THEMIS nighttime IR data (B), likely indicating a relatively young age. (C) Fresh *D*~1 km crater from the northernmost arrow in (A); note well-preserved ejecta with radial striations (CTX P21_009284_1649; 15.3°S, 52.5°E). (D) *D*~300 m crater with bright ejecta containing Al-clay (green/cyan), from outside area shown in (A) (FRT000060CF on CTX P08_003997_1613; 19.4°S, 47.2°E).

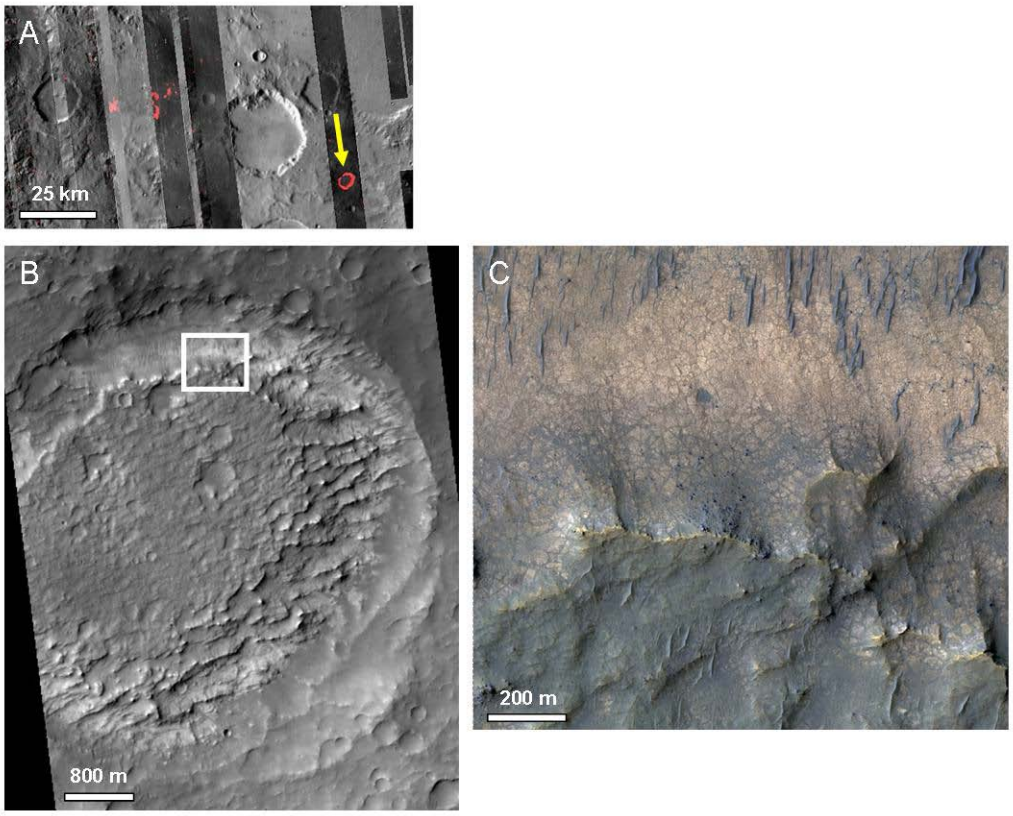

Figure 3.6: Clay-bearing crater fill in Sirenum. (A) CRISM multispectral data strips with Fe/Mg-phyllosilicate (red) shown on IR albedo, with THEMIS daytime IR mosaic as background. Note ring of clays (arrow). Clay-bearing deposits are also visible ~50 km to the northwest on the intercrater plains. (B) HiRISE image (PSP_010901_1510; 28.9°S, 172.9°W) shows the ring corresponds to light-toned materials inside a *D*~7 km crater, overlain by a darker, spectrally bland deposit. Box outlines image (C): Higher resolution reveals polygonal fractures in clay-bearing materials and boulders shedding from more resistant cap unit.

Adjacent to the Sirenum Fossae at 33°S, 206°E is one of the largest exposures of chloride-bearing plains and associated phyllosilicates in the southern highlands (Fig. 3.8) [*Osterloo et al.*, 2008; *Murchie et al.*, 2009b]. The chlorides occur in light-toned materials occupying broad topographic depressions fed by valley networks and in inverted channel deposits within the valleys (Fig. 3.8b). Fan-shaped landforms containing chlorides are found at the mouths of some channels (Fig. 3.8c). As elsewhere on Mars [*Osterloo et al.*, 2008], the chloride-bearing deposits here are polygonally fractured (Fig. 3.8d), consistent with desiccation or dehydration of constituent minerals.

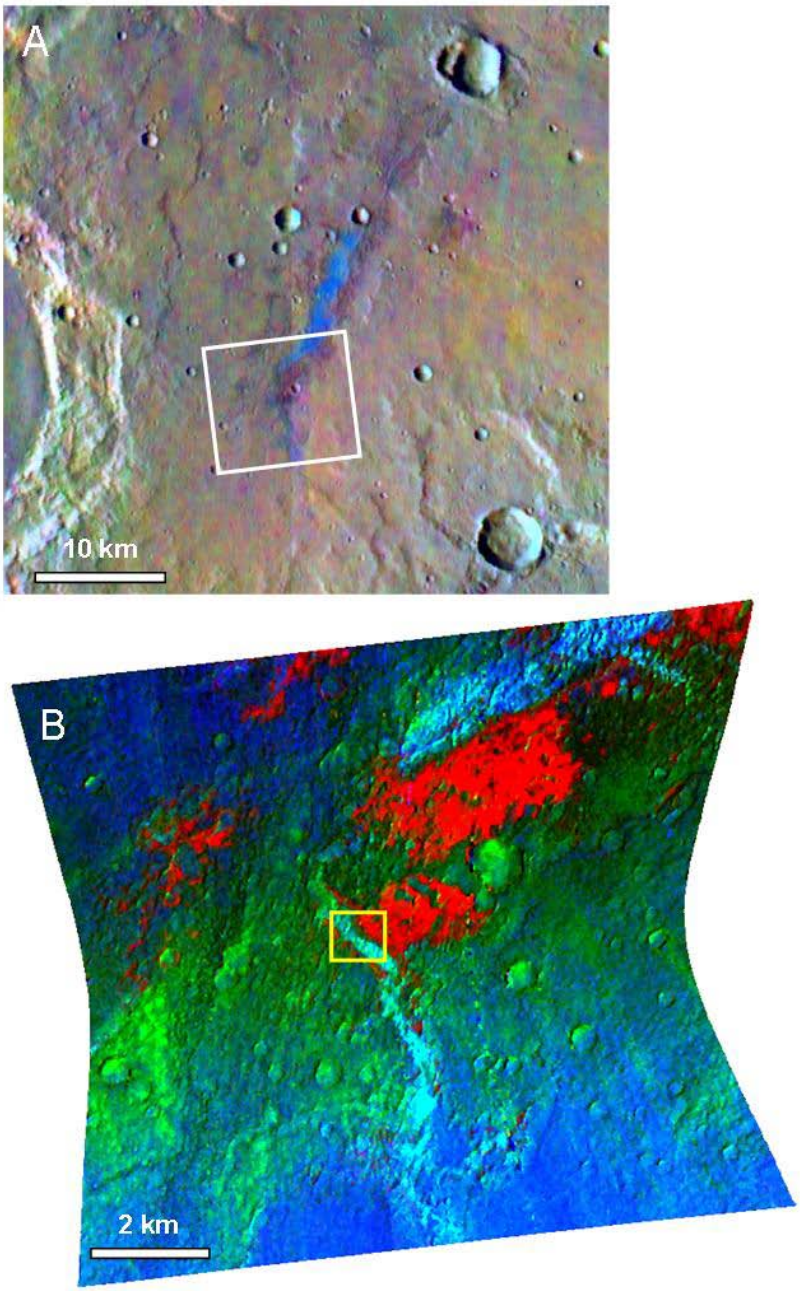

Figure 3.7: Clays and chlorides in Sirenum. (A) Mosaic of THEMIS images I08956002 and I07895002; chloride-bearing materials appear blue in these band 8/7/5 DCS images [*Osterloo et al.*, 2008]. White box outlines panel (B): CRISM FRT 9AAA (33.4°S, 143.8°W) parameter maps; yellow box outlines area shown in Fig. 3.4D. Red indicates Fe/Mg-phyllosilicates. As noted by *Murchie et al*. [2009b], chloride-bearing materials have an unusually weak 3 μm hydration band and a uniform positive slope from 1 to 2.6 μm. Here, green tracks the inverse of the 3 μm band depth, and blue tracks the slope from 1.8 to 2.5 μm; therefore, areas appearing cyan (i.e., both blue and green) are inferred to contain chlorides.

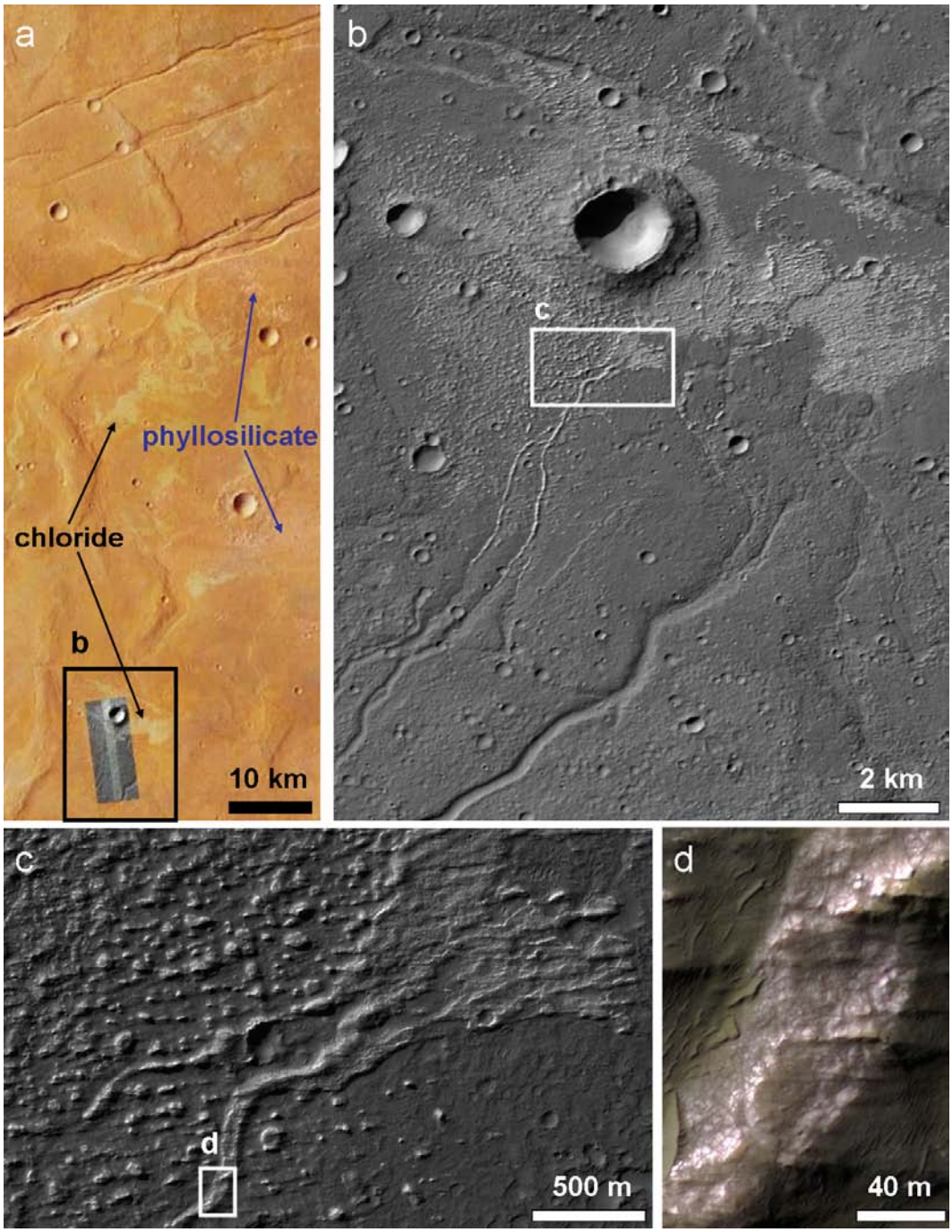

Figure 3.8: Aqueous minerals on the Terra Sirenum plains. (a) Plains surrounding the Sirenum Fossae at ~32.5°S, 205.5°E (HRSC H6382_0000). Chloride-bearing materials appear bright yellow, and phyllosilicate-bearing materials slightly pink. (b) Valleys and light-toned chloride deposits in an intercrater basin (CTX P21_009318_1463). Note chloride-bearing inverted channel deposits within valleys. (c) Chloride-bearing fan-shaped landform (upper right) at channel mouth (HiRISE PSP_009318_1465). (d) Fine-scale texture of inverted channel deposit; note polygonal fracturing.

Other examples of phyllosilicates associated with possible fluvial landforms are shown in Fig. 3.9. Panel (A) shows a crater floor in northeast Noachis with dendritic ridge networks (possibly inverted channels) oriented radially toward the crater interior; phyllosilicates are found upstream of these features, on the eastern crater wall (FRT00009318). Panel (B) shows a branching feature on the southern Huygens basin floor that appears to originate from the basin wall; CRISM multispectral data show probable Fe/Mg-phyllosilicates on the basin floor here. Panel (C) shows part of the southern wall of Asimov crater (47°S, 5°E), displaying gully alcoves that extend up to layers containing Fe/Mg-phyllosilicates according to CRISM FRT00009216. *Morgan et al.* [2010] argued that these and other gullies in Asimov crater formed via top-down snowmelt. In all of these cases, phyllosilicate formation may or may not have been directly related to the inferred fluvial activity.

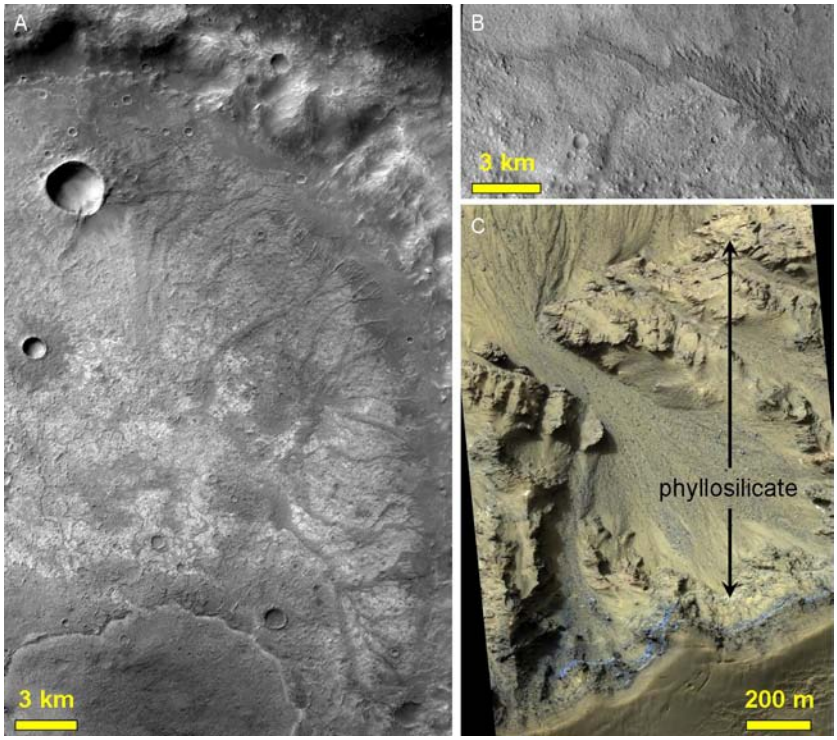

Figure 3.9: Possible fluvial features associated with phyllosilicates. (A) Dendritic ridge networks sourced from clay-bearing crater wall (CTX P14_006608_1596). (B) Branching inverted channel or depositional feature on southern Huygens basin floor (THEMIS V17323002). (C) Gullies on Asimov crater wall, exposing phyllosilicates (HiRISE ESP_016156_1320).

Al-clays and Fe/Mg-smectites are observed together in northeast Noachis along the walls of craters (FRT00009318 and FRT0000A2B8) and graben (HRL000062D9 and FRT00009100). Some of these Al-clay spectra are more consistent with montmorillonite, and others with kaolinite. Al-clay is difficult to isolate spectrally from the Fe/Mg-smectite in these images (Fig. 3.3A), suggesting that the phases coexist at sub-pixel scales. Where stratigraphic relations can be determined, the Al-clay-bearing materials overlie materials with only Fe/Mg-clays (Fig. 3.4E).

3.4 Hydrated Sulfates

Several craters in central Noachis (~50°S) have phyllosilicate-bearing layered floor deposits (CRISM FRTs 8431, 8F74, and 95AE—see Fig. 3.10). The first of these craters (Fig. 3.10B,C) has gullies that originate at a phyllosilicate-bearing layer in materials filling the crater (Fig. 3.4F), and it also contains strata (Fig. 3.11A) in which a different hydrated mineral is detected, with an absorption at 1.92 μm and an inflection at 2.4 μm, consistent with polyhydrated sulfate or with certain zeolites (Fig. 3.12B). The beds showing this spectrum are fractured, and in some places they exhibit polygonal textures consistent with desiccation or dehydration of constituent minerals. These outcrop at a lower elevation than the crater's Fe/Mg-phyllosilicates; however, the phyllosilicates may occupy ejecta from an adjacent crater to the south, and/or may be a remnant of a larger deposit that once filled the crater entirely [Fig. 33 of *Malin and Edgett*, 2001], complicating the stratigraphic interpretation.

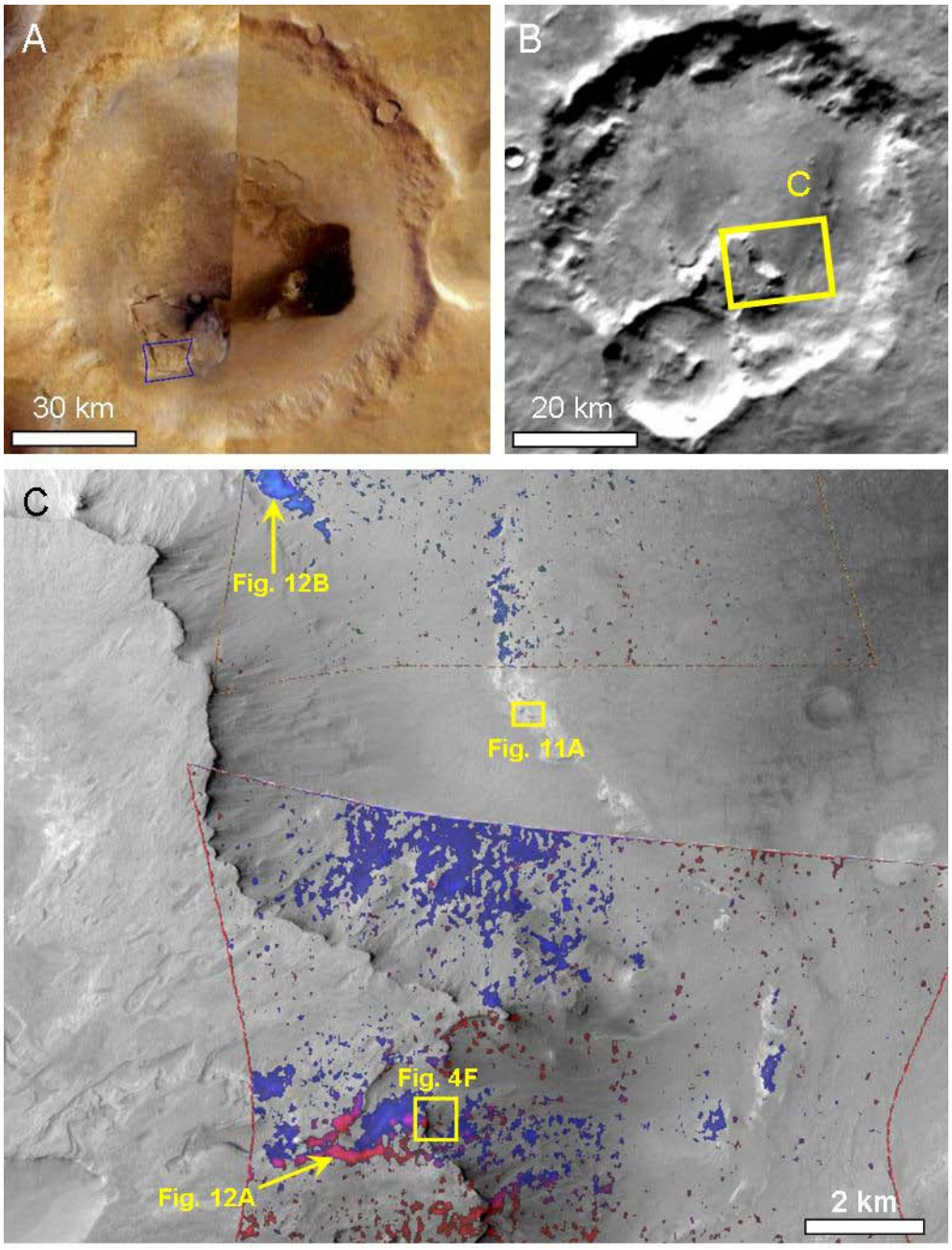

Figure 3.10: Noachis crater floors with hydrated minerals. (A) HRSC image mosaic of crater at 45°S, 28°E with Fe/Mg-phyllosilicate detected in CRISM FRT000095AE (blue outline) corresponding to eroded layers. (B) Viking MDIM context showing a mesa (perhaps partially comprising ejecta from smaller crater) on floor of large crater. Box outlines panel (C): Fe/Mg-phyllosilicates (red) and other hydrated materials including sulfates (blue). Phyllosilicates are exposed in the mesa walls, while sulfates appear in light-toned outcrops northeast of the mesa (FRT00006073 [top] and FRT00008431 [bottom] on CTX P08_003972_1306; 49.3°S, 14.5°E). Yellow boxes outline areas shown in other figures, and arrows point to source locations for spectra.

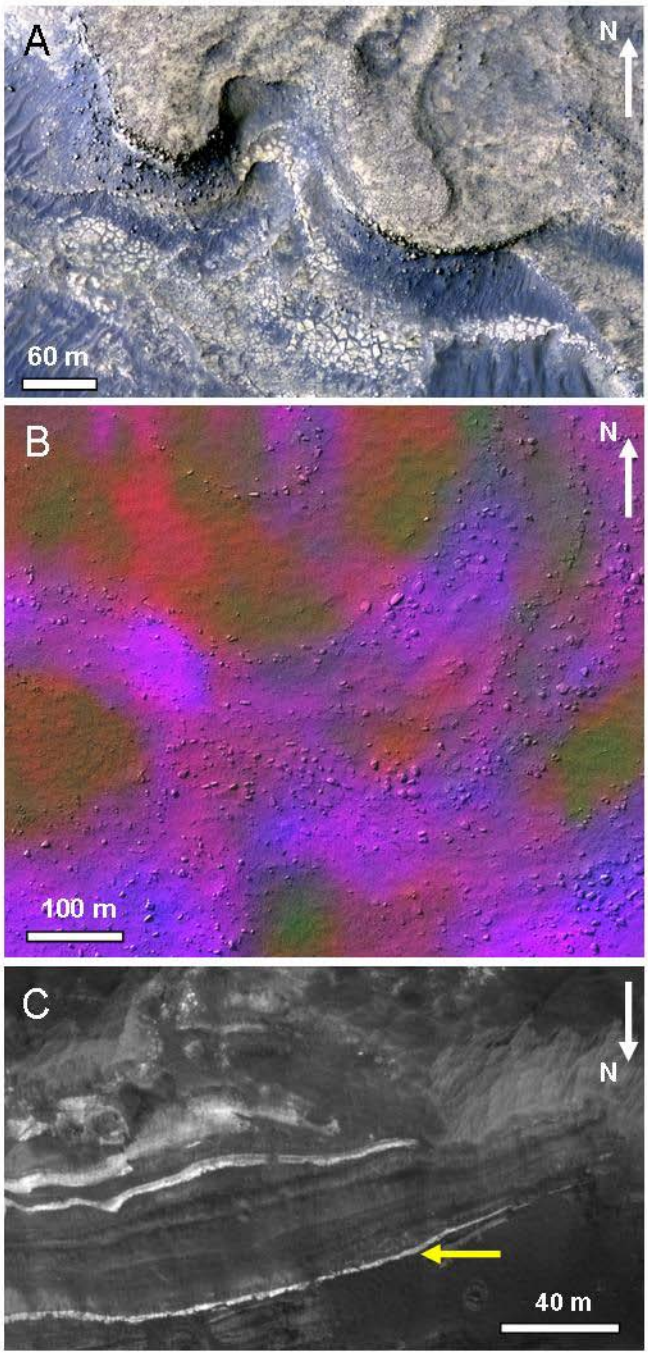

Figure 3.11: Sulfates in the southern highlands. (A) Sulfate or zeolite-bearing layers in Noachis crater (HiRISE PSP_003972_1305; 49.2°S, 14.5°E). (B) Sulfate signature (purple) correlated to boulders in Sisyphi Montes (FRT00007AE6 on PSP_005317_1165; 63.2°S, 18.2°E); green areas are spectrally bland. (C) Light-toned sulfate-bearing layer (yellow arrow) interbedded between darker clay-bearing layers in Columbus crater (PSP_005851_1510; 28.5°S, 166.0°W).

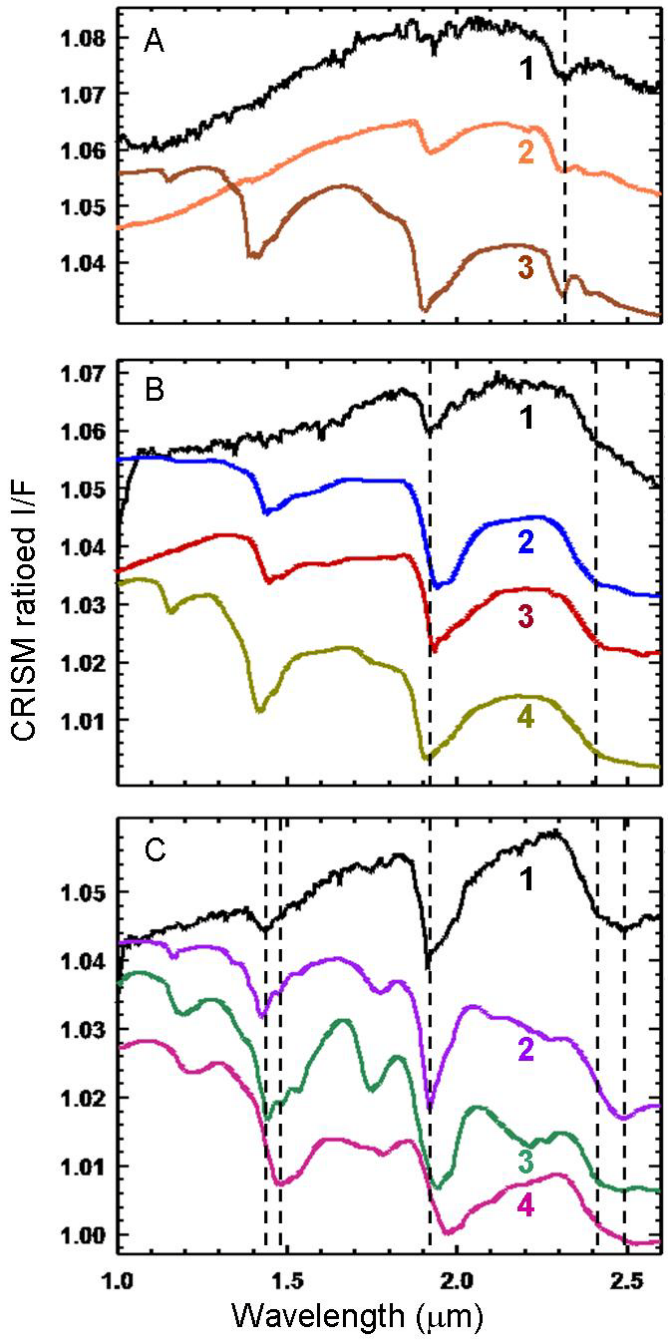

Figure 3.12: Spectra of sulfates and adjacent Fe/Mg-phyllosilicate in Noachis and Sisyphi Montes, with library spectra offset and scaled for comparison. (A): (1) Southern Noachis intracrater deposit (FRT00008431); (2) vermiculite; (3) saponite. (B): (1) Floor of same Noachis crater (Fig. 3.10C) as in (A) (FRT00006073); (2) hexahydrite ($MgSO_4 \cdot 6H_2O$); (3) botryogen ($MgFe^{3+}[SO_4]_2[OH] \cdot 7H_2O$); (4) stilbite (zeolite). (C): (1) Sisyphi Montes hilltop (FRT00007AE6); (2) bassanite ($CaSO_4 \cdot 0.5H_2O$); (3) gypsum ($CaSO_4 \cdot 2H_2O$); (4) kainite ($MgSO_4 \cdot KCl \cdot 3H_2O$). Compare also the library spectra shown in (B).

Farther south, polyhydrated sulfate (Fig. 3.12C) is seen in an image covering a mountain of the Sisyphi Montes at 63.2°S, 18.2°E (Fig. 3.13). Coordinated HiRISE images show scattered ~10 m blocks on the surface (Fig. 3.11B). The areal density of these blocks correlates with the strength of the characteristic sulfate absorptions, suggesting that the sulfate is concentrated in the blocks or occurs as a rock coating. Other images in Sisyphi Montes (FRT00007A8C and HRS00005E5A—Fig. 3.13) also contain hydrated minerals identified by absorptions at ~1.92 μm. These mountains have been interpreted as volcanoes that erupted beneath an ice sheet during the Early Hesperian, causing portions of the ice to melt [*Ghatan and Head*, 2002]. Hydrated minerals including sulfates could therefore have formed here in volcanic hydrothermal or acid fog systems.

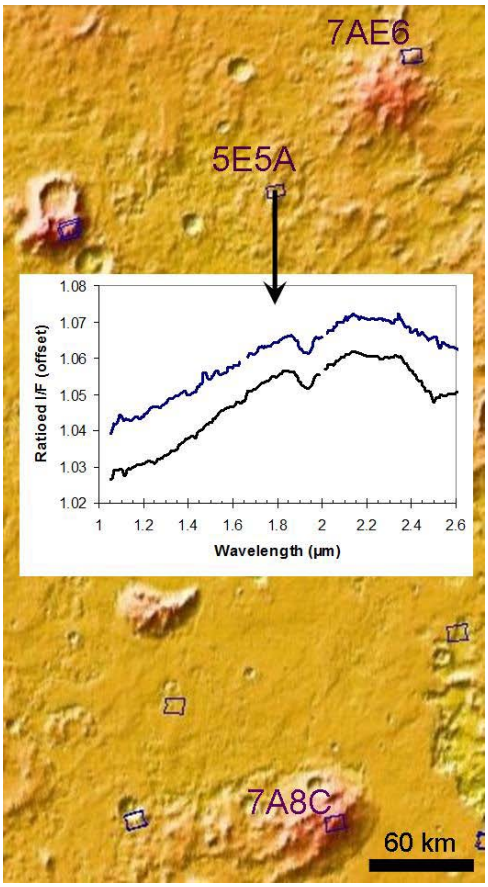

Figure 3.13: Three CRISM observations (labeled) containing hydrated minerals (likely sulfates) in the Sisyphi Montes (centered at 67.0°S, 14.0°E). MOLA colorized shaded topography. Inset shows two hydrated mineral spectra from HRS00005E5A.

In Terra Sirenum, images of the *D*~100 km Columbus crater (29°S, 166°W) reveal a complex assemblage of hydrated minerals. Polyhydrated sulfates and a kaolinite group clay (Fig. 3.3) are most widespread, but isolated outcrops of Fe/Mg-smectite, monohydrated sulfate, and jarosite are also observed (chapter 4). Two spectrally distinct polyhydrated sulfates are present, consistent with gypsum ($CaSO_4 \cdot 2H_2O$) and Mg- or Fe-sulfate, respectively. The polyhydrated sulfates occur in a finely layered, light-toned, polygonally fractured deposit ringing the inner crater walls, which generally overlies the darker clay-bearing materials, although interbedding of sulfates and clays is visible in some outcrops (Figs. 3.11C and 3.14). This assemblage of sulfates, kaolinite, and other minor phyllosilicates occurring in sedimentary layers inside a closed (crater) basin is reminiscent of terrestrial acid-saline lake precipitates [e.g., *Benison et al.*, 2007; *Story et al.*, 2010]. The nearby Cross crater has layered deposits of a kaolinite group clay and the Al-sulfate alunite [*Swayze et al.*, 2008b], and multispectral data show absorptions at ~2.2 μm due to Al-OH (possibly also from kaolinite) in layered floor deposits inside other adjacent large craters. Outside of this intriguing region in northwest Sirenum, only one example of Al-clays in a highlands crater floor deposit has been found to date, in Kashira crater at 27°S, 18.5°W.

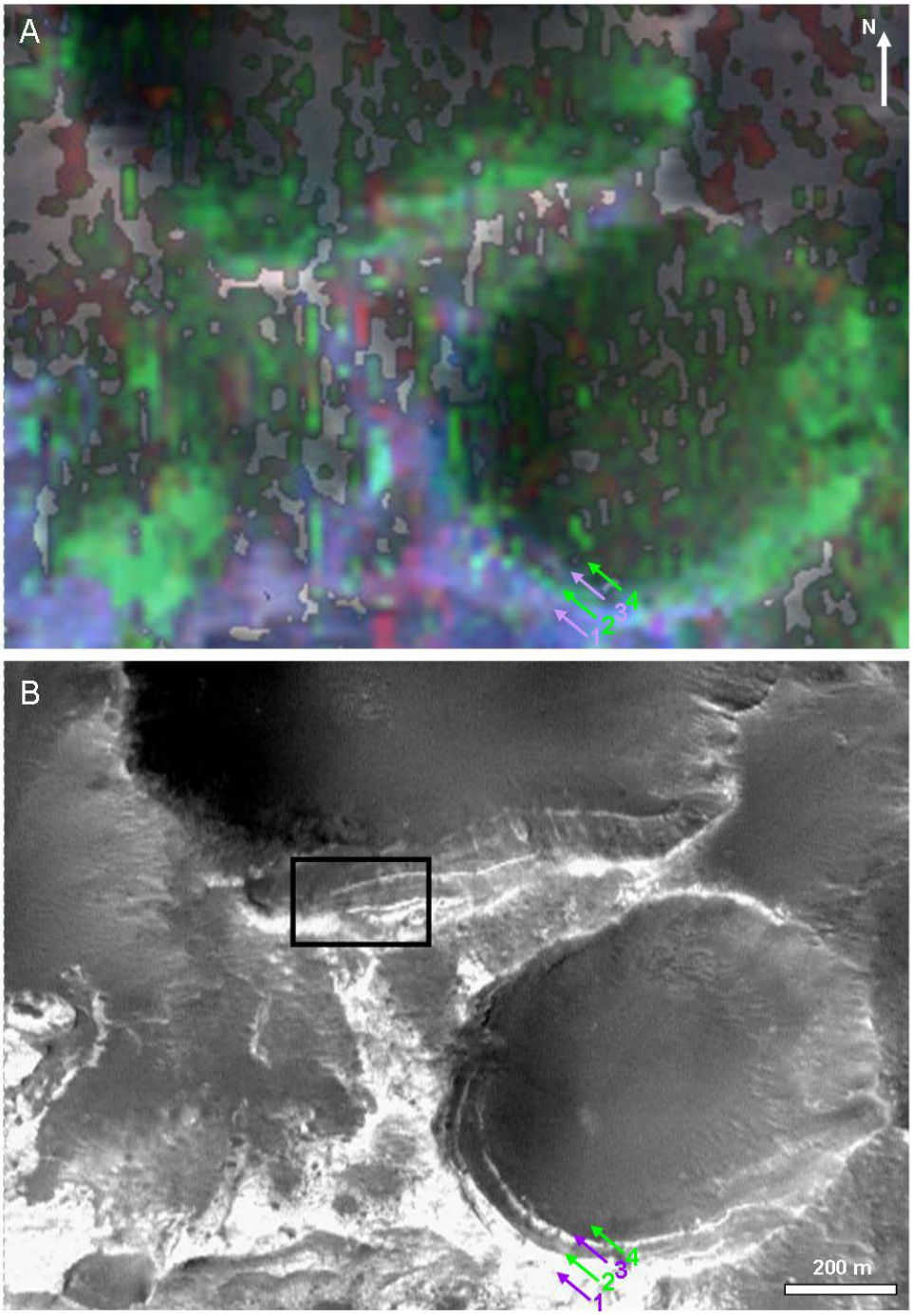

Figure 3.14: Interbedded clays and sulfates in Columbus crater. (A) Sulfate (purple) and kaolinite group clay (green) are found interbedded (arrows) in the wall of a *D*~800 m crater excavating through the layered materials within Columbus (FRT00007D87; 28.5°S, 166.0°W). Fig. 3.15 shows spectra from each layer. (B) Image showing the same area with arrows at same positions. Box outlines area shown in Fig. 3.11C, where interbedded layers exposed by a *D*~1 km crater are too narrow for CRISM to resolve (MOC R0900336).

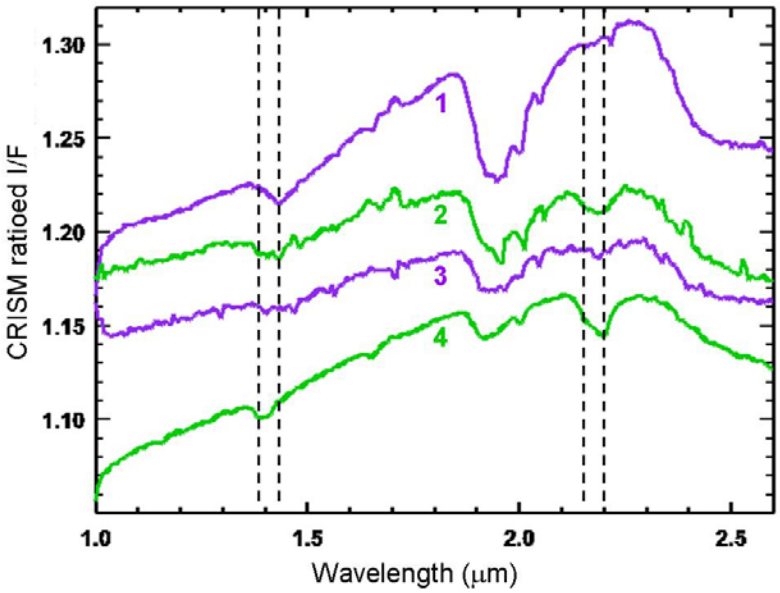

Figure 3.15: Interbedded clays and sulfates in Columbus crater. Numbered spectra correspond to numbered arrows in Fig. 3.14 (spectrum 4 is a 76-pixel average including points eastward of arrow 4, all of which appear stratigraphically equivalent). Spectrum 1 resembles polyhydrated sulfate and spectrum 4 a kaolinite group clay; spectra 2 and 3 are mixtures of both components, but spectrum 3 appears sulfate-dominated while 2 appears more clay-dominated (compare bands at ~2.2 μm).

3.5 Carbonates

A newly identified mineral is found in and around the ~450-km diameter Huygens basin (Fig. 3.16) northwest of Hellas. The most diagnostic spectrum found to date is from a central (floor) pit crater superposed on Huygens' northwestern rim crest (Fig. 3.17A). This spectrum has broad absorptions centered at 2.33 and 2.53 μm (Fig. 3.17B), consistent with Fe- or Ca-carbonate but not with the Mg-carbonate previously detected by CRISM [*Ehlmann et al.*, 2008b]. Adjacent outcrops have a spectral signature of Mg-phyllosilicate, and the spectrum in Fig. 3.17B likely represents a mixture of carbonate and phyllosilicate, with the latter contributing to the 2.3 μm band depth and adding the water-related absorptions at 1.4 and 1.9 μm. The broad curvature of the spectrum from 1 to ~1.7 μm is consistent with Fe-carbonate and/or with a different associated ferrous phase. Similar spectral features are found in

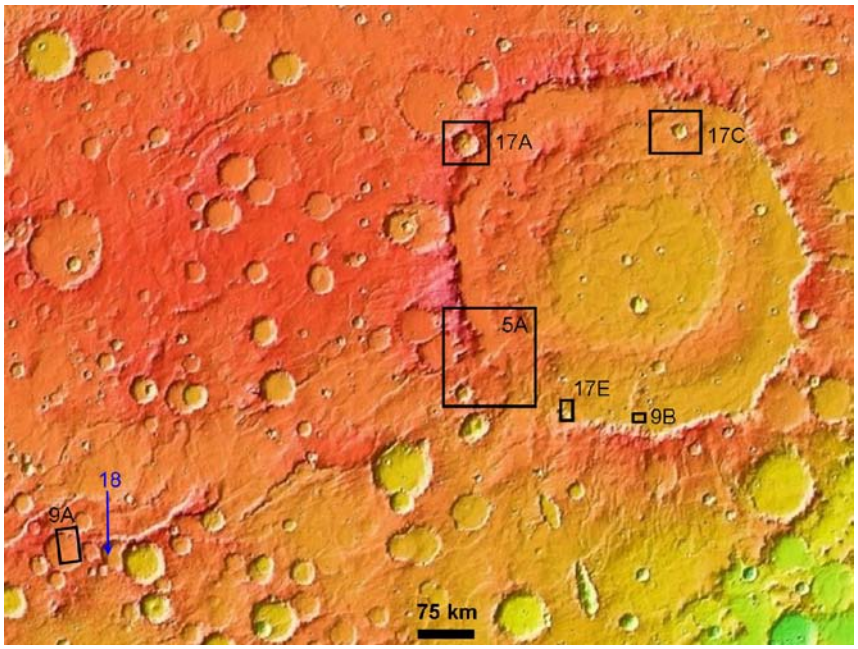

Figure 3.16: MOLA color shaded topography of the *D*~450 km Huygens basin (upper right) and surroundings. Locations of subsequent and some previous figures in this chapter are outlined.

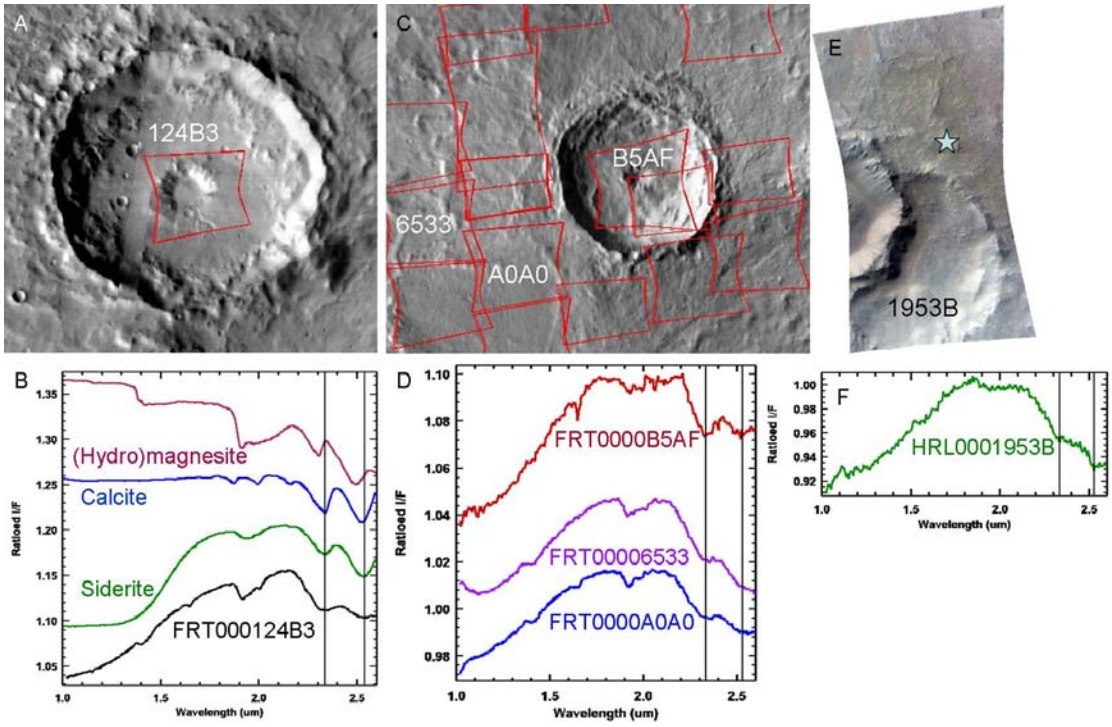

Figure 3.17: Craters exposing possible Fe/Ca-carbonate in Huygens basin. (A,C) are from THEMIS daytime IR mosaics with CRISM targeted observations outlined; (E) is a 3-band CRISM IR composite image. Laboratory spectra in (B) are from *R. Clark et al.* [2007]: magnesite+hydromagnesite ($MgCO_3$ + $Mg_5[CO_3]_4[OH]_2 \cdot 4H_2O$) HS47.3B, calcite ($CaCO_3$) HS48.3B, and siderite ($FeCO_3$) HS271.3B.

the ejecta of another crater superposed on Huygens' rim (Fig. 3.17E,F) and in the ejecta and interior of a floor pit crater inside Huygens basin (Fig. 3.17C,D). Another possible example of Fe/Ca-carbonate—in this case probably mixed with chlorite and a hydrated mineral—is found in a crater several hundred km southwest of Huygens, where it occurs in fine-grained material (Fig. 3.18).

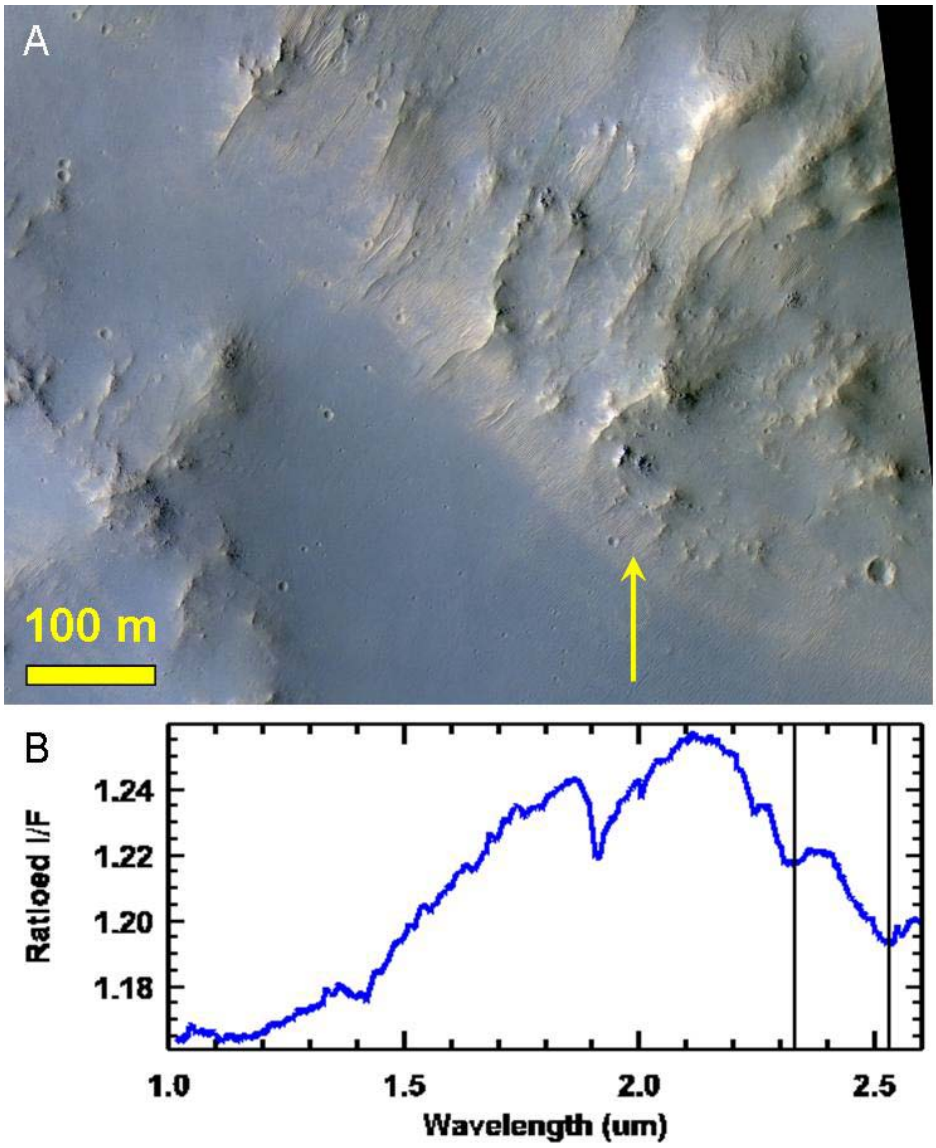

Figure 3.18: (A) Relatively light-toned, fine-grained material (arrow) on a crater floor west of Huygens basin (HiRISE ESP_011671_1590) exhibits spectral signature (B) consistent with Fe/Ca-carbonate (2.33, 2.53 µm bands) + chlorite (2.25 µm band) + an unknown hydrate (1.9 µm band); from CRISM FRT00009318.

In the crater of Fig. 3.17A, the carbonate and phyllosilicate can be mapped to specific outcrops on the wall of the central pit (Fig. 3.19A). Crater central pits throughout the solar system are thought to form from vaporization of target volatiles, central peak collapse into weak icy crust, and/or excavation into subsurface liquid [*Devries and Barlow*, 2009], with the first of these hypotheses seeming the most likely for equatorial modern Mars. Release of CO_2 and H_2O from carbonate- and phyllosilicate-rich target rocks may have formed this central pit, and the valleys emptying into it (Fig. 3.19A) could perhaps have been carved by impact-mobilized fluids. The carbonate-bearing rocks are fractured and possibly layered (Fig. 3.20A), and in some places are criss-crossed by protruding ridges (Fig. 3.20B) that could be dikes or large mineralized veins.

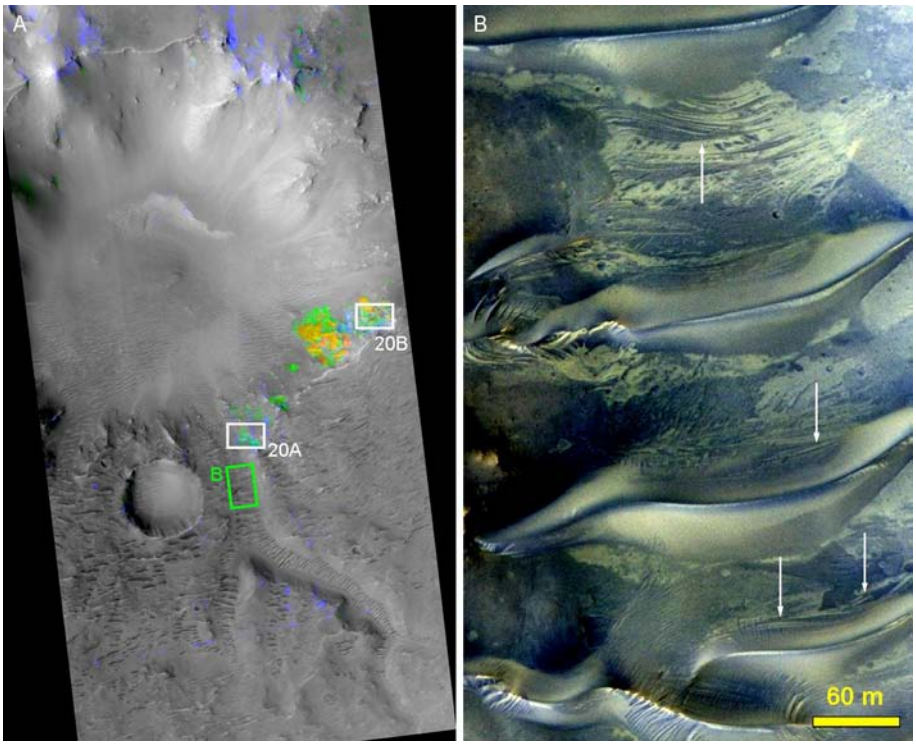

Figure 3.19: (A) Mineral indicator maps from CRISM FRT000124B3 overlain on HiRISE ESP_012897_1685. Red is D2300 (2.3 µm band), green is BDCARB (2.33 and 2.53 µm bands), and blue is CINDEX (3.9 µm band) from *Pelkey et al.* [2007]. Colors are stretched such that red to yellow tones reflect phyllosilicate-dominated spectra whereas green to blue tones indicate carbonate-dominated spectra. Only spots on the southeast pit wall are confirmed by plotting spectra. (B) Dunes on floor of central pit tributary valley, with cross-strata (e.g., arrows) visible in interdune areas.

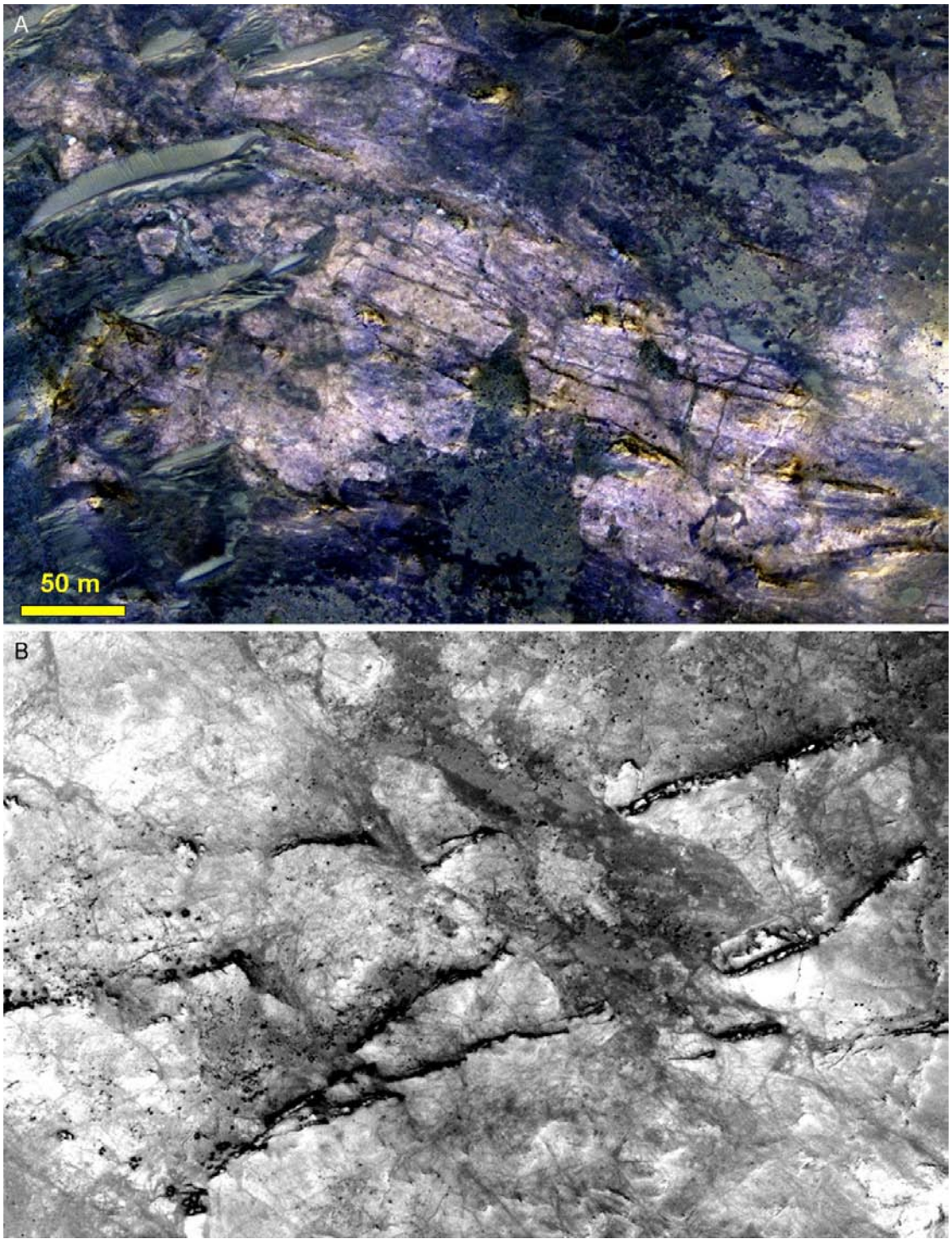

Figure 3.20: Carbonate-bearing outcrops in central pit of crater on Huygens rim; see Fig. 3.19A for context. Both panels are from HiRISE ESP_012897_1685, shown at the same scale. (A) Possible layering inferred from lineations striking from upper left to lower right. (B) Ridges protruding from outcrop may be dikes or mineralized veins.

The valleys entering into this crater's central pit are filled with younger aeolian dunes (Fig. 3.19), which appear to be inactive as several small impact craters are superposed on them. Just upstream from the carbonate-bearing outcrop shown in Fig. 3.20A, the plains between the dunes exhibit lineations that truncate each other in places (Fig. 3.19B). These patterns are strongly reminiscent of indurated cross-strata exposed after dune migration in (for example) Earth's White Sands Dune Field [Fig. 9 of *Szynkiewicz et al.*, 2010]. Similar features have also been observed in Mars' north polar region by *Bourke et al.* [2008], *Szynkiewicz et al.* [2009], and *Horgan et al.* [2010], who have interpreted them as aeolian cross-strata cemented by ice and/or by the gypsum known to be present in that region [e.g., *Langevin et al.*, 2005]. In Huygens crater, carbonate could be the cementing agent for the observed cross-strata, but this hypothesis comes with two caveats: (1) CRISM does not directly detect carbonate at the location of the cross-strata (Fig. 3.19A); and (2) Fe- and Ca-carbonates are expected to be relatively insoluble on Mars [e.g., *Tosca et al.*, 2008a], so substantial liquid water may be needed to dissolve this carbonate from the central pit strata prior to its later re-precipitation as cement.

3.6 Discussion

The results of this survey expand the range of secondary minerals, mineral assemblages, and geologic settings for alteration that have been identified on Mars to date. Many of the deposits discussed above are worthy of focused local or regional studies, and chapter 4 begins this work with a detailed look at Columbus crater. For now, the broad-scale distribution of newly identified aqueous mineral exposures enables several conclusions to be drawn.

The Fe/Ca-carbonates in and around Huygens crater are compositionally distinct from the Mg-carbonates previously identified on Mars by CRISM [*Ehlmann et*

al., 2008b, 2009] and by other orbital [*Bandfield et al.*, 2003; *Palomba et al.*, 2009] and surface [*Christensen et al.*, 2004b] spectrometers. However, Martian meteorites exhibit a broad compositional range including Fe-rich carbonates in the Nakhlites and Ca-rich cores in the carbonate grains of ALH84001 [*Bridges et al.*, 2001]. Also, Ca-carbonate has recently been found in high-latitude soils by the Phoenix lander [*Boynton et al*., 2009], and Fe-carbonate (with Mg-carbonate) in certain rocks of the Columbia Hills by Spirit [*Morris et al.*, 2010]. These examples add confidence to the interpretation of Fe/Ca-carbonate from the CRISM spectra in Fig. 3.17.

The Fe/Ca-carbonate exposures identified to date are all associated with mid-sized craters, suggesting impact-related formation and/or exposure of previously buried carbonate. Carbonates are indeed among the minerals found in impact hydrothermal assemblages on Earth, but unless the target rocks contained abundant carbonates [e.g., *Osinski*, 2003; *Osinski et al.*, 2001, 2004, 2005], they are typically a relatively minor component of the impactites [e.g., *Hagerty and Newsom*, 2003]. By analogy, it seems likely that buried carbonates existed in the subsurface around Huygens basin prior to the impacts that exposed—and possibly modified—them. Indeed, the presence of these carbonates within the Huygens rim rocks suggests that they may predate Huygens itself, an Early Noachian basin dated to ~3.98 Ga by *Werner* [2008]. Prior to the impact that formed the crater in Fig. 3.17A, these carbonates may have been buried ~5 km beneath the Martian surface, based on the ~3.3 km structural uplift predicted in the central pit wall [e.g., Equation (3) of *Tornabene et al.*, 2008] plus the ~1.8 km elevation difference between the central pit and the pre-impact Huygens rim crest. Early burial could have protected these carbonates from later acidic conditions at the surface hypothesized by *Bibring et al.* [2006a], and could help explain why no large exposures of carbonate-rich rocks have been identified previously [e.g., *Christensen et al.*, 2001a].

The sulfates in Columbus crater, Sisyphi Montes, and possibly Noachis show that these minerals are more widespread than previously observed. OMEGA results have been used to infer a distinct period of sulfate formation during the early-to-mid Hesperian, coupled to Tharsis volcanic activity [*Bibring et al.*, 2006a, 2007]. The newly detected sulfates are thousands of kilometers distant from those mapped by OMEGA, and they occur at substantially higher elevations, so they were likely not transported from the regional sulfate exposures near the equator. In addition, Columbus and the crater in Noachis are in geologic units mapped as Noachian in age. Although it is possible that the intracrater sediments are younger, the acidic conditions inferred for the formation of sulfates [e.g., *Bibring et al.*, 2006a] may have been locally present before the end of the Noachian, and/or sulfates may have been concentrated in some locations by evaporitic processes [e.g., *Andrews-Hanna et al.*, 2007] at near-neutral pH.

Thermal infrared mapping of the southern highlands at lower spatial resolution has demonstrated that the surface materials are dominated by unweathered basalt [*Christensen et al.*, 2001a], and OMEGA maps of hydrated minerals in my study regions show very few large exposures [*Bibring et al.*, 2006a; *Poulet et al.*, 2007]. However, impact craters throughout the highlands that have exposed phyllosilicates from depths <1 km suggest that these materials are widespread in the shallow subsurface. The Spirit rover's wheel track excavations of sulfates and opaline silica in the Columbia Hills [*Yen et al.*, 2008; *Squyres et al.*, 2008] provide *in situ* support for the presence of alteration minerals in the shallow subsurface of ancient terrains. Aqueous alteration was apparently widespread during the Noachian, not limited to localized regions.

The age of the chlorides that commonly accompany Terra Sirenum phyllosilicates is unknown, but globally they are found in Noachian to Early

Hesperian terrains [*Osterloo et al.*, 2008]. This age corresponds to that of the highland valley networks [e.g., *Fassett and Head*, 2008a; *Hoke and Hynek*, 2009], but Terra Sirenum has relatively few such valleys [*Carr*, 1995]. By contrast, global hydrologic models predict enhanced groundwater upwelling in Sirenum relative to the rest of the southern highlands during the Late Noachian/Early Hesperian [*Andrews-Hanna et al.*, 2007]. Terra Sirenum also hosts a dense concentration of geologically recent gullies, which has been interpreted as evidence for a regional aquifer [*Malin and Edgett*, 2001]. Several of these gully systems have been active within the past ten years [*Malin et al.*, 2006; *Dundas et al.*, 2010]. The formation mechanism(s) of gullies remain debatable; recent studies have argued that most gullies form from snowmelt [e.g., *Dickson and Head*, 2009] or possibly even dry CO_2 frost-related activity [*Dundas et al.*, 2010] rather than emerging groundwater. Nevertheless, there is morphologic evidence that at least some gullies in Terra Sirenum may have a groundwater source [*Kolb et al.*, 2007]. Combined with the arguments for Noachian/Hesperian groundwater, these youthful gullies are consistent with a long history of subsurface water in this region.

Al-phyllosilicates, if formed from basaltic precursor materials, may indicate greater alteration and leaching of divalent cations than Fe/Mg-phyllosilicates. The stratigraphic relationship between these two clay types observed in Noachis, with Al-clays overlying Fe/Mg-clays, is also observed at Mawrth Vallis (chapter 2), Nili Fossae [*Ehlmann et al.*, 2009], western Arabia Terra [*Noe Dobrea et al.*, 2010], Valles Marineris [*Murchie et al.*, 2009b], and Eridania basin [*Noe Dobrea et al.*, 2008c], suggesting that many of these Al-clays may have formed via a common, globally widespread process. The Al-clays at Mawrth Vallis were likely emplaced in the Late Noachian or Early Hesperian (chapter 2), when new models of atmospheric escape [*Tian et al.*, 2009] support a thickening CO_2 atmosphere, and the surface morphology

suggests a period of intense fluvial activity [*Howard et al.*, 2005; *Irwin et al.*, 2005, 2011]; indeed, all preserved valley networks appear to have formed during this time [*Hoke and Hynek*, 2009]. Liquid water would thus have been available for surface weathering, and since kaolinite can form under acidic conditions, Al-clay formation could have overlapped the inferred global reduction in pH during the Noachian-Hesperian transition [*Bibring et al.*, 2006a]. Kaolinite associated with the acid sulfate alunite in Cross crater supports this scenario.

The observation of sulfates in Noachian terrains, sometimes in intimate association with phyllosilicates, suggests a more complicated environmental history than previously proposed based on lower-resolution data, with local and regional exceptions to the global trends. The diverse mineral assemblages identified from CRISM observations of the southern highlands likely reflect a diversity of aqueous environments during the Noachian, with varied pH, water/rock, salinity, and temperature. Several distinct habitable niches may therefore have been present on ancient Mars, providing a range of opportunities for the origin of life.

CHAPTER 4

COLUMBUS CRATER AND OTHER POSSIBLE PALEOLAKES IN TERRA SIRENUM*

4.1 Introduction

The hydrous minerals discussed in the preceding chapters attest to widespread water-rock interactions on Mars during the Noachian and Hesperian Periods. Distinguishing surface vs. subsurface alteration from orbit is generally difficult, but valley networks in Noachian and Hesperian terrains suggest liquid water was at least occasionally present at the surface [e.g., *Baker*, 1982; *Carr*, 1995; *Fassett and Head*, 2008a]. Where this water flowed into closed basins, lakes may have formed.

Impact craters are the most common type of basin on the Martian surface in which ancient water could have ponded. Hundreds of candidate crater paleolakes have been identified based on morphologic evidence such as inlet and/or outlet valleys, fan-shaped (possibly deltaic) deposits, and putative shoreline features [e.g., *Goldspiel and Squyres*, 1991; *Forsythe and Blackwelder*, 1998; *Cabrol and Grin*, 1999; *Fassett and Head*, 2008b]. Because of their potential for habitability and preservation of biosignatures in sediments deposited in a quiescent environment, paleolakes are considered high-priority targets in the astrobiological exploration of Mars [e.g., *Farmer and Des Marais*, 1999].

Minerals formed in paleolakes record ancient environmental conditions because evaporites and other precipitates can reflect both lake chemistry and the composition of atmospheric or other volatile reservoirs with which the lake water was in contact; for example, the relative partial pressures of CO_2 and SO_2 in the Martian

* The work described herein was originally published by Wray, J. J., et al., Columbus crater and other possible groundwater-fed paleolakes of Terra Sirenum, Mars, *J. Geophys. Res.*, doi:10.1029/2010JE003694, in press.

atmosphere and their effects on surface water could have determined whether evaporites were carbonate-rich or sulfate-rich [*Bullock and Moore*, 2004]. The potential value of paleolake evaporites has prompted many searches for them, but while sulfates and chlorides have been identified in canyons, intercrater plains, and some craters [e.g., *Squyres* et al., 2004b; *Gendrin et al.*, 2005; *Osterloo et al.*, 2008], the mineralogic results for classic morphologic paleolakes have been largely negative [*Ruff et al.*, 2001; *Squyres et al.*, 2004a; *Stockstill et al.*, 2005, 2007]. Recent orbital detections of phyllosilicates in a few paleolakes [*Ehlmann et al.*, 2008a; *Dehouck et al.*, 2010; *Milliken and Bish*, 2010; *Ansan et al.*, in press] suggest that evaporite salts might be found using similar techniques.

A spectral survey covering much of the southern highlands in search of new hydrated mineral exposures (chapter 3) identified a unique group of craters in northwest Terra Sirenum that contain Al-phyllosilicates (first reported in Cross crater by *Poulet et al.* [2007]) and hydrated sulfates in finely bedded deposits. The alteration mineral assemblages in these craters are reminiscent of those associated with terrestrial acid-saline lakes and groundwaters [*Benison et al.*, 2007; *Baldridge et al.*, 2009; *Story et al.*, 2010]. By analogy, the Terra Sirenum crater deposits may be lacustrine evaporites; even if not, their mineralogic and morphologic properties define a distinct class of aqueous deposit on Mars [*Murchie et al.*, 2009b]. Here I investigate in detail the morphology, thermophysical properties, mineralogy, and stratigraphy of these deposits; I then examine hypotheses for their origin to better determine their implications for ancient Martian environments. I focus first on Columbus crater (29°S, 166°W), where the greatest diversity of hydrated minerals is observed, and then look at nearby craters with similar deposits.

4.2 Morphology of Columbus Crater

4.2.1 General characteristics

Columbus crater lies in northwest Terra Sirenum in the southern highlands of Mars. Immediately surrounding Columbus are highly cratered plains of the Npl_1 unit [*Scott and Tanaka*, 1986], dated to the Middle Noachian Epoch [*Tanaka*, 1986]. Fluvial dissection is sparse here compared to other regions of the Noachian southern highlands [*Carr*, 1995; *Hynek et al.*, 2010], although this may be partly due to poor preservation, as the plains ~100 km to the east, south, and west of Columbus were largely resurfaced in the Late Noachian by materials in the $Np1_2$ unit of *Scott and Tanaka* [1986].

Columbus itself has a well-preserved rim, with no breaches by valleys entering or exiting the crater (Fig. 4.1). A few small valleys cut the northeast inner crater wall (Fig. 4.1b), but their alcoves do not extend beyond the crater rim and they probably did not supply substantial fluvial sediment to the crater. The crater diameter is ~110 km, with a rim crest at 3000 ± 200 m (MOLA elevation relative to the geoid; *Smith et al.* [1999])—well above the surrounding plains, which span 2200–2700 m in elevation. This rim height is typical for minimally degraded large craters of this size [*Garvin et al.*, 2003]; by contrast, Columbus' flat floor at 920 ± 30 m implies a current depth ~1.5 km less than fresh craters of this diameter, suggesting substantial infill by sedimentary and/or volcanic materials. Further evidence for significant infill and/or erosion of the crater interior is furnished by the lack of a central peak or peak ring. A single hill complex ~15 km NNW of crater center (Fig. 4.1) could be a lone remnant of a peak ring (or an off-center peak), although its height (~700 m above the floor) exceeds that typical for central peaks in craters of this size (~440 m based on *Garvin et al.*'s [2003] relation for craters up to 100 km in diameter). These hills expose megabreccia (Fig. 4.2), like many crater central uplifts on Mars [*McEwen et al.*, 2008].

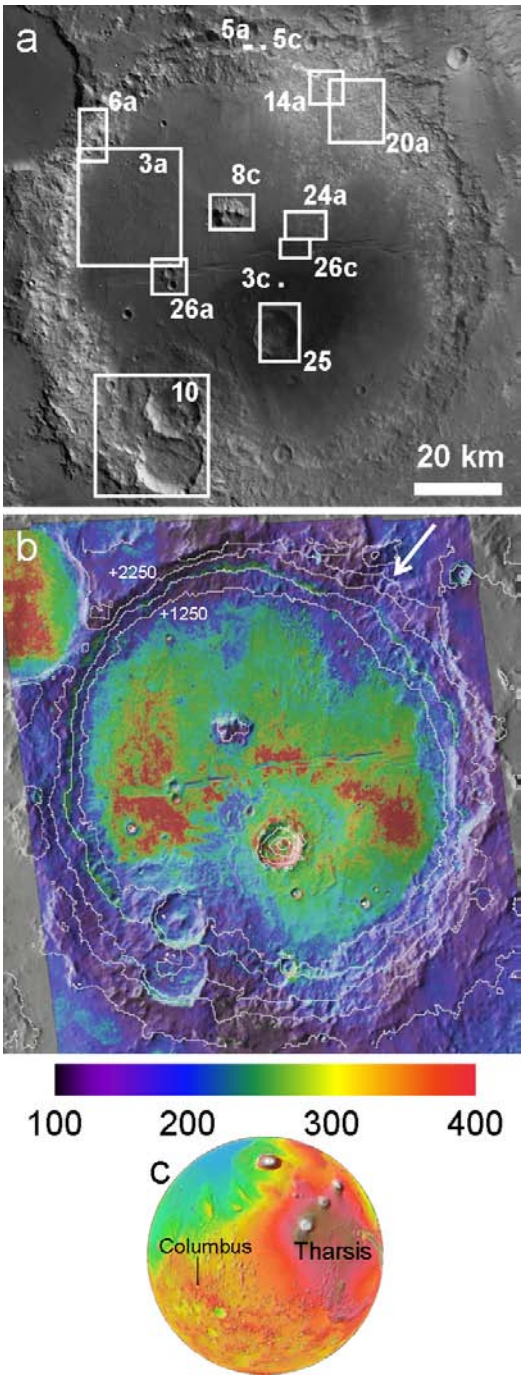

Figure 4.1: Two views of Columbus crater (29°S, 166°W). (a) HRSC nadir channel mosaic. Here and subsequently, numbered outlines indicate locations of other figures in this chapter. (b) THEMIS daytime IR band 9 mosaic, colorized with THEMIS-derived thermal inertia (scale bar units are tiu). Superposed contours are MOLA elevations spaced 500 m apart, beginning at +250 m. Note medium-inertia (green) materials following the 1750 m contour around the crater walls. Arrow indicates small valleys on northeast wall, as described in the text (sections 4.2 and 4.5). (c) Location of Columbus crater on MOLA global topographic map.

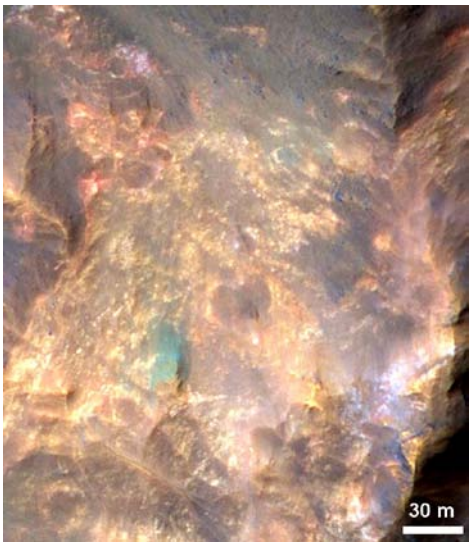

Figure 4.2: Megabreccia in hills on Columbus crater floor; from HiRISE ESP_016083_1505. Diverse colors likely indicate diverse rock compositions. Context shown in Fig. 4.8c.

The flat portions of Columbus' floor have a relatively high thermal inertia (Fig. 4.1b). The thermal inertia map (~100 m/pixel) was provided by Matt Chojnacki, who derived it from THEMIS nighttime infrared (IR) images [*Fergason et al.*, 2006] using the thermal model of *Putzig and Mellon* [2007]. This method uses THEMIS band 9 (12.57 μm) nighttime brightness temperature images to derive best-fit thermal inertia by interpolation with a seven-dimensional lookup table using season, time of day, latitude, thermal inertia, albedo, elevation, and visible dust opacity [*Putzig and Mellon*, 2007]. Columbus' eastern crater floor exhibits thermal inertia up to ~510 ± 30 $J \cdot m^{-2} s^{-0.5} K^{-1}$ (units hereafter abbreviated "tiu," after *Putzig and Mellon* [2007]). For comparison, thermal inertias >386 tiu were classified as "very high" by *Putzig et al.* [2005] and likely indicate high rock abundance and/or exposures of bedrock or other indurated surfaces. For example, in the Nili Patera caldera of Syrtis Major, thermal inertias of ~500 tiu are interpreted as indicative of a relatively fresh lava flow surface underlying minor amounts of unconsolidated material [*Fergason et al.*, 2006].

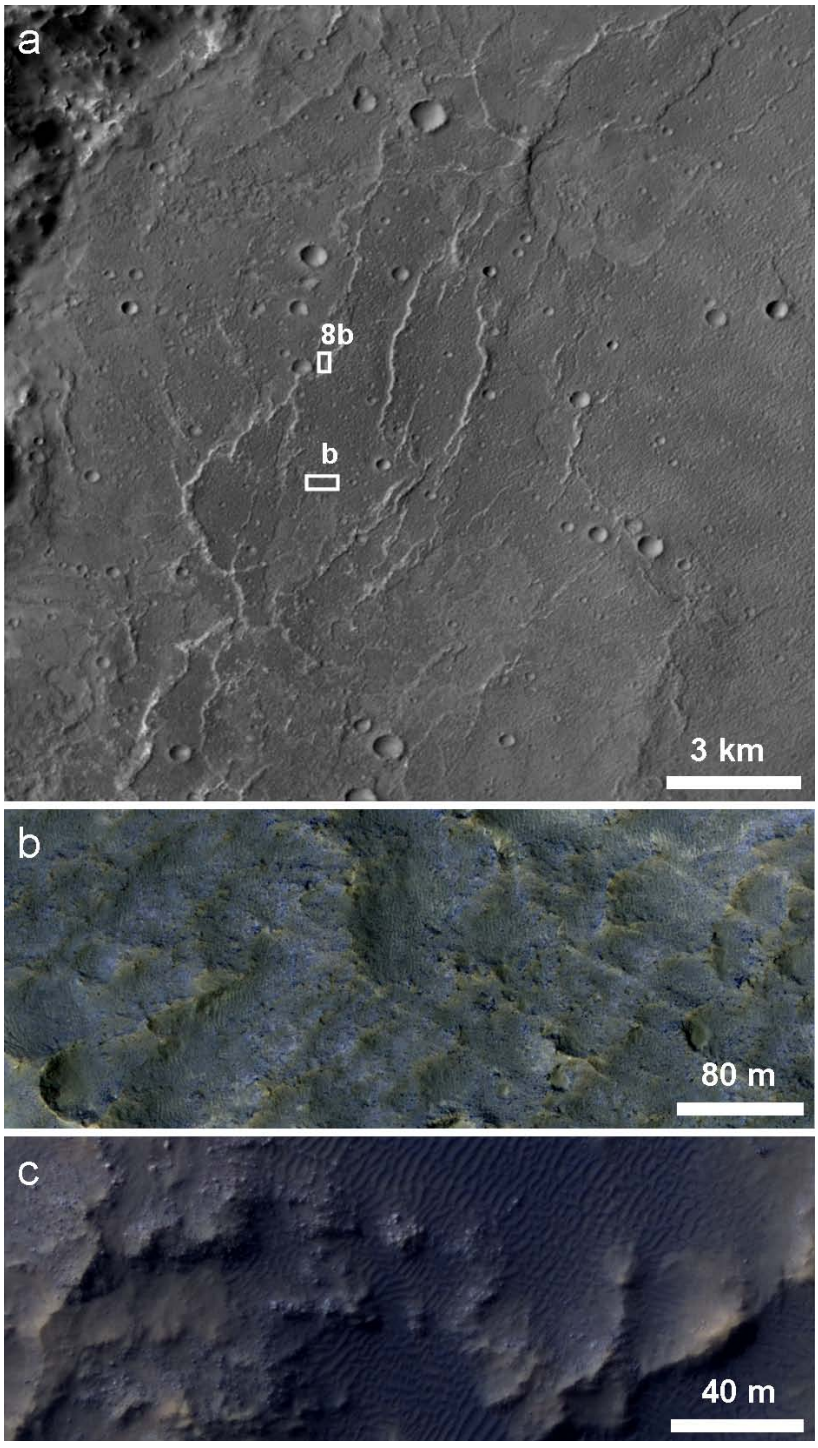

Figure 4.3: (a) Ridged western floor of Columbus crater; from CTX P03_002739_1505. (b) Dark rugged materials covering much of Columbus' floor, with meter-scale boulders just visible; from HiRISE PSP_004018_1505. (c) Sample of dark, lobate ejecta of *D*~11 km crater on Columbus' floor; from HiRISE PSP_008356_1500. Dark materials occur in both aeolian bedforms and meter-scale blocks.

High-resolution images of the Columbus crater floor reveal a rugged texture at decameter scales (Fig. 4.3b), with good retention of small craters. Meter-scale boulders are also visible, further suggesting a cohesive surface material that breaks up to form the boulders; this material could be a strongly cemented sedimentary deposit or a lava flow. On the western crater floor, a series of ridges is observed (Fig. 4.3a). These are generally segmented in planform and asymmetric in profile, with one steep scarp (most commonly west-facing) and a broader, shallower rise on the other side. This morphology is characteristic of wrinkle ridges, as observed in layered materials—most commonly lava flows—on the Moon and terrestrial planets including Mars [*Mueller and Golombek*, 2004]. Wrinkle ridges are generally interpreted as blind thrust faults. On Mars, they are typically observed in Early Hesperian ridged plains, interpreted as low-viscosity lava flows [*Scott and Tanaka*, 1986]. Taken together, the wrinkle ridges and other textural and thermophysical characteristics of Columbus crater's floor are strongly suggestive of a lava flow, although other possibilities such as lithified aeolian deposits cannot be ruled out. A 40-km diameter crater that cuts the northwest rim of Columbus (Fig. 4.1) has a similarly flat floor with wrinkle ridges and a relatively high thermal inertia (~420 ± 30 tiu), suggesting that it contains similar deposits. The source of these putative lavas is not apparent, as is typically the case for ridged plains on Mars [*Greeley and Spudis*, 1981].

Other notable characteristics of Columbus crater include a graben cutting east to west across the crater floor, and an 11-km diameter crater whose radial ejecta have darkened a large portion of Columbus' southern floor (Fig. 4.1a). These dark materials (TES albedo ~0.11) form aeolian bedforms and have a thermal inertia (~250 tiu) consistent with medium sand [*Presley and Christensen*, 1997], but meter-scale blocks are also present (Fig. 4.3c). This 11-km crater and a 14-km diameter crater on the southwest floor have lobate, single-layer ejecta, which are thought to result from

fluidization of subsurface volatiles in the impact target materials [e.g., *Barlow and Perez*, 2003].

4.2.2 Light-toned layered deposits

Fig. 4.1a shows outcrops of relatively light-toned materials scattered across the northeast quadrant of Columbus crater's floor, and in a discrete band approximately halfway down its walls—especially the northern and eastern walls. This band of material is more evident in Fig. 4.1b (see also Fig. 4.4a, inset), which shows its higher thermal inertia relative to adjacent crater wall materials, consistent with a more indurated surface. Thermal inertia of the light-toned materials is ~290 ± 40 tiu, within the range of values found for light-toned layered deposits in Terra Meridiani [*Arvidson et al.*, 2003] and Valles Marineris [*Fergason et al.*, 2006; *Mangold et al.*, 2008; *Chojnacki and Hynek*, 2008]. These values contrast with thermal inertias of ~130–190 tiu for the adjacent darker crater wall materials, which are likely surfaces dominated by loose fines.

The light-toned deposits trace a nearly continuous ring around the eastern, northern, and western crater walls, at a near-constant elevation of 1800 ± 150 m (Fig. 4.1b). At this elevation, crater wall profiles from an HRSC digital elevation model (DEM) show a convex-up break in slope at many—though not all—azimuths (Fig. 4.4). The ring is interrupted by the *D*~14 km crater on the southwest floor, and by the previously mentioned valleys on the northeast wall. On the southeast wall, it is poorly exposed at the resolution of Fig. 4.1, but higher-resolution images (HRSC, CTX, HiRISE) reveal small exposures of light-toned outcrop here as well, albeit largely covered by darker surficial materials. This 360° ring of light-toned, indurated material is perhaps the most striking morphologic aspect of Columbus crater, and to my knowledge it is unique—or at least uniquely well preserved—among Martian craters.

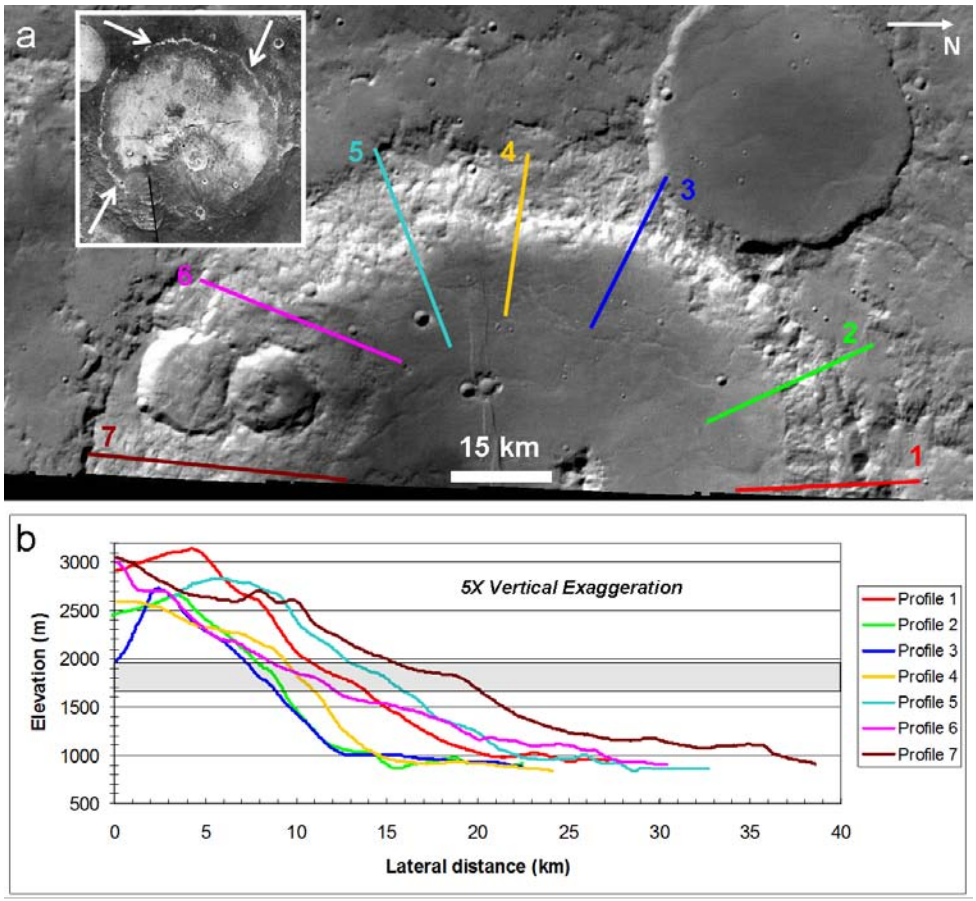

Figure 4.4: (a) Portion of HRSC h0538_0000 (red filter) covering western half of Columbus crater. Inset is THEMIS nighttime IR mosaic of Columbus crater, showing ring of light-toned deposits on the crater walls (arrows). (b) Crater wall elevation profiles, with colors and numbers corresponding to transects shown in (a). Gray zone marks elevation range of light-toned ring, at which many profiles show a convex-up break in slope.

High-resolution images of Columbus' ring show stratification at meter scales (Fig. 4.5). Beds are typically light-toned, but some darker beds are observed low in the section (Fig. 4.5c; see also Fig. 3.11C). Successive beds exposed in cross section appear approximately parallel, and to date no unambiguous angular unconformities have been observed. Further insight into bed geometries can be gleaned via strike and dip measurements from a high-resolution DEM. I use a DEM with 1 m grid spacing and vertical precision ~0.2 m produced by Sarah Mattson from HiRISE images PSP_005429_1510 and PSP_005851_1510 via the techniques of *Kirk et al.* [2008]. These images cover a well-exposed portion of the Columbus wall ring (Fig. 4.5a

shows a subset), where some individual beds can be traced across >1 km of outcrop.

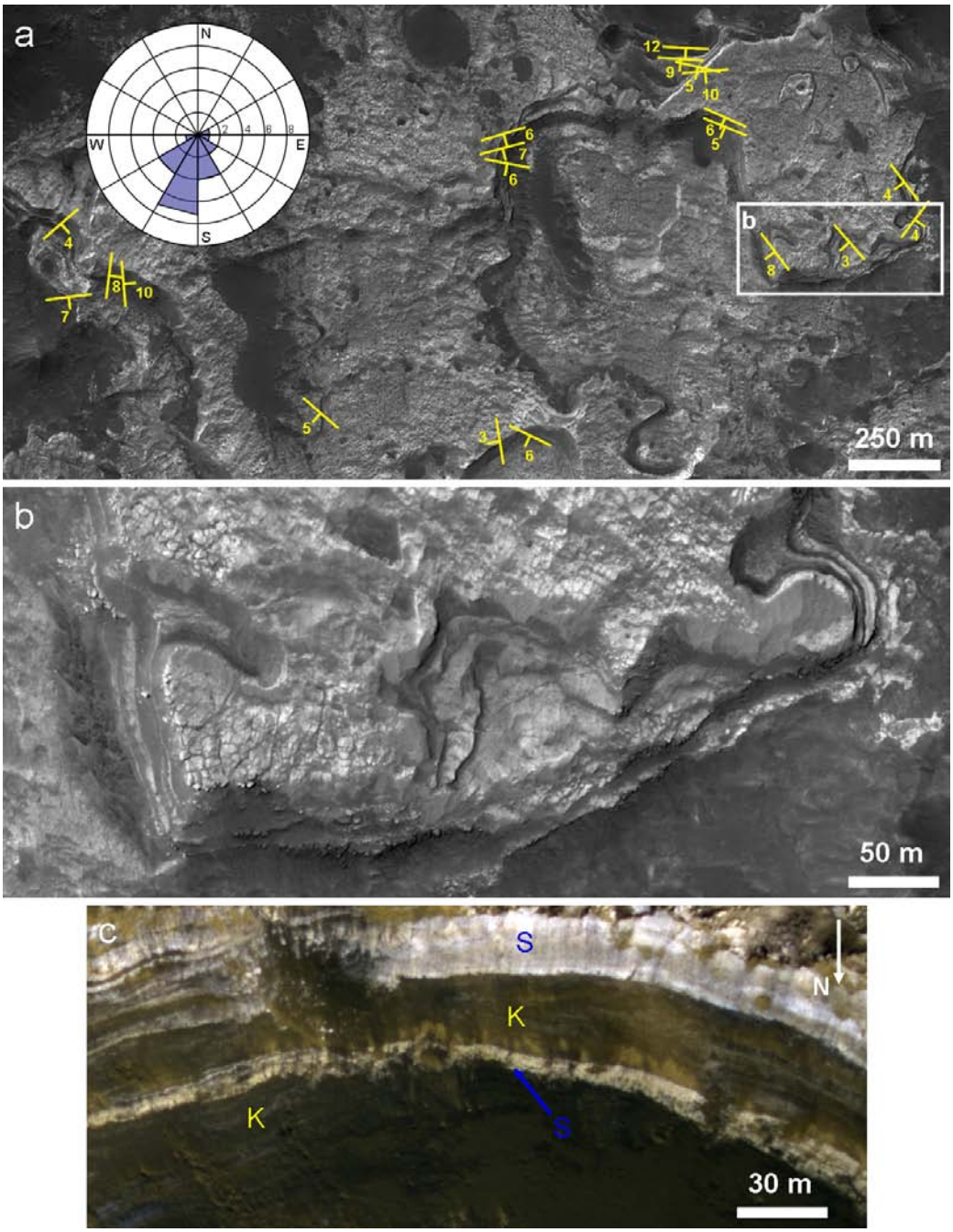

Figure 4.5: Light-toned layered materials on Columbus' northern wall, part of the deposit that rings the crater walls. (a) Portion of HiRISE PSP_005429_1510, with bedding strike and dip measurements (degrees) from HiRISE DEM superposed. Dip direction histogram "rose plot" (inset) highlights the predominance of southward dips. (b) Meter-scale bedding and meter-to-decameter-scale polygonal fracture patterns. (c) Light-toned beds and underlying darker beds of Columbus wall ring, exposed in southern wall of small (*D*~750 m) superposed crater; from ESP_013182_1515. S=sulfate-bearing, K=kaolinite-bearing (Figs. 3.14, 3.15).

Bed strike and dip angles were measured from the DEM using multi-linear regression to find the best-fit plane through a set of points chosen manually along a bed. For each of twenty beds exposed within the area of Fig. 4.5a, I selected between 8 and 28 points, which in all cases were well fit by a plane, with r^2 values of 99.5% or higher. Measured dip angles generally range from 3° to 10°, with a mean of 6.4° (median 6.3°) and typical uncertainties of ~1.0° (95% confidence level). Dip directions generally range from 125° to 235° clockwise from north, with most uncertainties <10°. Where multiple overlying beds can be measured on the same escarpment, their dips and dip directions are typically consistent with each other within the uncertainties, supporting the inference that bedding is conformable. The mean dip direction at this location is 183°, almost directly due south and toward the crater interior. These dip directions are measured from escarpments facing a range of azimuths (Fig. 4.5a).

DEM measurements also allow estimation of the total thickness of the Columbus wall ring deposits. Bed dips are used to calculate their true stratigraphic thickness (which is only equivalent to scarp height if bedding is horizontal), yielding an estimate of ~20 m total thickness of light-toned beds in the deepest exposures.

Ring bed surfaces have a range of textures, but fracturing is common, typically yielding polygonal “tiles” a few to ~10 m across (Figs. 4.5b and 4.6b). Polygon borders are typically darker than their interiors, probably due to shadowing and/or filling of fractures by fine-grained materials darker than the outcrop. However, bright polygon borders are observed in a few outcrops of the darker rocks immediately underlying Columbus’ light-toned ring (Fig. 4.7). Relative brightness may indicate these polygon borders are intrinsically lighter-toned and/or relatively high-standing.

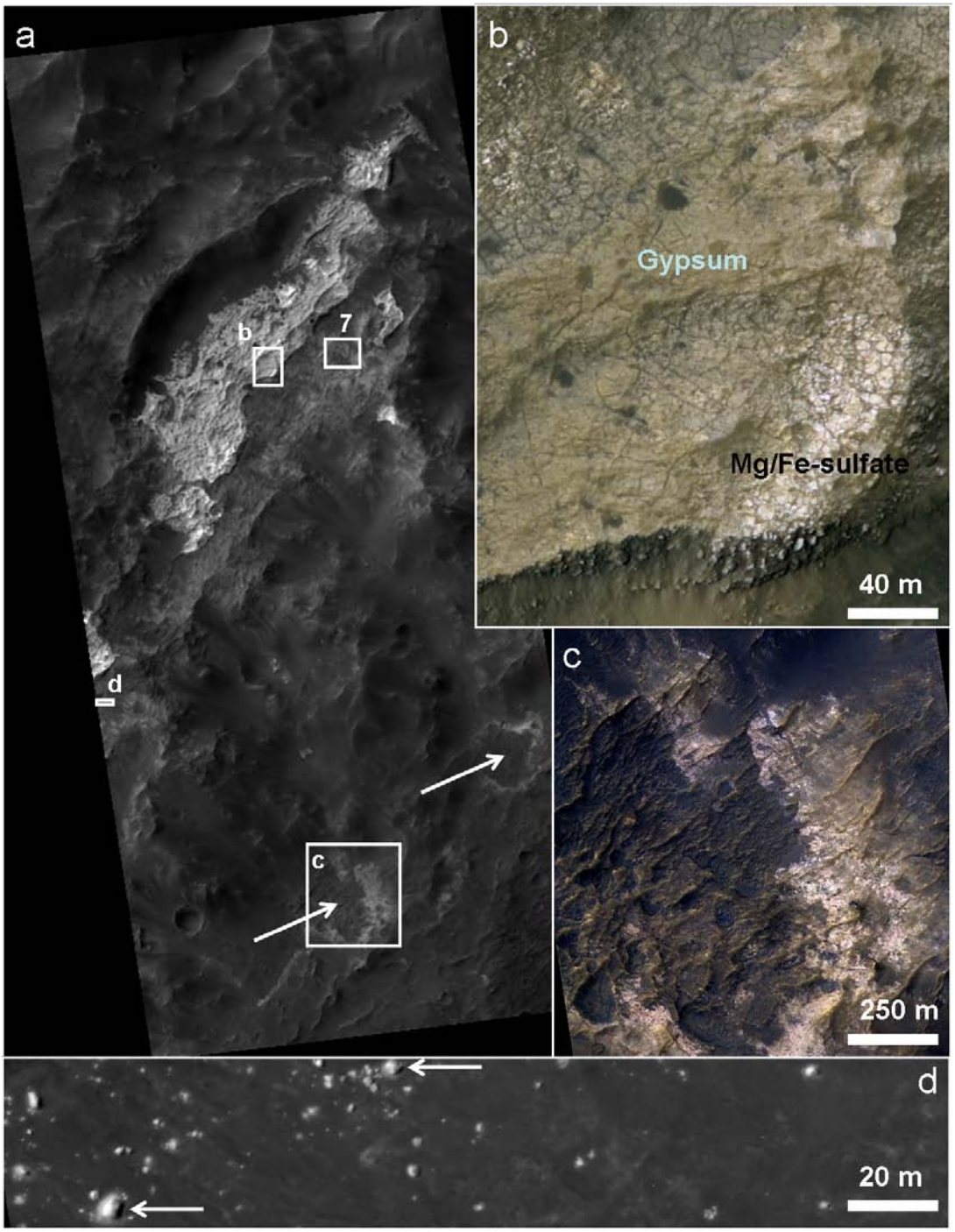

Figure 4.6: (a) HiRISE image ESP_013960_1510, showing a portion of the Columbus ring perched on a wall terrace, as well as two bright-ringed pits (arrows) on the crater floor. (b) Textural and albedo contrast between different spectral (mineralogic) units within the ring. (c) Color diversity in the light-toned materials ringing a pit on Columbus' floor, which is filled with dark-toned materials. (d) Light-toned blocks downslope from Columbus' wall ring; note "halos" of bright-toned material surrounding many blocks (e.g., arrows).

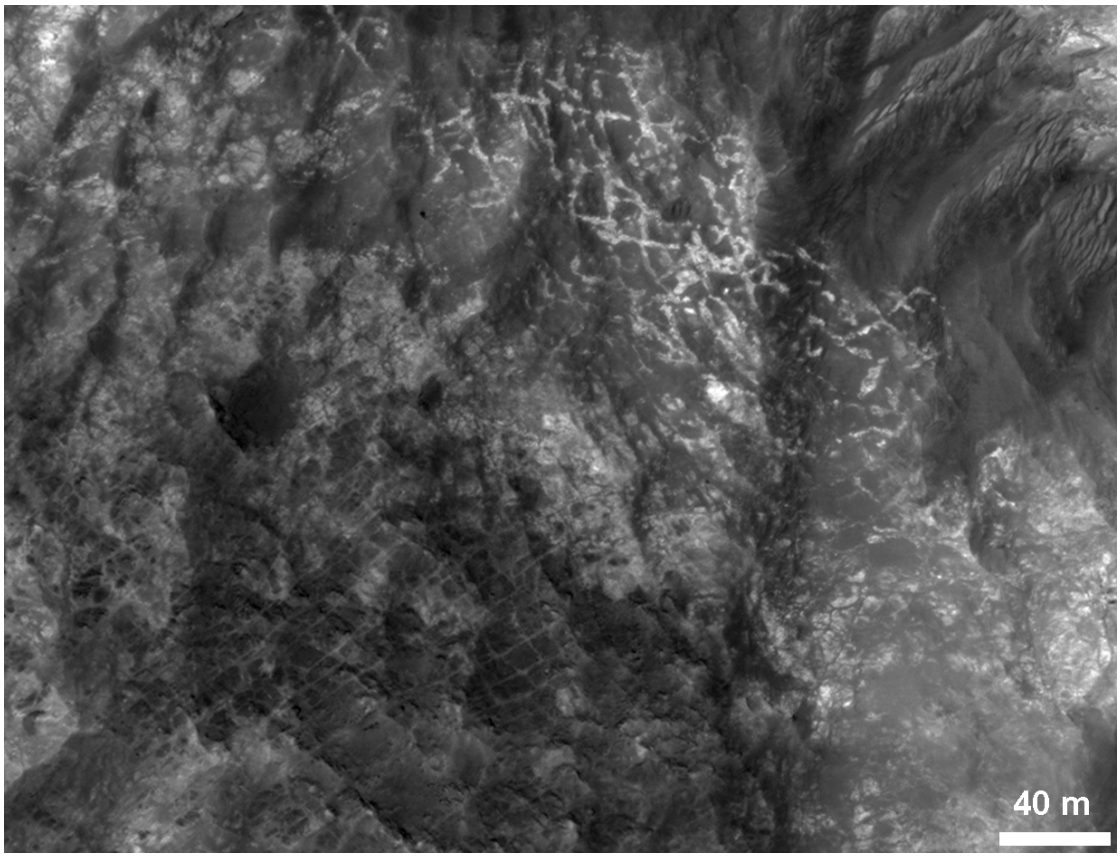

Figure 4.7: Light-toned material filling fractures in kaolinite-bearing outcrop underlying Columbus' wall ring; from HiRISE ESP_013960_1510. Location is shown in Fig. 4.6a.

Immediately downslope (toward the crater interior) from escarpments of Columbus ring materials, light-toned blocks up to several meters across are observed (Fig. 4.6d). Many of these blocks are surrounded by "halos" of light-toned surface material, reminiscent of the "Gray Rock Soil" concentrations observed around "Gray Rocks" by the Imager for Mars Pathfinder [*Bell et al.*, 2002]. Those soils were inferred to be flakes or spalls from the rocks that they surround, subsequently comminuted and mixed with other aeolian fines. In the rocks of the Columbus ring, pervasive fractures may promote physical weathering and rockfall, after which blocks are worn away by aeolian erosion and further weathering.

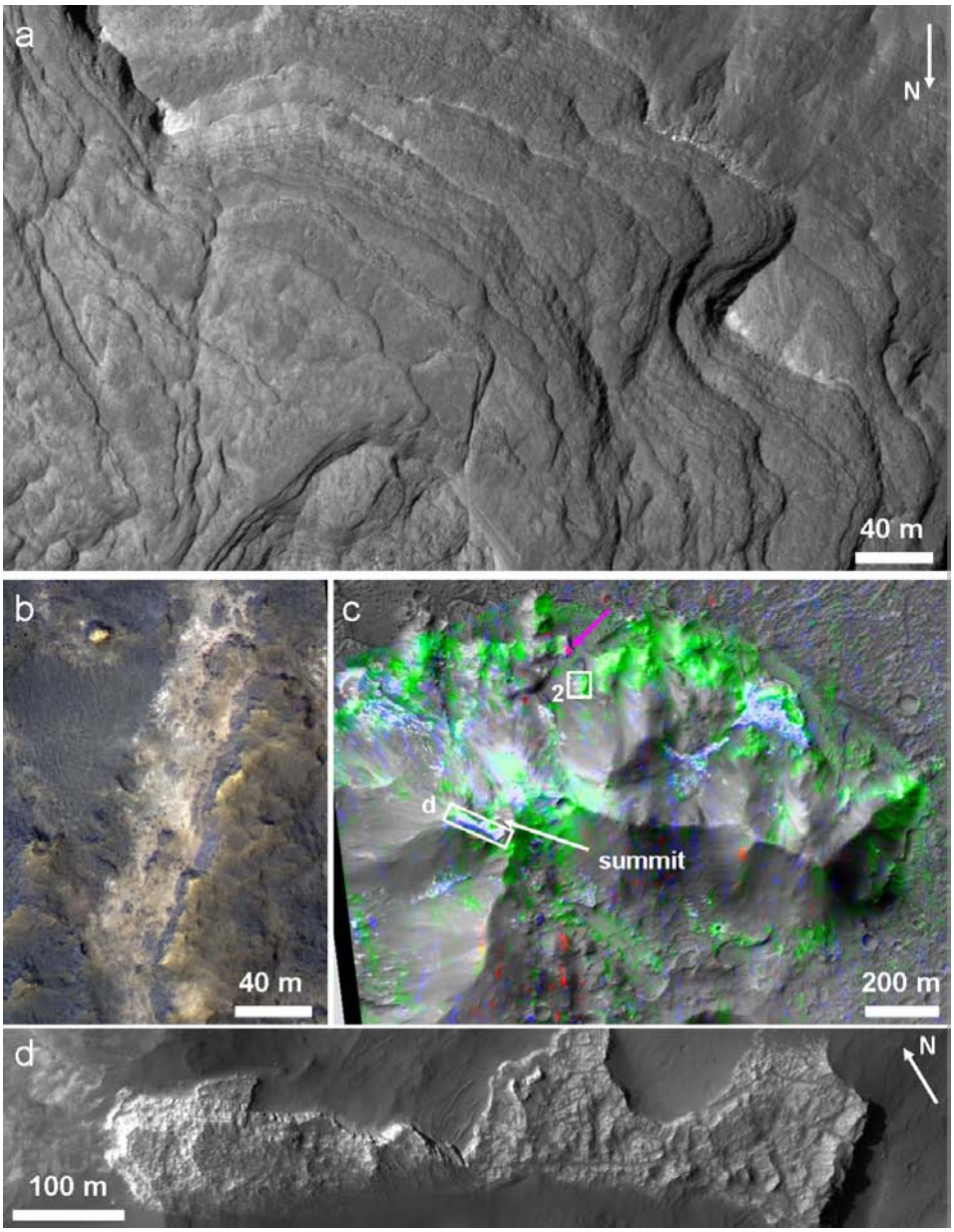

Figure 4.8: Light-toned deposits on Columbus crater floor. (a) Bedded outcrop on northeast crater floor; from HiRISE PSP_010281_1510. Location is shown in Fig. 4.20a. (b) Light-toned material exposed in west-facing escarpments of ridges on western crater floor; from HiRISE PSP_004018_1505. Location is in Fig. 4.3a. (c) Light-toned deposits in hills on north/central crater floor; from CTX P12_005851_1505, colored with spectral parameter maps from CRISM FRT0001663B. Red is BD2100 [*Pelkey et al.*, 2007], green BD2200 [*Ehlmann et al.*, 2009], and blue SINDEX [*Roach et al.*, 2009]. Green materials contain kaolinite, blue polyhydrated sulfate, and magenta monohydrated sulfate (arrow). (d) Sample of light-toned deposits near summit of Columbus floor hill complex; from HiRISE ESP_016083_1505. Note morphologic similarity to deposits ringing Columbus' walls (e.g., Fig. 4.5b).

Light-toned materials are visible (Fig. 4.1a) not only in the ring around Columbus' walls, but also on parts of the crater floor not covered by the possible lava flows discussed previously, particularly in the crater's northeast quadrant. Fig. 4.8a shows a representative outcrop from this area, with dozens of meter-scale beds exposed in cross-section. Strata exposed on the crater floor are typically darker-toned and show less relative contrast than strata in the ring along the crater wall. Boulders sourced from these beds are rare. As with the wall ring deposit, no clear angular unconformities between successive beds are visible, although it is difficult to trace the beds over long distances due to debris cover and erosional topography.

Light-toned materials on the western crater floor are most commonly exposed in (typically west-facing) escarpments of wrinkle ridges (Fig. 4.3a). Fig. 4.8b shows an example, where light-toned materials crop out beneath darker materials. Other exposures of light-toned material on the crater floor are generally limited to the ejecta and walls of small superposed craters (see section 4.5), and to a narrow zone at the base of Columbus' crater walls where the younger lava flow may be thin to absent. For example, Fig. 4.6a shows two bright-ringed pits on the northwestern crater floor edge, both filled with dark materials. Color diversity in the light-toned rocks exposed in these pits (Fig. 4.6c) suggests that diverse lithologies may be present. One final location where light-toned materials are found is in the hills ~15 km NNW of the crater's center (Fig. 4.8c). These hills, which have a fairly sharp crest line, appear to be predominantly composed of dark-toned material along with megabreccia (Fig. 4.2). However, light-toned deposits that are morphologically (and mineralogically) similar to those in the Columbus wall ring are present at a range of elevations, up to the highest peak in the hills (Fig. 4.8c-d).

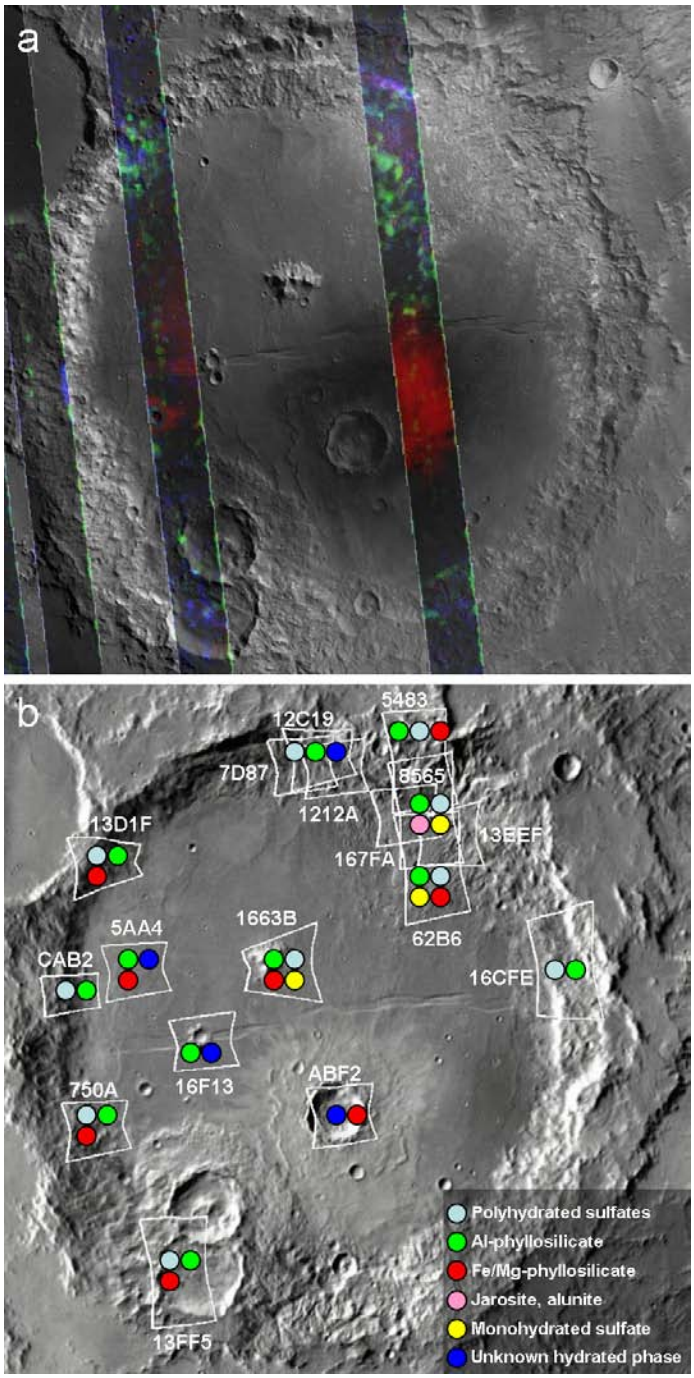

Figure 4.9: (a) CRISM multispectral mapping data from MRDR tile 553 overlain on HRSC nadir channel mosaic of Columbus crater. Red is OLINDEX, green BD2210 [*Pelkey et al.*, 2007], and blue SINDEX [*Roach et al.*, 2009], respectively corresponding to olivine, Al-phyllosilicates, and hydrated sulfates. (b) CRISM targeted observation footprints mapped on THEMIS daytime IR mosaic of Columbus. Numbers correspond to observation IDs (e.g., "ABF2" is FRT0000ABF2), and colored dots indicate secondary minerals identified through analysis of each observation.

4.3 Mineral Identification and Distribution at Columbus

4.3.1 Overview and methodology

To constrain the compositions of materials in Columbus crater—especially the light-toned deposits described in section 4.2.2—I use orbital infrared spectroscopy. Although preliminary estimates of Martian secondary mineral abundances from NIR spectra are intriguing [*Poulet et al.*, 2008b], the scope of this section is limited to simply identifying these minerals using CRISM data; abundances are discussed in section 4.4 on the basis of thermal emission spectra.

Fig. 4.9a shows maps corresponding to olivine, Al-phyllosilicates, and hydrated sulfates derived from ~200 m/pixel CRISM multispectral mosaics. Olivine is present in the ejecta of small craters superposed on Columbus' floor (red tones in Fig. 4.9a); in particular, the dark ejecta of the *D*~11 km crater on the southern floor contain the strongest olivine signature observed by CRISM within several hundred km of this location. Al-phyllosilicates (green tones in Fig. 4.9a) are present in the light-toned materials widespread across the northeast crater floor, at several locations on the crater walls, and in a narrow strip on the southeast floor at the foot of the crater wall. Weak signatures of hydrated sulfates are detected in some locations on the crater floor (blue tones), but they are most apparent in the light-toned ring around the crater wall, including where this ring extends onto the floor of the *D*~17 km crater shown in Fig. 4.10.

For more specific mineral identifications and correlations to surface morphology, the remainder of this section is devoted to analysis of CRISM hyperspectral targeted observations. These data were processed as described in section 2.2, but using an updated atmospheric correction [*McGuire et al*., 2009] and a spatial and spectral noise filtering procedure developed by *Parente* [2008]. I have processed and analyzed all CRISM targeted observations of Columbus crater acquired

as of spring 2010. Fig. 4.9b shows their distribution and the secondary minerals identified in each location. Minerals were identified by examining maps of the relevant spectral summary parameters defined by *Pelkey et al.* [2007], *Roach et al.* [2009], and *Ehlmann et al.* [2009], and then plotting CRISM spectra against laboratory spectra to confirm detections. For one CRISM observation with especially strong spectral signatures (FRT00007D87), Roger Clark provided an analysis using the USGS Tetracorder system [*Clark et al.*, 2003] to search for additional spectral phases that might have been missed by my manual approach.

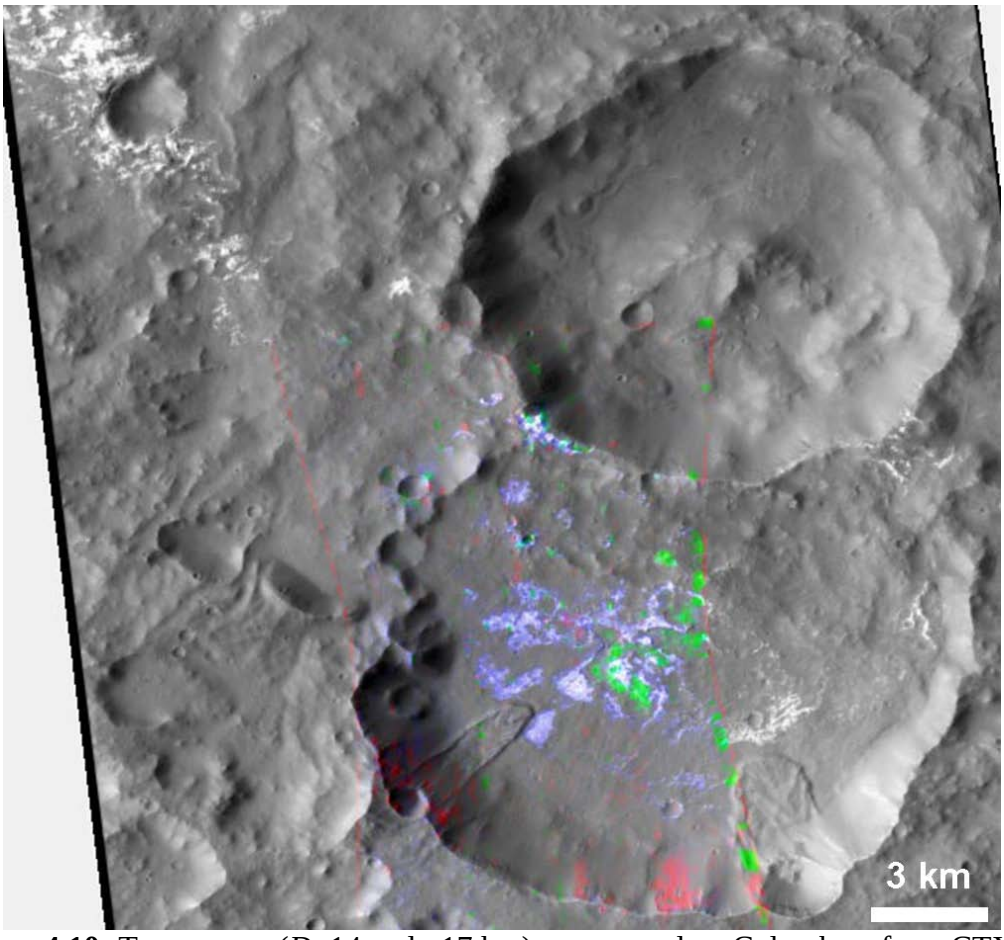

Figure 4.10: Two craters (*D*~14 and ~17 km) superposed on Columbus; from CTX P04_002739_1505 colored with spectral parameter maps from CRISM HRL00013FF5. Red is D2300 [*Pelkey et al.*, 2007], green BD2200 and blue BD1900H [*Ehlmann et al.*, 2009]. Like all the light-toned deposits ringing Columbus' walls (e.g., upper left of figure), deposits on the floor of the 17-km crater contain hydrated sulfates (blue) and kaolinite (green); Fe/Mg-phyllosilicate (red) is exposed in the crater's southern wall.

The following subsections give the rationale for each mineral identification and present representative spectra. The location and setting of each mineral within the crater is also described.

4.3.2 Aluminum phyllosilicates

As mentioned in chapter 3, the most commonly detected phyllosilicate type in Columbus crater is the kaolin group (Fig. 4.11). This group of $Al_2Si_2O_5(OH)_4$ polymorphs includes kaolinite, halloysite, and the less common minerals dickite and nacrite. Kaolin group clay minerals are spectrally distinct from Al-smectite clays such as montmorillonite and beidellite: the former exhibit doublets near 1.4 and 2.2 µm, whereas the latter exhibit single absorptions at these wavelengths as well as the H_2O band near 1.9 µm [e.g., *Clark et al.*, 1990; *Bishop et al.*, 2008a]. Halloysite can be difficult to distinguish from kaolinite when the latter is mixed with another hydrated mineral, but dickite and nacrite are distinguished by their more symmetric and narrower 2.2 µm doublet absorptions [*Ehlmann et al.*, 2009]. The kaolin group clay spectra in Columbus crater are most consistent with kaolinite or halloysite.

Tetracorder analysis of FRT00007D87 identifies not only kaolinite, but also the Al-smectite montmorillonite in some outcrops. Montmorillonite, especially when mixed with kaolinite, can be challenging to distinguish from halloysite, poorly crystalline kaolinite, or other kaolinite-smectite mixtures, because all of these have a less distinct 2.2 µm doublet than well-crystalline kaolinite. Perhaps the most diagnostic effect of adding montmorillonite to kaolinite is the broadening of the long-wavelength edge of the 2.2 µm absorption [*McKeown et al.*, 2010; Fig. 13a of *Clark et al.*, 2003]. Spectra from locations in Columbus crater mapped by Tetracorder as montmorillonite-bearing indeed have a broad rise from 2.20 to 2.27 µm and a weak or absent 2.16 µm kaolinite doublet feature (Fig. 4.11, bottom CRISM spectrum), consistent with montmorillonite being the spectrally dominant phase at these locations.

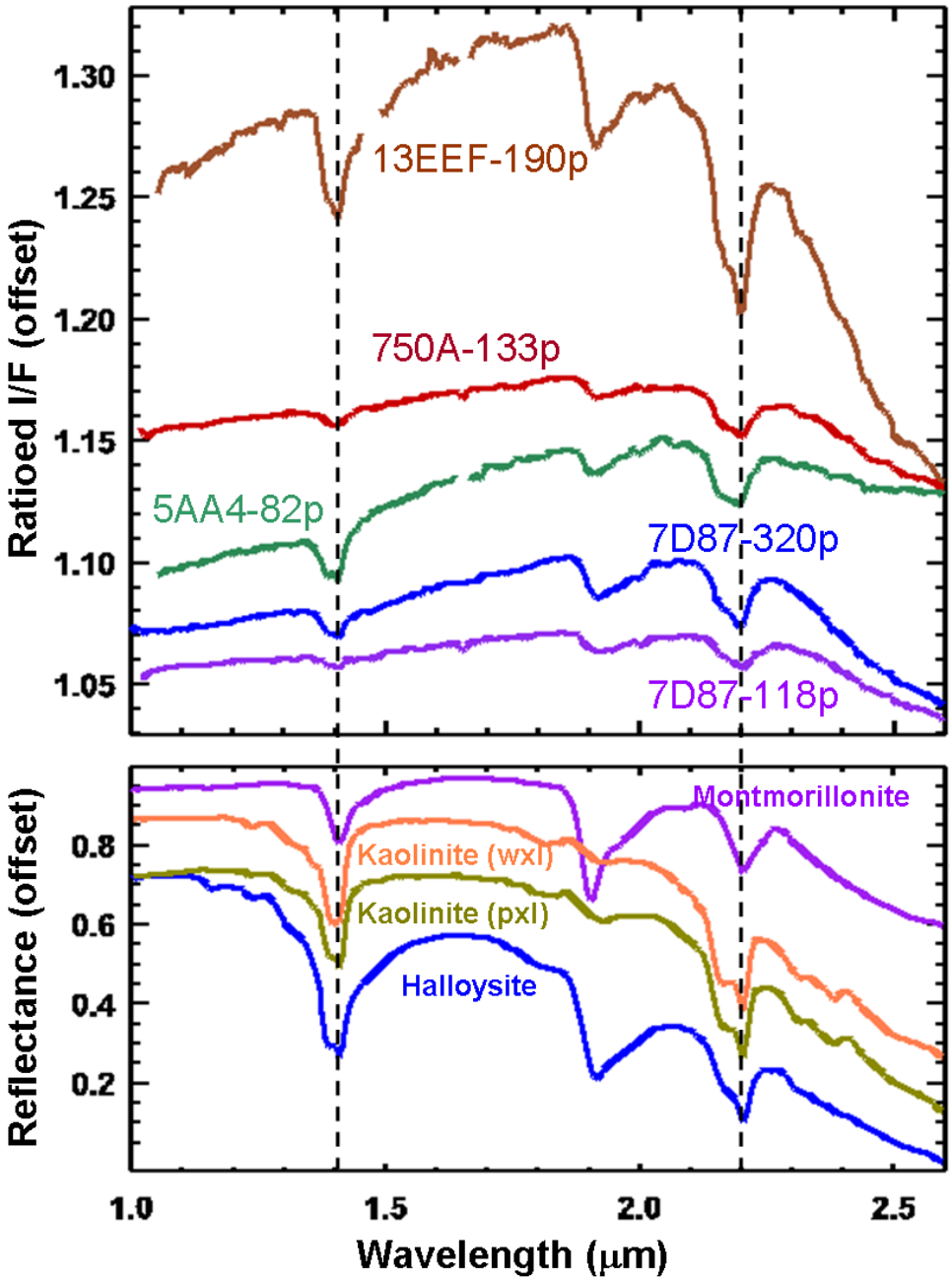

Figure 4.11: CRISM spectra from Columbus crater (top) and lab spectra of Al-phyllosilicates (bottom). Here and in other figures in this chapter, CRISM spectra are labeled with abbreviated image IDs (e.g., 750A is FRT0000750A) and the number of pixels averaged in each spectral numerator. Vertical dashed lines are provided to aid visual comparisons of spectra. The bottommost CRISM spectrum has a 2.2 μm band shape largely consistent with montmorillonite, but is most likely a mixture; other CRISM spectra are consistent with kaolinite group clays. Montmorillonite is sample SWy-1, well-crystalline (wxl) kaolinite is KGa-1, poorly crystalline (pxl) kaolinite is KGa-2, and halloysite is KLH503 from *R. Clark et al.* [2007].

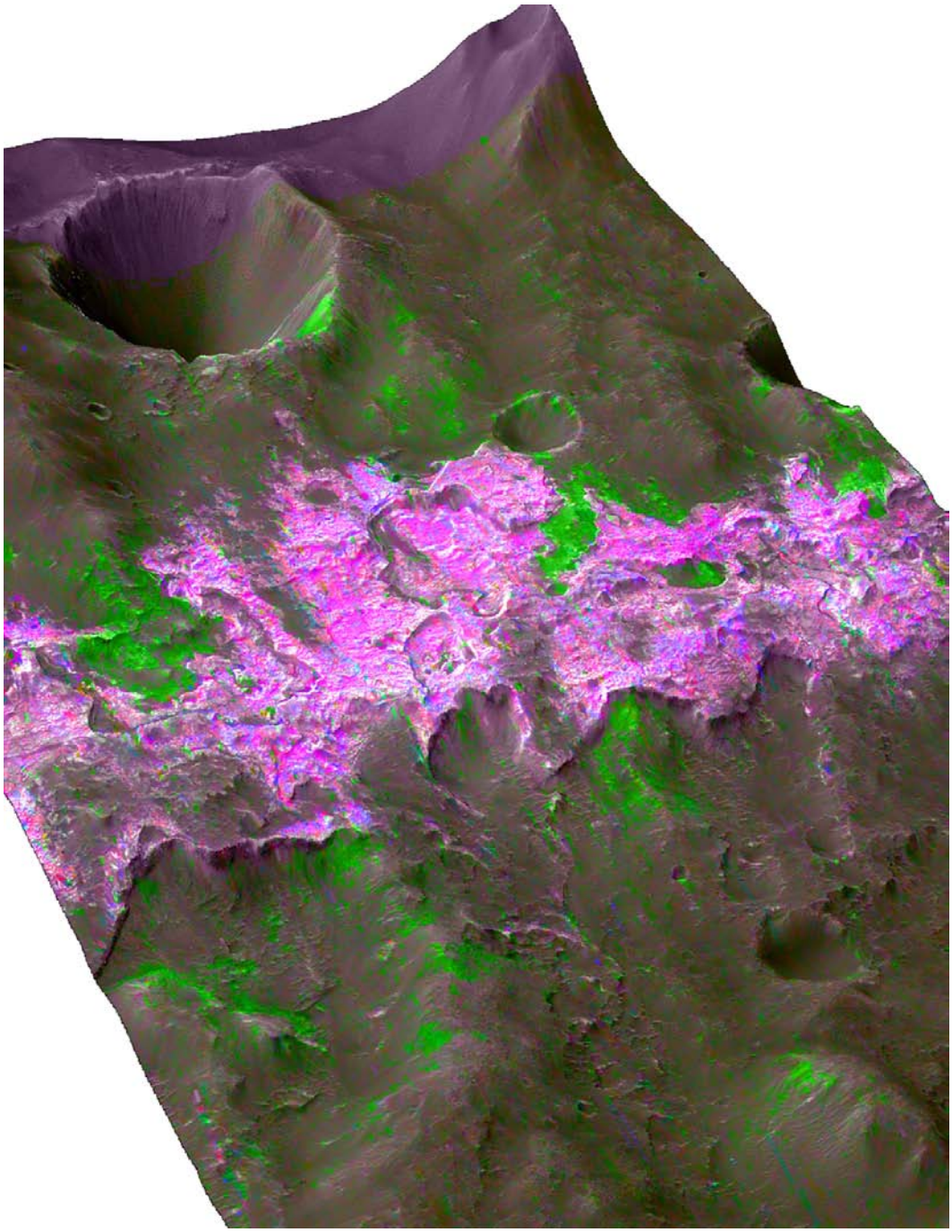

Figure 4.12: Perspective view of a portion of HiRISE PSP_005429_1510 (area near center is shown in Fig. 4.5a), colored with spectral parameter maps from CRISM FRT00007D87 using the techniques described by *Delamere et al.* [2010, section 6.1] and projected on HiRISE DEM. Red is SINDEX [*Roach et al.*, 2009], green BD2200 and blue BD1900H [*Ehlmann et al.*, 2009]; purple/pink colors correspond to hydrated sulfates and green to Al-phyllosilicates. The latter are exposed in erosional windows, including along the edges of the light-toned, sulfate-bearing deposits. Crater at upper left is ~1.6 km in diameter.

Aluminum phyllosilicates are found in every CRISM observation of Columbus except for one covering the *D*~11 km crater on the southern floor. Kaolinite is found on both Columbus' walls and floor. Fig. 4.12 shows a perspective view of the northern crater wall, in which the green areas contain Al-phyllosilicates. These phyllosilicates are seen directly adjacent to—and, for the most part, stratigraphically beneath—Columbus' light-toned ring deposit, as well as several km upslope and downslope. At this particular location, where montmorillonite was mapped independently from kaolinite, the strongest kaolinite signatures are adjacent to the ring deposit, whereas the largest montmorillonite-bearing exposures occur farther from the ring. However, the two Al-phyllosilicates are typically mixed in Columbus crater, with evidence for a kaolinite component in all exposures.

Many crater wall exposures of Al-phyllosilicate are morphologically unremarkable (e.g., dark materials beneath the light-toned layers in Fig. 4.5b), but in some cases these exposures exhibit stratification (e.g., dark layers in Fig. 4.5c) and/or fracture patterns (Fig. 4.7). In rare instances, Al-phyllosilicates are interbedded with the lighter-toned rocks of the wall ring (Fig. 4.5c; see also chapter 3). This interbedding likely reflects changing depositional environments or sediment sources, although it could alternatively result from *in situ* alteration that was strongly controlled by variations in porosity, permeability, and primary mineralogy between strata.

4.3.3 Polyhydrated sulfates

As shown in chapter 3, hydrated sulfate is also detected in Columbus crater, specifically gypsum ($CaSO_4 \cdot 2H_2O$) and another polyhydrated phase consistent with Mg-sulfate (Fig. 4.13). Gypsum can be uniquely identified by an absorption at 1.74–1.75 μm and diagnostic triplets at 1.44, 1.49, 1.53 μm and 2.17, 2.21, 2.27 μm [*Crowley,* 1991; *Cloutis et al.,* 2006].

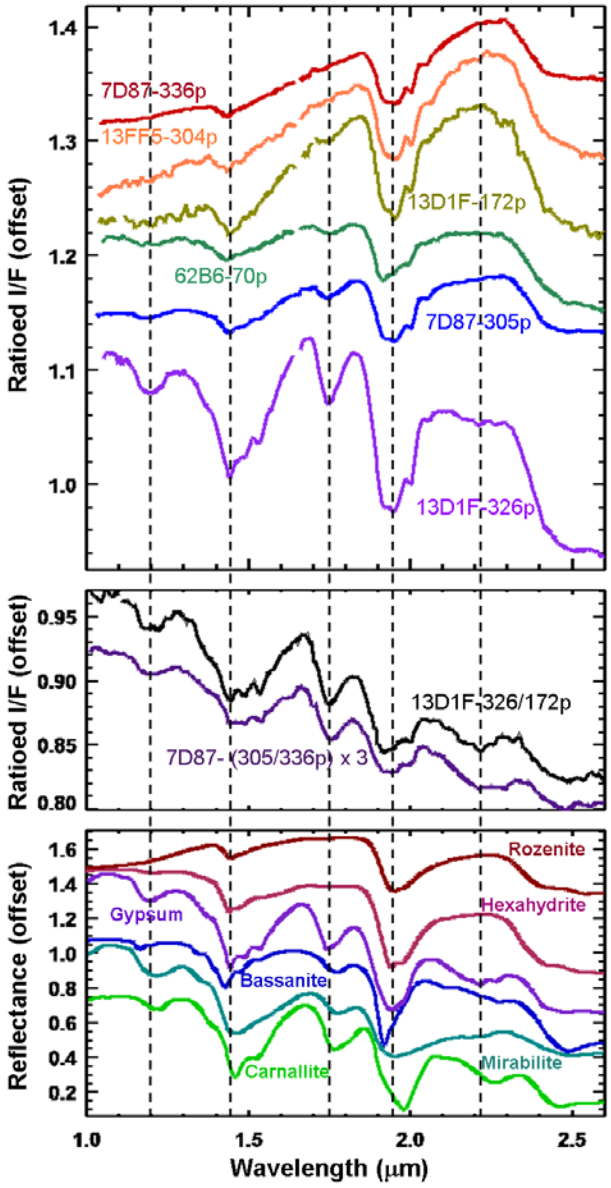

Figure 4.13: CRISM spectra from Columbus crater (top) and lab spectra of polyhydrated salts (bottom); format similar to Fig. 4.11. Spectra in top panel show increasing strength of the 1.75 μm band (interpreted as due to gypsum) relative to the 1.94 μm band. No spectra from Columbus crater are consistent with pure gypsum, but in the middle panel I attempt to isolate the gypsum component by plotting intra-scene ratios between spectra shown in the top panel. These ratios (especially from FRT00013D1F) show the ~1.5 and ~2.2 μm triplet absorptions that are unique to gypsum among hydrated salts (see bottom panel). Rozenite ($FeSO_4 \cdot 4H_2O$) is BKR1JB626B and hexahydrite ($MgSO_4 \cdot 6H_2O$) is LASF57A from the CRISM spectral library. Gypsum ($CaSO_4 \cdot 2H_2O$) is HS333.3B, bassanite ($CaSO_4 \cdot ½H_2O$) is GDS145, mirabilite ($Na_2SO_4 \cdot 10H_2O$) is GDS150, and carnallite ($KMgCl_3 \cdot 6H_2O$) is NMNH98011 from *R. Clark et al.* [2007].

Other sulfates, including Mg-sulfates, have less diagnostic near-IR spectral characteristics. Spectra with absorptions only at 1.43, 1.93 μm and an inflection at 2.4 μm (Fig. 4.13, top two CRISM spectra) are commonly interpreted as polyhydrated sulfates [e.g., *Gendrin et al.*, 2005], with the 2.4 μm feature attributed to an S–O overtone and/or OH/H_2O-related absorption(s) [*Cloutis et al.*, 2006]. However, caution is warranted because some non-sulfate hydrated salts [*Crowley*, 1991; *Lane et al.*, 2008; *Hanley et al.*, 2010] and some zeolites (e.g., thomsonite) [*Ehlmann et al.*, 2009] have a similar feature at 2.4 μm. In the case of Columbus crater, the occurrence of this hydrated phase with gypsum and other sulfates described below suggests it is likely a polyhydrated sulfate or possibly a hydrous chloride salt.

NIR spectroscopy alone does not always allow unique identification of the cation(s) in polyhydrated sulfates, but this technique does provide some constraints. Ca and Na are unlikely because—like gypsum—bassanite ($CaSO_4 \cdot ½H_2O$) and mirabilite ($Na_2SO_4 \cdot 10H_2O$) have strong bands near 1.75 μm [*Crowley*, 1991] that are absent from spectra of Columbus' non-gypsum polyhydrate. Eugsterite ($Na_4Ca[SO_4]_3 \cdot 2H_2O$) lacks a strong 1.75 μm band but absorbs at 2.48 μm [*Crowley*, 1991], a wavelength distinctly longer than the 2.4 μm band in the CRISM spectra. Mg and Fe are therefore the most geologically plausible candidate cations if this phase is indeed a sulfate. Either or both may be present, but at least some Mg seems likely because all Fe-sulfates have a broad absorption centered near 1 μm (centered at 0.9–1.2 μm for Fe^{2+} or 0.8–0.95 μm for Fe^{3+}) [*Burns*, 1993a; *Crowley et al.*, 2003; *Cloutis et al.*, 2006; *Lane et al.*, 2008]. These absorptions are not apparent in CRISM IR detector spectra (Fig. 4.13), nor in VNIR detector spectra of Columbus' polyhydrate-bearing materials (section 4.3.4; see also *Murchie et al.* [2009b]). Furthermore, Mg-sulfates are the most abundant salts in Meridiani bedrock [*Clark et al.*, 2005] and in Martian soils and rock coatings at all landing sites prior to Phoenix [*Vaniman et al.*,

2004]; they have now also been identified in Phoenix soils [*Kounaves et al.*, 2010]. They are a major component of secondary mineral assemblages produced in laboratory experiments [*Tosca et al.*, 2004] and geochemical models [*Tosca et al.*, 2005] of olivine-bearing rock alteration under Mars-like conditions. Nevertheless, the lack of a strong ~1 μm absorption in CRISM spectra is not in itself sufficient to rule out Fe^{2+} or Fe^{3+} sulfates; in fact, Fe-sulfates are identified elsewhere in Columbus crater (sections 4.3.5 and 4.3.6) even though no ~1 μm band is apparent in those cases. Therefore, I refer to this non-gypsum sulfate generically as polyhydrated Mg/Fe-sulfate(s).

The sulfate hydration state is also not well-constrained by the CRISM spectra. The spectrum of hexahydrite ($MgSO_4 \cdot 6H_2O$) is plotted in Fig. 4.13, but it is quite similar to spectra of epsomite ($MgSO_4 \cdot 7H_2O$), pentahydrite ($MgSO_4 \cdot 5H_2O$), and starkeyite ($MgSO_4 \cdot 4H_2O$) [*Crowley*, 1991], making these sulfates difficult to distinguish with CRISM. However, the monohydrate kieserite is spectrally distinct [*Cloutis et al.*, 2006] and inconsistent with the CRISM spectra in Fig. 4.13. Analogously, polyhydrated Fe^{2+}-sulfates including melanterite ($FeSO_4 \cdot 7H_2O$) have spectra similar to rozenite ($FeSO_4 \cdot 4H_2O$) shown in Fig. 4.13 [*Bishop et al.*, 2005], but the monohydrate szomolnokite is distinctive (section 4.3.5). In any case, these sulfates may have experienced hydration state changes since their formation [*Vaniman et al.*, 2004].

Polyhydrated sulfates are identified in every CRISM observation of the Columbus crater walls and in some observations of the northeast crater floor. They are the spectrally dominant phase in the finely bedded, light-toned deposits ringing Columbus' walls (e.g., Fig. 4.5a–b), and in a few comparably bright-toned outcrops at lower elevations within the crater (e.g., Figs. 4.8c and 4.14). The Mg/Fe-sulfate is ubiquitous in these materials, with varying contributions from gypsum. Spectral parameters can be used to map the two polyhydrates independently (Fig. 4.15a).

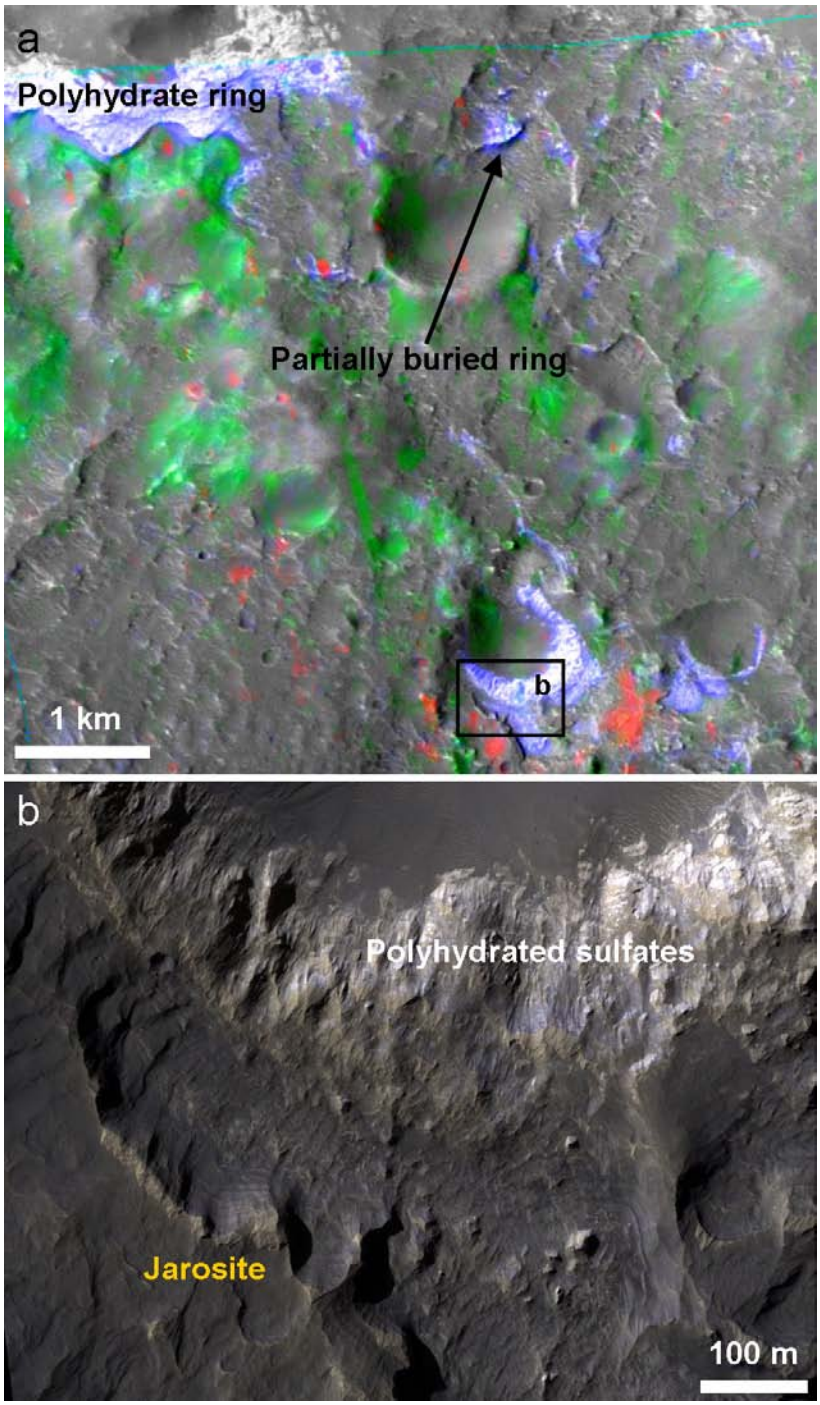

Figure 4.14: (a) Portion of northeast Columbus crater; from CTX P06_003306_1504 colored with spectral parameter maps from CRISM FRT000167FA. Red is 2.265 µm band depth, green BD2200 and blue BD1900H [*Ehlmann et al.*, 2009], respectively corresponding to jarosite, Al-phyllosilicates, and polyhydrated sulfates. Several hundred meters of elevation separate the wall ring deposit at ~1750 m (MOLA) from (b) jarosite-bearing beds and polyhydrated sulfates on the crater floor (elevation ~1100 m); from HiRISE PSP_010281_1510.

However, inspection of co-located images reveals no clear stratigraphic relationship between the relatively gypsum-rich outcrops and gypsum-poor outcrops. In some cases, the outcrops with gypsum appear relatively high-standing, darker, and more rugged than those without gypsum (Fig. 4.6b).

4.3.4 Crystalline ferric oxide/hydroxide

The sulfate-rich layered rocks examined by the Opportunity rover in Meridiani Planum contain coarse-grained gray hematite [e.g., *Christensen et al.*, 2000, 2004c], and orbital spectroscopy suggests that crystalline ferric oxides are found in many sulfate-bearing deposits on equatorial Mars [e.g., *Bibring et al.*, 2007]. Yet, at visible wavelengths, Columbus' light-toned layered deposits are spectrally similar to Martian dust [*Murchie et al.*, 2009b], lacking the absorptions at 0.8–0.9 μm due to crystalline ferric oxides [e.g., *Morris et al.*, 2000] identified in Mawrth Vallis (chapter 2) and found by CRISM elsewhere on Mars [*Murchie et al.*, 2009a; *Roach et al.*, 2010b]. Thermal emission spectra (section 4.4) also show no evidence for crystalline gray hematite in the Columbus layered deposits.

However, crystalline ferric oxides/hydroxides are present in dark-toned debris immediately downslope from Columbus' light-toned ring (Fig. 4.15a). Their spectra have an absorption centered at 0.92 μm (Fig. 4.15b), consistent with ferric minerals including goethite or ferrihydrite [e.g., *Morris et al.*, 2000; *Bishop and Murad*, 2002]. Aeolian bedforms are observed at the locations with ferric oxides (Fig. 4.15c). This concentration of ferric oxide in dark-toned debris adjacent to lighter sulfate-bearing outcrops is similar to the distribution of crystalline ferric oxides at many other locations on Mars [*Christensen et al.*, 2001b; *Soderblom et al.*, 2004; *Bibring et al.*, 2007; *Noe Dobrea et al.*, 2008a; *Weitz et al.*, 2008; *Mangold et al.*, 2008; *Le Deit et al.*, 2008; *Chojnacki and Hynek*, 2008; *Murchie et al.*, 2009a; *Bishop et al.*, 2009a], except that a comparable ferric oxide signature is not observed in Columbus' light-

toned deposits themselves.

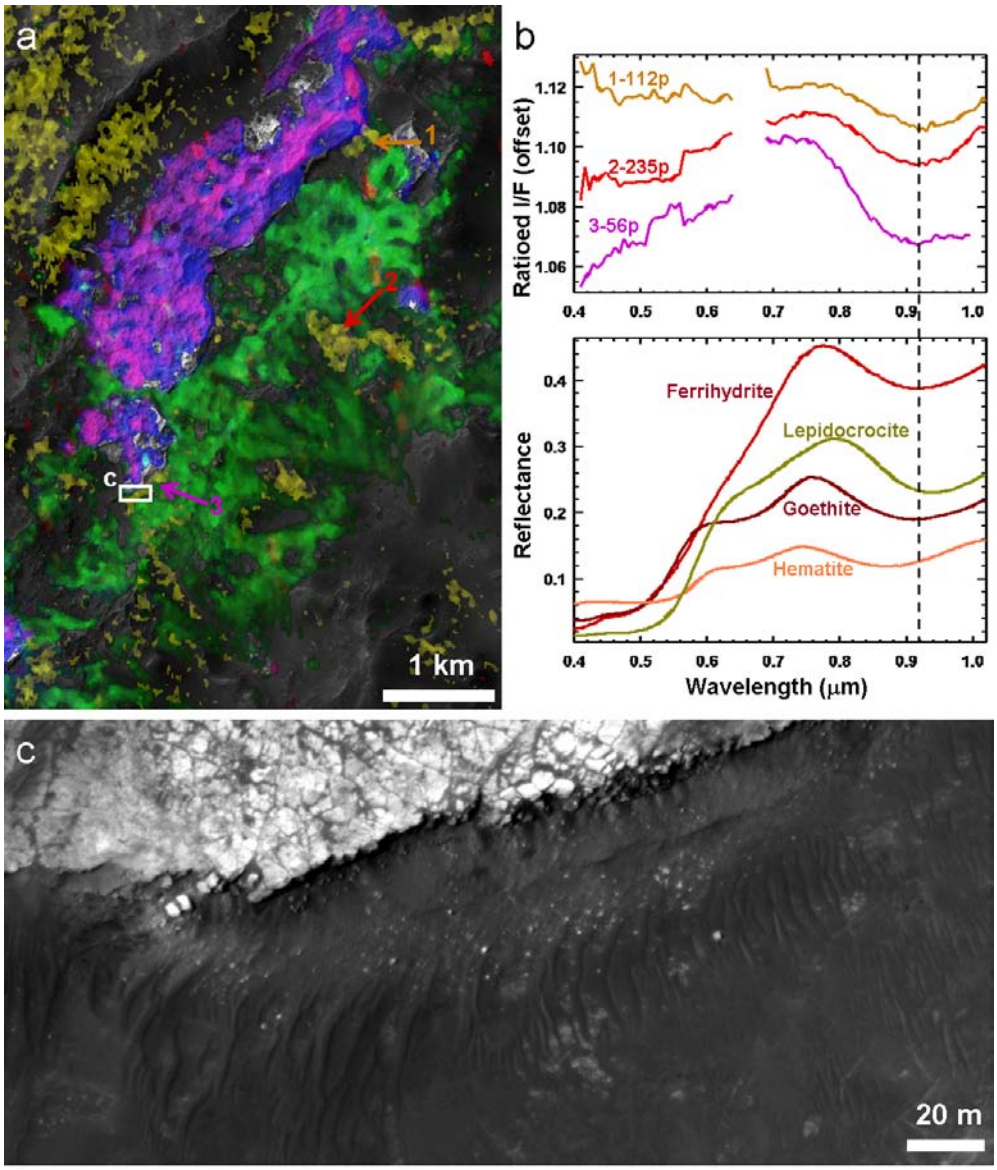

Figure 4.15: (a) A subset of HiRISE ESP_013960_1510 (Fig. 4.6a), colored with spectral parameters from CRISM FRT00013D1F. Red is BD1750, yellow BD920 [*Pelkey et al.*, 2007], green BD2200, and blue BD1900H [*Ehlmann et al.*, 2009]. Gypsum-bearing materials appear pink/purple, Mg/Fe-polyhydrate appears blue, Al-phyllosilicates green, and ferric oxides yellow. The ferric oxide map is imperfect, as yellow areas northwest of the light-toned ring (upper left) do not actually have a spectrum consistent with this phase. Numbered arrows indicate source locations for (b) ratio spectra from CRISM FRT00013D1F (top, with number of pixels averaged in spectral numerator indicated), with lab spectra of crystalline ferric oxides (bottom) shown for comparison. Ferrihydrite ($5Fe_2O_3 \cdot 9H_2O$) is C1092F55, lepidocrocite (γ-FeOOH) is 892F51, goethite (α-FeOOH) is C1GO01, and hematite (α-Fe_2O_3) is F1CC17B from CRISM spectral library. (c) Sample area with ferric oxide signature adjacent to light-toned bedrock, showing darker-toned aeolian bedforms.

4.3.5 Monohydrated sulfate

Monohydrated sulfates such as kieserite ($MgSO_4 \cdot H_2O$) and szomolnokite ($FeSO_4 \cdot H_2O$) are distinguished from more hydrated sulfates by a broad absorption that is deepest near 2.1 μm. Natural samples of kieserite have the band minimum at 2.13 μm, while for szomolnokite it occurs at 2.09–2.10 μm [*Crowley et al.*, 2003; *Cloutis et al.*, 2006; *Bishop et al.*, 2009a]. However, pure synthetic kieserite has been observed to have a shorter-wavelength minimum coincident with that observed for szomolnokite, potentially making it difficult to distinguish between these minerals [*Milliken,* 2006]. Only a few other minerals have a similarly broad absorption near 2.1 μm, including some NH_4-bearing minerals [e.g., *Bishop et al.*, 2002a], but these lack the 2.4 μm absorption typical of monohydrated sulfate spectra and/or have additional absorptions not observed in hydrated sulfates (Fig. 4.16). With band minima at ~2.11 and ~2.40 μm, the Columbus crater spectra in Fig. 4.16 appear most consistent with monohydrated sulfate.

A weaker, narrow absorption at 2.22–2.23 μm is also observed in the spectra of Fig. 4.16 (top panel), especially in the bottommost spectrum. A comparably narrow absorption at 2.23–2.24 μm has been observed in light-toned layered deposits on the plains west of Juventae Chasma [*Milliken et al.*, 2008; *Bishop et al.*, 2009a], in Aram Chaos [*Lichtenberg et al.*, 2010], and in Cross crater (G. A. Swayze et al., manuscript in preparation, 2010). This absorption has been attributed to Fe^{3+}-OH in the hydroxylated ferric sulfate $Fe(OH)SO_4$, a phase that has been formed in the laboratory at temperatures >200°C via dehydration of ferric sulfates such as hydronium jarosite [*Swayze et al.*, 2008a] or (ferri)copiapite [*Milliken et al.*, 2008; *Bishop et al.*, 2009a], or via oxidation and dehydration of ferrous sulfates such as melanterite or szomolnokite [*Morris et al.*, 2009; *Lichtenberg et al.*, 2010]. In Cross crater—a mere ~400 km from Columbus crater in northwest Terra Sirenum (see also sections 4.3.6

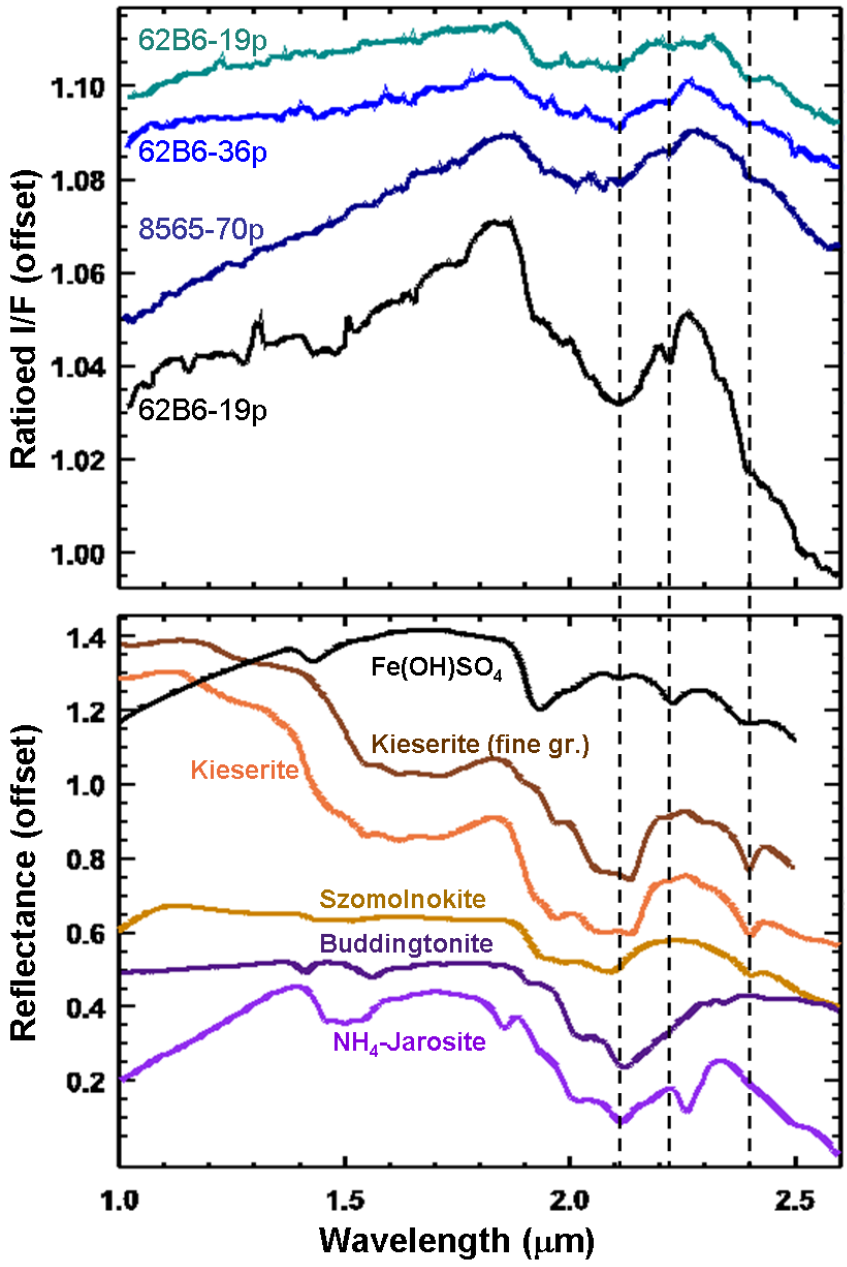

Figure 4.16: CRISM spectra from Columbus crater (top) and lab spectra of monohydrated sulfates and NH_4-bearing minerals (bottom); format similar to Fig. 4.11. Columbus crater spectra appear more consistent with monohydrated sulfates—plus an additional phase that absorbs at 2.22–2.23 μm, possibly $Fe(OH)SO_4$—than with NH_4-bearing minerals such as buddingtonite ($NH_4AlSi_3O_8$, a feldspar) or ammoniojarosite ($NH_4Fe_3[SO_4]_2[OH]_6$). $Fe(OH)SO_4$ is from copiapite dehydrated at 300°C, from *Bishop et al.* [2009a]. Fine-grained kieserite ($MgSO_4 \cdot H_2O$) is KIEDE1.b, buddingtonite is GDS85, and ammoniojarosite is SCR-NHJ from *R. Clark et al.* [2007]; other kieserite is F1CC15 and szomolnokite ($FeSO_4 \cdot H_2O$) is BKR1JB622A from CRISM spectral library.

and 4.6.1)—the 2.23 μm band has been found to date only in association with monohydrated sulfate (G. A. Swayze et al., manuscript in preparation, 2010), consistent with where it is found in Columbus crater. If the monohydrate in both craters is (at least partially) szomolnokite, then the 2.23 μm band could imply partial oxidation and dehydration of szomolnokite to form $Fe(OH)SO_4$.

The strongest monohydrate + $Fe(OH)SO_4$ signature yet observed in Columbus crater (Fig. 4.16, bottom spectrum in top panel) is found in a *D*~200 m crater on Columbus' northeast floor (Fig. 4.17a). Radial rays attest to the relative freshness of this impact crater, and exposures within the crater reveal that it excavated light-toned layered deposits. Several thin beds appear green in HiRISE enhanced color images (Fig. 4.17b), but their exposures are too narrow to be resolved by CRISM. While this color is rare in Columbus crater and in HiRISE enhanced color images of Mars in general, I have observed it in other locations where ferric sulfates are detected from orbit (Aram Chaos—e.g., Fig. 6.6—and the plains surrounding Valles Marineris). HiRISE IRB color composites [*McEwen et al.*, 2010] display IR (~875 nm), RED (~700 nm), and BG filter (~500 nm) images [*McEwen et al.*, 2007] in the red, green, and blue channels, respectively; therefore, a green hue indicates high RED I/F relative to the IR and BG, as would be expected for a ferric mineral such as $Fe(OH)SO_4$ due to its strong electron charge transfer absorption at <530 nm and crystal field transition absorption at 800–970 nm [*Milliken et al.*, 2008; *Lichtenberg et al.*, 2010] reducing reflectance in the BG and IR filters, respectively. Thus the green color is consistent with the CRISM-based inference of a ferric mineral such as $Fe(OH)SO_4$.

Most monohydrate exposures in Columbus are found on the northeast crater floor, although one outcrop has been identified at the base of the hills on the central floor (Fig. 4.8c). Monohydrate-bearing outcrops exhibit internal stratification (Figs. 4.8a, 4.17c) and, in comparison to beds within the polyhydrate-bearing crater wall ring

(Fig. 4.5), monohydrate beds are somewhat darker-toned, with weaker albedo contrasts between successive beds. The fracture patterns observed in the polyhydrate ring are less common in monohydrate-bearing outcrops, which in some cases display a "scalloped" or "reticulate" texture (Fig. 4.17d) reminiscent of that seen on some wind-

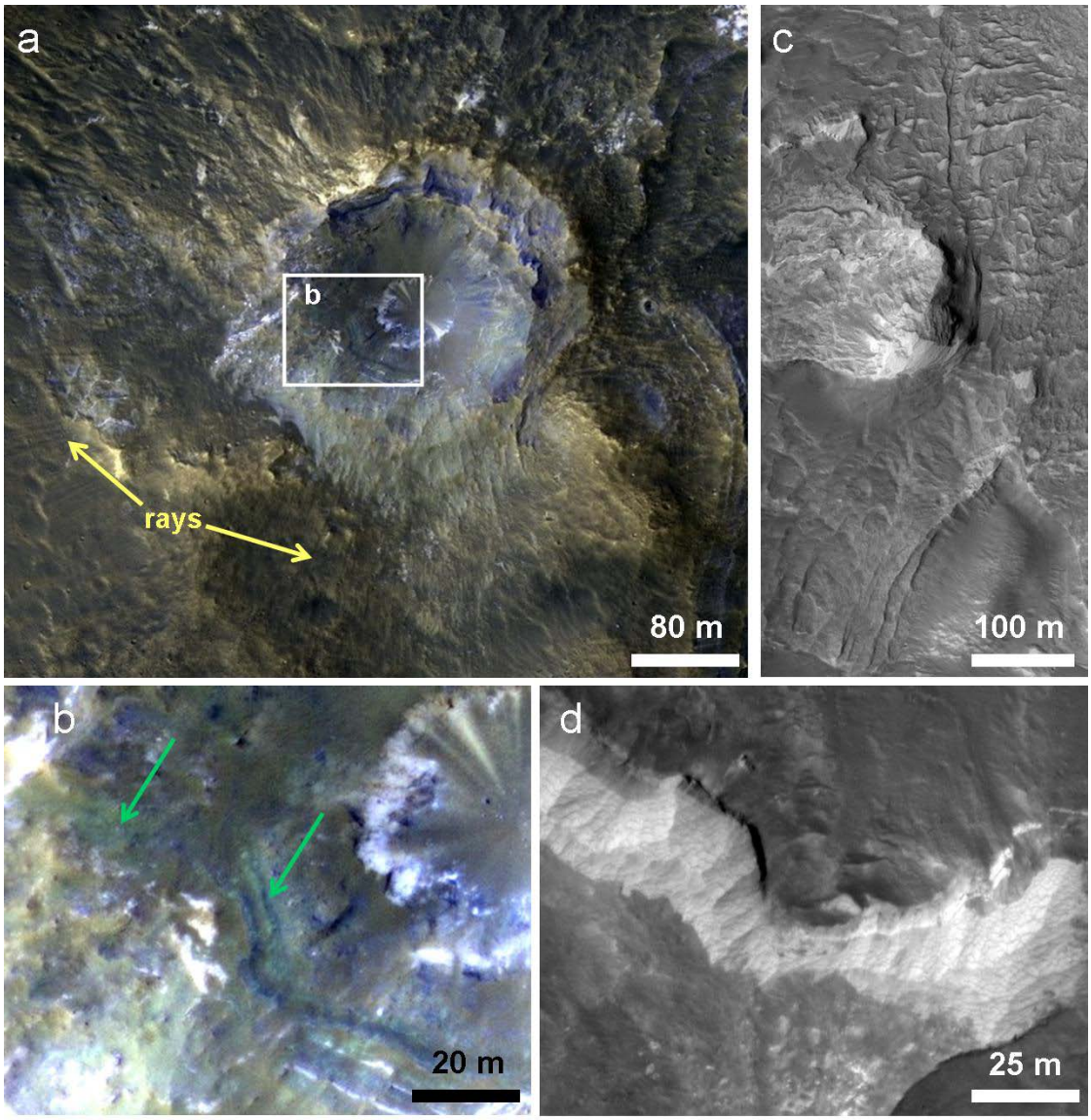

Figure 4.17: Columbus crater outcrops with spectral evidence for monohydrated sulfate; see Fig. 4.20a for locations. (a) Relatively fresh impact crater (note radial rays) with strongest monohydrated sulfate signature yet observed in Columbus crater (bottom spectrum in top panel of Fig. 4.16); from HiRISE ESP_014039_1510. (b) Subset of (a), showing layers with relatively green enhanced-color hue (arrows), possibly due to crystalline ferric minerals including sulfates. (c) Bedded outcrop with monohydrated sulfate (70-pixel spectrum in Fig. 4.16); from PSP_003306_1510. (d) Outcrop with possible "reticulate" texture; from ESP_014039_1510.

eroded surfaces elsewhere on Mars [*Bridges et al.*, 2010]. This texture is specifically associated with monohydrated sulfate in other regions [*Chojnacki and Hynek*, 2008; *Karunatillake et al.*, 2009; *Lichtenberg et al.*, 2010]. These morphologic characteristics are shared by the majority of light-toned outcrops on Columbus' floor, many of which are unresolved or not yet observed by CRISM.

4.3.6 Jarosite and alunite

The acid sulfate jarosite ($KFe_3[SO_4]_2[OH]_6$) was first identified on Mars in Meridiani Planum by Opportunity [*Klingelhöfer et al.*, 2004] and subsequently by CRISM in other regions [*Milliken et al.*, 2008; *Metz et al.*, 2009; *Farrand et al.*, 2009; *Weitz et al.*, 2010a]. A related acid sulfate, alunite ($KAl_3[SO_4]_2[OH]_6$), has been identified by *Swayze et al.* [2008b] in Cross crater—again, only ~400 km from Columbus. Here I present evidence for jarosite and possible alunite in Columbus crater.

Jarosite has a nearly unique absorption at ~2.265 μm, with additional absorptions at ~1.5, 1.85, 2.51, and 2.62 μm [*Crowley et al.*, 2003; *Bishop and Murad*, 2005; *Cloutis et al.*, 2006; *Swayze et al.*, 2008a]. K-jarosite has an additional band at ~2.21 μm that is weak to absent in Na- and H_3O-jarosites [*Cloutis et al.*, 2006; *Swayze et al.*, 2008a]. One location in Columbus crater has a spectrum exhibiting all of these absorptions except the ~1.5 μm band(s), and a ~1.93 μm band attributed to H_2O (common in lab spectra of jarosites formed at low temperature). The 1.85, 2.51, and 2.62 μm absorptions are near the noise level but are present in both CRISM observations covering the location of interest (Fig. 4.18). The 2.21 μm band observed in the CRISM spectra is most consistent with K-jarosite, similar to the Mawrth Vallis jarosite reported by *Farrand et al.* [2009]; however, in all K-jarosite lab spectra the 2.21 μm band is significantly weaker than the 2.265 μm band, so their comparable strength in the spectrum from HRL00008565 (Fig. 4.18) may indicate an additional

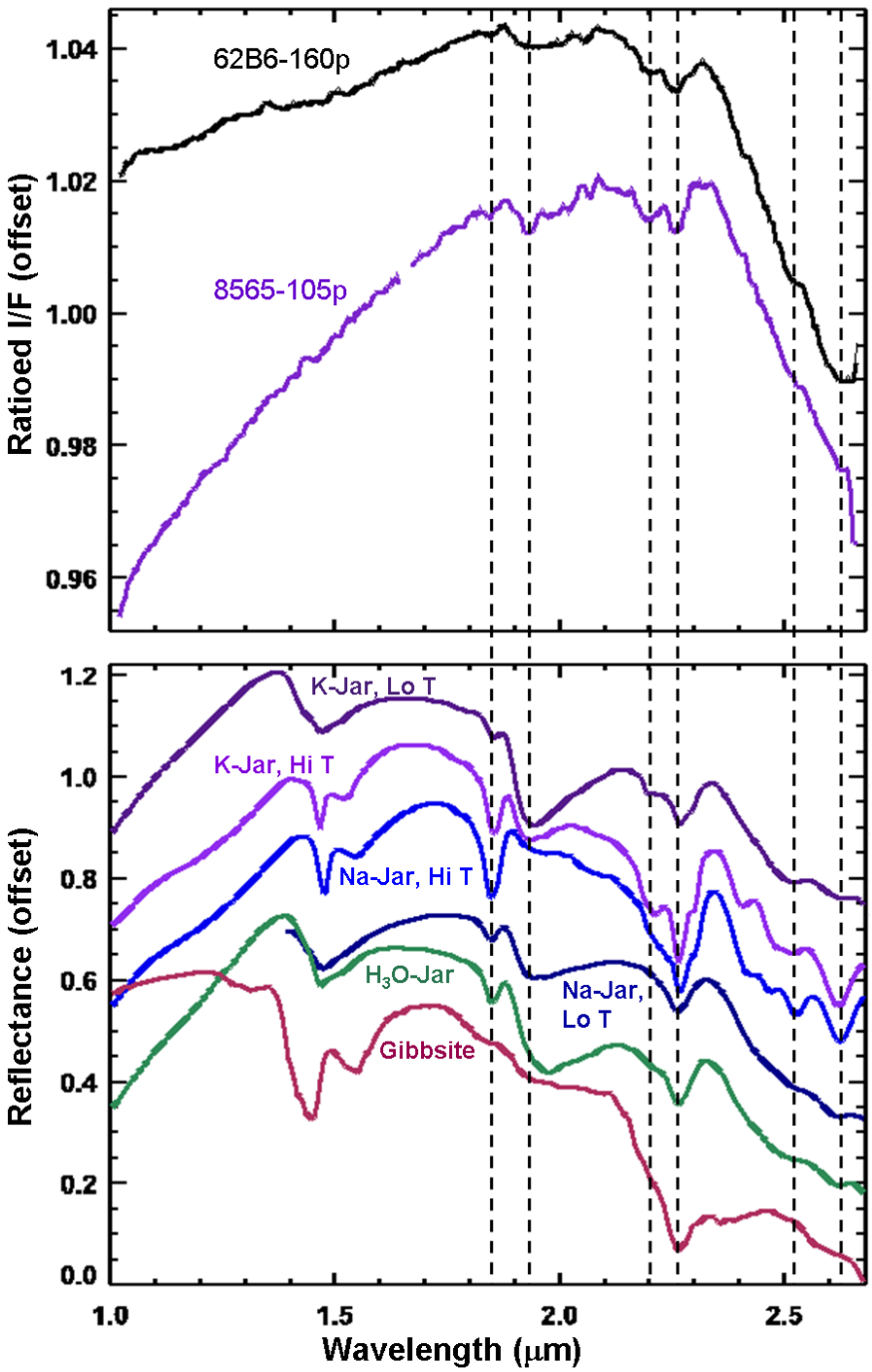

Figure 4.18: CRISM spectra from Columbus crater (top) and lab spectra of jarosites (bottom); format similar to Fig. 4.11. Gibbsite ($Al[OH]_3$) is also plotted because it shares a ~2.27 μm band, but lacks other characteristics of jarosites. CRISM spectra were extracted from essentially the same area, but from two different (overlapping) observations. Low-temperature (90°C) K-jarosite is sample GDS98, high-temperature (200°C) K-jarosite is GDS99, high-T Na-jarosite is GDS101, low-T Na-jarosite is GDS100, H_3O-jarosite is SJ-1, and gibbsite is WS214 from *R. Clark et al.* [2007].

absorber at ~2.2 μm (e.g., Al-phyllosilicate). Additional hydrous minerals could also contribute to the observed 1.93 μm band, but to the extent that this band is due to H_2O in jarosite, its strength suggests a relatively low formation temperature and minimal subsequent recrystallization [*Swayze et al.*, 2008a]. Similarly, a low-temperature formation has been inferred from the spectrum of alunite in Cross crater [*Swayze et al.*, 2008b] and for jarosite found on the plains surrounding Valles Marineris [*Milliken et al.*, 2008].

The only common mineral other than jarosite with an absorption at ~2.27 μm is gibbsite ($Al[OH]_3$) [*Cloutis and Bell*, 2000]. While a mixture of gibbsite + montmorillonite could account for the major absorptions in the Fig. 4.18 CRISM spectra, such a mixture would not reproduce the weak feature observed at 1.85 μm. Gibbsite also has a very different spectral shape from 2.1 to 2.5 μm, and strong bands near 1.5 μm that are not observed in these CRISM spectra. The presence of many other sulfates in Columbus crater as well as alunite in nearby Cross crater further supports the identification of jarosite in Columbus. Alternatively, an acid-sulfate environment could have induced partial acid weathering of Fe/Mg-clay minerals (see section 4.3.7), resulting in silica formation and the appearance of a 2.21/2.28 μm doublet [*Madejová et al.*, 2009]. Again, however, this would not explain the weak feature at 1.85 μm in the CRISM spectra, which is most consistent with jarosite. The one exposure of jarosite found to date is on Columbus' northeast floor; it exhibits internal bedding and lies adjacent to a circular depression containing lighter-toned polyhydrate-bearing outcrops (Fig. 4.14).

Alunite is distinguished by a strong, broad absorption centered at 2.17 μm, with additional bands at 1.43–1.44, 1.47–1.49, 1.76, 2.32, and 2.51–2.53 μm (those with a range of positions are at longer wavelengths in Na-alunite than in K-alunite) [*Bishop and Murad*, 2005; *Cloutis et al.*, 2006]. In Cross crater, alunite has been

identified as the spectrally dominant phase in some outcrops, and in others it is mixed with kaolinite [*Swayze et al.*, 2008b]. In Columbus crater, several relatively small (up to ~1 km wide) outcrops have spectra consistent with a contribution from alunite (Fig. 4.19), although the signatures are not as strong as in Cross crater, and all are probably mixtures with Al- (and possibly Mg-) phyllosilicates. To varying degrees, these spectra contain absorptions at the six positions described above for alunite, and the band centers at 1.44 and 1.49 μm in some spectra are most consistent with Na-alunite. The relative weakness of the 1.76 and 2.32 μm absorptions and the presence of a band at ~1.93 μm—if the latter is due to H_2O in alunite—are most consistent with laboratory spectra of alunite formed at relatively low temperature, similar to the alunite in Cross crater [*Swayze et al.*, 2008b].

It is worthwhile to consider whether the CRISM spectra in Fig. 4.19 could alternatively be explained by mixtures of minerals identified elsewhere in Columbus. For example, gypsum mixed with kaolinite could explain bands at 1.44, 1.49, and 1.75 μm (gypsum) and a shoulder at 2.32 μm (kaolinite). However, the 2.2 μm doublet of kaolinite (or singlet of montmorillonite) cannot account for the 2.17–2.18 μm band minimum in some CRISM spectra shown in Fig. 4.19. Aside from alunite, the phyllosilicates pyrophyllite [*Clark et al.*, 1990] and beidellite [*Kloprogge*, 2006; *Bishop et al.*, 2010] have bands centered at 2.17 and 2.18 μm, respectively. Beidellite has been previously identified elsewhere on Mars [*Noe Dobrea et al.*, 2010]. However, the absorptions in beidellite and especially in pyrophyllite are too narrow to account for the broad band observed in some of the CRISM spectra, even if mixed with kaolinite and/or gypsum (Fig. 4.19). Furthermore, linear mixtures of gypsum, kaolinite, and beidellite do not have absorptions with the same proportionate strengths or precise wavelengths as in alunite or as observed in the CRISM data, although intimate mixtures may have slightly different spectral properties. From spectral

evidence combined with the proximity of Columbus crater to the most definitive alunite detection on Mars [*Swayze et al.*, 2008b], an alunite component appears plausible for some outcrops in Columbus.

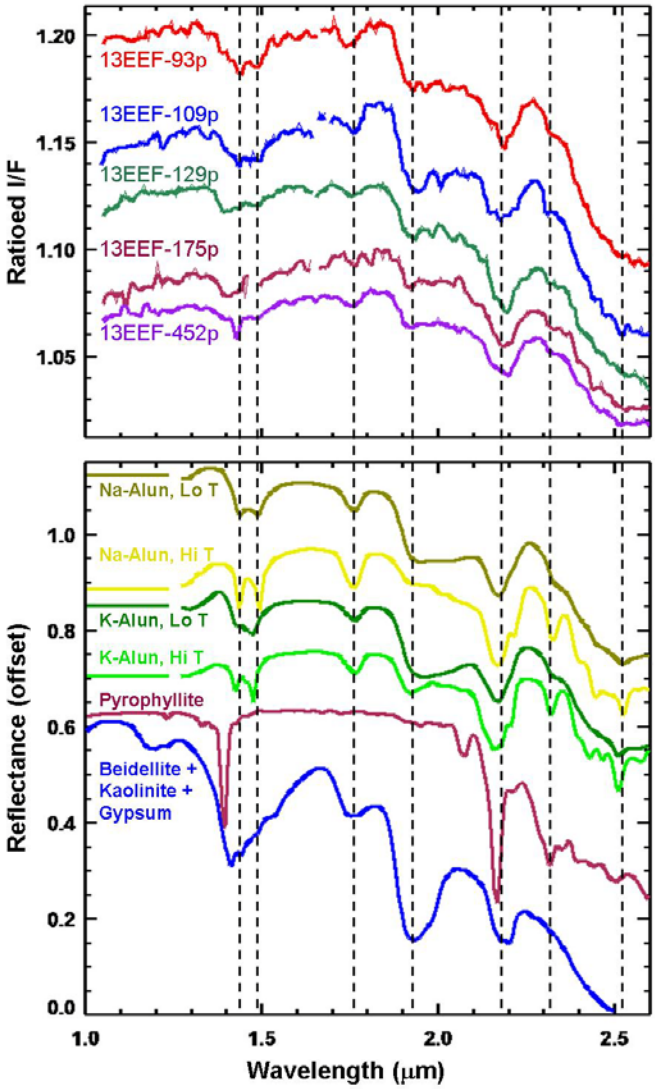

Figure 4.19: CRISM spectra from Columbus crater (top) and lab spectra of alunites (bottom); format similar to Fig. 4.11. Pyrophyllite and a linear mixture including beidellite are also plotted because these Al-phyllosilicates also absorb at 2.17–2.18 μm. However, pyrophyllite's narrow absorptions at 1.39 and 2.17 μm are inconsistent with the CRISM spectra; the slightly broader 1.41 and 2.18 μm bands of beidellite are marginally more consistent, but linear mixtures excluding alunite still fail to reproduce the exact band positions and relative strengths observed in CRISM data. Low-temperature (150°C) Na-alunite is sample GDS95, high-temperature (450°C) Na-alunite is RES-3, low-T K-alunite is GDS97, high-T K-alunite is RES-2, pyrophyllite is PYS1A (fine gr), and the mixture is equal parts beidellite(+montmorillonite) GDS124, kaolinite CM7, and gypsum HS333.3B, all from *R. Clark et al.* [2007].

The outcrops with a possible alunite component are on the northeast floor of Columbus crater and on the northeast wall just below the polyhydrate-bearing ring (Fig. 4.20a). Morphologically, these outcrops are distinguished by their smoothness at meter scales (Fig. 4.20b-c); in contrast to other hydrated mineral-bearing outcrops in Columbus, these strata appear more massive and lack fractures. Bedding is exposed along the edges of the alunite-bearing outcrops, but it is unclear whether all of these beds contain alunite. Outcrops of alunite-bearing material in Cross crater appear similarly smooth at meter scales (G. A. Swayze et al., manuscript in preparation, 2010).

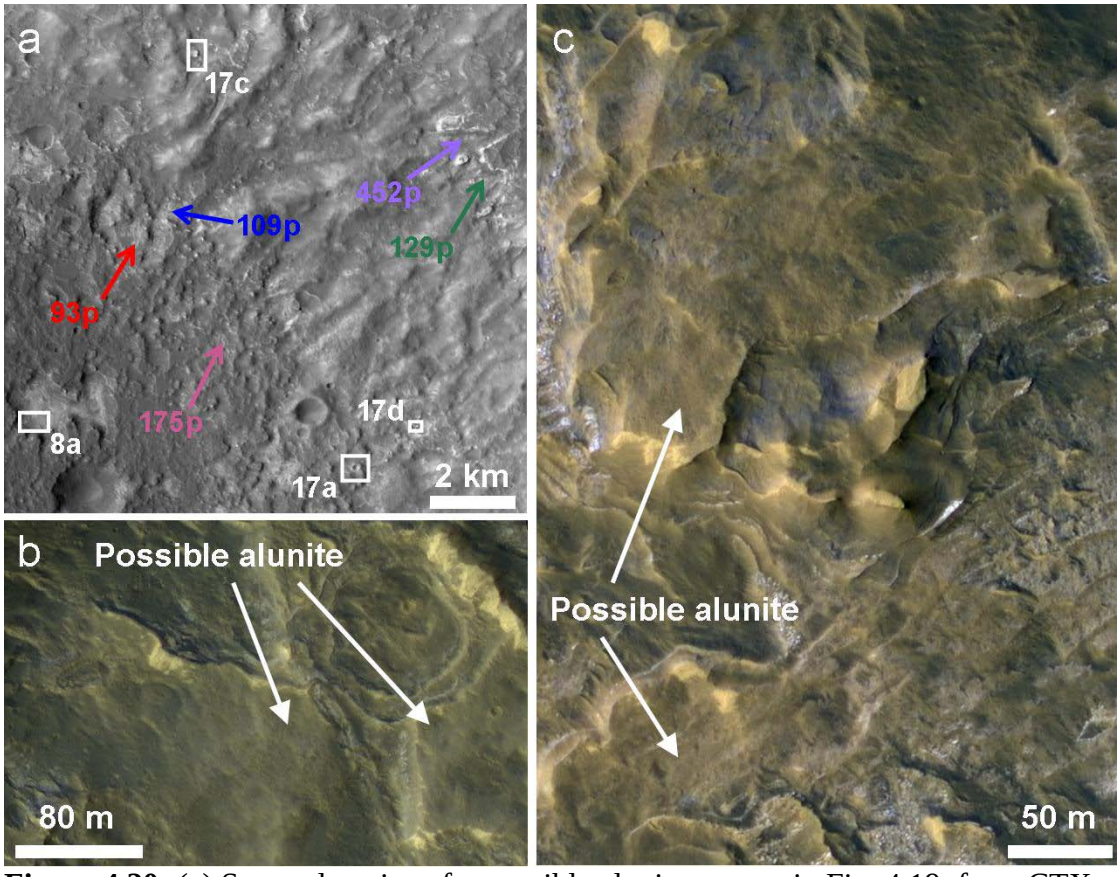

Figure 4.20: (a) Source locations for possible alunite spectra in Fig. 4.19; from CTX P06_003306_1504. The 452 and 129-pixel spectra are from outcrops adjacent to Columbus' bright polyhydrate wall ring. Locations of monohydrate-bearing outcrops from previous figures are also shown. (b,c) Smooth-textured outcrops on Columbus crater floor with possible alunite component; from PSP_003306_1510. Area shown in (b) corresponds to the 175-pixel spectrum in Fig. 4.19, and (c) to the 109-pixel spectrum.

4.3.7 Iron/magnesium phyllosilicates

Although Al-phyllosilicates are the spectrally dominant alteration phase in most CRISM scenes in Columbus crater, Fe/Mg-phyllosilicates are the most common alteration product detected from orbit in most other regions on Mars [e.g., *Bibring et al.*, 2006a; *Mustard et al.*, 2008]. Fe/Mg-phyllosilicates have absorptions at 2.28–2.35 μm, which in smectites occur shortward of 2.32 μm (the exact position depending on Fe vs. Mg content) and with a ~1.9 μm H_2O band [e.g., *Clark et al.*, 1990; *Bishop et al.*, 2002b; *Swayze et al.*, 2002]. To date, I have identified ~10 relatively small areas on the walls and floor of Columbus that are spectrally consistent with Fe/Mg-phyllosilicates, possibly including smectites (Fig. 4.21). Specifically, Fe/Mg-phyllosilicates are exposed in the southern wall of the *D*~17 km crater shown in Fig. 4.10 (CRISM HRL00013FF5), in hectometer-scale resistant knobs on Columbus' northwest wall (FRT00013D1F), in materials eroding from the hills on the central floor (FRT0001663B), and in areas up to a few km wide on the crater floor (e.g, HRL000062B6). Some of these materials may predate the formation of Columbus crater, but the crater floor deposits likely represent infilling materials that postdate the impact event.

The spectra consistent with Fe/Mg-phyllosilicates are diverse, with varying relative strengths of the 1.9 and 2.3 μm bands; the position of the latter band ranges from 2.29 to 2.32 μm. A 1.39 μm band is observed in some cases, consistent with Mg-rich phyllosilicates [*Clark et al.*, 1990; *Bishop et al.*, 2002b]. In most cases, a mineral identification more specific than "Fe/Mg-phyllosilicate" is not possible.

4.3.8 Other hydrated phases

Still other locations on the walls and floor of Columbus crater have spectral absorptions at ~1.4 and ~1.9 μm consistent with hydrated minerals, but they lack other strong, diagnostic absorptions that would enable specific identification (Fig. 4.22). In

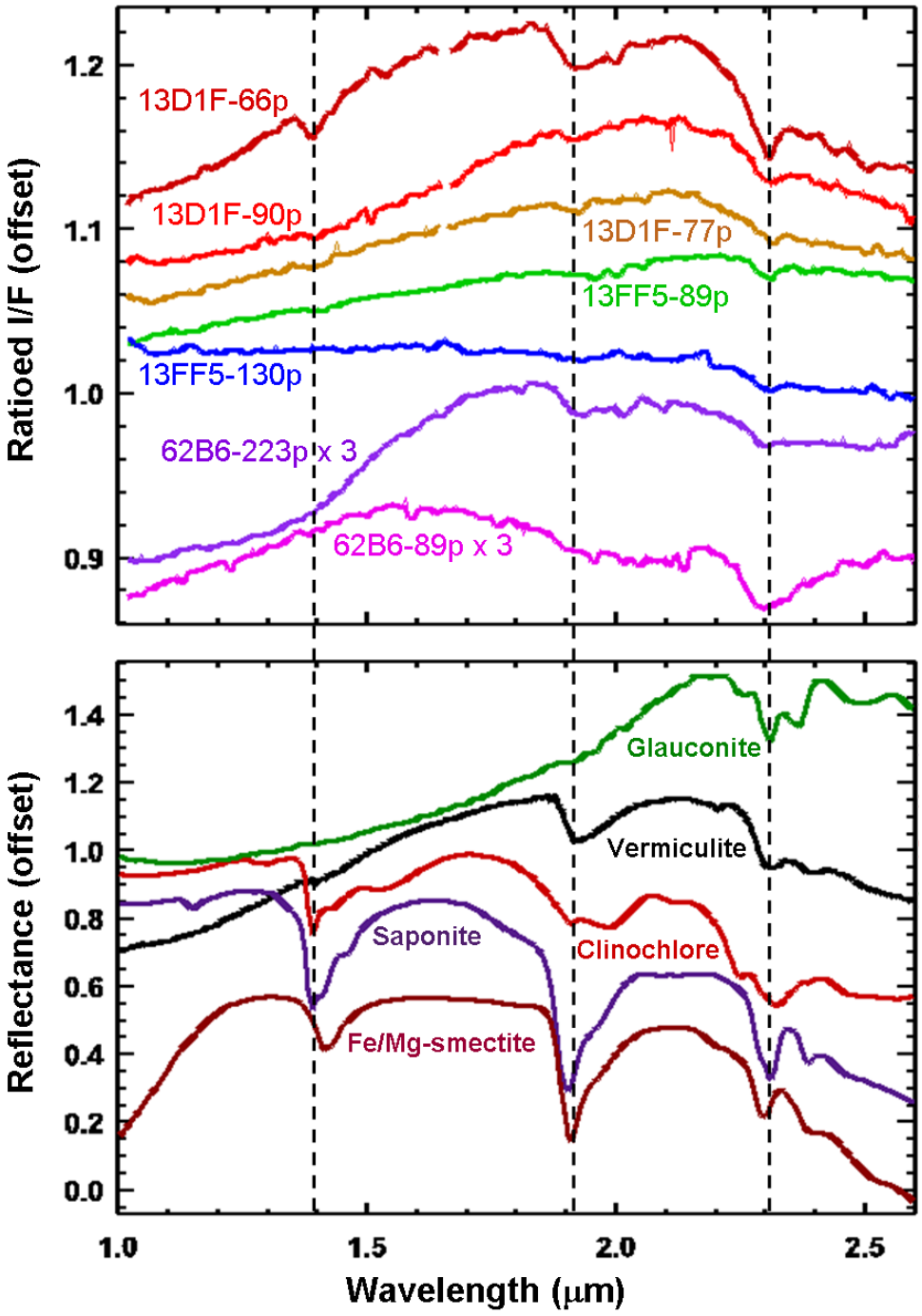

Figure 4.21: CRISM spectra from Columbus crater (top) and lab spectra of Fe/Mg-phyllosilicates (bottom); format similar to Fig. 4.11. Vermiculite is sample LAVE01 from CRISM spectral library; glauconite (K,Fe-mica) is HS313.3B, clinochlore (chlorite) is GDS159, and saponite (Mg-smectite) is SapCa-1.AcB from *R. Clark et al.* [2007]; Fe/Mg-smectite (scaled x8 for ease of comparison) is GDS759A from Flagstaff Hill, CA (courtesy G. Swayze). No single lab spectrum is an excellent match to the CRISM spectra.

some cases, weak features in the 2.2–2.3 μm range are likely due to metal-OH vibrational absorptions. In particular, spectra from the *D*~11 km crater on Columbus' southern central floor (CRISM FRT0000ABF2) exhibit weak features at 2.19–2.20 and 2.27–2.28 μm (Fig. 4.22). These wavelengths are slightly too short and too long (respectively) for jarosite (section 4.3.6). They are somewhat reminiscent of the 2.21/2.27 μm doublet feature observed by *Roach et al.* [2010a] in spectra from Valles Marineris, although the features observed here are much weaker. *Roach et al.* [2010a] attributed this doublet to either a mineral mixture or a poorly crystalline Fe/SiO_2-bearing phase similar to that described by *Tosca et al.* [2008b], formed via acid weathering of Fe-bearing clays [*Madejová et al.*, 2009].

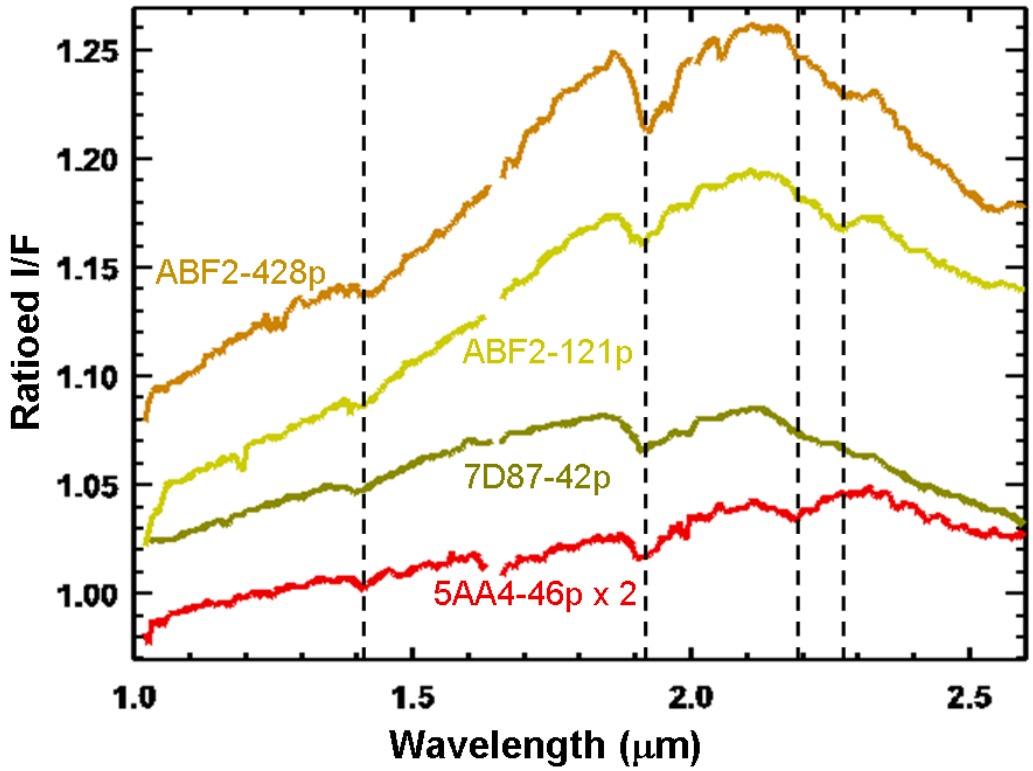

Figure 4.22: CRISM spectra from Columbus crater with ~1.4 and ~1.9 μm bands suggestive of hydrated minerals, but with few other diagnostic absorptions. Weak features in the 2.2–2.3 μm range may be due to metal-OH vibrations in poorly crystalline minerals.

4.3.9 Phases not observed: carbonate, chloride, zeolite, prehnite

As described above, Columbus crater contains a wealth of phyllosilicate and sulfate minerals not commonly observed on Mars. However, several types of secondary minerals detected elsewhere on Mars by CRISM and THEMIS have not been found to date in Columbus crater. These include salts such as carbonates [*Ehlmann et al.*, 2008b] and chlorides [*Osterloo et al.*, 2008] as well as hydrated silicates that form under alkaline (zeolites) and/or high-temperature conditions (prehnite) [*Ehlmann et al.*, 2009]. The potential absence of these minerals in Columbus crater would be consistent with an alteration environment of relatively low temperature and low-to-neutral pH. However, non-detection of a mineral via orbital spectroscopy does not necessarily imply the absence of that mineral [e.g., *Kirkland et al.*, 2003]

4.4 Constraints on Modal Mineralogy

Thermal emission spectra of Columbus crater enable an independent assessment of the surface mineralogy. In particular, the ~100 m/pixel THEMIS dataset is ideal for studying the small-area outcrops in Columbus crater. I have collaborated with Alice Baldridge, who has analyzed the highest-quality THEMIS observation of Columbus available as of late 2009, I07746002 (Fig. 4.23a), which covers a ~30 km swath across the crater, including the well-exposed sulfate-bearing ring of material on the northern crater wall. Fig. 4.23 and the TES spectral deconvolution results described below are from *Baldridge* [personal communication].

Emissivity spectra of the dark materials covering most of Columbus' floor (Fig. 4.23b) are similar to that of TES Surface Type 1 (ST1; Fig. 4.23c), the dominant spectral unit in the Martian southern highlands [*Bandfield et al.*, 2000] that is generally interpreted as representing a basaltic composition. Spectra of the plains

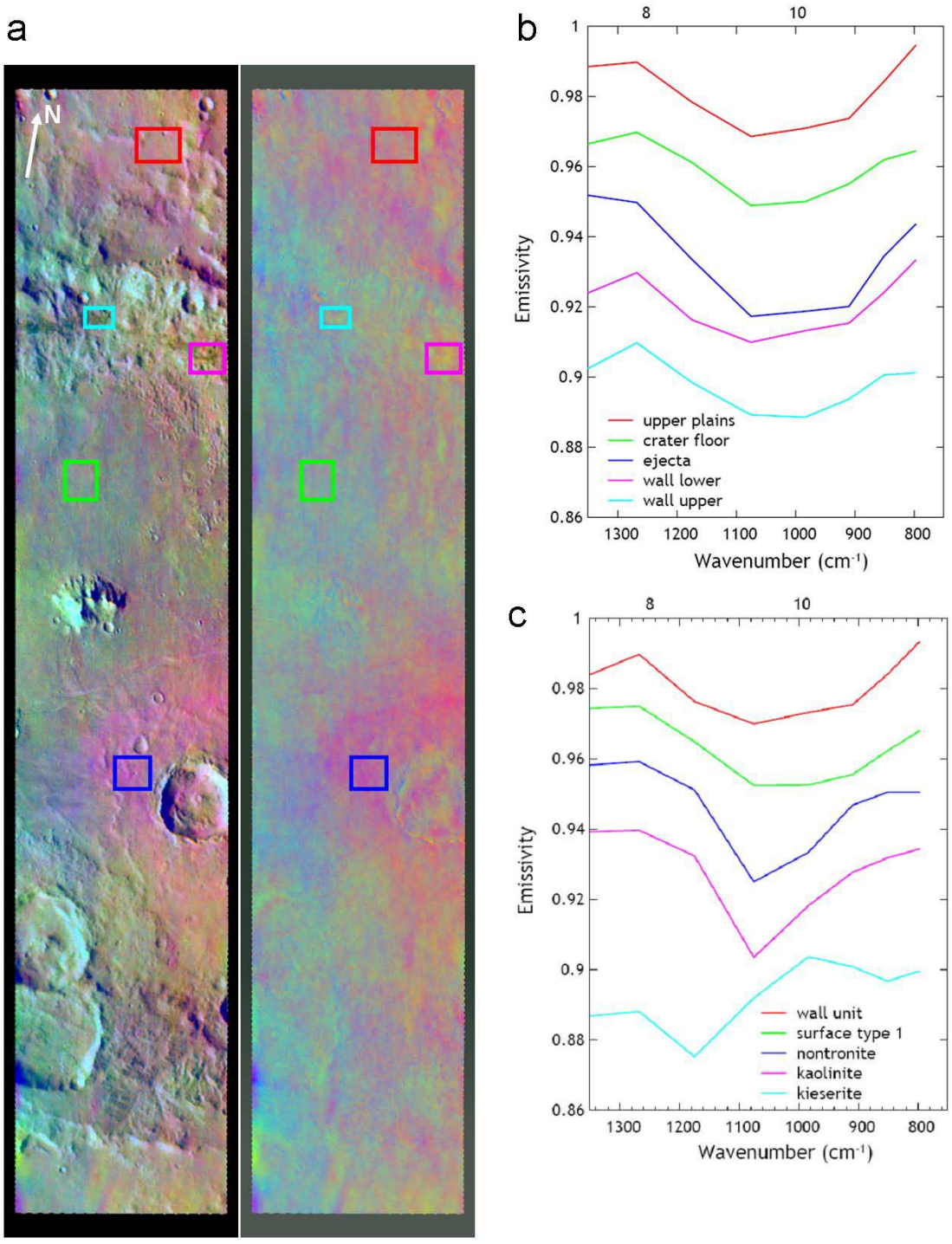

Figure 4.23: (a) Daytime IR DCS band 9-6-4 image covering central ~30-km swath across Columbus crater, from THEMIS I07746002. Left image is radiance, right is emissivity. (b) Spectra extracted from boxed areas in (a). (c) "Wall lower" spectrum from (b) (magenta box in (a)) compared to spectra of TES Surface Type 1, phyllosilicates, and a sulfate.

outside Columbus and of ejecta surrounding the *D*~11 km crater on the southern central floor are also consistent with basalt, but with a stronger absorption at ~11 μm (THEMIS band 7). This feature, which is especially strong in the *D*~11 km crater ejecta, suggests higher olivine abundance in the ejecta relative to the rest of Columbus' floor [e.g., *Hamilton and Christensen*, 2005]. This is consistent with the detection of olivine in this small crater's ejecta by CRISM (Fig. 4.9a).

Decorrelation stretch (DCS) images show that the sulfate-bearing ring is spectrally distinct from the adjacent wall materials (Fig. 4.23a). Where this spectral distinction is strongest ("wall lower" spectrum in Fig. 4.23b), the slope from 9.4 to 11 μm (1070 to 910 cm^{-1}) is greater than that seen in ST1, suggesting a greater abundance of high-silica phases that could include phyllosilicates (Fig. 4.23c). In addition, the "wall lower" spectrum has an absorption at 8.6 μm (band 4, 1170 cm^{-1}), consistent with the presence of sulfates. In particular, absorptions at this relatively short wavelength are most consistent with water-poor sulfates—e.g., kieserite or sanderite ($MgSO_4 \cdot 2H_2O$), but not the more hydrated Mg-sulfates [*Baldridge and Christensen*, 2006; *Lane*, 2007]. Ca-sulfates including gypsum (which CRISM detects in Columbus' polyhydrate ring) would also be consistent with the observed 8.6 μm feature [Fig. 7a of *Christensen et al.*, 2004a]. In either case, this feature provides independent support for the CRISM detections of sulfates in Columbus crater.

Linear mixing models of higher spectral resolution thermal emission data can be used to estimate mineral abundances with ~5–15% precision [e.g., *Ramsey and Christensen*, 1998; *Feely and Christensen*, 1999]. The TES instrument is ideal for this, although its ~3 km resolution is coarse compared to most outcrops in Columbus. A TES spectrum from the "wall lower" location in Fig. 4.23 was modeled using the standard ASU mineral library including smectites [*Rogers et al.*, 2007], supplemented with Mg-sulfate spectra measured by *Baldridge and Christensen* [2006]. The results

yield an estimate of roughly 40% phyllosilicates by volume, 16% hydrated sulfates, 15% olivine, and the balance in feldspars. The modeled sulfate abundance does not substantially exceed the TES detection limit of ~10–15% [*Christensen et al.*, 2001a]. However, the modeled spectrum was extracted from an area that includes several distinct spectral units at CRISM resolution (sulfate-bearing vs. clay-bearing vs. non-hydrated), so abundances of sulfates and phyllosilicates are likely higher within the light-toned outcrops specifically.

4.5 Stratigraphy and Chronology at Columbus

Sections 4.2 and 4.3 described the diversity of deposits in Columbus crater. Here I describe their stratigraphic relationships and use crater counting to estimate the ages of some events in Columbus' geologic history.

The diverse hydrated minerals in Columbus crater may have formed during numerous alteration events spanning significant time or during a single, geologically brief period of aqueous activity. Exposures in the walls of small craters (e.g., Fig. 4.5c) and other steep scarps provide some insights, including the significant observation of polyhydrated sulfate-bearing beds alternating with kaolinite-bearing beds (Figs. 3.11, 3.14, 3.15). However, in many cases the stratigraphic relations are less clear; for example, Fig. 4.14 shows polyhydrated sulfates on the crater wall, jarosite-bearing beds on the crater floor, and additional polyhydrated sulfates at still lower elevations in a depression adjacent to the jarosite. But does this topographic distribution indicate a period of jarosite formation separating two distinct periods of polyhydrate formation? Or did the jarosite form first, followed by a single period of polyhydrate formation on the crater walls and in local depressions on the crater floor? Or could the jarosite have formed diagenetically after the polyhydrates were precipitated/deposited, as in some acid saline lakes on Earth [*Benison et al.*, 2007]?

These questions are difficult to resolve based on orbital imagery alone, preventing the construction of a simple stratigraphic column to compare to theoretical evaporite sequences [e.g., *Tosca et al.*, 2008a; *Altheide et al.*, 2010a].

One constraint on the timing of aqueous activity is provided by Fig. 4.10, which shows a *D*~17 km crater superposed on Columbus' southwest wall. The crater's flat floor and strongly degraded rim contrast with the similarly sized crater to its northeast, which retains its central peak, implying that the 17 km crater's interior has experienced significant infilling and/or erosion; the materials exposed on its modern floor therefore postdate the crater. The crater floor is at the elevation of the polyhydrate ring, and polyhydrated sulfates are indeed found in layered deposits on its floor. This implies that aqueous activity postdated the formation of the 17 km crater; therefore, at least some aqueous activity must have occurred some time after the formation of Columbus crater (i.e., not all aqueous activity predated or coincided with crater formation).

Other observations show that the dark deposit covering much of Columbus' floor—which has been argued to be consistent with lava (section 4.2.1)—postdates the light-toned deposits containing hydrated minerals. As described in section 4.2.2, the probable lava overlies light-toned materials on the northwest crater floor (Fig. 4.8b), and CRISM FRT00005AA4 shows these light-toned materials to be hydrated (Fig. 4.22). Images of the northeast crater floor show the lava embaying mesas of light-toned material (e.g., Fig. 4.24a). In addition, the *D*~11 km crater on Columbus' southern central floor exposes decameters of stratigraphy in its upper walls, with light-toned beds overlain by darker, relatively blue beds (Fig. 4.24b). Boulders are eroding from the darker beds, which have a rougher texture and (according to CRISM) an enhanced olivine signature; I interpret these darker beds as lavas, possibly olivine-bearing basalt flows. By contrast, erosion of the lighter-toned beds appears to yield

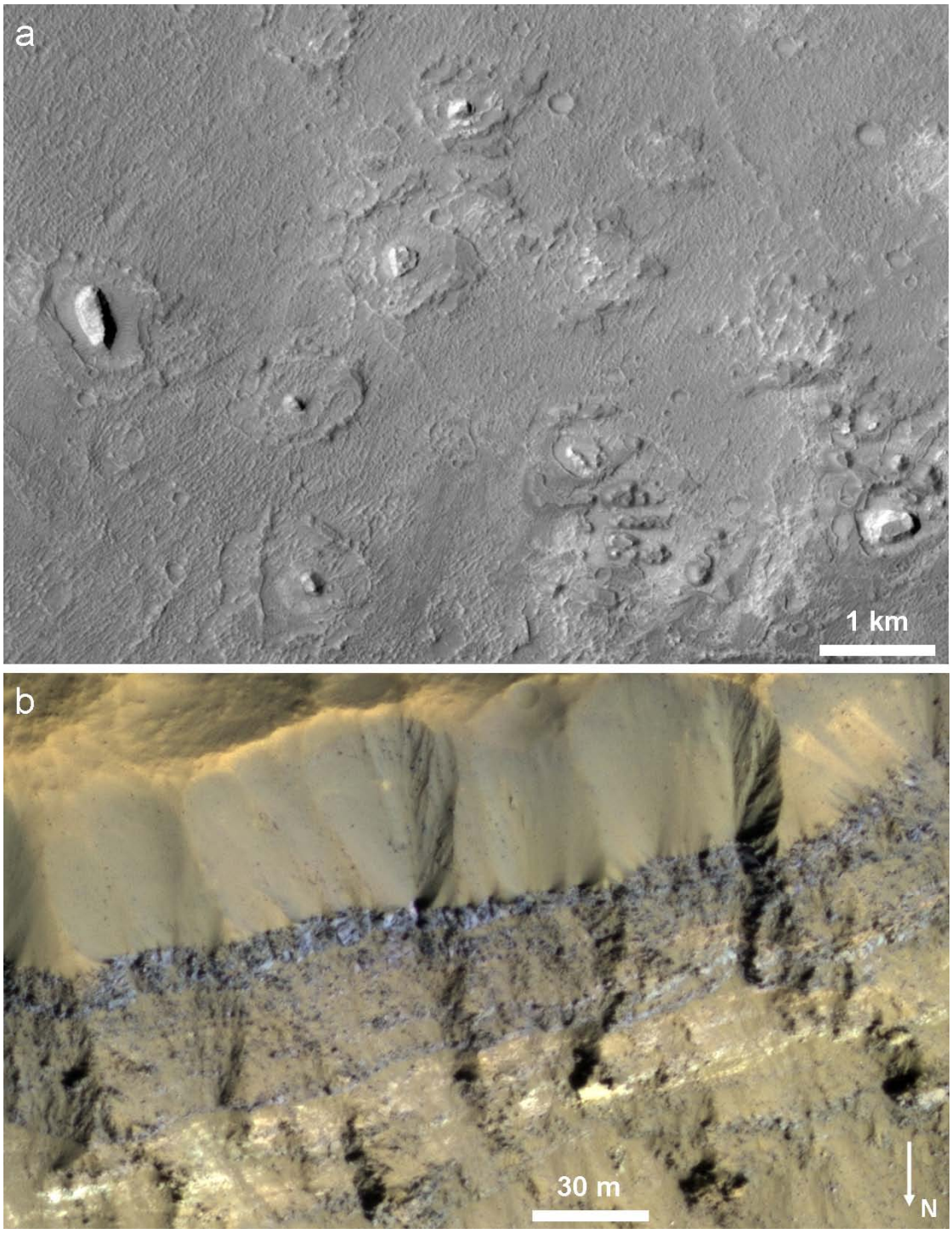

Figure 4.24: Stratigraphic relations on Columbus crater floor. (a) Mesas of light-toned layered materials on the eastern floor, embayed by darker ridged material interpreted as lava; from CTX P05_003095_1518. (b) Stratigraphy of Columbus crater floor exposed in the wall of a superposed *D*~11 km crater; from HiRISE PSP_008356_1500. Light-toned layered deposits underlie darker, rubbly, olivine-bearing layers. Location shown by black box in Fig. 4.25.

finer-grained, hydrated material that is transported downslope to form scree deposits (Fig. 4.25). These and other probable colluvial materials mantle the lower crater walls

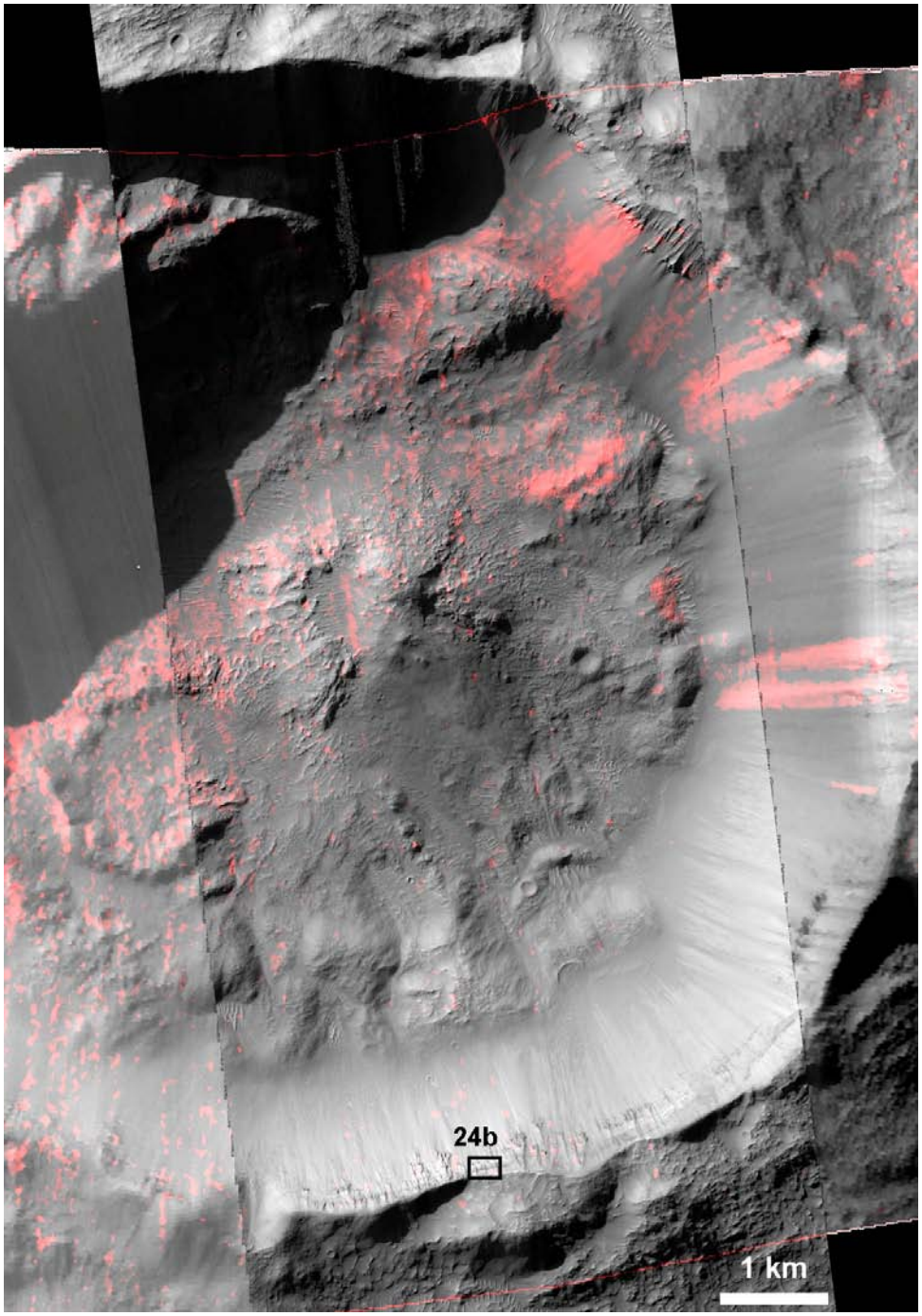

Figure 4.25: Hydrated materials (red) inside *D*~11 km crater on the floor of Columbus crater. Hydrated colluvial deposits extend down crater walls from beds exposed in upper walls. Background is HiRISE PSP_008356_1500 and CRISM FRT0000ABF2 IR albedo (IRA from *Pelkey et al.* [2007]); hydration mapped using BD1900H [*Ehlmann et al.*, 2009].

and conceal the >1 km thickness of underlying deposits inferred to occupy Columbus' floor (section 4.2.1). Overlying the dark-toned beds in Fig. 4.24b is a somewhat lighter-toned, smooth-textured deposit with sparse boulders <1 m in diameter and a relatively weak olivine (or other ferrous mineral) spectral signature. These characteristics are consistent with those of the Late Hesperian-aged "Electris deposits" of Sirenum Fossae as described by *Grant et al.* [2010], who interpreted them as probable aeolian loess. From an HRSC DEM, I estimate a crater wall slope of ~20° at the location of Fig. 4.24b, so the lateral extent of the deposits indicates a vertical thickness of ~10 m hydrated layered deposits, ~15 m olivine-bearing lava, and ~20 m Electris-like deposits at this location. While I cannot exclude the alternative that some of these layers are stratigraphically inverted ejecta from the *D*~11 km crater itself, they occur some ~200 m below the crater rim crest and their stratigraphy is consistent with that observed elsewhere in Columbus.

As discussed in section 4.2.1, a graben cuts the floor of Columbus crater approximately in half (Fig. 4.1). The ENE–WSW orientation of this graben is similar to that of the larger Memnonia and Sirenum Fossae to the north and south of Columbus, respectively. These graben systems are in turn part of a hemisphere-wide collection of structures oriented radially to Tharsis, which formed over a large span of Martian history [*Plescia and Saunders,* 1982; *Anderson et al.*, 2001]. Some graben in Terra Sirenum may date to the Noachian "stage 1" of tectonic activity, but many likely date to the Late Noachian/Early Hesperian, overlapping wrinkle ridge formation in the Early Hesperian Epoch ("stage 3" of *Anderson et al.* [2001]).

The graben in Columbus crater appears to predate the light-toned layered deposits, as revealed by the stratigraphy surrounding a *D*~2.5 km crater on the western floor (Fig. 4.26a). Mesas surrounding this crater consist of light-toned layered deposits overlain by darker materials (Fig. 4.26b) and extend to a height of ~100 m

above the surrounding plains, twice the typical rim height for a fresh crater of this size [*Garvin et al.*, 2003]. These mesas are therefore probably not composed solely of crater ejecta; instead, the uppermost dark materials may be ejecta that armored

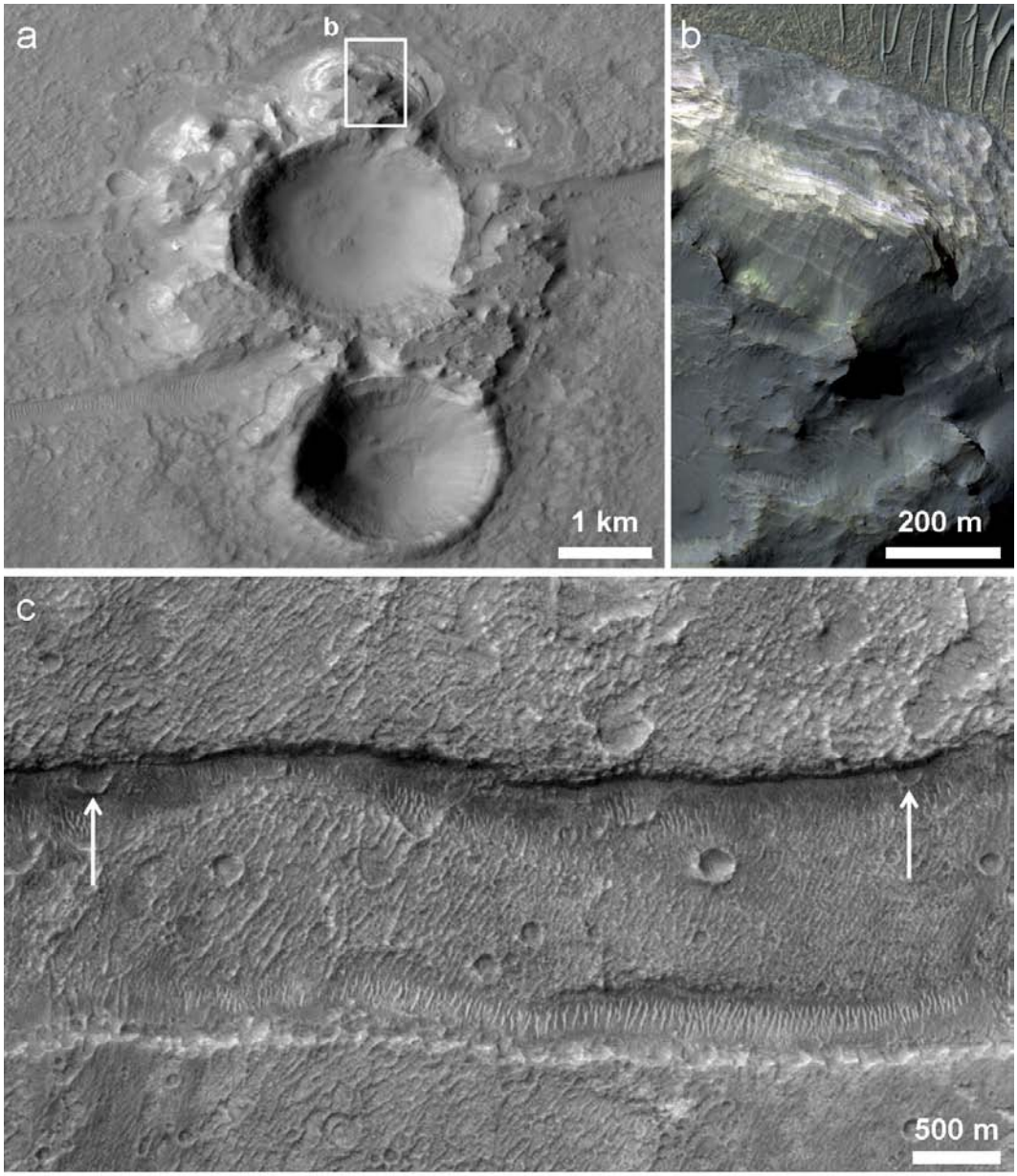

Figure 4.26: (a) A ~2.5 km impact crater superposing the graben in Columbus crater; from CTX P03_002739_1505. The *D*~2 km crater immediately to the south is fresher and probably younger, as indicated by its greater depth (note shadows) and more pronounced rim crest. (b) Dark-toned materials overlying light-toned layered deposits in the mesas surrounding the *D*~2.5 km crater; from HiRISE ESP_016861_1505. (c) Graben segment on Columbus eastern floor, disrupting two small craters (arrows); from CTX P12_005851_1505.

underlying light-toned layered deposits against an erosional process that stripped the deposits from adjacent terrain [e.g., *McCauley,* 1973]. Neither the *D*~2.5 km crater nor the mesas surrounding it are visibly deformed by the graben, suggesting a sequence of (1) graben formation, (2) layered deposit formation, (3) formation of the 2.5 km crater, and (4) erosion of adjacent layered deposits. Lava deposition is inferred to postdate these events because the probable lavas embay the erosional remnant mesas. Lava would be expected to fill and bury a preexisting graben, so the fact that the graben remains visible may be explained by its later reactivation following lava flow emplacement, as evidenced by the graben's disruption of some small craters on the lava flow surface (Figure 4.26c).

As mentioned in section 4.2.1, a few poorly developed valleys are visible on the northeast wall of Columbus (Fig. 4.1b). The crater walls and floor near the mouths of these valleys host a dark-toned deposit with relatively low thermal inertia (~230 ± 10 tiu) and a spectrum dominated by broad bands near 1 and 2.1–2.2 μm, consistent with a basaltic composition [e.g., *Mustard et al.*, 1997]. This dark deposit overlies the light-toned deposits on this part of the crater floor and has partially buried the sulfate-bearing ring on the crater walls (Fig. 4.14a). These superposition relationships suggest that gradation of the crater wall likely occurred here after the period during which aqueous minerals and light-toned deposits formed in Columbus. The dark-toned deposit may have preferentially armored light-toned deposits on this part of the crater floor against erosion. Columbus crater lies at the southern edge of the latitude band (18–29°S) in which *Moore and Howard* [2005] identified alluvial fans dating to the Noachian-Hesperian boundary in 18 mid-sized to large craters. The dark deposit in northeast Columbus could be a highly degraded alluvial fan. A deltaic interpretation seems less plausible given the lack of clear stratal geometries or clay minerals; for comparison, two of the most likely deltaic deposits identified on Mars contain

phyllosilicates and exhibit clear bedding [*Ehlmann et al.*, 2008a; *Milliken and Bish*, 2010].

An estimate of the absolute age of Columbus and its interior deposits can be made by counting superposed impact craters. Columbus' interior and proximal ejecta represents a small area for counting craters (~17,000 km^2), so the formal statistical uncertainties—which are proportional to $1/\sqrt{(n)}$, where n is the number counted—are large. In the notation of *Tanaka* [1986], in which the measured crater densities are scaled to an area of 10^6 km^2, Columbus has N(16) = 120 ± 85 craters >16 km in diameter per 10^6 km^2, and N(5) = 420 ± 160. These values are most consistent with a Middle Noachian age for Columbus, although a Late Noachian age (that of the Upper Noachian units described by *Tanaka* [1986]) is within the uncertainties. As stated in section 4.2.1, the cratered plains unit in which Columbus occurs has similarly been dated to the Middle Noachian. I also counted separately only those craters that clearly superpose (i.e., postdate) Columbus' light-toned layered deposits, yielding densities of N(5) = 280 ± 160 and N(2) = 1210 ± 340, consistent with a Late Noachian age (although Early Hesperian is within the uncertainties). Finally, the probable lava flow on the floor of Columbus has crater densities N(5) = 130 ± 130, N(2) = 920 ± 350, and N(1) = 3410 ± 670, consistent with an Early Hesperian age like most ridged plains on Mars. For each of these (Columbus, layered deposits, and lava), 1–3 craters were counted in the largest size category and 7–26 craters in the smaller size categories.

In summary, Columbus crater likely formed in the Middle-to-Late Noachian, and it accumulated >1 km of fill prior to a distinct period of light-toned deposit formation and aqueous activity during the Late Noachian. A probable lava flow subsequently covered most of the crater floor during the Early Hesperian, and it was modified during this period by compressional and extensional tectonics likely related to Tharsis loading. Sediment accumulation continued at a lower rate during the Late

Hesperian and possibly later, emplacing a mantle of likely aeolian origin on at least some portions of the crater interior. In the more recent Amazonian, the dominant geologic processes have likely been mass wasting and aeolian erosion of the intracrater deposits, as well as impact events that have exposed older deposits in the walls and ejecta of fresh craters such as that in Fig. 4.25.

4.6 Other Aqueous Deposits of Northwest Terra Sirenum

As mentioned in chapter 3, CTX images and CRISM multispectral data hint that several craters near Columbus in northwest Terra Sirenum may host similar layered deposits, and this region's intercrater plains also contain aqueous mineral deposits. Here these deposits are described as regional context for the Columbus crater observations.

4.6.1 Intracrater deposits

The most striking feature of northwest Terra Sirenum in CRISM multispectral data is the presence of a ~2.2 μm Al- or Si-OH absorption in materials occupying most of the region's large craters (Fig. 4.27). In particular, this spectral feature is found in the region's most degraded (and therefore probably oldest) craters, which have flat floors, degraded rims, and superposed impact craters. By contrast, a *D*~80 km crater ~300 km east of Columbus with fresh-appearing ejecta and a well-preserved central peak has no detectable hydrated minerals. Of the northwest Sirenum craters other than Columbus, so far the greatest mineralogic diversity has been found in Cross crater, which hosts alunite, kaolinite, and montmorillonite or hydrated silica in finely bedded deposits on its walls and floor [*Swayze et al.*, 2008b]. Cross crater is the focus of a manuscript in preparation by G. A. Swayze et al., so I focus on other craters here.

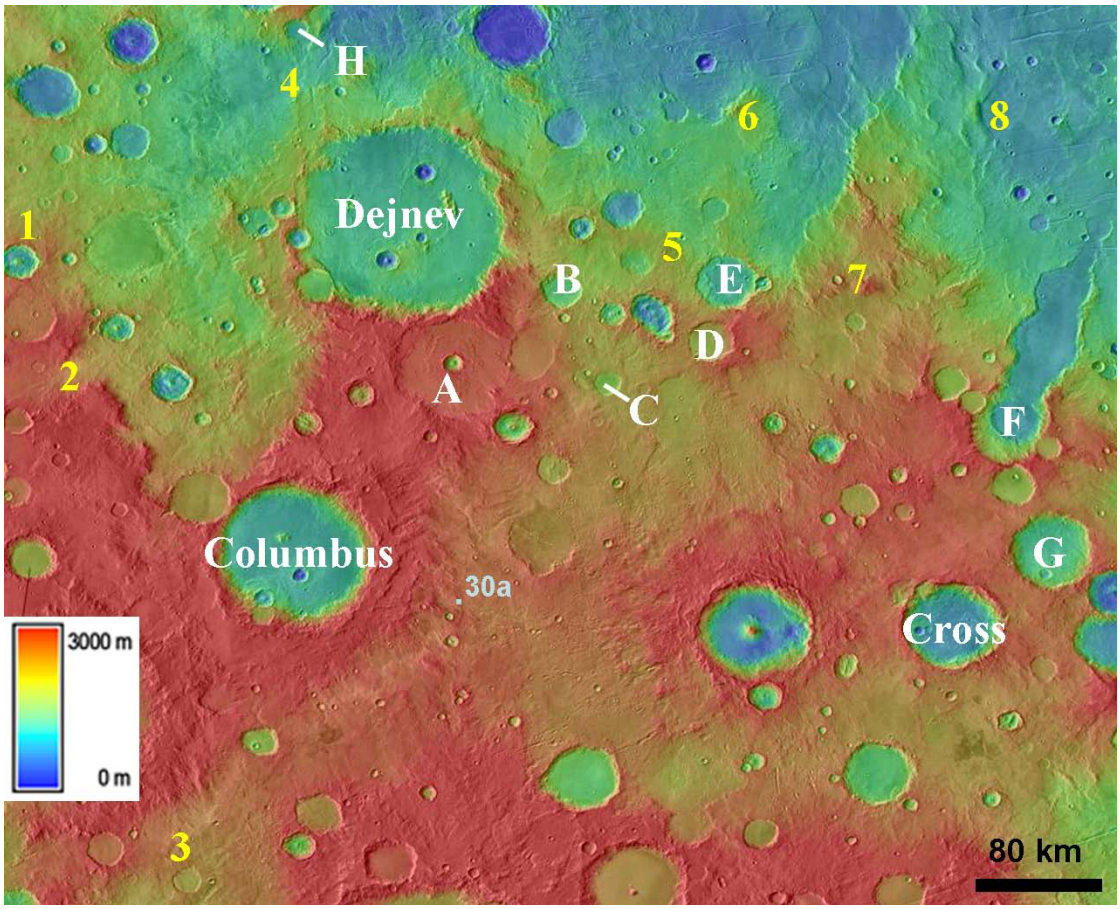

Figure 4.27: THEMIS daytime IR mosaic of northwest Terra Sirenum (190–205°E, 22.5–34°S) colorized with MOLA elevations. Named impact craters and those designated A–H exhibit a ~2.2 µm Al/Si-OH absorption in CRISM multispectral data, and/or contain light-toned layered deposits. Numbered locations correspond to possible Al/Si-OH detections on intercrater plains. Chloride and Fe/Mg-phyllosilicate exposure shown in Fig. 4.30a is also indicated.

Of the nine craters identified with a ~2.2 µm band in CRISM multispectral data, three are named (Columbus, Cross, Dejnev) and to the other six I assign letters (A–F) for convenience (Fig. 4.27). Two other craters (G and H in Fig. 4.27) lack CRISM coverage but have light-toned floor deposits morphologically similar to those on the floor of Columbus (see CTX P18_008237_1505 and HiRISE ESP_017573_1570, respectively). Craters A, D, E, and Dejnev have recently been observed by CRISM in hyperspectral mode, and all craters exhibiting the 2.2 µm absorption have been imaged by HiRISE. Light-toned layered deposits are observed

in most of these craters (Fig. 4.28). These deposits are especially widespread across the floor of crater E (Fig. 4.28a), where they have likely been significantly eroded to yield the scattered mesas observed on the modern crater floor. Each hectometer-scale mesa exposes dozens of meter-scale beds in cross section (Fig. 4.28e). The morphology and color of beds in craters F and Dejnev (Figs. 4.28c,d) are reminiscent of beds on the floor of Columbus crater, including those that contain monohydrated sulfate. In HiRISE enhanced-color images, the green appearance of some beds in crater B (Fig. 4.28b) suggests a crystalline ferric mineral might be present (possibly ferric sulfate—see discussion in section 4.3.5), but this possibility has not yet been tested with CRISM hyperspectral data.

As in Columbus and Cross craters, kaolinite is identified in hyperspectral images of craters A, D, E, and Dejnev (Fig. 4.29). Fe/Mg-phyllosilicate is also found in each of these locations except in crater D, and montmorillonite is detected in crater E. Somewhat surprisingly, these minerals generally are not found within the light-toned layered units of Fig. 4.28c–e. Instead, kaolinite and Fe/Mg-phyllosilicate most commonly occur in massive materials on the crater walls, and montmorillonite—possibly mixed with kaolinite—is found on the somewhat darker, rough-textured (but layered) floor of crater E (Fig. 4.28a). Some detections of kaolinite in crater E (CRISM FRT000106E4) appear to correspond to light-toned layered deposits, but the higher spatial resolution of HiRISE is needed to confirm this. Stratigraphic relations between the kaolinite and Fe/Mg-phyllosilicates are not always clear, but in the case of crater E the latter are found eroding from the uppermost southeast crater wall (analogous to Fig. 4.10 from Columbus), whereas Al-phyllosilicates are seen deeper within the crater.

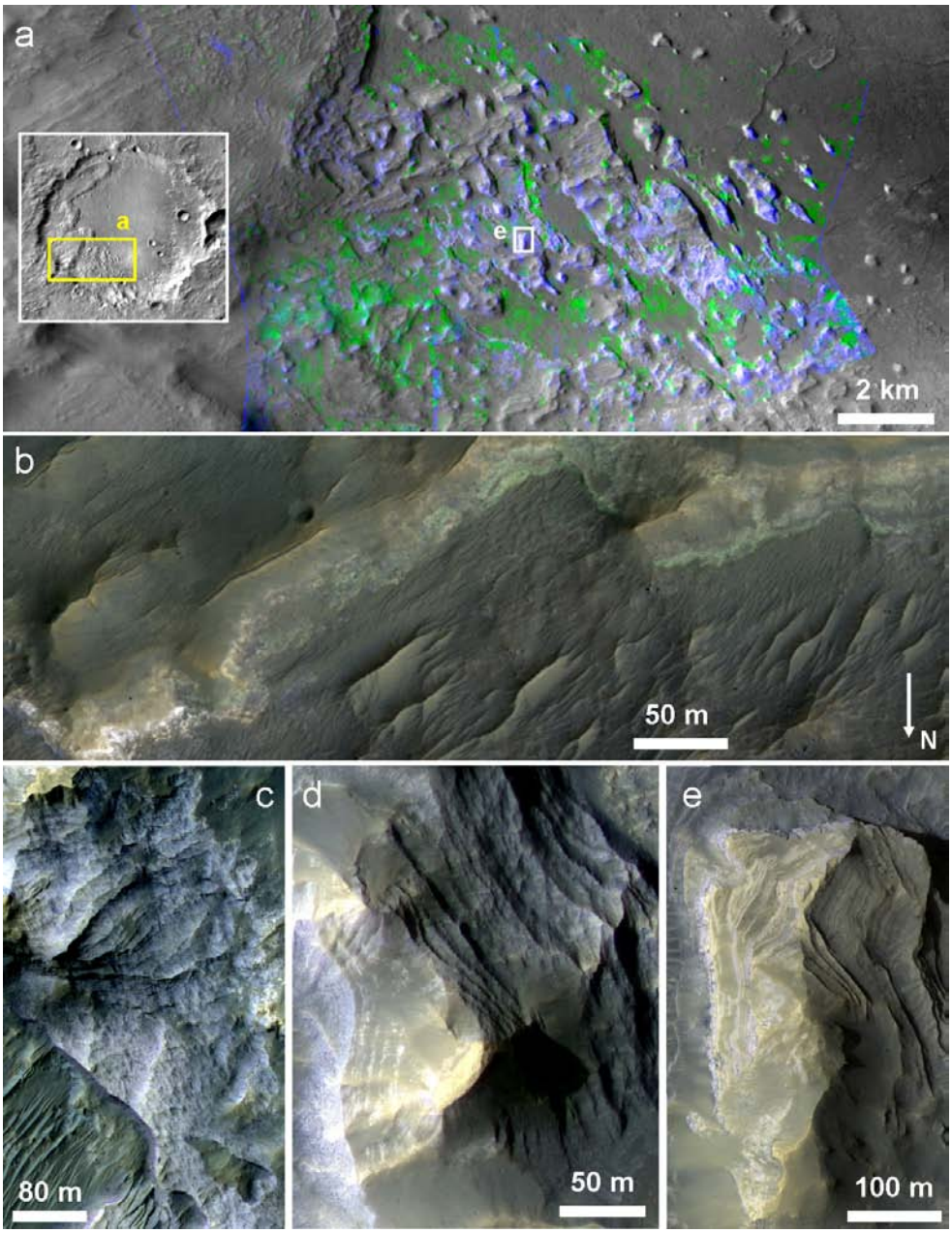

Figure 4.28: Light-toned layered deposits in craters near Columbus. (a) Portion of western wall and floor of crater E in Fig. 4.27 (see inset for context); from CTX P03_002330_1539, colored with parameter maps from CRISM FRT000106E4. Green is BD2200 [*Ehlmann et al.*, 2009] and blue is BD3000 [*Pelkey et al.*, 2007], tracking Al-phyllosilicates and H_2O-bearing materials, respectively. Light-toned mesas are hydrated, and darker areas between mesas near image center are spectrally consistent with montmorillonite. (b) Colorful layers on floor of crater B; from HiRISE ESP_015951_1535. Green materials may contain ferric sulfate. (c) Layered deposits in crater F; from ESP_016109_1525. (d) Layered deposits at base of southern wall of Dejnev crater; from ESP_011560_1535. (e) Mesa on floor of crater E, exposing dozens of meter-scale layers; from ESP_011639_1535.

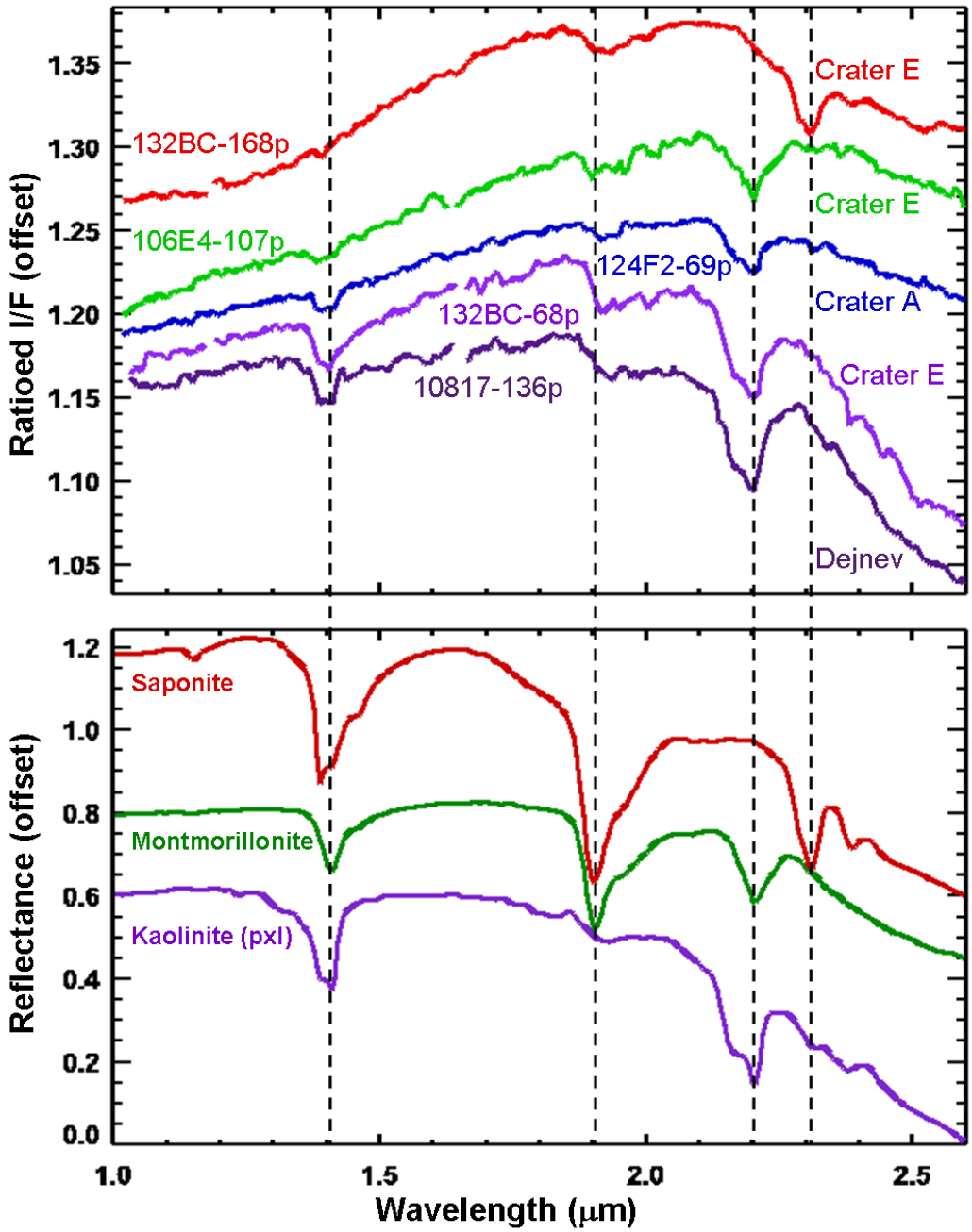

Figure 4.29: CRISM spectra from northwest Terra Sirenum craters (top) and lab spectra of phyllosilicates (bottom); format similar to Fig. 4.11. Saponite is SapCa-1.AcB, montmorillonite is SWy-1, and poorly crystalline (pxl) kaolinite is KGa-2 from *R. Clark et al.* [2007].

What, then, is the mineralogy of the light-toned beds on these crater floors? In crater E, spectra of most layered outcrops contain no obvious absorptions from 1.0 to

2.6 μm; however, these outcrops have stronger ~3 μm bands than other materials in the same CRISM scene (Fig. 4.28a). Absorptions at ~3 μm are ubiquitous on Mars, though variable in strength; they are attributed to adsorbed or structural H_2O and/or OH in surface materials [*Jouglet et al.*, 2007; *Milliken et al.*, 2007]. Many nominally anhydrous minerals have a ~3 μm absorption in spectra obtained under terrestrial laboratory conditions [*R. Clark et al.*, 2007]. Still, this absorption is typically stronger for hydrated minerals such as phyllosilicates, including those on Mars [*Jouglet et al.*, 2007; *Milliken et al.*, 2007], but in crater E the ~3 μm band is weaker in the montmorillonite-bearing crater floor materials and stronger in the layered mesas. The mesas have a higher albedo, a property that is also positively correlated with ~3 μm band depth in I/F spectra on a global scale, possibly because the greater absorptivity of darker materials results in higher daytime temperatures, driving off adsorbed water [*Jouglet et al.*, 2007]. Alternatively, *Milliken et al*. [2007] showed that the hydration–albedo correlation can result from nonlinear absorption processes, and that high albedo regions do not contain more water than dark regions once these effects are accounted for by converting spectra to single scattering albedo. Regardless, the precise mineralogy and nature of hydration in the layered mesas of crater E (and Dejnev) are currently unconstrained.

4.6.2 Intercrater deposits

Whereas Al-phyllosilicates and sulfates are the dominant secondary minerals in the craters of northwest Terra Sirenum, Fe/Mg-phyllosilicates (smectites) and chloride salts are more common on the intercrater plains, as in other regions of the southern highlands [chapter 3; *Osterloo et al.*, 2008; *Murchie et al.*, 2009b; *Glotch et al.*, 2010]. *Baldridge et al.* [2009, Fig. 2C] identified putative chlorides in a shallow basin just ~10 km south of Columbus crater's southwestern rim, and Fig. 4.30a shows another location ~60 km east of Columbus where THEMIS identifies chloride in

bright outcrops; these outcrops overlie materials in which CRISM (FRT0000B59A) detects Fe/Mg-phyllosilicates. To date, chlorides have not been identified within any of the larger craters discussed in section 4.6.1.

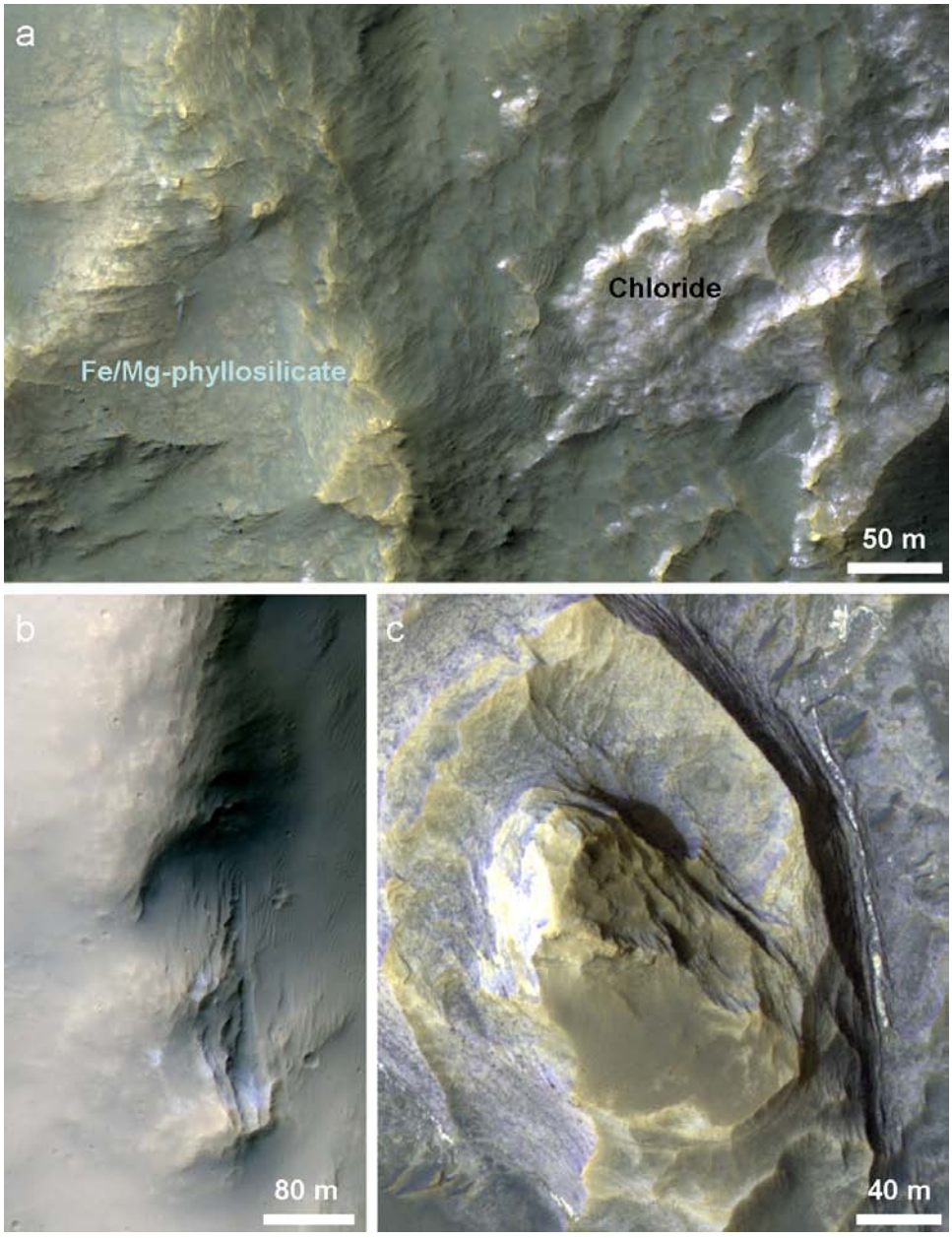

Figure 4.30: Light-toned deposits on the intercrater plains of Terra Sirenum. (a) Sample chloride/phyllosilicate exposure ~60 km east of Columbus crater; from HiRISE ESP_016162_1495. Context shown in Fig. 4.27. (b) Light-toned, relatively blue outcrops exposed in crater rim corresponding to Al/Si-OH site 6 in Fig. 4.27; from ESP_016030_1560. (c) Layered mesa near Al-OH site 5 in Fig. 4.27; from ESP_012562_1545.

A few locations on the intercrater plains of northwest Sirenum do contain Al-phyllosilicates. Fig. 4.27 enumerates eight intercrater sites at which a ~2.2 μm absorption is found in multispectral and/or hyperspectral CRISM data. All except site 8 have been imaged by HiRISE, revealing a range of exposure types. At sites 1 and 4 (Figs. 4.31a,b), CRISM detects kaolin group phyllosilicates in the ejecta of small impact craters (*D*~700 m and 600 m, respectively). The site 4 crater appears relatively unmodified (i.e., young), with bright rays visible in THEMIS nighttime IR images and abundant meter-scale blocks on the rim and proximal ejecta. This crater's proximal ejecta contain Fe/Mg-phyllosilicates (Fig. 4.31a), which may underlie kaolinite-bearing materials in the subsurface here. Sites 2 and 7 each contain a cluster of small craters with kaolinite-bearing ejecta (Figs. 4.31c,d); the largest of these craters exposes light-toned strata in its upper walls (Fig. 4.31e) that may be the source of the kaolinite. At site 6, a *D*~1.4 km crater exposes light-toned materials in its rim (Fig. 4.30b). All of these craters are probably too small to have initiated long-lived hydrothermal activity to form phyllosilicates [*Rathbun and Squyres*, 2002], and given the general paucity of evidence for phyllosilicate formation in post-Noachian terrains [*Poulet et al.*, 2005; *Bibring et al.*, 2006a; *Mustard et al.*, 2008], these craters likely excavated preexisting Al-phyllosilicates from the shallow subsurface.

At intercrater Al-OH site 5, only a single hectometer-scale exposure of Al-phyllosilicate is identified in CRISM HRL00011D66, but adjacent light-toned layered deposits (Fig. 4.30c) are spread across an area tens of km wide on the plains northwest of crater E. Similar to crater E's floor deposits, the layered deposits at site 5 have a relatively strong ~3 μm band as their only distinguishing feature in CRISM data. These deposits provide evidence that the sedimentation and aqueous processes that occurred in the large craters of northwest Terra Sirenum were not restricted to these locations but also affected at least some portions of the intercrater plains.

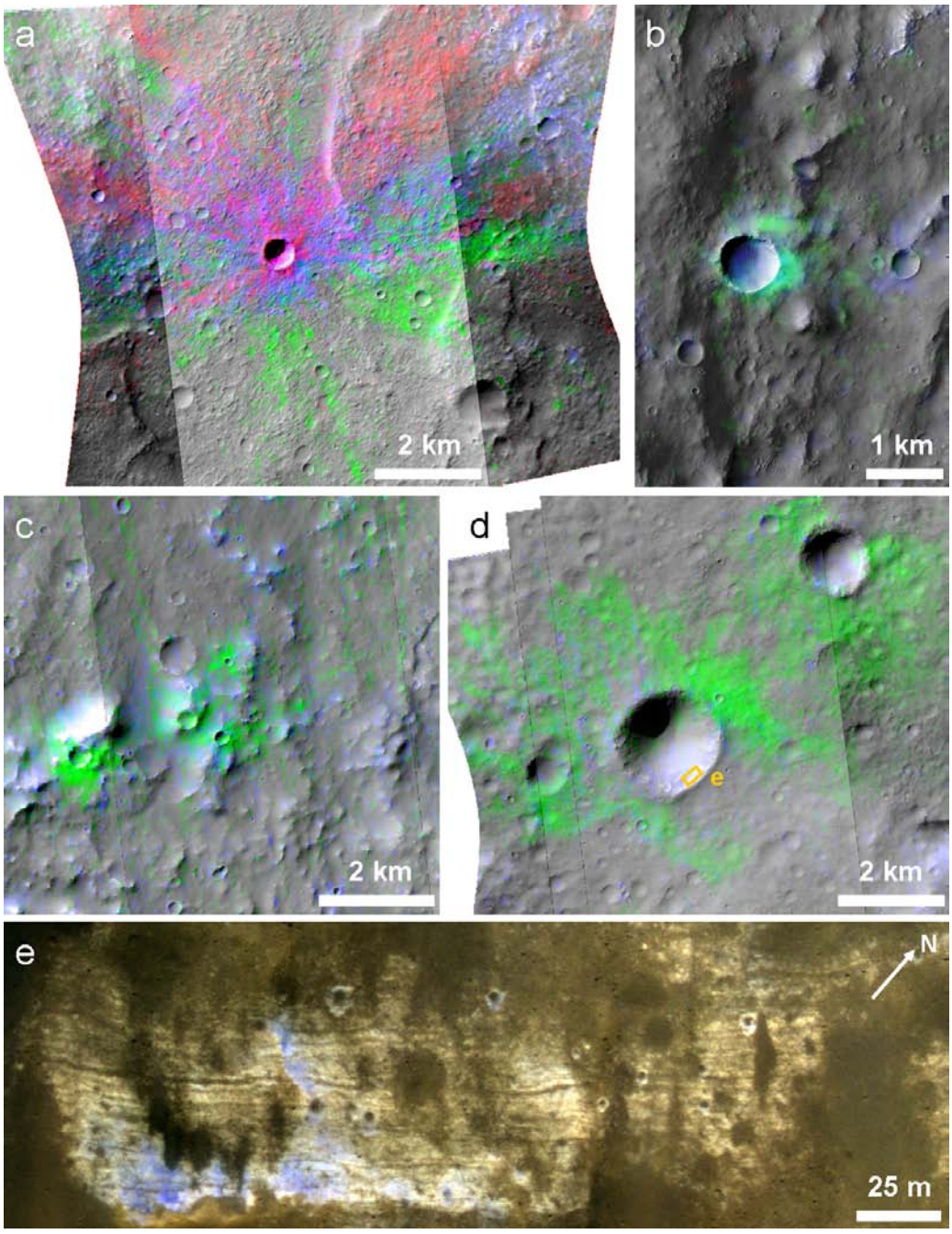

Figure 4.31: Craters in northwest Terra Sirenum with Al-phyllosilicate-bearing ejecta. Red is D2300 [*Pelkey et al.*, 2007], green is BD2200 and blue is BD1900H [*Ehlmann et al.*, 2009]; these respectively map Fe/Mg-phyllosilicates, Al-phyllosilicates, and hydrated minerals. (a) Site 4 from Fig. 4.27; CRISM FRT00009D7E parameters overlain on IR albedo and HiRISE PSP_008290_1565. (b) Site 1; CRISM HRL00009C1F on HiRISE ESP_016149_1550. (c) Site 2; FRT000176BD on ESP_017138_1525. (d) Site 7; FRT00017199 on ESP_016953_1540 and ESP_017164_1540. (e) Layers exposed in crater wall at site 7; from ESP_017164_1540.

At intercrater site 3—the only 2.2 μm site south of Columbus and Cross craters—the ~2.2 μm band identified in CRISM mapping data is not primarily due to Al-OH, but instead to Si-OH. Although this site's relationship to the Columbus crater deposits is unclear, it is described here in the interest of fully exploring the region's aqueous history.

At this location (167.45°W, 33.15°S), a mound ~3 km by 5 km wide protrudes ~100 m from the surrounding plains (Fig. 4.32a). The central mound has a weak spectral signature consistent with hydrated silica (i.e., opal), with stronger signatures present on its flanks and on the adjacent plains. Hydrated silica is distinguished from Al-phyllosilicates by its broader 2.2 μm band with an asymmetric long-wavelength edge extending to 2.3 μm or beyond [*Milliken et al.*, 2008; *Ehlmann et al.*, 2009]. In well-hydrated opaline silica this band is in fact a doublet with minima at 2.21 and 2.26 μm. Removal of H_2O from opal at moderate temperature or low relative humidity causes the 2.26 μm band to disappear, weakens the 1.9 μm H_2O band, and "shifts" the Si-OH overtone absorption from 1.41 μm to 1.38 μm [*Anderson and Wickersheim*, 1964; *Milliken et al.*, 2008; *Cloutis et al.*, 2009; *Ehlmann et al.*, 2009]. Hydroxylated glasses have similar features, but their single 2.2 μm absorption is more symmetric and commonly centered at a slightly longer wavelength of 2.22–2.23 μm, and their ~1.4 μm overtone does not shift upon dehydration [*Milliken et al.*, 2008].

Spectra observed on and around the mound at site 3 are most consistent with opaline silica with variable degrees of hydration (Fig. 4.33a). H_2O-poor silica is found in bright materials (Fig. 4.33b) on the plains around the mound, whereas more fully hydrated silica occurs on the mound itself and in some intermediate-toned exposures on the plains (Fig. 4.32a). These spectral differences are observed even when the same denominator is used for all ratio spectra in the scene. There is no obvious stratification or zoning pattern of the hydration states. The presence of variably

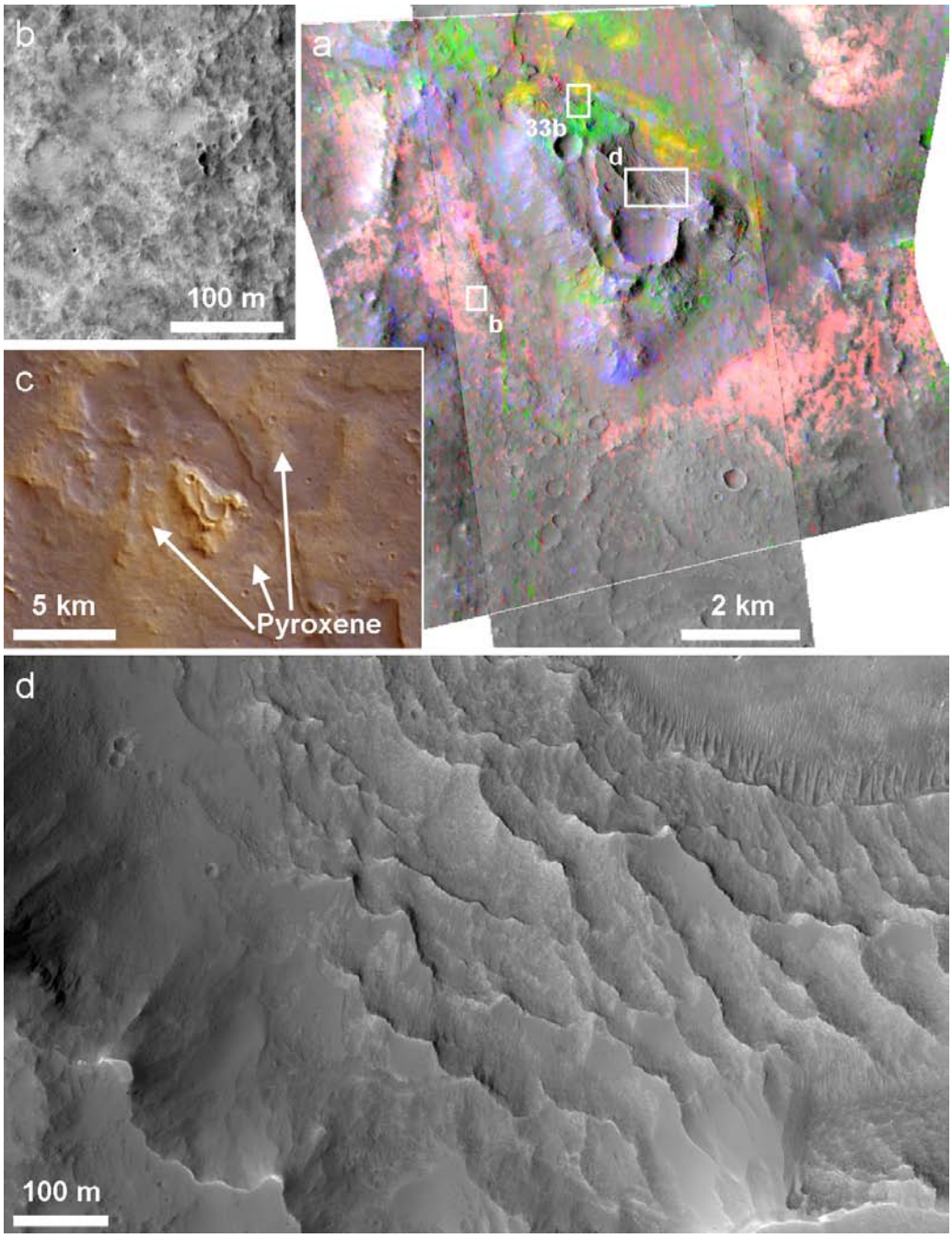

Figure 4.32: Intercrater Al/Si-OH site 3 from Fig. 4.27. (a) Mineralogy of mound and surrounding plains. Red is LCPINDEX [*Pelkey et al.*, 2007], green BD2200, and blue BD1900H [*Ehlmann et al.*, 2009]; yellow is a parameter tracking wide 2.2 µm absorptions due to Si-OH. I have confirmed that red areas correspond to low-calcium pyroxene, blue to hydrated silica, yellow to partially dehydrated opal or altered glass, and green to kaolinite. Background is HiRISE ESP_011903_1465 and CRISM FRT00010EC5 IR albedo. (b) Surface texture of pyroxene-bearing materials. (c) Broader context of the mound and surrounding plains, from HRSC h0538_0000. (d) Exposure showing the mound's layered or terraced structure.

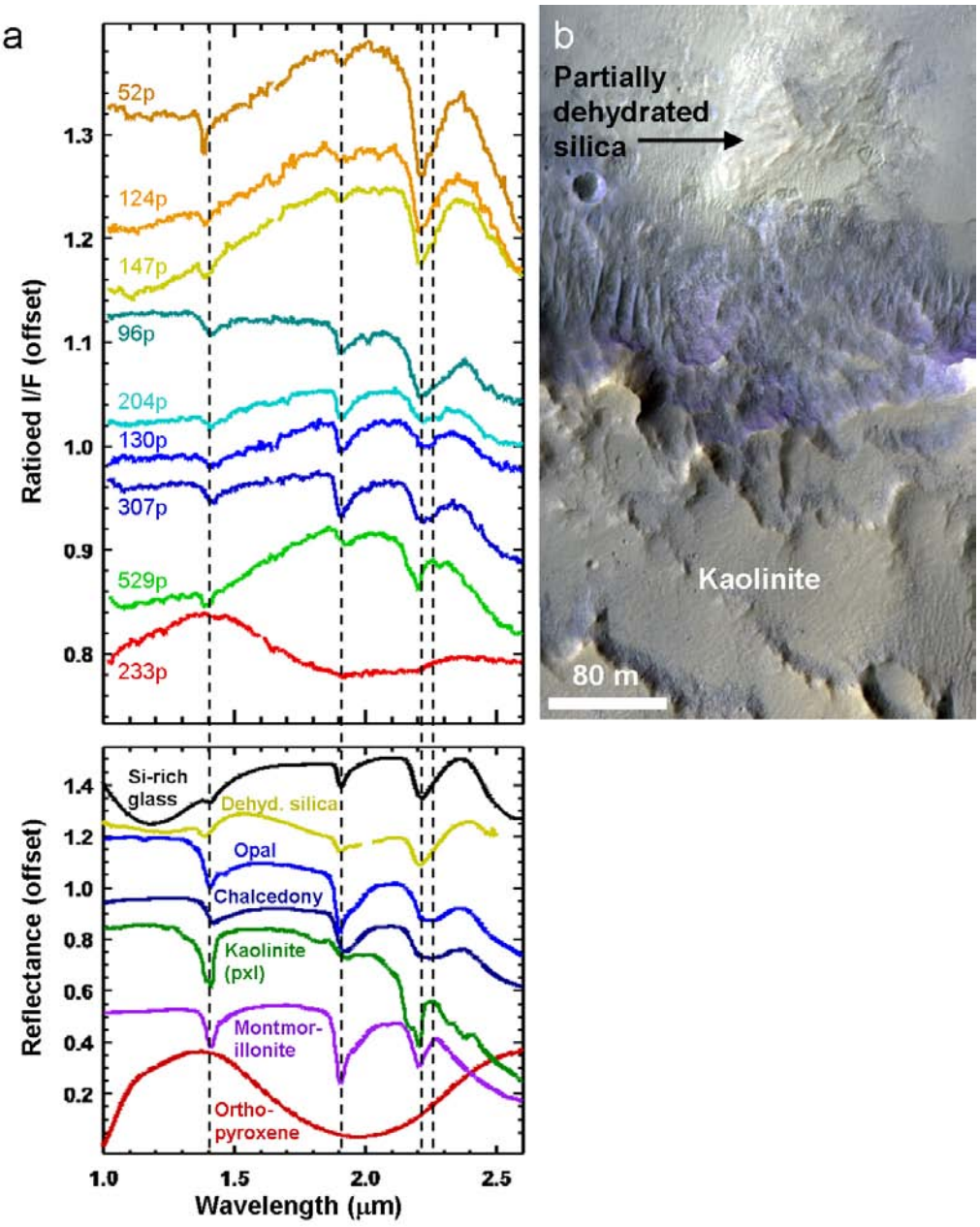

Figure 4.33: (a) CRISM spectra from mound at Sirenum intercrater at site 3 (top) and relevant lab spectra (bottom); format similar to Fig. 4.11. All CRISM spectra are from FRT000010EC5. Si-rich glass is obsidian JB578 (scaled x10 for ease of comparison) from *McKeown et al.* [2010]. Dehydrated silica is altered (silica-coated) glass measured at Mars-like pressure and temperature (scaled x20 for comparison) from *Milliken et al.* [2008]. Opal is sample TM8896, chalcedony (cryptocrystalline silica) is CU91-6A, poorly crystalline (pxl) kaolinite is KGa-2, and montmorillonite is SWy-1 from *R. Clark et al.* [2007]. Orthopyroxene is sample CBSB52 from CRISM spectra library. (b) Sample of mound texture (including kaolinite-bearing area) and adjacent light-toned materials containing partially dehydrated silica; from HiRISE ESP_011903_1465.

hydrated materials in close proximity may suggest differences in formation temperature or a dehydration process driven by local thermal gradients rather than atmospheric humidity, consistent with a hydrothermal environment for silica formation; alternatively, varying physical properties could have made some silica-bearing materials more susceptible to dehydration than others.

Parts of the mound and surrounding plains have a narrower 2.16/2.20 μm doublet consistent with a kaolin group clay (Fig. 4.33a), providing a possible mineralogic link to the kaolinite-bearing materials identified elsewhere in northwest Sirenum. Finally, a relatively strong low-calcium pyroxene signature is observed in plains several km distant from the mound, but the broader geologic context (Fig. 4.32c) suggests no obvious connection between the mound and the pyroxene-bearing unit; the latter appears to be a more widespread underlying unit.

Three alternative hypotheses for this topographic mound associated with opaline silica are: it could be (1) an erosional remnant mesa, (2) a siliceous spring mound [e.g, *Guidry and Chafetz,* 2003], or (3) a volcanic construct that has been aqueously altered, possibly under acidic conditions [e.g., *Seelos et al.,* 2010]. Opaline silica has previously been identified adjacent to volcanic mounds both in the Columbia Hills of Gusev crater [*Squyres et al.*, 2008] and in the Nili Patera caldera of Syrtis Major [*Skok et al.,* 2010]. The Nili Patera mound is quite similar to site 3 in lateral scale and in the localization of its partially dehydrated silica to bright outcrops adjacent to the mound. However, the Nili mound is ~3 times taller than that at site 3, is texturally massive, and sheds abundant meter-scale boulders (see HiRISE ESP_013582_1895). Fewer boulders are visible on the flanks of the mound at site 3, suggesting the material is friable and thus consistent with a sedimentary nature; the mound's lower profile, constituent silica, and bedded or terraced morphology (Fig. 4.32d) are more consistent with silica-cemented sediments or a spring mound than

with a volcanic construct. Also unlike the Columbia Hills and Nili Patera, there are no other obvious volcanic features in the vicinity of site 3; whereas pyroxene and olivine-bearing ridged materials adjacent to the Nili mound are likely lava flows [*Skok et al.*, 2010], the pyroxene-bearing outcrops near site 3 have a fractured texture (Fig. 4.32b) uncharacteristic of typical Martian lavas. If site 3 is a siliceous spring mound, its size would rival the largest known spring mounds on Earth [*Crumpler*, 2003], but would be 1–2 orders of magnitude smaller than many Martian crater and canyon mounds that have previously been proposed as spring mounds [*Rossi et al.*, 2008]. Alternatively, this mound could simply be an erosional remnant of a previously more widespread deposit, possibly sediments that have been cemented by silica precipitating out of groundwater. If the kilometer-wide depression near the mound's summit is a degraded impact crater, then it may have made this portion of the deposit more resistant to erosion (e.g., by armoring the surface with its ejecta). In this scenario, the process of silica formation would be poorly constrained.

4.7 Regional hydrologic modeling*

The diverse hydrated minerals found in Terra Sirenum—a region in which surface valley networks are relatively sparse [*Carr*, 1995; *Fassett and Head*, 2008b; *Hynek et al.*, 2010]—motivate consideration of a groundwater-dominated hydrology to explain the aqueous deposits. Global-scale hydrological models representing the groundwater evolution of early Mars can explain the distribution of sulfate-rich evaporite deposits in Meridiani Planum and surrounding regions [*Andrews-Hanna et al.*, 2007]. In those models, the region west of Tharsis—i.e., northern Terra Sirenum—is another preferred location for a shallow water table and evaporite

* The regional modeling and parts of the discussion in this section were contributed by Jeff Andrews-Hanna.

formation at smaller scales, driven by a combination of groundwater flow from the nearby high topography of Tharsis and the presence of a shallow topographic trough surrounding the rise [*Phillips et al.*, 2001]. Ejection of water from aquifers buried deep beneath Tharsis may also play a role [*Andrews-Hanna et al.*, 2007].

In Terra Sirenum, hydrological activity in the vicinity of Columbus crater should be encouraged by a confluence of factors. These include its location roughly equidistant from the dichotomy boundary and a mid-sized basin to the south, each of which should act to draw down the water table in their immediate vicinity (so, by comparison, the water table would be relatively high near Columbus crater). Farther south, the water table drops deeper beneath the surface as a result of the southern limit of the low-latitude precipitation belt in the models and regional drawdown of the water table in high southern latitudes by the Hellas and Argyre impact basins [*Andrews-Hanna and Lewis*, 2011].

The detailed distribution of evaporites in Sirenum can be predicted via regional hydrologic modeling. Specifically, a high-resolution (0.25 degree per pixel, corresponding to ~15 km at the equator) local hydrological model of the region west of Tharsis is considered; it uses the precipitation rates and hydrologic head from the global simulations of *Andrews-Hanna et al.* [2010] as boundary conditions. The precipitation is set to follow a cosine distribution between ±45° latitude, to approximately match the distribution of valley networks. The local model extends from 180° to 230°E and from 50°S to 10°N, boundaries sufficiently far from the region of interest (Fig. 4.27) to avoid significantly affecting the results. The model assumes that groundwater evaporates upon reaching the surface, resulting in the formation of evaporites and evaporite-cemented sediments that can accumulate to substantial thickness in some regions. There is a dynamic coupling between the groundwater flow and the surface topography, in which groundwater-mediated

sedimentation modifies the surface topography, which in turn modifies the paths and rates of groundwater flow. Ponding of emergent groundwater (e.g., in a crater lake) would affect the local hydrology in the same way as sediment accumulation would. The models assume a ratio between evaporated water column height and resulting sediment thickness of 50 to 1, consistent with evaporation of deep groundwater with salinity comparable to seawater and a 40% volumetric contribution from non-evaporitic sediments [*Handford*, 1991; *Moller et al.*, 1997; *Andrews-Hanna et al.*, 2007]. Higher or lower rates of deposit formation could result from increased or decreased sediment flux and fluid salinities. However, because the surface topography evolves slowly relative to the fluid flow, the system is in a state of quasi-equilibrium at any one time, and the impact of different sedimentation rates can be achieved by simply scaling the timescale for evolution. Similarly, changing the mean crustal permeability primarily changes the rate of water cycling through the hydrologic system without altering the gross distribution and flow paths of water. The model results should, therefore, yield insights into the spatial distribution of relative evaporite thicknesses even if their absolute thicknesses are poorly constrained.

As found in the global models [*Andrews-Hanna et al.*, 2010], the water table initially intersects the surface only within scattered impact craters and other topographic lows. The intersection of the water table with major impact craters can be clearly seen in maps of the hydraulic head at the beginning of the simulation (Fig. 4.34b). As the simulation evolves, shallower craters fill with sediments resulting in a concomitant decrease in the rate of groundwater upwelling. In most cases, this trend progresses until the crater depth reaches some minimum value at which the groundwater flux to the surface terminates. The water table follows a smoothed approximation of the topography (Fig. 4.34b), with the shorter-wavelength structure diminishing as the smaller craters are filled with sediments, resulting in the dominance

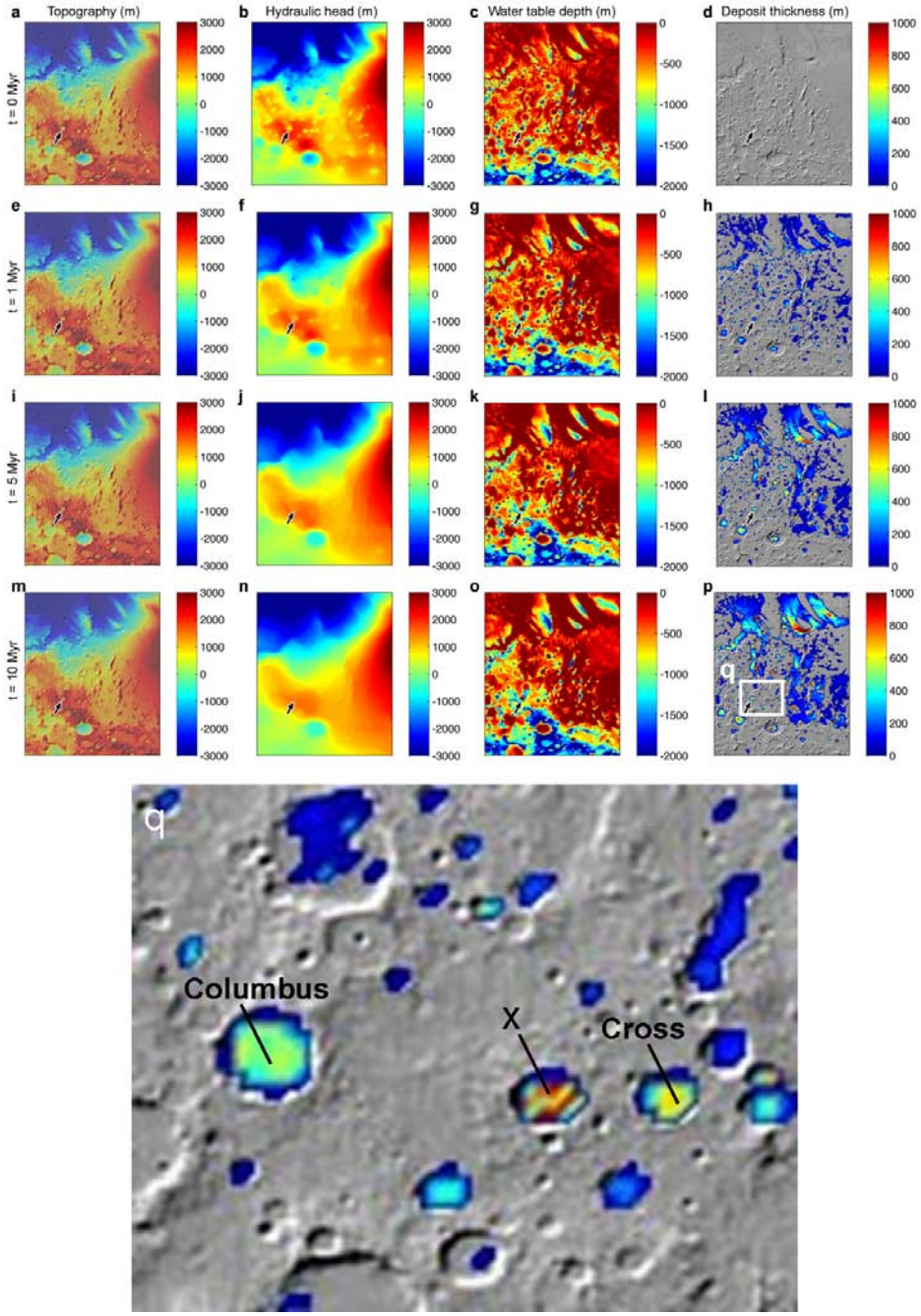

Figure 4.34: Topography, hydraulic head (the elevation of the water table relative to an equipotential), the depth to the water table, and the predicted deposit thickness as a function of time in the hydrological simulations. Results are shown after 0, 1, 5, and 10 Ma of elapsed model time. Columbus crater is indicated by the arrow in each panel. Panel q provides a zoomed view of predicted deposit thicknesses after 10 Ma across the approximate area of northwest Terra Sirenum shown in Fig. 4.27. Crater "X" is predicted to be a site of significant groundwater inflow, but appears morphologically fresh and is interpreted to postdate regional aqueous activity, explaining its lack of observed hydrated minerals.

of longer-wavelength flow paths (Fig. 4.34f,j,n). Nevertheless, Columbus crater still features prominently as a locus of groundwater upwelling and evaporation after the groundwater flux into many of the smaller craters has ceased (Fig. 4.34i–l). Although the models assume that groundwater evaporates immediately upon reaching the surface, this groundwater flux could support the formation of either playas or deeper lakes depending on the local climatic conditions.

These models have used the present-day topography of Mars as a starting condition, though the current topography is the end product of 4.5 billion years of evolution. Although it is not possible to recreate the surface of Mars at any one time in its history, the effects of changes over time can be inferred. It is noteworthy that the older craters in the region (Dejnev, Columbus, Cross, and others) typically contain hydrated minerals and/or layered deposits, whereas younger craters do not (Fig. 4.27 and section 4.6.1). For example, the relatively fresh D~80 km crater approximately 300 km east of Columbus ("X" in Fig. 4.34q) is predicted to be a site of significant groundwater inflow, but no mineralogical evidence of such hydrological activity is seen. This would be expected if this crater postdated the active hydrological cycle, as is suggested by the lack of erosion of its ejecta blanket, raised crater rim, and central peak. Ignoring this crater, the remaining craters in Fig. 4.27 with the greatest predicted evaporite thicknesses are Columbus and Cross (Fig. 4.34q), consistent with the identification of hydrated sulfates exclusively in these two craters to date.

Nevertheless, the true complexity of the Martian hydrologic cycle cannot be captured in these simple models. For example, the depth of the craters present during the active hydrological cycle is uncertain; many Martian craters appear to have experienced substantial erosion in the Noachian Period, resulting in flat-floored, shallow craters without raised rims [*Craddock and Howard*, 2002]. Some craters may have already been substantially eroded and infilled by the time active sulfate

deposition occurred in the Late Noachian to Early Hesperian, while others may have been significantly deeper than their current state. Hydrological activity may have spanned a period of hundreds of millions of years, as evidenced by the presence of large craters interstratified within the Meridiani sulfate deposits [*Edgett and Malin*, 2002], but might not have been continuous. Craters formed during the period of hydrological activity west of Tharsis would have intersected and drawn down the water table in their immediate vicinity, possibly cutting off groundwater flow into nearby craters. In addition, many large craters west of Tharsis (including Columbus) are crossed by graben radial to Tharsis, some of which may date to the Noachian [*Anderson et al.*, 2001]. The faults underlying these graben would have channeled fluids along strike down the slope of the Tharsis rise, potentially enhancing groundwater flux into the craters they intersect, in contrast with the homogeneous and isotropic hydraulic properties assumed in the models. Therefore, the actual sequence of hydrological activity would have been much more complicated than the simple monotonic evolution predicted by the models.

Although the study region west of Tharsis is a preferred location for evaporite formation, the model results suggest that intracrater hydrated mineral deposits should be relatively common in large Noachian-aged craters across much of Mars. In particular, Figs. 4.34h,l,p show that evaporite formation is predicted beyond the specific sub-region of Terra Sirenum in which hydrated minerals are identified. The restricted distribution observed by CRISM may indicate that the hydrologic-climatic environment in northwest Sirenum was particularly amenable to formation of such deposits, or alternatively conditions here may simply favor the preservation or exposure of deposits that were originally more widespread. Specifically, pervasive dust cover north of ~20°S in this longitude range [*Ruff and Christensen*, 2002] may obscure the bedrock mineralogy north of the area in Fig. 4.27. Likewise, south of

~30°S the Amazonian ice-dust mantle described by *Mustard et al.* [2001] obscures older deposits. West of my study region, a group of larger, interconnected basins experienced a distinct hydrologic history that has been considered in detail elsewhere [*Irwin et al.*, 2002; *Noe Dobrea et al.*, 2008c]. The circum-Tharsis trough to the east has been completely resurfaced by Hesperian lava flows, which would have buried any older evaporites.

In summary, both the general concentration of aqueous deposits in northwest Terra Sirenum and the specific subset of craters with sulfates detected from orbit are consistent with groundwater upwelling predicted by tested hydrologic models, although post-depositional modification of the aqueous deposits has surely also affected their observed distribution. Although these models have focused on deposition of evaporitic sulfates, such groundwater activity may also have altered the Noachian crust to form phyllosilicates.

4.8 Discussion

In this section, I present several hypotheses to explain the observations described above. I focus on Columbus crater but also discuss observations from elsewhere in northwest Terra Sirenum. I begin with a summary of key findings and their general implications.

Columbus crater is a Middle-to-Late Noachian-aged crater in a Middle Noachian-aged terrain. It contains layered deposits with diverse hydrous minerals, as do at least ten neighboring craters and small areas of the plains surrounding those craters. These deposits appear to date to the Late Noachian, an epoch during which significant groundwater upwelling and evaporation is predicted in this region, with Columbus being a location of especially significant modeled evaporite deposition. Based on the 50-to-1 water-to-evaporite volume ratio assumed in the hydrologic

model of section 4.7, forming the ~10–20 m thickness of aqueous deposits on the walls and floor of Columbus crater (sections 4.2.2 and 4.5) via evaporation would have required ~500–1000 m total depth of water in the crater, integrated over time; this is similar to the ~900 m elevation difference between the modern crater floor and the sulfate ring around the crater walls.

Thermal infrared measurements suggest that the light-toned deposits of Columbus are highly altered, with estimated phyllosilicate and sulfate abundances in the tens of percent by volume. Visual evidence for ongoing physical weathering and erosion of these deposits (e.g., Fig. 4.6b,d) argues for pervasive alteration throughout the deposits rather than a surficial alteration rind. The specific minerals observed indicate that pH, water activity (a_{H2O}), and possibly redox conditions of the alteration environment varied in space and/or time: Fe/Mg-smectites typically form at circum-neutral pH [e.g., *Chevrier et al.*, 2007], whereas localized deposits of jarosite and alunite suggest pH < 3–4 at least locally, based on terrestrial analogs [*Bigham et al.*, 1996; *Fernandez-Remolar et al.*, 2005; *Benison et al.*, 2007]. Gypsum on Mars precipitates at water activity exceeding that of terrestrial seawater (0.98), whereas monohydrated Mg-sulfate precipitates at $a_{H2O} \sim 0.5$ [*Tosca et al.*, 2008a]. Szomolnokite (suggested in section 4.3.5 to constitute at least part of Columbus' monohydrate) is a ferrous sulfate, whereas ferric sulfates (including jarosite) and oxides/hydroxides are observed elsewhere in Columbus, implying variable redox conditions. Columbus is also one of the few known locations on Mars with interbedded phyllosilicates and sulfates, suggesting episodic changes in environmental conditions or sediment source regions. Whereas most Martian phyllosilicates are detected in apparent isolation from the salts that must have formed with them [*Milliken et al.*, 2009], Columbus crater—perhaps like Gale crater [*Milliken et al.*, 2010]—may retain its full alteration assemblage.

Terrestrial lab experiments require moderate temperatures to convert polyhydrated Mg-sulfate into monohydrate [*Freeman et al.*, 2007] or to form $Fe(OH)SO_4$ from hydrated Fe-sulfates [*Milliken et al.*, 2008; *Swayze et al.*, 2008a; *Morris et al.*, 2009; *Lichtenberg et al.*, 2010]. Therefore it is intriguing that the strongest monohydrate and $Fe(OH)SO_4$ signatures in Columbus crater correspond to one of the freshest ~200 m impact craters on its light-toned deposits (Fig. 4.17a), whose impact event could have provided the heat needed for these mineralogic transitions. However, other monohydrate-bearing outcrops on Columbus' floor have no obvious connection to impact craters; possible origins for these monohydrates are discussed in sections 4.8.2 and 4.8.4.

A possible geochemical analog for the deposits of northwest Sirenum is provided by Western Australian acid saline lakes and groundwaters [e.g., *Benison et al.*, 2007; *Baldridge et al.*, 2009; *Story et al.*, 2010]. These playa lakes precipitate halite, gypsum, kaolinite, and ferric oxides, while associated groundwaters precipitate the same minerals in addition to jarosite, alunite, and Fe-bearing phyllosilicates. All of these minerals are identified in Columbus crater, with the single exception of halite, which—like other anhydrous chlorides—has no diagnostic infrared spectral absorptions, and therefore may be difficult to identify unless it occurs in high abundance over large areas [see *Osterloo et al.*, 2008]. Furthermore, theoretical and experimental studies both predict that Ca and Mg/Fe-sulfates should dominate Martian evaporite assemblages, with halite formation occurring much later and less abundantly than in terrestrial evaporites due to the low Na content of basalt [*Tosca et al.*, 2004, 2005, 2008a; *Tosca and McLennan*, 2009]. Therefore, although the Mg-sulfates likely present in Columbus are missing from many Western Australian lakes, this is readily explained by a difference in primary compositions: the bedrock of Western Australia is granitic and gneissic [*Benison et al.*, 2007], whereas the plains outside Columbus

(like much of Mars) appear to be basaltic (section 4.4) and therefore more Mg-rich. Terrestrial acid-saline lakes and groundwaters also typically exhibit substantial geochemical gradients over relatively short spatial scales, leading to variations in the precipitated minerals reminiscent of those found in Columbus crater [*Baldridge et al.*, 2009].

Although acid-saline lakes precipitate kaolinite directly, elsewhere on Mars kaolinite formation has been attributed to top-down (possibly acid rainfall-driven) weathering [e.g., *Noe Dobrea and Swayze*, 2010], and some of the intercrater kaolinite in northwest Sirenum may have formed in this way (e.g., Fig. 4.31a). If this weathering predated sulfate formation in Columbus crater—which may have occurred under acidic conditions as proposed for Late Noachian/Early Hesperian Mars globally [*Bibring et al.*, 2006a]—then kaolinite could have survived these conditions more effectively than other phyllosilicates (e.g., smectites) due to its greater stability at lower pH [e.g., *Altheide et al.*, 2010b] and its comparatively slow dissolution rate [*Zolotov and Mironenko*, 2007b]. However, the finding of kaolinite associated with a possible spring mound or silica-cemented sediments (section 4.6.2) supports a groundwater- (not surface weathering-) related origin for some Al-phyllosilicates in this region if these clays are authigenic. Indeed, the bright fracture fill observed in some kaolinite-bearing materials in Columbus crater (Fig. 4.7) may reflect mineralization from subsurface fluids migrating through the fractures [e.g., *Okubo and McEwen*, 2007; *Okubo et al.*, 2009]. Alteration may have been greatest within the impact craters labeled in Fig. 4.27, in which emergent groundwater could have ponded. The region's Al-phyllosilicates may thus have formed via multiple processes over a range of time.

The origin of the Sirenum layered deposits will be considered in more detail below; for now, I make only the general point that thin, conformable, laterally

continuous beds (as are found in Columbus crater—see section 4.2.2) are commonly cited as evidence for deposition from suspension [e.g., *Wilson et al.*, 2007; *Grant et al.*, 2008], either as marine/lacustrine or airfall sediment. In the case of Holden crater, the additional characteristic of a restricted elevation distribution—as is also observed for Columbus' polyhydrate ring—has been argued to support subaqueous deposition [*Grant et al.*, 2008]. The polygonal fracture patterns observed on sulfate-bearing outcrops in Columbus crater are similar to fracture polygons observed on sulfate-bearing rocks in Meridiani Planum [*McLennan et al.*, 2005], and on chloride- [*Osterloo et al.*, 2008, 2010] and phyllosilicate-bearing (e.g., chapter 2) outcrops across much of Mars. Their preferential occurrence in materials containing aqueous minerals suggests that these polygons formed via desiccation of sediments and/or dehydration of constituent minerals.

Also during the Late Noachian Epoch, groundwater upwelling and evaporation on the other side of Mars may have produced the aqueous deposits in Meridiani Planum [*Andrews-Hanna et al.*, 2007]. These materials share many mineralogic characteristics with those in Columbus crater, including significant abundances of Mg/Ca/Fe-sulfates and secondary aluminosilicates with minor crystalline ferric oxide and possibly Fe-phyllosilicates [*Clark et al.*, 2005; *Glotch et al.*, 2006]. The deposits in both regions also appear to lack carbonates. An apparent difference between Meridiani and Terra Sirenum is the presence of Al-phyllosilicates and Al-sulfates in the latter. Although modest amounts of kaolinite or alunite cannot be excluded by rover analyses of Meridiani rocks [*Clark et al.*, 2005], there is no evidence for either in remote sensing data [e.g., *Poulet et al.*, 2008a]. The dearth of these Al-bearing secondary phases in Meridiani and much of the rest of Mars has been cited as evidence for low water-to-rock ratios in the alteration environments [*Hurowitz and McLennan*, 2007]. The distinctive mineralogy of northwest Sirenum could reflect higher water-to-

rock conditions, perhaps facilitated by the presence of large craters in which upwelling groundwater could pond. Similar conditions may have initially been present in Meridiani Planum, with the evidence now buried beneath the extensive younger playa deposits [*Andrews-Hanna et al.*, 2010].

I now consider several hypotheses (Fig. 4.35) for the particular sedimentary processes that may have emplaced the layered deposits of northwest Sirenum, with an emphasis on the sulfate-bearing ring around the walls of Columbus crater. Most of these hypotheses conflict with some observations and/or with other knowledge of Martian geology, with the possible exception of the deep lake hypothesis (section 4.8.4).

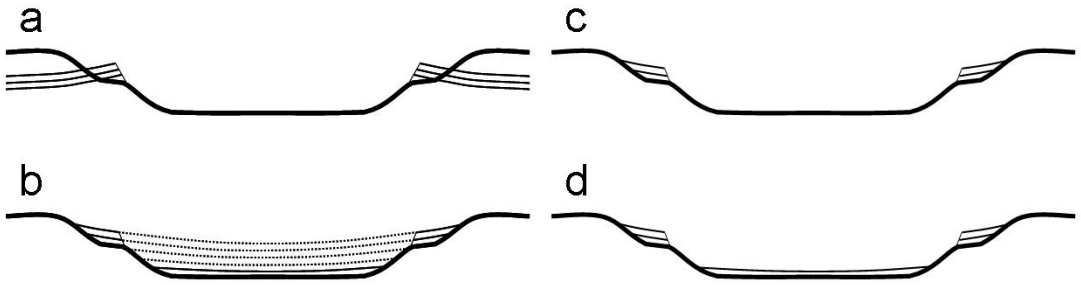

Figure 4.35: Hypotheses for the hydrous light-toned layered deposits in Columbus crater. (a) Hypothesis 1: preexisting layers exposed by the crater-forming impact. (b) Hypothesis 2: erosion of layers that once filled the crater (dotted lines). (c) Hypothesis 3: a tufa-like deposit from a spring ringing the crater walls. (d) Hypothesis 4: sedimentation from a deep lake that once filled the crater.

4.8.1 Hypothesis 1: Columbus ring as a preexisting layer

In general, layered materials at roughly constant elevation around the walls of a crater could indicate impact exposure of preexisting layers in the subsurface. In the case of Columbus crater, I consider this hypothesis untenable for several reasons.

First, as described in section 4.5, a degraded D~17 km crater superposed on Columbus' southwest wall contains polyhydrated sulfate-bearing layered deposits superposed on its floor (Fig. 4.10). These crater-filling deposits are essentially contiguous with the polyhydrate ring on this portion of the crater wall, implying that

the 17 km crater was present before the ring was emplaced. This in turn implies that Columbus crater predates the polyhydrate ring.

Second, impact crater formation affects the geometry of strata exposed in crater walls and rims. Specifically, uplift of a crater rim and subsequent terrace formation via wall slumping along listric faults both cause preexisting strata to be back-tilted—i.e., to dip away from the crater interior—relative to their pre-impact geometries [*Melosh*, 1989]. As an example, back-tilted strata are observed in the rim of Endeavour crater in Meridiani Planum, where they are inferred to predate that crater (see chapter 5). By contrast, the beds within Columbus crater's polyhydrate ring show the opposite trend, with an average dip direction almost exactly toward the crater interior and no beds observed to dip away from the crater (section 4.2.2). In addition to these quantitative measurements, images such as Fig. 4.12 give the qualitative impression that the sulfate-bearing beds onlap the crater wall.

Additional shortcomings of the preexisting layer hypothesis include the non-detection of this layer—or any polyhydrated sulfates—at similar (or any) elevations within adjacent craters, and the hypothesis' inability to account for the layered deposits with diverse hydrated minerals on the floors of Columbus and its neighboring craters, which must postdate these craters. Because of these numerous weaknesses, I discard this hypothesis for the sulfate-bearing ring of Columbus crater, while noting that some (but probably not all) kaolinite-bearing materials in Columbus and its neighboring craters might predate these craters.

4.8.2 Hypothesis 2: Columbus ring as an erosional remnant

Another explanation for the ring planform of polyhydrate-bearing deposits in Columbus crater is that this ring is the erosional remnant of beds that once spanned the entire crater. A variety of processes may have emplaced these beds, although their morphologic features in orbital images appear most consistent with deposition from

suspension. In this hypothesis, hydrated mineral formation may or may not be coeval with sedimentation; i.e., the sulfates and phyllosilicates could have formed (1) elsewhere and been transported into these craters, (2) during subaqueous sedimentation, or (3) subsequently via diagenesis. A combination of these alternatives is also possible; for comparison, evaporite minerals in the Meridiani Planum sediments are inferred to have formed elsewhere, been modified during deposition in playa lakes, and later experienced multiple episodes of diagenetic overprinting [*McLennan et al.*, 2005].

If hydrated mineral formation predated deposition in the Sirenum craters, then the alteration environment is unknown. However, there is no known plausible source for these sulfates and Al-phyllosilicates elsewhere in the southern highlands (see chapter 3). Alunite in particular has been identified nowhere else on Mars to date.

Alternatively, the aqueous minerals in these craters could have formed via diagenesis of layered deposits, which could have initially been composed of relatively unaltered mineral grains. Diagenesis (which likely occurred here, whether or not it produced most of the hydrated minerals) could account for Columbus' trend of polyhydrated sulfate at higher elevations on the crater walls vs. monohydrated sulfate below on the crater floor. If all the sulfates were originally polyhydrated, then increased temperatures during burial diagenesis could have enabled conversion to monohydrate in the lowermost layers; this mechanism is one of several proposed to explain the stratification of polyhydrated over monohydrated sulfates in Candor Chasma and other canyons of Valles Marineris [*Murchie et al.*, 2009a]. However, diagenetic formation of all hydrated minerals in Columbus seems unlikely given the alternating kaolinite and sulfate-bearing beds seen in some locations (section 4.3.2), which are difficult to explain unless these beds originally had strikingly different primary compositions, porosities or permeabilities.

The third possibility—that the hydrated minerals formed in shallow playa lakes coeval with sediment deposition—would be consistent with the playa environments of Meridiani Planum and Western Australia cited above as analogs. If Columbus crater was once filled with evaporitic sediments to at least the level of its polyhydrate ring, then these ~900 m of evaporites would have required tens of km total equivalent depth of water to evaporate in the crater over time, according to the assumptions of section 4.7.

Late Noachian sediments filling Columbus crater would have needed to be almost entirely removed by the Early Hesperian (the age of the probable lava now spanning the crater floor), requiring average erosion rates of at least a few μm/yr. These rates are modest by terrestrial standards, but have not existed globally on Mars since the Noachian, during which they have been attributed to precipitation-driven fluvial processes [e.g., *Craddock and Maxwell*, 1993; *Hynek and Phillips*, 2001]. Such processes could not have removed sediments from Columbus crater, which has no outlet; aeolian erosion and transport is the only conceivable mechanism for sediment removal. There is evidence for at least some erosion of light-toned layered deposits on Columbus' floor (Fig. 4.26a and associated discussion in section 4.5), but the inferred eroded thickness is only a few tens of meters, over an order of magnitude less than that needed to fill the crater to the level of its wall ring.

More broadly, there is strong evidence for substantial erosion of crater-filling layered deposits across Mars; in fact, enough examples are known that an evolutionary sequence can be defined [*Malin and Edgett*, 2000]. It appears that erosion typically begins along the crater walls and then proceeds inward, such that incomplete removal leaves behind intracrater mounds such as those found in Gale and Henry craters [*Malin and Edgett*, 2000]. To my knowledge, no Martian crater other than Columbus exhibits a remnant sedimentary ring along the crater walls instead of a central mound.

Therefore, while current understanding of the erosional process(es) is sufficiently poor that this scenario cannot be ruled out, it would make Columbus unusual or possibly unique among Martian craters.

4.8.3 Hypothesis 3: Springline "tufas"

If the sulfate ring at Columbus is not an erosional remnant of crater-filling sediments, but rather was deposited originally as a ring, then it could be an evaporitic deposit formed when groundwater emerged along an impermeable layer exposed in the crater walls. Carbonate deposits formed in this way on Earth are called perched springline tufa or travertine, where the latter term applies to thermal springs and the former to ambient-temperature precipitates [e.g., *Ford and Pedley*, 1996]. In principle, similar processes could occur with sulfate-rich solutions on Mars. Given the spectral evidence for relatively low formation temperatures of jarosite in Columbus crater and alunite in Cross crater (section 4.3.6), the term tufa is used for the remainder of this discussion.

Terrestrial springline tufas exhibit distributary channels and discontinuous distal fan-shaped deposits, as well as rimmed terraces in the proximal deposits where water has ponded and evaporated [*Pedley*, 1990; *Ford and Pedley*, 1996; *Fouke et al.*, 2000]. None of these features is evident in images of Columbus' light-toned deposits. It is also unclear how the perched springline model could account for the other craters of northwest Sirenum that have laterally continuous hydrated beds spread across their floors, but no preserved ring structures on their walls. Finally, the observation most difficult to reconcile with the springline tufa hypothesis is the presence of light-toned layered deposits in Columbus crater at the summit of the hills near its center, ~700 m above the crater floor (Fig. 4.8c,d). CRISM data indicate that these deposits contain polyhydrated sulfates similar to those identified in the beds ringing the crater walls.

Although I cannot rule out a more complex scenario combining springline tufa

with other sedimentation and diagenetic processes on the Sirenum crater floors, I now turn to a single hypothesis that could account for all aqueous deposits in Columbus crater.

4.8.4 Hypothesis 4: Deep lake(s)

A deep lake filling Columbus crater to at least the level of its preserved sulfate ring could account for sediments deposited on both the crater walls and floor, including the (submerged) hills in Fig. 4.8c. It would explain the lateral continuity and conformability of the intracrater beds, as well as the observed mineralogic sequence of polyhydrated sulfates on the crater walls vs. monohydrated on the floor: the latter would have been precipitated after evaporation or freezing had lowered the lake level and yielded a concentrated brine. The observed alternation of clay vs. sulfate-bearing beds could reflect alternating periods of lake level rise followed by evaporation. Highly localized deposits of jarosite and possibly alunite on the crater floor could have formed during the final stage of lake evolution in shallow ponds of highly concentrated fluid (Fig. 4.6c may show another example of this), and/or via subsequent diagenesis as in the Western Australian acid saline systems [*Benison et al.*, 2007].

Terrestrial saline lakes and playas commonly display "bathtub ring" patterns of evaporite deposition, with less soluble minerals (e.g., carbonates and/or polyhydrated sulfates) precipitating early on the lake margins and soluble salts (e.g., chlorides) later on the lakebed during the final stages of evaporation [e.g., *Baldridge et al.*, 2004]. Chlorides have not yet been identified on Columbus' floor, but this may be due to (1) the lack of diagnostic infrared spectral absorptions for anhydrous chlorides, (2) burial by younger sediments and Early Hesperian lavas, and/or (3) dissolution during later aqueous or diagenetic episodes. Indeed, multiple aqueous episodes in Columbus are suggested by the intimate association of Ca- and Mg/Fe-sulfates in its polyhydrate ring

(section 4.3.3); in a monotonically evaporating lake, Ca-sulfate would be expected to precipitate early, and Mg/Fe-sulfates later at lower a_{H2O} [*Tosca et al.*, 2008a]. The fact that some outcrops in Columbus with gypsum appear as rugged, relatively high-standing masses compared to adjacent outcrops with only Mg/Fe-sulfate (Fig. 4.6b) could indicate that more soluble Mg/Fe-sulfate has been dissolved from the upper beds during a later aqueous episode, leaving relict gypsum. In general, the minerals identified in Columbus agree reasonably well with those predicted by geochemical models to form in a deep lake on Mars [*Altheide et al.*, 2010a], although widespread kaolinite (if precipitated from lake water) and possible alunite suggest greater dissolved aluminum than is typically assumed for Martian solutions.

The minimum ~900 m depth of the hypothesized Columbus paleolake is equivalent to that required by hydrologic modeling (section 4.7) to form evaporite deposits of the thickness (~10–20 m) observed on the crater walls and floor. This could indicate that the lake was flooded to this level only once; alternatively, the lake may have been maintained or refilled if the salinity and/or clastic sediment fraction were lower than assumed in section 4.7. For a crater of Columbus' size, this depth implies a paleolake volume of ~6000 km^3, fractionally larger than Earth's Lake Michigan or the inferred Holden crater paleolake on Mars [*Grant et al.*, 2008], although the depth of the Columbus lake would have been several times greater than either. Assuming evaporation (or freezing and sublimation) as the dominant water loss process, Columbus' greater depth would have given it longer life than the Holden paleolake. For a rough estimate of Martian paleolake lifetime, several authors have assumed terrestrial evaporation rates of ~1–10 m/yr [e.g., *Lewis and Aharonson*, 2006; *Grant et al.*, 2008; *Orofino et al.*, 2009], giving a minimum lifetime of several centuries for Columbus if the lake were filled only once. However, evaporation rates can be lowered by a factor of ~20 for highly concentrated sulfate brines [*Chevrier and*

Altheide, 2008], which could greatly prolong the final stages of lake evaporation.

Alternatively, the hypothesized lake in Columbus crater may have been capped by ice. If the Late Noachian climate was similar to that of modern Mars, the surface of a lake would freeze very rapidly; even if emergent groundwater were initially warm, freezing would occur within a few years [*Kreslavsky and Head*, 2002]. Permafrost conditions might have posed challenges for recharge of the groundwater aquifers inferred to be the main source of lake water, but a relatively thin, latitudinally restricted, and/or temporary permafrost layer would be consistent with the groundwater model. Pure water lakes on modern Mars would freeze to a depth of hundreds of meters, but under (for example) a 300 mbar atmosphere the ice cover could have been only tens of meters thick [*Squyres*, 1989]. Saline water (as inferred from Columbus' sulfates) would remain liquid at lower temperature, allowing thinner ice in any climate. Water would be lost via ice sublimation at rates typically ~10–100 times slower than evaporation of liquid water [*McKay et al.*, 1985; *Squyres*, 1989], although these rates are strongly temperature-dependent. Detailed thermal models of lakes initially ~1000 m deep yield estimated lifetimes of ~10^5–10^6 years under present Martian conditions [*Moore et al.*, 1995; *Rivera-Valentin et al.*, 2010]; of course, Noachian Mars could have been quite different [e.g., *Craddock and Howard*, 2002].

A deep lake in Columbus crater could have produced concentrated near-shore deposits of sulfate-bearing sediment in several ways. On Earth, lacustrine tufas form near the margins of large, deep lakes; *Zimbelman et al.* [2009] have noted the potential utility of such tufas for identifying the level of Martian paleo-shorelines. On Earth these structures (sometimes termed "freshwater reefs") appear to be largely biogenic in origin [*Pedley*, 1990], but abiotic salt precipitation may also be enhanced in shallow water near the shore. In Columbus, crater wall profiles (Fig. 4.4) typically have surface slopes <10° at the elevation of the sulfate ring and up to 20–30° below this

level. Evaporites may have accumulated on a shallow-water topographic "platform" here when the lake level was just above this point. Greater input of clastic sediment along the lake margins (e.g., from mass wasting or slope wash off the steep upper crater walls) may also have led to thicker and/or more resistant deposits forming there. This effect would have been strongest if the lake were ice-covered: many lakes in the Antarctic dry valleys experience summer melting in a narrow "moat" around the lake margins [e.g., *Nedell et al.*, 1987]. Evaporation (and evaporite deposition) would then be limited to this melted zone. Of course, some light-toned layered deposits did also form on Columbus' central floor, but they have been largely eroded (Fig. 4.26a) and/or buried by lava and other materials (e.g., Fig. 4.24b).

Historically, large paleolakes on Mars have been identified almost exclusively via morphologic criteria, such as inlet or outlet channels, fan/delta deposits, and/or possible shoreline features such as wave-cut terraces [e.g., *Cabrol and Grin*, 1999; *Fassett and Head*, 2008b]. For Columbus crater (and possibly some of the neighboring craters) I propose a groundwater-fed lake, which would not require inlet channels or deltas. As for shorelines, where these have been identified previously on Mars, this interpretation is generally not unique [e.g., *Malin and Edgett*, 1999; *Leverington and Maxwell*, 2004]. Furthermore, laboratory experiments [*Lorenz et al.*, 2005] and modeling results [*Kraal et al.*, 2006] suggest that waves needed for shoreline development could not form in the tenuous atmosphere of modern Mars. And if the hypothesized lake in Columbus crater was covered by ice, then terrestrial polar beach analogs suggest that many traditional shoreline morphologies would never have developed [*Rice*, 1994]. Ice-push ramparts might have developed at the lake margins, but these are rarely preserved in paleolakes [*Gilbert*, 1890, p. 72]. Even if beach morphologies were once more apparent in Columbus crater, they have been attacked by gradational processes for over three billion years. The best-preserved

evidence for Noachian/Hesperian paleolakes may therefore be mineralogic rather than morphologic in some cases.

4.8.5 Astrobiological implications

If a deep, groundwater-fed paleolake did exist in Columbus crater—or anywhere else on ancient Mars—then such an environment may have been promising for habitability and fossilization of prospective Martian life forms. The detection of gypsum in Columbus crater indicates a high water activity during part of its aqueous history. Temperatures might have been low, but hypersaline environments on Earth host organisms capable of growth at temperatures below 0°C [*Niederberger et al.*, 2010]. The acid saline lakes in Western Australia to which I have appealed as possible mineralogic analogs are not only inhabited, but contain diverse microbial populations [*Mormile et al.*, 2009]. These lakes preserve microfossils and organic matter within crystals of gypsum and halite [*Benison et al.*, 2008], and similar preservation has been observed in Mg-sulfate crystals precipitated from groundwater-fed lakes in British Columbia [*Foster et al.*, 2010].

The thick ice covers that may have been present on Martian paleolakes would have presented a challenge for photosynthetic life, as opaque aeolian materials accumulating on the ice would substantially reduce light flux into the lake. Under this scenario, chemosynthetic life may have been more plausible in Martian paleolakes, and from this perspective groundwater-fed lakes may be more promising than those fed by surface runoff. In Earth's Lake Huron, for example, redox gradients between oxygenated lake water and anoxic waters emergent from sinkhole plumes are exploited by sulfate-reducing chemoautotrophs living at depths of <100 m [*Biddanda et al.*, 2006]. Redox gradients between groundwater and the surface/atmosphere have been proposed for ancient Mars [*Hurowitz et al.*, 2010], and terrestrial experience suggests that the interface between these two volatile reservoirs can be a source of

chemical energy for life.

4.8.6 Future investigations

Future work will enable additional tests of the hypotheses described above. The Mars Odyssey spacecraft has recently transitioned to an early afternoon orbit that will enable higher-SNR observations for THEMIS, potentially yielding stronger constraints on the mineralogy of light-toned deposits in Columbus and other Sirenum craters. Expanded CRISM coverage may also lead to the identification of additional minerals; this is especially true for the nine craters other than Columbus and Cross craters marked in Fig. 4.27, which have minimal coverage to date. The work described here has focused strongly on Columbus crater but has benefited greatly from consideration of the regional context. Future orbital studies of comparable detail focused on craters such as Dejnev or crater E (Fig. 4.27) may lead to evolution of some interpretations made here. Ongoing geochemical and physical modeling of Columbus crater [*Altheide et al.*, 2010a; *Rivera-Valentin et al.*, 2010] will further inform these interpretations.

Many questions about the deposits in Columbus crater could be most effectively answered by a landed mission. High-resolution imaging on the surface could resolve sedimentary textures, stratigraphic contacts and mineralogic boundaries, providing new insights into the depositional and diagenetic history of the light-toned layered deposits. The diverse secondary minerals identified from orbit would allow a rover or sample return mission to probe a range of chemical conditions and explore variations in ancient habitability over space and time.

More broadly, the mere possibility that Columbus crater once hosted a groundwater-fed lake highlights the value of mineralogy for identifying Martian paleolakes. Previous studies have focused on morphologic indicators such as channels and deltas that may provide more definitive evidence for ponded water, but which

cannot be used to identify groundwater-fed paleolakes. As the CRISM global mapping dataset nears completion, broader searches for evaporites in paleolakes will be possible. Exploring the range of evaporites in Martian paleolakes could reveal not only how lake chemistry varied in space and time, but it may also constrain the composition of the ancient Martian atmosphere [e.g., *Moore et al.*, 2010].

CHAPTER 5

OPPORTUNITY FOR GROUND TRUTH[*]

5.1 Introduction

Orbital detection of an alteration mineral (crystalline gray hematite) guided the Mars Exploration Rover (MER) Opportunity to its landing site in Meridiani Planum [*Christensen et al*., 2000; *Golombek et al*., 2003]. Within weeks of landing there, rover measurements revealed that both the hematite and abundant sulfates had formed in sedimentary rocks that were diagenetically altered—and in some cases deposited—in an aqueous environment [*Squyres et al.*, 2004b]. Orbital detection of hydrated sulfates in northern Meridiani—although not in the hematite-bearing plains sampled by Opportunity—suggested this aqueous environment was regionally extensive [*Arvidson et al*., 2005]. But this environment was characterized by low pH and low water activity, suggested to be significant challenges for habitability on Mars [*Tosca et al.*, 2008a]. All bedrock examined by the rover to date likely formed under a similar range of conditions, spanning a small fraction of Martian history [*Squyres et al.*, 2006b; 2009].

Elsewhere on Mars, as discussed in the preceding chapters, phyllosilicates have been detected in orbital near-infrared spectra. The observed phyllosilicates typically form under neutral to alkaline conditions [*Chevrier et al*., 2007], and on Mars they are hypothesized to reflect an early period of more abundant water and possibly more habitable conditions than existed during the period when sulfates formed [*Bibring et al*., 2006a]. However, much remains unknown about the context of phyllosilicate formation: whether wet conditions were persistent or transient, at the

[*] Much of the work described herein was originally published by Wray, J. J., et al. (2009), Phyllosilicates and sulfates at Endeavour Crater, Meridiani Planum, Mars, *Geophys. Res. Lett., 36*, L21201, doi:10.1029/2009GL040734.

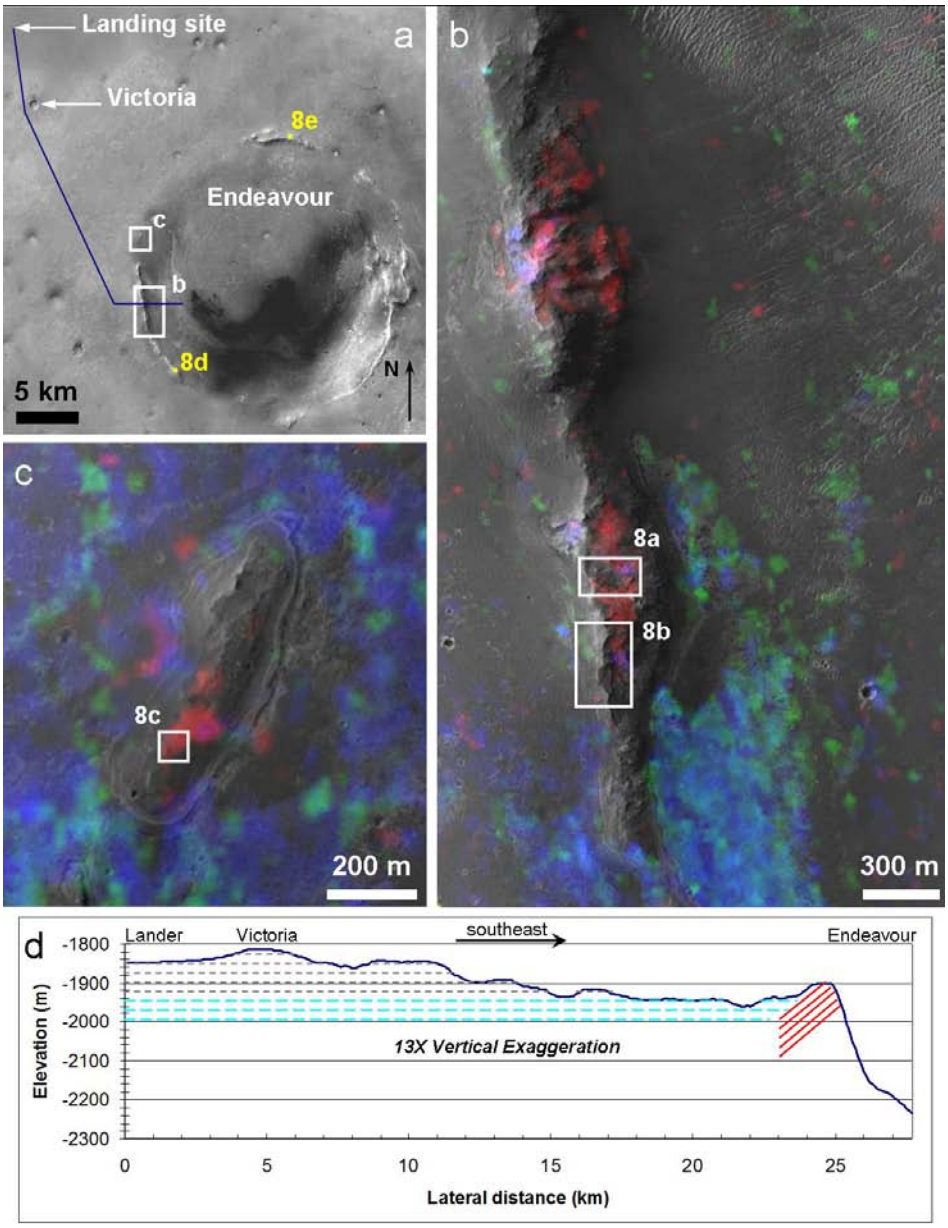

Figure 5.1: (a) CTX image mosaic of Endeavour crater (2.3°S, 5.2°W) and surroundings, with boxes outlining subsequent figures. Blue line indicates profile in (d). (b–c) Distribution of Fe/Mg-phyllosilicates (red) and polyhydrated sulfates (cyan) in CRISM spectral parameter maps (b=FRT00008541, c=FRT0000CE1D) overlain on HiRISE PSP_010486_1775. Red=D2300, green=SINDEX [*Pelkey et al.*, 2007], blue=BD1900H [*Ehlmann et al.*, 2009]. Mapped band depths are typically 0.4–1.1% for D2300 and BD1900H, 0.6–1.8% for SINDEX. (d) Median-filtered elevation profile (transect shown in (a); from HRSC h1183_0000 digital elevation model, relative to spheroid) and hypothesized stratigraphy, with sub-horizontal hematitic plains layers (gray, short dashes) overlying layers with hydration signature (cyan, long dashes), which onlap tilted phyllosilicate-bearing layers (red lines) exposed in Endeavour rim.

surface or beneath it, and whether the observed phyllosilicates formed *in situ* or have been redistributed by sedimentary and impact processes. Mineral abundances are difficult to constrain from near-infrared spectra, and additional phases in the phyllosilicate-bearing rocks remain largely unidentified [e.g., *Milliken et al*., 2009]. Ground truth would significantly advance understanding of Martian phyllosilicates and is a major goal of future landed missions [e.g., *Grotzinger*, 2009].

This chapter reports the orbital identification of both phyllosilicates and hydrated sulfates in outcrops that may be accessible by Opportunity. The rover is driving southward from Victoria crater toward the much larger (20 km diameter) Endeavour crater (Fig. 5.1a). Endeavour crater was largely buried by the Late Noachian to Early Hesperian sulfate-rich sediments studied by the rover to date, and therefore its formation predates these sediments [*Arvidson et al*., 2006]. Segments of its eroded rim protrude above the sediments, exposing ancient strata. MRO data are used to investigate the mineralogy and morphology of the exposed Endeavour rim segments and the adjacent plains sediments.

5.2 Spectral Analysis

CRISM hyperspectral data were processed as described in section 2.1, but using an updated atmospheric correction [*McGuire et al*., 2009] and a spatial and spectral noise filtering procedure developed by *Parente* [2008].

5.2.1 Phyllosilicates

Spectra of portions of the Endeavour crater rim contain absorption bands diagnostic of phyllosilicates (Fig. 5.2a). In particular, bands at ~1.9, 2.3, 2.4 μm and a weaker feature at 1.4 μm are characteristic of Fe/Mg-smectite clays [e.g., *Bishop et al*., 2002b]. Higher Mg content shifts the wavelength of the 2.3 μm band, from ~2.28 μm in Fe^{3+}-rich dioctahedral nontronite to ~2.31–2.32 μm in Mg-rich trioctahedral

saponite [*Swayze et al.*, 2002]. The positions of the 2.3 and 2.4 μm bands in Endeavour rim spectra are intermediate between those of nontronite and saponite, suggesting that both Fe and Mg are present, similar to other smectite occurrences on Mars [e.g., *Bishop et al.*, 2008b].

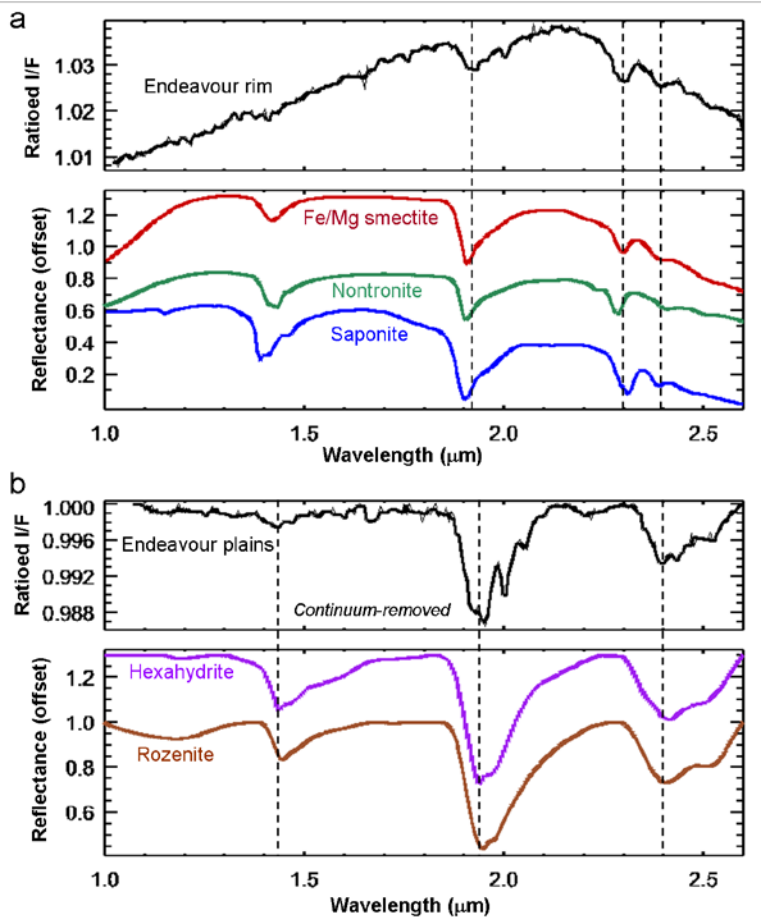

Figure 5.2: Ratio spectra from CRISM FRT00008541 (top, bold lines median-filtered) and lab spectra (bottom, vertically offset for clarity). Small features near 1.65 and 2.0 μm in CRISM spectra result from a filter boundary and from imperfect removal of atmospheric CO_2 bands, respectively. (a) Endeavour spectrum is 232-pixel average from rim segments in Fig. 5.1b. Fe/Mg smectite (scaled x8) is sample GDS759A from Flagstaff Hill, CA (courtesy G. Swayze). Nontronite is sample NG-1 from the Clay Minerals Society, Source Clays Repository (spectrum NBJB26 in CRISM spectral library). Saponite is SapCa1.AcB from USGS spectral library [*R. Clark et al.*, 2007]. (b) Spectra were continuum-removed in ENVI to eliminate an artificial slope resulting from the use of spectral ratios. Endeavour spectrum is 562-pixel average from plains adjacent to rim segments in Fig. 5.1b. Hexahydrite ($MgSO_4 \cdot 6H_2O$) is LASF57A and rozenite ($FeSO_4 \cdot 4H_2O$) is BKR1JB626B from CRISM spectral library.

In comparison to laboratory spectra of terrestrial smectite samples, the Endeavour rim spectrum has a weak 1.9 μm band relative to its 2.3 μm band (Fig. 5.2a), possibly due to dehydration under Martian atmospheric conditions [*Bishop and Pieters*, 1995; *Milliken and Mustard*, 2005]. Mixing with other components and/or rock coatings could also weaken the bands at 1.9 and especially 1.4 μm relative to pure lab samples, as Fe-minerals in coatings can dominate spectra shortward of ~2 μm, but become more transparent at longer wavelengths [*Swayze*, 2004]. Additional hydrated phase(s) with bands at 1.92–1.98 μm, such as hydrated salts or zeolites [*Crowley*, 1991; *Cloutis et al*., 2006], could account for the 1.9 μm band minimum occurring at a slightly longer wavelength than that observed in lab spectra of pure phyllosilicates.

CRISM FRT 8541 (Fig. 5.2a) is the highest-SNR observation of the rim segments in Fig. 5.1b, Cape Tribulation and Cape Byron [*Arvidson et al.*, 2011], but consistent spectral results are obtained from other CRISM observations covering this area (HRL D09A and FRTs CE1D, 11A38). FRT 8541 does not cover the Endeavour rim segment—informally known as Cape York—that is nearest Opportunity's current position. However, a spectrum of Cape York from HRL D09A has a 2.3 μm absorption that appears similar to (though weaker than) those in spectra from the phyllosilicate-bearing portions of the western rim (Fig. 5.3). Cape York, therefore, also appears to contain Fe/Mg-phyllosilicate, although here it cannot be identified specifically as smectite.

Fig. 5.1b suggests possible spatial variations in the strength of phyllosilicate signatures and/or the strength of hydration in these phyllosilicates across Cape Tribulation and Cape Byron. However, comparison of overlapping CRISM observations here shows only partial repeatability (Fig. 5.4a,b), implying that the apparent spatial patterns are at least partly due to noise. For further comparison,

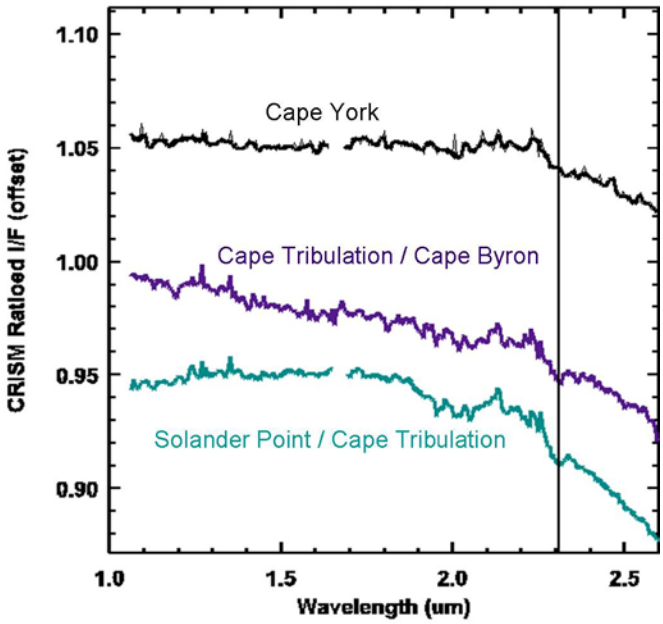

Figure 5.3: Spectra from CRISM HRL D09A. Cape York spectrum has 2.3 µm feature consistent with those observed on rim segments with confirmed Fe/Mg-phyllosilicates (cf. Fig. 5.2a).

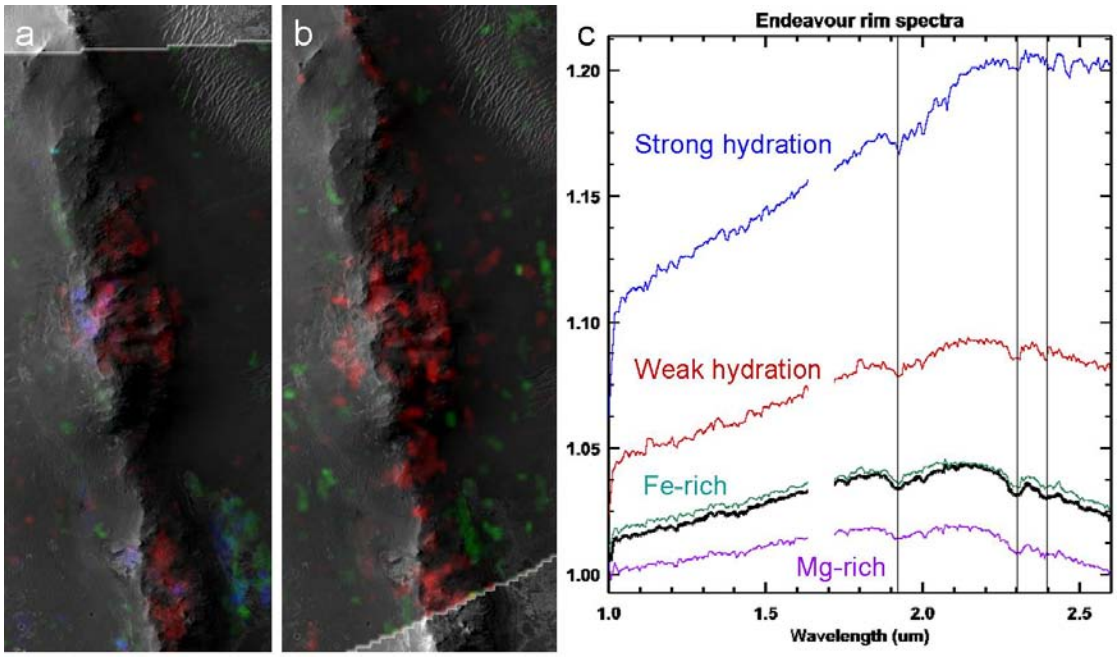

Figure 5.4: (a–b) Distribution of phyllosilicates (red) and hydrated sulfates (green/blue) from CRISM spectral parameter maps (a=FRT 8541, b=FRT CE1D) overlain on HiRISE PSP_010486_1775. (a) is similar to Fig. 5.1b. (c) Little spectral variation is evident among the clay-bearing portion's of Endeavour's western rim. These ratios from CRISM FRT 8541 all use the same spectral denominator; black spectrum is that shown in Fig. 5.2a.

spectra were extracted from rim locations mapped as especially strongly hydrated (using the BD1900H parameter of *Ehlmann et al.* [2009]) vs. less hydrated, and locations mapped as more Fe-rich phyllosilicates (using the BD2290 parameter of *Pelkey et al.* [2007]) vs. more Mg-rich. All of these spectra exhibit bands at 1.92, 2.3 and 2.4 μm, with no significant variation in relative band strengths (Fig. 5.4c). In summary, the existing orbital spectra show no direct evidence for compositional variation in the phyllosilicates of Endeavour crater.

5.2.2 Hydrated sulfates

Spectra of the plains adjacent to the western Endeavour rim segments (Figs. 5.1b,c) contain an absorption band at ~1.9 μm and an inflection at ~2.4 μm characteristic of polyhydrated sulfates (Figs. 5.2b, 5.5). In particular, laboratory spectra of Mg-sulfates such as hexahydrite ($MgSO_4 \cdot 6H_2O$) are consistent with the Endeavour plains spectra, although other sulfate cations such as Fe^{2+} or Fe^{3+} cannot be ruled out. An additional weak feature at ~2.2 μm could reflect a contribution from another hydroxyl-bearing mineral; candidates include gypsum (compare spectra in Fig. 4.13) and/or hydrated silica (compare Fig. 4.33a). Although the ~2.4 μm inflection has been attributed at least in part to an S–O overtone absorption [*Cloutis et al*., 2006], some hydrated minerals other than sulfates do have similar features in this spectral region [e.g., *Crowley*, 1991]. Nevertheless, Opportunity results indicate that abundant Mg-sulfate is present in nearby Meridiani plains outcrops [*Squyres et al.*, 2006b and references therein], supporting its identification in the CRISM spectrum in Fig. 5.2b.

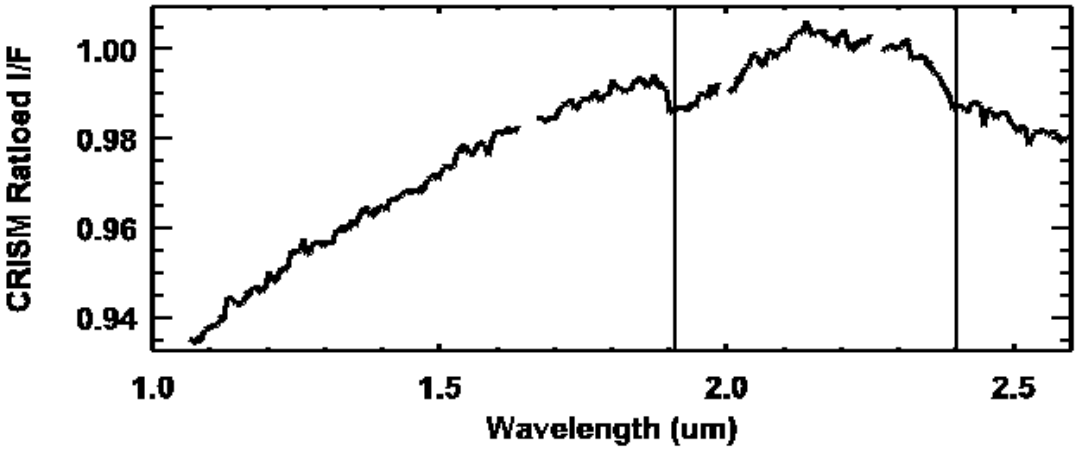

Figure 5.5: Spectral average of 919 CRISM pixels from plains surrounding Cape York, showing absorptions at 1.9 and 2.4 μm consistent with polyhydrated sulfates (FRT CE1D).

Polyhydrated sulfate has previously been identified several hundred kilometers to the northeast in Sinus Meridiani [*Griffes et al.*, 2007; *Poulet et al.*, 2008a; *Wiseman et al.*, 2010], but the first sulfate detected from orbit in this region was monohydrated [*Arvidson et al.*, 2005]. The fresh *D*~2.2 km crater Ada in southeast Meridiani Planum exposes bright outcrop along its upper walls (Fig. 5.6) with a texture similar to that of monohydrated sulfates elsewhere on Mars, and a new CRISM observation confirms monohydrated sulfate in Ada's bright layer (Fig. 5.7). A darker, resistant layer is exposed lower on Ada's walls (Fig. 5.6), but CRISM spectra from this layer reveal no strong mineralogic signature. The plains surrounding Ada contain polyhydrated sulfate, but from CRISM's limited coverage it is unclear whether the polyhydrate is widespread or confined to Ada's ejecta; therefore the pre-impact stratigraphy of the two sulfate types is presently unknown. Ada crater is fully ~140 km from Opportunity's current position, but indicates that monohydrated sulfate is present within the hematite-bearing plains unit explored by the rover [e.g., *Arvidson et al.*, 2006]. If this monohydrate is widespread, then it might be found along the rover traverse in ejecta blocks from other young craters nearer the rover. Although such

blocks may be friable, those on Ada's rim (Fig. 5.6) have apparently withstood erosion for ~50,000 years [*Golombek et al.*, 2010].

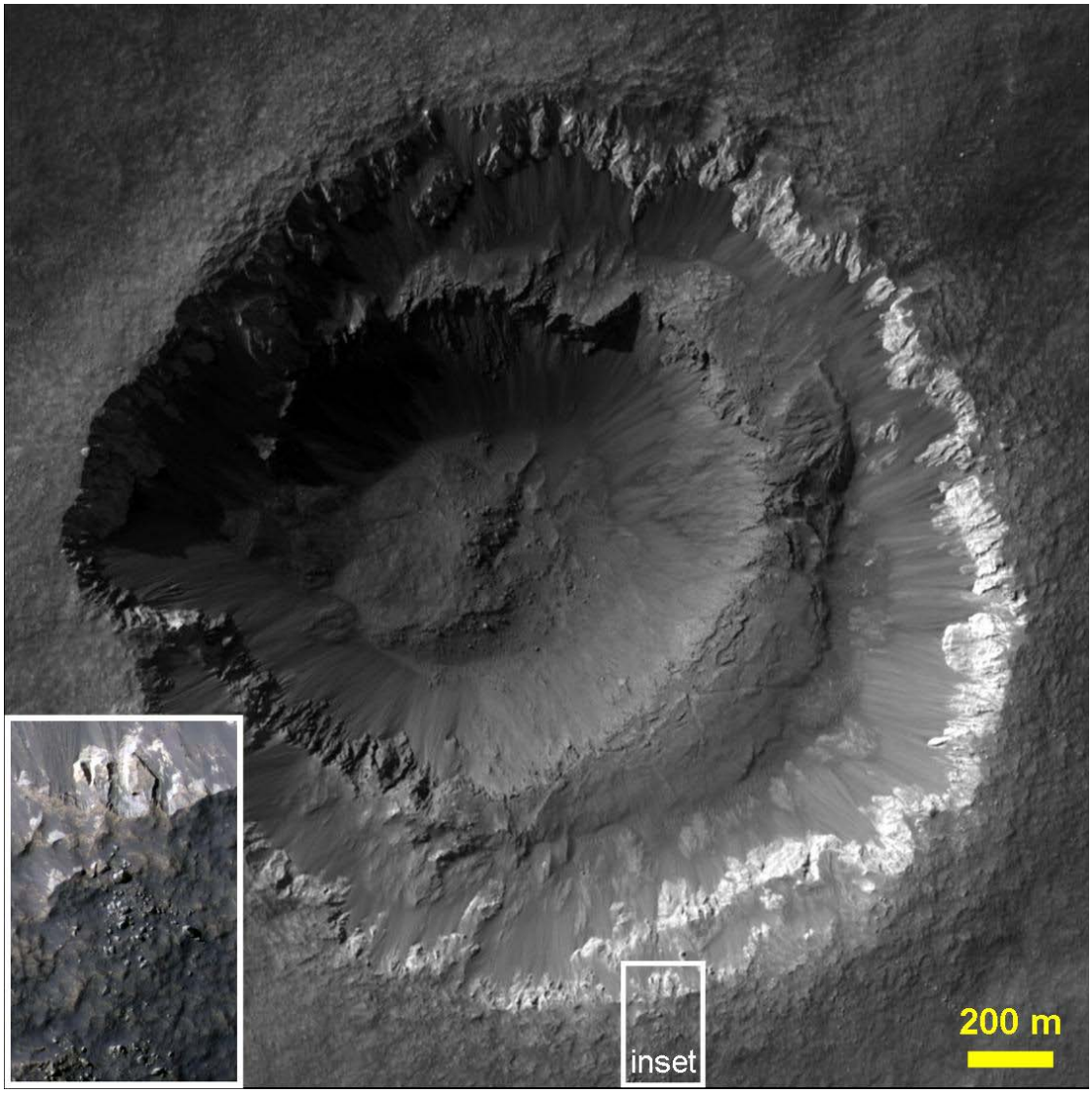

Figure 5.6: Ada crater in southeast Meridiani Planum, ~140 km east/southeast of Opportunity. Bright layer exposed in upper wall contains monohydrated sulfate. Inset shows sample of light-toned blocks on proximal ejecta, just south of crater rim crest. From HiRISE PSP_001348_1770.

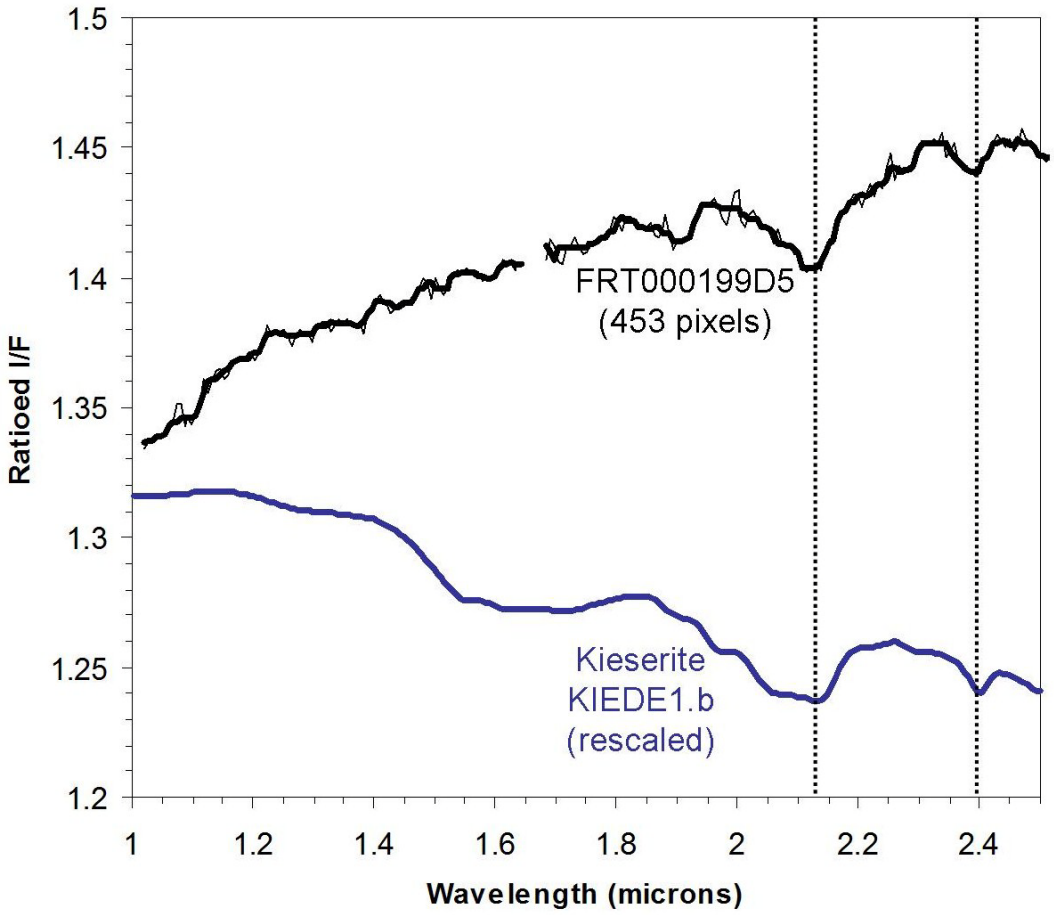

Figure 5.7: Ratioed spectral average over light-toned layer exposed in upper walls of Ada crater, with laboratory spectrum of kieserite ($MgSO_4 \cdot H_2O$) from *R. Clark et al.* [2007] for comparison.

5.3 Morphology and Stratigraphy

HiRISE images of the phyllosilicate-bearing crater rim segments reveal layering and a range of polygonal textures (Fig. 5.8a), similar to other phyllosilicate-bearing outcrops in Meridiani [*Wiseman et al.*, 2008; *Marzo et al.*, 2009] and many other locations on Mars (e.g., chapter 2). Stereo views (Fig. 5.8b) show that layers within the western rim dip away from the crater interior, as expected if the beds predate Endeavour crater and were back-tilted by the impact. In contrast, bright layers

bounding many Endeavour rim segments (Fig. 5.9) appear to dip down toward the crater interior [Fig. 29 of *McEwen et al*., 2010]; it is unclear from orbital images whether these rim-bounding layers predate or postdate the Endeavour impact.

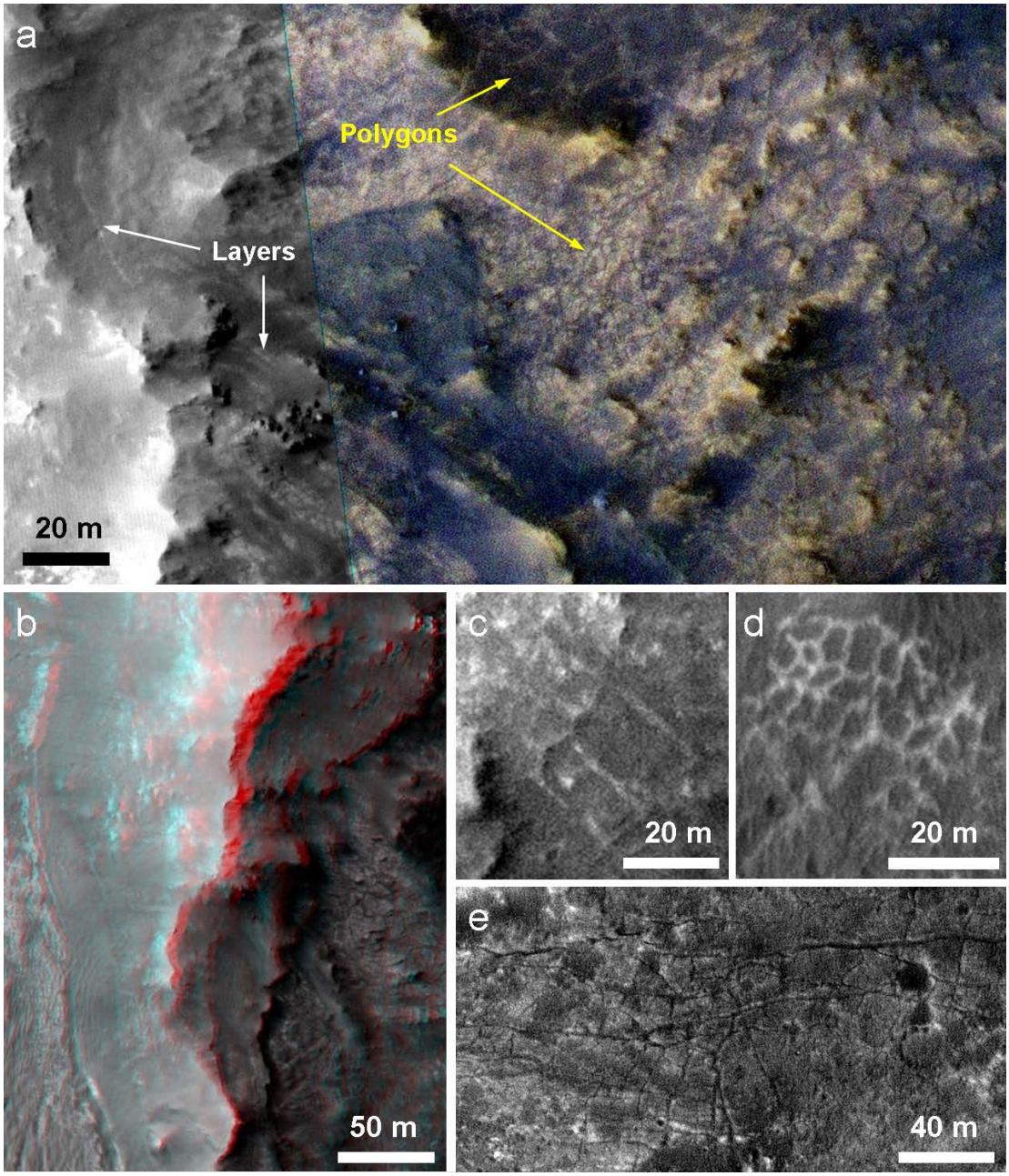

Figure 5.8: Fine-scale textures of phyllosilicate-bearing rim materials, illuminated from lower left. (a) Western rim; enhanced color from HiRISE ESP_012398_1775, grayscale from PSP_010486_1775. (b) Western rim anaglyph; PSP_010341_1775/ PSP_010486_1775. Light-toned materials in lower left are sulfate-bearing sediments inferred to onlap the rim. (c) Northwest rim; PSP_010486_1775. (d) Southwest rim; PSP_010341_1775. (e) Northern rim; ESP_013044_1775.

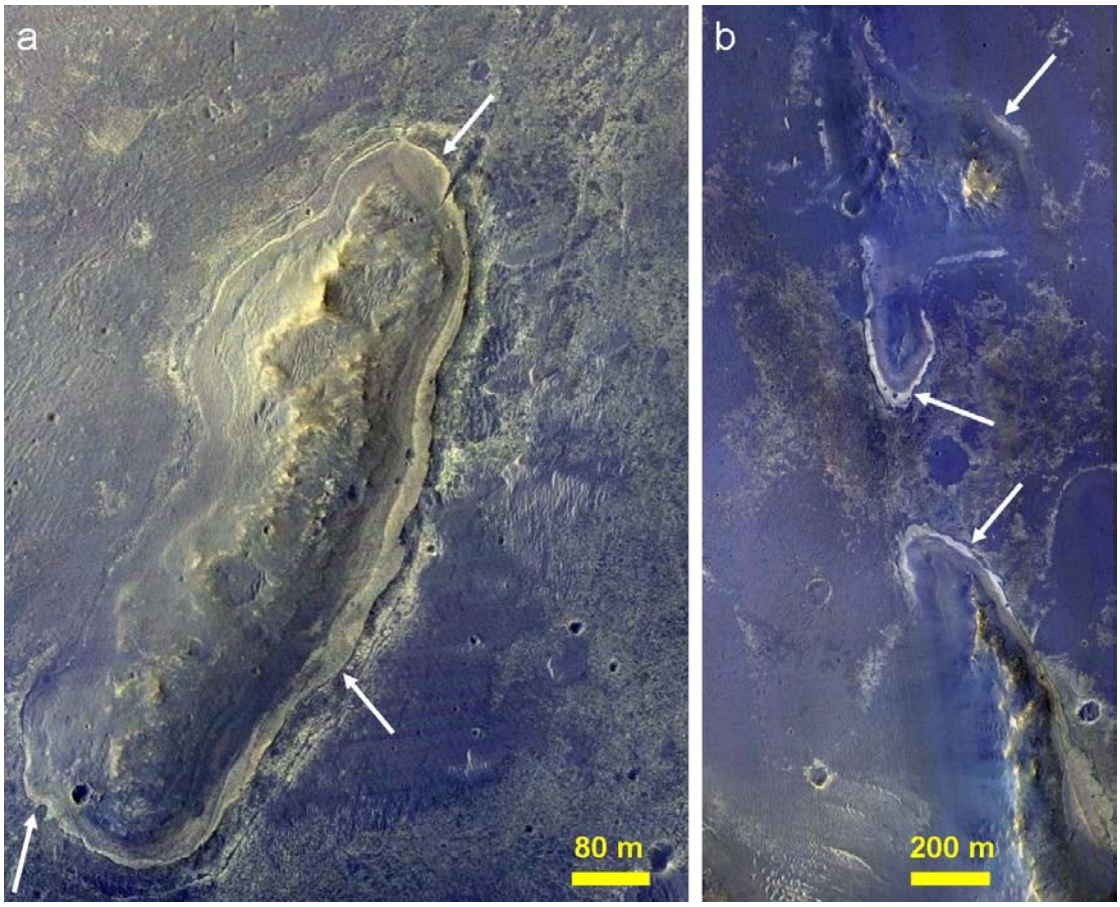

Figure 5.9: Bright layers (arrows) bounding Endeavour crater rim segments. (a) Cape York, the portion of the northwest rim nearest Opportunity (HiRISE ESP_012398_1775). (b) Eastern rim of Endeavour (ESP_012477_1775).

Polygonal patterns are observed on bedrock exposures in all segments of the rim imaged to date (e.g., Figs. 5.8c–e). Cape York (Fig. 5.8c) and Cape Tribulation (top of Fig. 5.8a) have decameter-scale polygons bounded by bright rims, reminiscent of some chlorite- and prehnite-bearing surfaces in the Nili Fossae region [Fig. 21F of *Ehlmann et al.*, 2009]. Other fracture patterns are reminiscent of surfaces around Mawrth Vallis, including some locations where sparse linear fractures are observed instead of dense polygons (Fig. 5.10). The presence of these patterns virtually everywhere that rim bedrock is exposed suggests that the bedrock is pervasively altered. Indeed, portions of the crater rim that lack phyllosilicate signatures appear to be soil-covered areas rather than exposures of unaltered bedrock (Fig. 5.11). The

diversity of textures in Figs. 5.8 and 5.10 likely reflects diversity in composition and/or physical properties of the Endeavour rim materials.

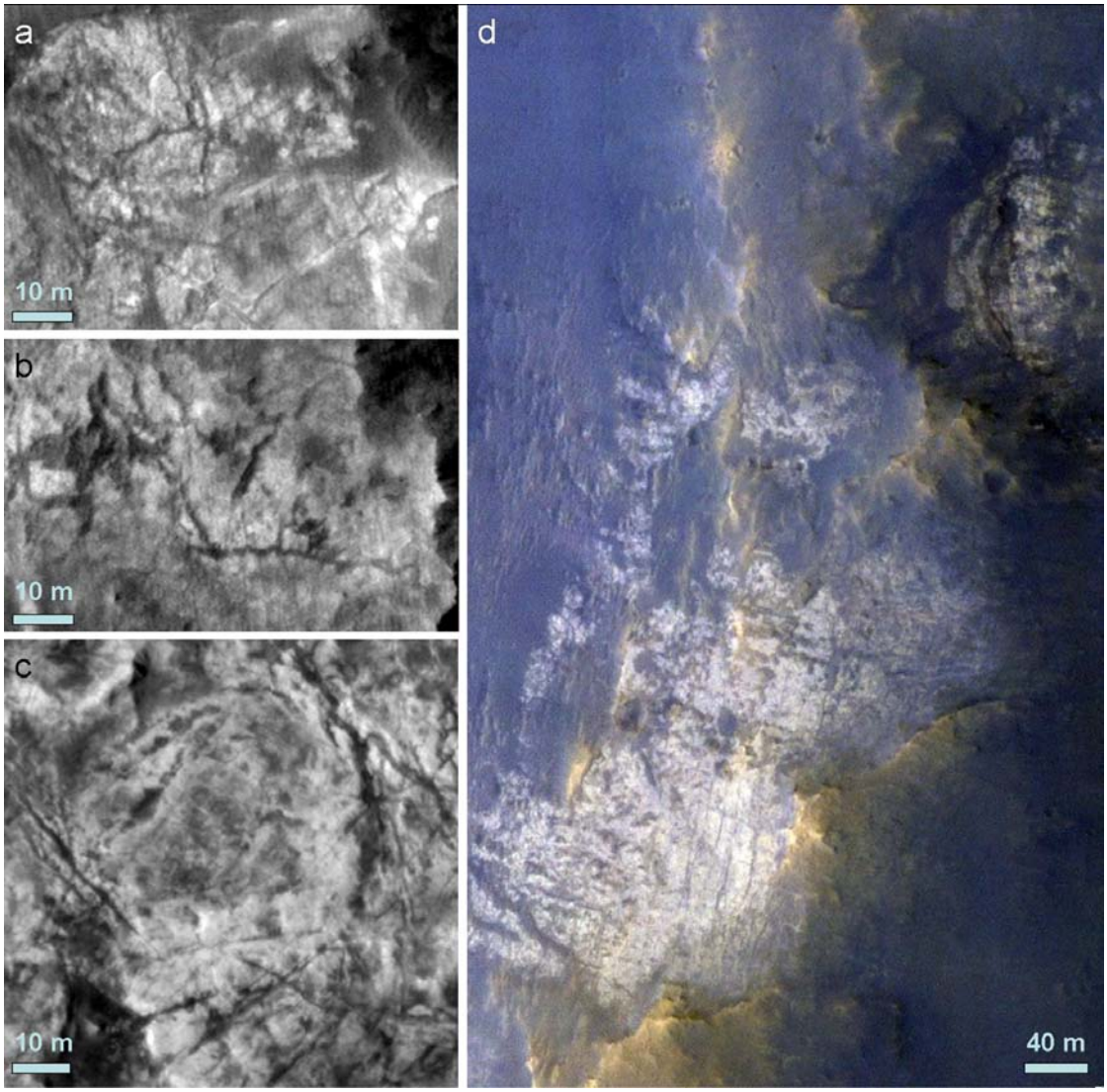

Figure 5.10: Fractures in light-toned rocks of Endeavour rim (a–b; HiRISE PSP_010486_1775) compared to Mawrth Vallis (c; PSP_002140_2025). (d) Light-toned rocks exposed in eastern rim of Endeavour crater (ESP_012477_1775). This outcrop has a 1.9 µm hydration band in CRISM spectra (FRT 11C15), but low SNR prevents determination of specific mineralogy.

As with the traverse to Victoria crater [*Squyres et al*., 2009], the traverse to Endeavour involves an elevation change, in this case ~100 m downward and thus possibly down-section (Fig. 5.1d). The detection of hydrated sulfates in the lower-

elevation plains adjacent to Endeavour may be stratigraphically consistent with their detection in the Meridiani "etched terrains" underlying the hematitic plains [*Arvidson et al.*, 2005]. On the other hand, *Wiseman et al.* [2010] have recently inferred that the latter hydrated sulfates unconformably overlie older etched terrain deposits and could possibly postdate the hematitic plains. At Endeavour crater, orbital images (e.g., Fig. 5.8b) suggest that the sulfate-bearing plains onlap the crater rim segments [*Arvidson et al.*, 2006], leading to the hypothesized, simplified stratigraphy shown in Fig. 5.1d. These interpretations can be tested and refined by rover observations.

Figure 5.11: Portion of Endeavour western rim (north end of Cape Tribulation in Fig. 5.4a,b) lacking clay spectral signature, which appears to be covered by fine-grained material (note smooth texture and bedforms). From HiRISE PSP_010486_1775.

5.4 Discussion

As with the crystalline gray hematite in Meridiani Planum, obtaining ground truth on both phyllosilicates and hydrated sulfates identified from orbit would allow a

more refined evaluation of what these mineral detections imply about environmental conditions on ancient Mars. For example, definitive identification of hydrated sulfate cations is difficult using near-infrared spectroscopy (e.g., Fig. 5.2b), but possible with Opportunity's Athena science payload [*Squyres et al.*, 2003]. Hydrated Fe^{3+}-sulfates could be directly detected by the Mössbauer spectrometer, as Spirit has done in the Columbia Hills [*Morris et al.*, 2006a]; hydrated Fe^{2+}-sulfates are also detectable and were initially inferred from Spirit Mössbauer data by *Lane et al.* [2004], but are ruled out there by chemical trends, stoichiometry, and infrared spectroscopy—see *Morris and Klingelhöfer* [2008]. Other sulfate cations could be inferred from Alpha Particle X-Ray Spectrometer (APXS) data, which implicate Mg- and Ca-sulfates in Meridiani outcrops studied to date based on chemical trends and on stoichiometry, respectively [*Clark et al.*, 2005]. Hydration state of sulfates can be somewhat constrained by photon scatter peak intensities from APXS [*Campbell et al.*, 2008], Pancam spectral data [*Johnson et al.*, 2007; *Rice et al.*, 2010], and—for Fe-sulfates—detailed consideration of the Mössbauer parameters for different sulfates [*Yen et al.*, 2008]. The Miniature Thermal Emission Spectrometer (Mini-TES) has illuminated Meridiani outcrop hydration in the past [*Glotch et al.*, 2006], but as of this writing two persistent problems with Opportunity's Mini-TES prevent further mineralogic observations [*Arvidson et al.*, 2011]. Regardless, hydration is widespread across Meridiani [e.g., *Gendrin et al.*, 2005], but H_2O or OH-related absorptions are not observed in OMEGA or CRISM spectra at the locations sampled by Opportunity to date [*Arvidson et al.*, 2006; *Poulet et al.*, 2008a]. Abundant hydroxylated and possibly hydrated sulfates exist at these locations [e.g., *Squyres et al.*, 2006b], but may be spectrally masked by effects such as surface dehydration and coatings. Rover measurements of the polyhydrated sulfates at Endeavour crater could provide insight into the relative importance of such outcrop characteristics vs. absolute mineral abundances or

hydration states in controlling the band strengths observed from orbit.

Ground truth for Endeavour's phyllosilicates could be even more illuminating. Fe/Mg-smectites are the most commonly detected phyllosilicates on Mars [e.g., *Bibring et al*., 2006a; *Mustard et al*., 2008]. They have been identified elsewhere in Meridiani [*Poulet et al*., 2008a; *Wiseman et al*., 2008, 2010; *Marzo et al.*, 2009] and more broadly in western Arabia Terra, in scattered outcrops stretching northward to the extensive exposures around Mawrth Vallis [*Poulet et al*., 2005; *Bishop et al*., 2008b; *Noe Dobrea et al.*, 2010]. The Fe/Mg-smectites in the rim of Endeavour crater may therefore record a process of regional (or larger)-scale aqueous alteration distinct from any yet sampled by a landed mission. It has been suggested that the correlation of remotely sensed phyllosilicates to Early–Mid Noachian terrains and hydrated sulfates to Late Noachian–Hesperian terrains reflects a global change in aqueous conditions, with decreasing pH and water activity, and a corresponding decline in the planet's habitability over time [*Bibring et al*., 2006a]. Endeavour crater may represent the first opportunity to test this hypothesis *in situ*.

Cape York, the closest point on the rim of Endeavour (Fig. 5.1c), exposes bedrock with polygonal textures (Fig. 5.8c) and a tentative phyllosilicate signature (Fig. 5.3). If Opportunity reaches this location with its payload still largely functional, the Mössbauer spectrometer will likely provide the best opportunity for independent confirmation of Fe-bearing phyllosilicates. Three different forms of structural iron would be detectable: Fe^{2+} or Fe^{3+} in octahedral coordination or Fe^{3+} substituting for Si in tetrahedral coordination [e.g., *Rancourt*, 1994]. The CRISM spectra (Fig. 5.2a) indicate octahedrally coordinated Fe, but do not constrain its oxidation state nor whether tetrahedral Fe^{3+} is also present.

For octahedral Fe^{3+}, the Mössbauer spectral parameters for phyllosilicates may not be unique: the isomer shift (IS) is typically ~0.35–0.45 mm/s and quadrupole

splitting (QS) ranges from ~0.45 to 1.0 mm/s [e.g., *Dyar and Schaefer*, 2008]. This range largely overlaps with the nanophase ferric oxide (QS~0.7–1.1) and "Fe3D3" (QS~0.5–0.7) phases previously identified by Opportunity [*Klingelhöfer et al.*, 2004; *Morris et al.*, 2006b]; the latter has been interpreted generically as a ferric oxide/hydroxide/oxysulfate or a phyllosilicate. Natural clay samples often contain associated ferric oxides, which can be adsorbed to interlayer surfaces [*Bishop et al.*, 1993], and distinguishing Fe^{3+} in clays vs. oxides may be impossible using Mössbauer spectra alone [*Murad and Wagner*, 1989]. However, Fe-rich clays can also have Fe^{3+} in tetrahedral sites, producing a distinctive doublet with IS~0.20 [*Dyar and Schaefer*, 2008]—or possibly up to 0.31 in nontronite [*Goodman et al.*, 1976]—significantly lower than the IS in any phase identified to date by either rover [*Morris et al.*, 2006b, 2008]. (Fuzzy Smith in the Columbia Hills had IS~0.28, but its QS~0.68 was significantly higher than the ~0.5 expected for phyllosilicates).

For Fe^{2+}-phyllosilicates, IS~1.1–1.2 is comparable to that of olivine and pyroxene, but QS~2.4–2.9 [e.g., *Pollak and Stevens*, 1986; *Dyar et al.*, 2008] falls between that of olivine (~3.0) and typical pyroxene (~2.1–2.2). The "Fe2D2-B" phase found by Spirit in some rocks of the Columbia Hills, with IS~1.16 and QS up to 2.45, was indeed noted to be consistent with an Fe^{2+} alteration phase (e.g., a phyllosilicate) [*Wang et al.*, 2006; *B. Clark et al.*, 2007; *Morris et al.*, 2008]; however, the lack of corroborating evidence for phyllosilicates in Mini-TES spectra may favor the alternative interpretation of Fe2D2-B as pyroxene. At Endeavour crater, where corroborating evidence for phyllosilicates is provided by CRISM, similar Mössbauer parameters could plausibly be attributed to Fe^{2+} in phyllosilicates.

In summary, the prospects for uniquely confirming Fe-phyllosilicates with Mössbauer depend on the form of the Fe, as well as the chemistry of neighboring sites in the phyllosilicate crystal structure. *Bishop et al.* [2007] note that definitive clay

mineralogy (beyond the Fe^{2+}/Fe^{3+} ratio) can be difficult to establish for complex natural samples using only Mössbauer data; complementary information from Opportunity's other instruments will therefore be very important. If Mini-TES is usable, then it could independently confirm the presence of phyllosilicates and constrain their composition [e.g., *Michalski et al*., 2006]. APXS could determine major and minor element chemistry, and a better understanding of the rocks hosting the phyllosilicates could be gleaned from Pancam and Microscopic Imager views of grain sizes, shapes, and possible sedimentary textures (e.g., cross-bedding or laminations too fine to resolve from orbit).

Aside from confirming phyllosilicates and constraining their composition, questions Opportunity could address at Endeavour crater include: What is the full mineral assemblage? For example, will the "missing salts" expected to accompany clay formation [*Milliken et al.*, 2009] be found? Are they predominantly carbonates, halides, sulfates, or something else? Are there remnant primary minerals that could constrain the precursor mineralogy and the degree of alteration? From the full mineral suite combined with textural information, can we infer whether these clays formed *in situ* via alteration of an igneous precursor, precipitated from standing water, or formed elsewhere and were subsequently transported to Endeavour by eolian, fluvial, or impact processes? Whatever is found may inform interpretations of remotely sensed clays elsewhere on Mars as well, just as Opportunity's findings to date have informed orbital studies of other sulfate and hematite-bearing regions [e.g., *Murchie et al.*, 2009a]. Based on the analogy of hematite's initial detection from orbit, the diverse hypotheses put forward for its origin, and its eventual identification as a lag deposit of spherical concretions, surprises at Endeavour crater should be expected.

CHAPTER 6

CONCLUSIONS AND OUTLOOK

6.1 Summary of Results and Conclusions

As the preceding chapters have demonstrated, the high-resolution instruments on MRO reveal the aqueous history of Mars to be more complex than previously pictured. Nevertheless, coanalysis of HiRISE, CRISM, and other orbital data allows observation and integration of the surface morphology, stratigraphy, and composition, which in combination can be used to formulate and test hypotheses on the evolution of Martian environments.

Applying MRO instrumentation to the largest previously identified exposure of hydrated minerals—the Mawrth Vallis region—reveals several new secondary minerals, including kaolinite, bassanite, and hematite reported here for the first time. These minerals and the previously identified clays are compositionally stratified, with Al-clays overlying Fe/Mg-clays (a relationship subsequently found elsewhere on Mars) and hydrated sulfates exposed beneath these clays in a few locations. This ubiquitous stratigraphy and its relationship to topography constrains the age and formation mechanisms for at least a subset of the hydrated minerals—e.g., they did not all form in an Early/Mid Noachian sea. Meter-scale textures provide further evidence for a complex aqueous history, including possible soft sediment deformation, mineralized fracture fill, and polygonal crack patterns possibly related to water cycling.

MRO (particularly CRISM) data were next used to search for localized aqueous deposits that could have previously escaped detection by lower-resolution instruments. A new type of carbonate (Fe/Ca-rich) is found in a region distinct from that in which CRISM identifies Mg-carbonate; this new carbonate is chiefly exposed

by mid-sized impact craters and could be a widespread phase in the Martian subsurface. At least a dozen different secondary minerals are reported in regions of the southern highlands where they had previously been missed, indicating widespread aqueous alteration on Noachian Mars. These minerals occur in diverse assemblages and geologic settings, likely reflecting diverse chemical and thermodynamic conditions for water throughout Martian history.

The interbedded clays and sulfates of Columbus crater in the Terra Sirenum highlands prompted its selection for a case study utilizing virtually all relevant orbital datasets to unravel its environmental history. CRISM data from Columbus and surrounding terrains reveal this to be one of the most mineralogically diverse areas on Mars, with multiple phyllosilicate and sulfate minerals, crystalline ferric oxide/hydroxide, and inferred chlorides and opaline silica on the neighboring plains. Most of these minerals occur in light-toned layered deposits that are found within many of the region's large craters. The stratigraphy and spatial distribution (including topography) of these deposits indicate that they postdate the craters in which they are exposed, and suggest that deposition within a deep, groundwater-fed lake is a plausible explanation for the layered materials in Columbus crater.

Of course, some key questions about these or any other aqueous deposits will only be answered with measurements from a landed mission. Fortunately, both major hydrous mineral classes identified by OMEGA and confirmed by CRISM—phyllosilicates and hydrated sulfates—are exposed in or near Endeavour crater, the current long-term traverse target for the Opportunity rover. Endeavour's phyllosilicates are Fe/Mg-smectites, the most commonly identified type on Mars and one that should be detectable by the rover's Mössbauer spectrometer, potentially yielding new insights into regional or even global alteration processes during the Noachian. For the hydrated sulfates, *in situ* constraints on cation composition and/or

hydration state will inform interpretation of the generically named "polyhydrated sulfates" detected in Meridiani and elsewhere on Mars.

These studies prompt numerous new questions and hypotheses that can be addressed by future work. Some of this work must await future missions, but many intriguing problems can in fact be tackled with existing MRO (and other spacecraft) data, supplemented by modeling and terrestrial field or lab studies.

6.2 Suggested Future Work

6.2.1 Further studies with currently operating spacecraft

As described in chapter 3, the Al-over-Fe/Mg-clay stratigraphy first identified in Mawrth Vallis (chapter 2) has more recently been observed in several other regions of Mars (Fig. 6.1). These regions are globally widespread across the Martian low-to-mid-latitudes, implicating a globally widespread process. In each region, the observations are consistent with a Late Noachian age for the Al-clays; this was estimated from their stratigraphic relation to the outflow channel at Mawrth Vallis (chapter 2)—and, by extension, throughout western Arabia Terra [*Noe Dobrea et al.*, 2010]. In Valles Marineris, the Al-clays are overlain by Early Hesperian materials of the Hpl_3 unit, and the Fe/Mg-smectites underlain by the Late Noachian Npl_2 unit [*Murchie et al.*, 2009b; *Scott and Tanaka*, 1986]. At Nili Fossae, kaolinite is inferred to postdate the Late Noachian Isidis basin-forming impact but to predate the Early Hesperian Syrtis Major lava flows [*Mustard et al.*, 2009]. The Late Noachian is the estimated period of widespread aqueous activity in the Eridania basin [*Irwin et al.*, 2002] and in northwest Terra Sirenum (chapter 4), and the Al-clays overlying Fe/Mg-clays in northeast Noachis Terra (chapter 3) occur in Late Noachian-aged terrain [*Greeley and Guest*, 1987]. One potential explanation for all of this is an evolution in primary compositions—e.g., Late Noachian volcanics more plagioclase-rich (and

therefore more Al-rich) than their Early-to-Mid Noachian counterparts, yielding more Al-rich alteration products. However, remote sensing reveals no evidence for global evolution in plagioclase abundance [*Rogers and Christensen*, 2007], whereas the compositions of Martian meteorites are in fact consistent with progressive Al-depletion in younger Martian volcanics [e.g., *Longhi et al.*, 1992], a trend opposite from that required to explain the clay stratigraphy. An alternative explanation would be uniform (mafic-rich) primary compositions that experienced stronger alteration near the surface, leaching divalent cations to leave only relatively insoluble Al-rich clays in the uppermost horizons. Alteration would therefore be a top-down process—e.g., surface weathering, possibly driven by atmospheric precipitation. The Martian clay stratigraphy may thus be chemical evidence for rainfall during the period when it is most strongly suggested by the surface morphology [e.g., *Howard et al.*, 2005; *Irwin et al.*, 2005, 2011; *Hoke and Hynek*, 2009].

The surface weathering hypothesis for Martian Al-clays could be evaluated quantitatively using a coupled kinetic-thermodynamic model of top-down alteration. Kinetic-thermodynamic models have previously been used to study alteration on Mars [*Zolotov and Mironenko*, 2007a,b], but these were "point" models (no spatial gradients) run under a limited range of conditions and primary compositions. Spatial gradients are modeled by terrestrial geochemists using reactive transport codes [e.g., *Steefel et al.*, 2005]; *Hausrath et al.* [2008] used one of these codes to model weathering rind formation on Gusev crater basalts. The same code could be applied to the larger-scale gradients in clay composition observed by CRISM. Constrained by the observed mineralogies and layer thicknesses, such a model should reveal what ranges of temperature, pH, and duration of aqueous weathering are most consistent with the CRISM results. By varying the temperature, this model could also be applied to scenarios such as hydrothermal alteration resulting from emplacement of an impact

melt sheet [*Noe Dobrea et al.*, 2010].

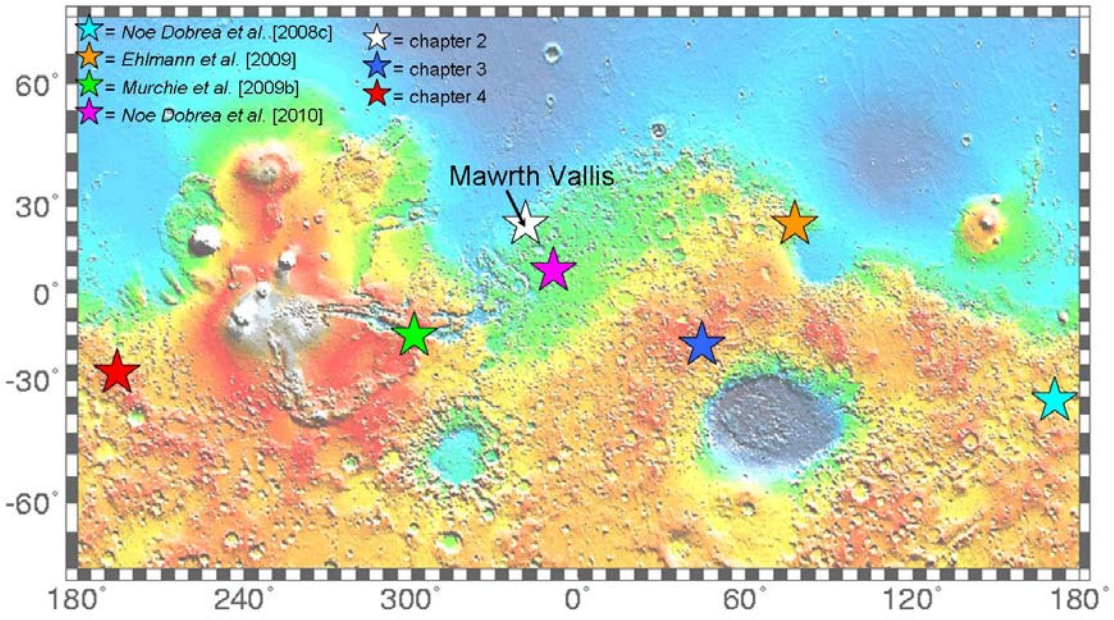

Figure 6.1: Locations on Mars at which both Al- and Fe/Mg-phyllosilicates are exposed with a clear stratigraphic relationship. In all cases, Al-phyllosilicates overlie Fe/Mg-phyllosilicates.

Another pattern observed initially at Mawrth Vallis and subsequently in hydrated mineral exposures across Mars is the ubiquity of polygonal fractures. As discussed in chapter 2, these can form through a range of processes including desiccation of water-rich sediments, periglacial processes (e.g., freeze-thaw, ice or sand wedging), rock weathering (e.g., thermal stresses or salt/dirt cracking), or even impacts or regional tectonics. Determining which process formed a given set of polygons requires consideration of the geologic context, cross-cutting relationships, material properties and compositions, and the detailed crack morphologies. For quantifying morphology (e.g., polygon sizes and crack junction angles), the vast size of the HiRISE dataset presents both an opportunity and a challenge; automated polygon detection and characterization would greatly accelerate progress in this area. *Pina et al.* [2006] have developed an algorithm for accurate automated polygon detection in MOC images, and have more recently applied it to HiRISE images of the

northern plains near the Phoenix landing site [*Saraiva et al.*, 2009; *Pina et al.*, 2009]. This algorithm or a similar one could be applied to HiRISE images of the lower-latitude phyllosilicate, sulfate, and chloride-bearing outcrops that also exhibit polygons, enabling their characterization to facilitate comparisons to physical models [e.g., *Mellon et al.*, 2008; *El Maarry et al.*, 2010], terrestrial field studies [e.g., *Chan et al.*, 2008; *Chavdarian and Sumner*, 2008] and laboratory experiments [e.g., *Müller*, 1998; *Shorlin et al.*, 2000; *Mal et al.*, 2007]. *Watters and Squyres* [2009] have conducted an analogous study of smaller-scale polygons in the sulfate-rich rocks observed by Opportunity, combining manual image analysis with modeling and measurements at a terrestrial analog field site. Comparing their results with those that could be obtained from HiRISE images of diverse aqueous deposits would yield new insight into the range of processes, environments, and material properties responsible for polygonal crack formation across Mars.

The survey described in chapter 3 uncovered many new aqueous deposits of interest, but spanned only a subset of Noachian terrains. Since the survey's completion, the CRISM dataset has more than doubled in size, and new calibration and spectral filtering methods have been developed to aid analyses. The survey could usefully be repeated using these new data and techniques, over the same or slightly different regions. As an example, contributions to future exploration could be maximized by focusing on the nominal latitude and altitude ranges for landing of the next two planned Mars rovers after MSL [*MEPAG MRR-SAG*, 2010; *MEPAG 2R-iSAG*, 2010].

Further CRISM analysis of the MSL candidate landing sites [*Grant et al.*, in press] may also be warranted. The Mawrth Vallis site has received the greatest attention from orbital spectroscopists [reviewed by *Michalski et al.*, 2010], but the bassanite described in chapter 2 was only recently identified. CRISM studies to date

of the Gale, Eberswalde, and Holden crater sites [*Milliken et al.*, 2010; *Milliken and Bish*, 2010] have had intriguing results but have been more limited in scope. My own recent work on the Holden crater site identified two hydrated minerals previously undetected there: probable hydrated silica in the landing ellipse and zeolite or hydrated sulfate in the crater wall upstream of the landing area (Fig. 6.2). Further efforts incorporating all available CRISM data at Eberswalde and Gale craters may be comparably fruitful, informing site selection and later traverse definition for MSL.

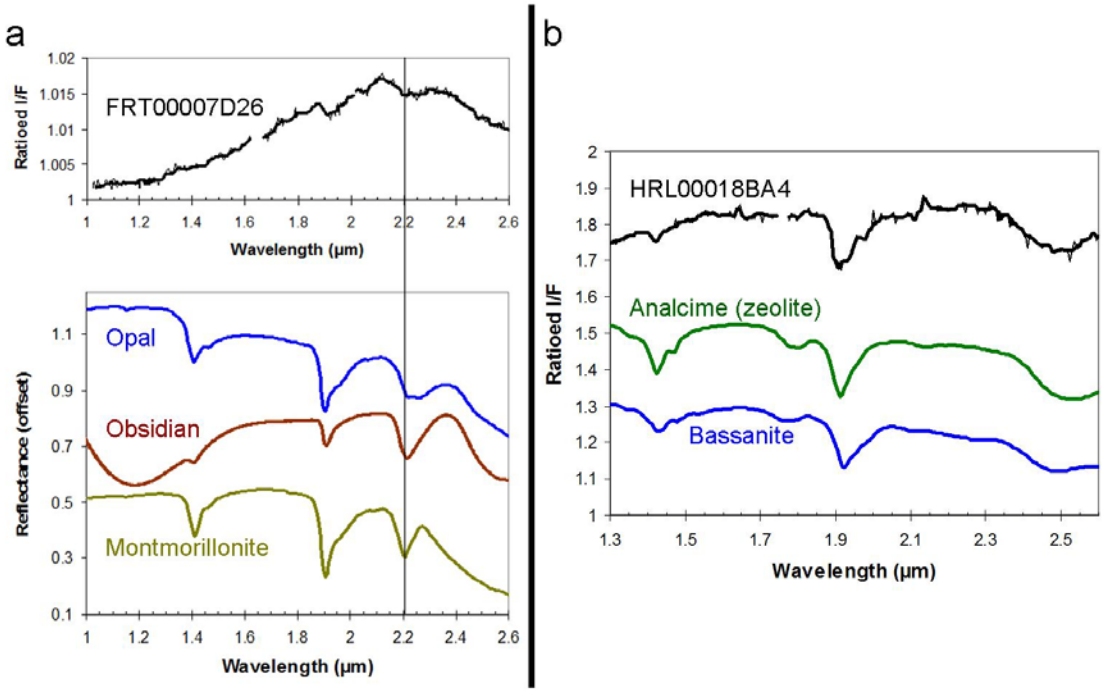

Figure 6.2: Newly identified hydrated phases in Holden crater wall (a) and proposed MSL landing ellipse (b). Laboratory spectra in (b) have been scaled and offset for comparison to the CRISM spectrum.

The Eberswalde and Holden crater sites highlight an unresolved problem: the "missing salts" expected to accompany formation of clays such as those detected in these craters [*Milliken et al.*, 2009], and which would also be predicted if substantial lakes evaporated here as has been inferred [e.g., *Bhattacharya et al.*, 2005; *Lewis and*

Aharonson, 2006; *Grant et al.*, 2008]. Chapter 4 describes one of the first candidate deep paleolakes on Mars in which salts are actually detected, including probable Mg-sulfates. A new CRISM image reveals sulfate in another deep lacustrine setting: a depression within Shalbatana Vallis (3°N, 43.3°W) has been described as a Hesperian-aged paleolake based on topography and morphology, including inlet channels that feed six fan-shaped deposits interpreted as deltas, the largest of which preserves features inferred to be shorelines [*Di Achille et al.*, 2007, 2009]. The valley wall adjacent to this fan contains Fe/Mg-phyllosilicate, and near the bottom of the depression, over 300 meters below the shoreline elevation, polyhydrated (plausibly Mg-) sulfate is detected in finely bedded deposits (Fig. 6.3). This contrasts with the Mg-carbonate found in Jezero crater, a paleolake near the Nili Fossae [*Ehlmann et al.*, 2008a,b, 2009]. These differences in evaporite chemistry could reflect differences in groundwater vs. meteoric inputs, or possibly a change in atmospheric composition over time, since the dominant anion precipitated from evaporating (or freezing) water is affected by the composition of atmospheric or other volatile reservoirs with which the water is in equilibrium. The composition and density of the Noachian atmosphere (especially greenhouse gas components) remain poorly understood, but are critical to evaluating whether the Martian surface environment was ever habitable. Future targeting and analysis of CRISM observations of many more proposed paleolakes could be used to derive quantitative thermodynamic constraints on pCO_2 vs. pSO_2 and other atmospheric properties on ancient Mars.

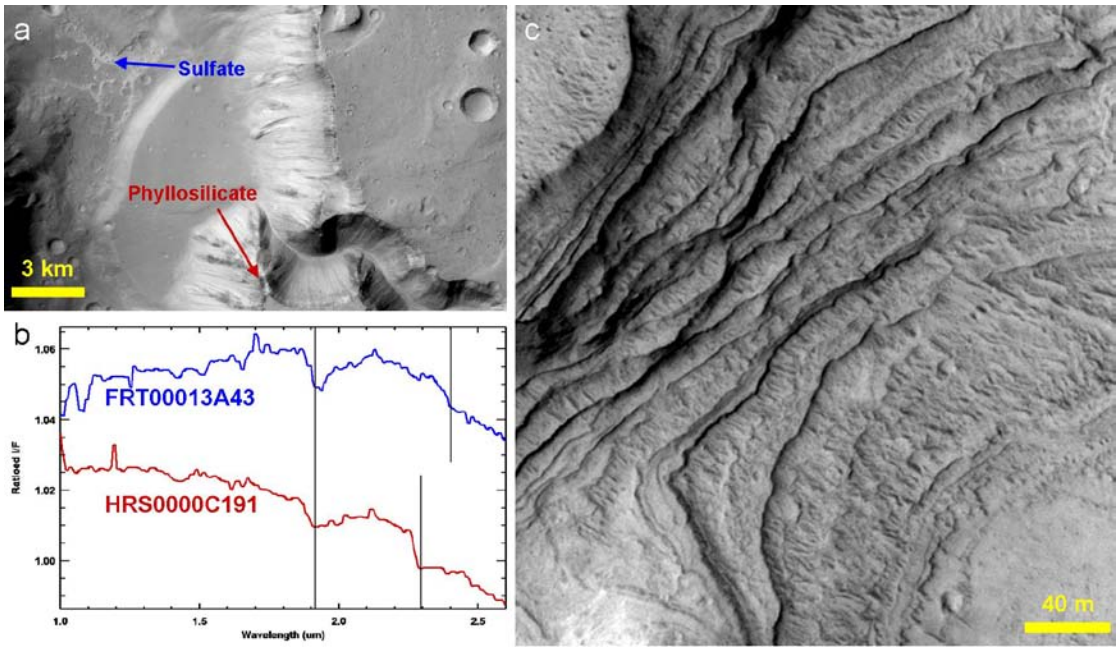

Figure 6.3: Paleolake in Shalbatana Vallis identified by *Di Achille et al.* [2007, 2009]. (a) Phyllosilicates on valley wall eroded to form fan/delta, and light-toned hydrated deposits on basin floor (CTX P17_007824_1812). (b) CRISM spectra, colored as in (a). (c) Hydrated (probably sulfate-bearing) deposits are finely layered (HiRISE PSP_010316_1830).

Chapter 3 described a type of carbonate (Fe/Ca-rich) newly identified in CRISM data. Independent from this work, *Michalski and Niles* [2010] very recently reported a spectrally similar carbonate in CRISM data from the *D*~65 km Leighton crater on the western flank of Syrtis Major. This carbonate is associated with phyllosilicates in layered deposits exposed in Leighton's central uplift; *Michalski and Niles* have interpreted this as possible evidence for widespread, buried layered carbonates. Their detection adds to the geographic distribution of carbonate-bearing rocks identified on Mars to date (Fig. 6.4), but are these carbonates globally widespread or only regional? At low spectral resolution, carbonates can be difficult to distinguish from Fe/Mg-phyllosilicates in the NIR; indeed, the crater-exposed carbonate in Fig. 3.17A was initially identified as a "phyllosilicate exposure" based on CRISM multispectral data. Chapter 3 reported ~10^2 new exposures of Fe/Mg-phyllosilicate in the southern highlands, and even more such exposures were reported

in the highlands by *Mustard et al.* [2008] and *Murchie et al.* [2009b]. Some of these may in fact be carbonates (or carbonate+phyllosilicate); where possible, analysis of follow-up hyperspectral observations to distinguish carbonate from phyllosilicate would be illuminating. By analogy to the exposures described in chapter 3, central uplifts of mid-sized craters [*Tornabene et al.*, 2010] should be prime targets in the search for additional Fe/Ca-carbonates.

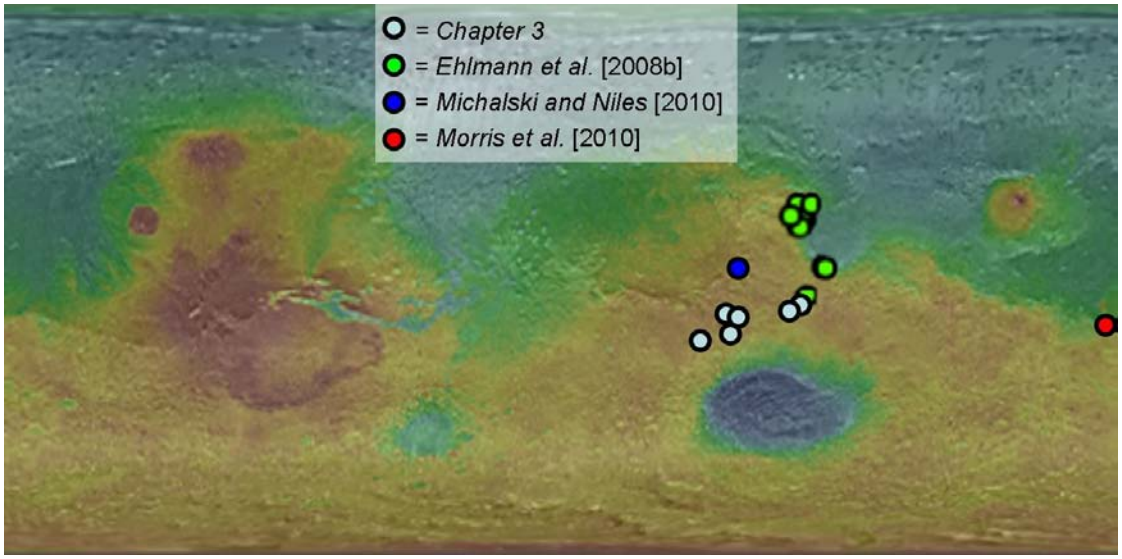

Figure 6.4: Locations of carbonate-bearing rocks found on Mars to date. Background is THEMIS daytime IR mosaic colorized with MOLA topography (modified from *Ehlmann et al.* [2008b]).

As for other salts, the chlorides identified by *Osterloo et al.* [2008] may be spectrally unremarkable in the infrared, but they are morphologically diverse (Fig. 6.5). *Osterloo et al.* [2010] identified ~640 distinct exposures of these materials and illustrated their textural variability, but much work remains to understand this variability—e.g., is it related to geologic context or to accompanying mineralogy? CRISM data can be used to identify accompanying minerals, which might be expected to include other evaporite phases such as hydrated sulfates.

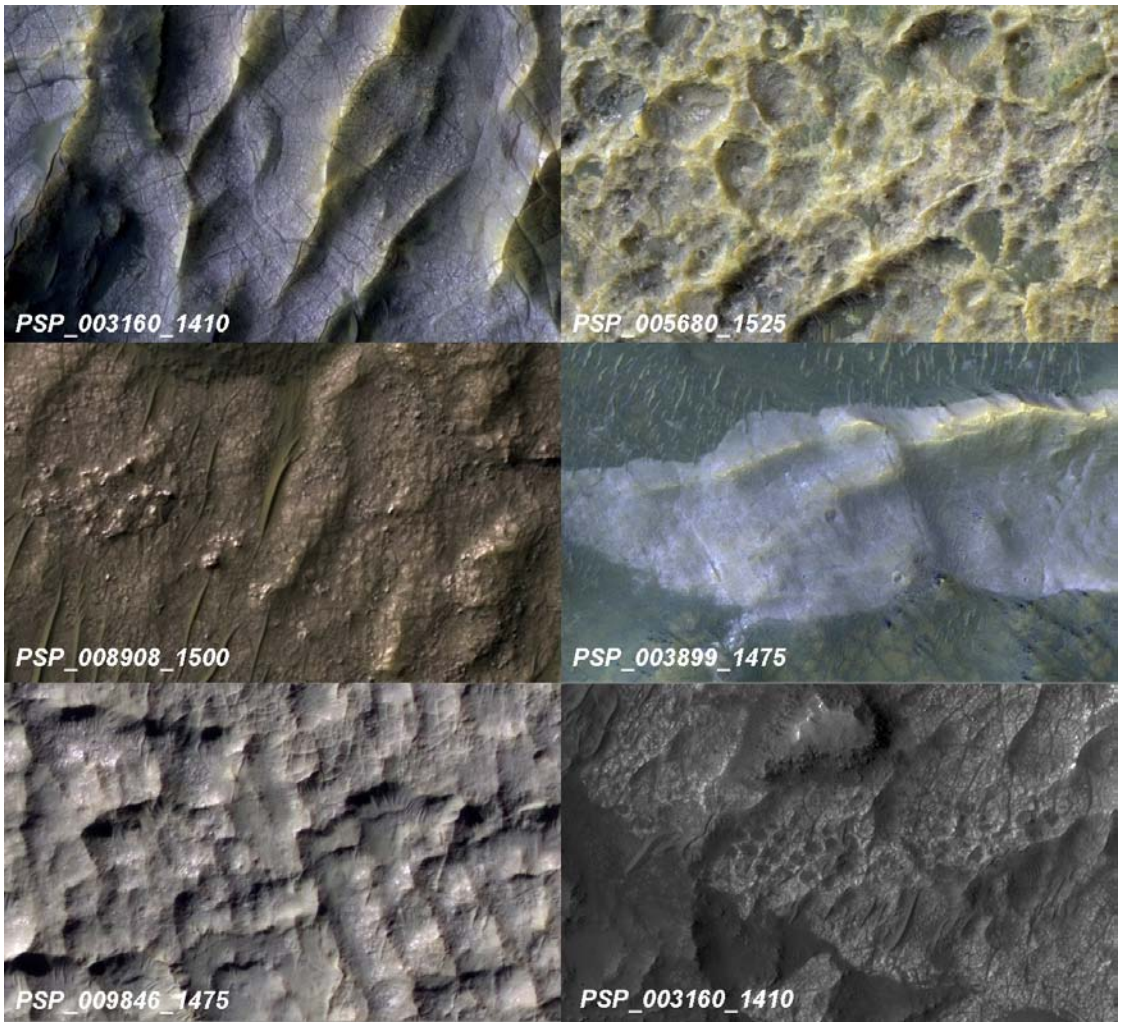

Figure 6.5: Diverse textures of chloride-bearing materials in the southern highlands. Each HiRISE image cutout is ~300 m wide.

Chemical trends described by *Karunatillake et al.* [2009] suggest that hydrated sulfates may be present in the Late Amazonian dust mantle that blankets the Tharsis volcanic region, in striking contrast to the *Bibring et al.* [2006a] model positing no significant hydrated mineral formation since the Hesperian. The "reticulate" texture of this dust mantle [*Bridges et al.*, 2010] is similar to that of numerous Hesperian-aged outcrops in which monohydrated sulfates are detected by CRISM (e.g., Fig. 6.6). This similarity, along with recent reanalyses of Mini-TES data indicating surficial alteration of Gusev crater basalts to form monohydrated sulfate [*Ruff*, 2009], suggests that

changes in alteration processes on Mars since the Hesperian may have been gradual rather than abrupt, and it may be possible to learn about Hesperian sedimentation by studying the modern Martian dust cycle. Future work should include more detailed comparative studies of the morphology, stratigraphy, and thermophysical properties of sulfate-bearing outcrops across Mars.

Figure 6.6: Diverse colors of sulfate-bearing deposits in Aram Chaos (HiRISE ESP_012860_1830). The orange-toned unit exposed at upper left has a "reticulate" texture [*Bridges et al.*, 2010] and contains monohydrated sulfate. The green-toned unit in the lower half of the image is the ferric hydroxysulfate described by *Lichtenberg et al.* [2010].

Images such as Fig. 6.6 highlight the significant color variations observed in HiRISE images of some aqueous deposits, which correlate with mineralogic variations sensed by CRISM in some locations. HiRISE can generally distinguish ferric vs. ferrous minerals via the BG/RED filter ratio [*Delamere et al.*, 2010] and crystalline ferric minerals vs. Martian dust via IR/BG [*McEwen et al.*, 2007]. Experience

suggests that further discrimination is possible; as described in chapter 4, ferric sulfate-bearing rocks typically have a distinct green tone in HiRISE IRB images (e.g., Fig. 6.6). Chlorides (Fig. 6.5), by contrast, commonly have a relatively pink or purple tone (i.e., relatively high I/F in the HiRISE BG and IR filters), presumably due to their paucity of iron compared to surrounding geologic materials—Fe^{3+} absorbs strongly shortward of ~530 nm (BG filter) and crystalline Fe-minerals absorb at ~1 μm (IR filter). At local to regional scales, further inferences may be made based on direct comparison of HiRISE and CRISM data; one example is the blue vs. red colors of Al- vs. Fe/Mg-clays in Mawrth Vallis (chapter 2). Such correlations can be used to extend remotely sensed mineralogy to a smaller scale of mapping [e.g., Figs. 13 and 15 of *Mustard et al.*, 2009]. These methods of using HiRISE color data to infer composition have been minimally exploited to date, but will be valuable for future studies, especially as the CRISM coolers age and new IR data become difficult to obtain at reasonable SNR.

6.2.2 Studies with proposed future spacecraft

Coanalyses of HiRISE color and CRISM observations will inform future investigations such as that of the high-resolution camera on the ExoMars Trace Gas Orbiter currently planned for launch in 2016 [*Zurek et al.*, in press]. The High-resolution Stereo Color Imager (HiSCI) recently selected for this orbiter's payload will obtain ~2 m/pixel images with a swath width of ~8.5 km, building color coverage of the Martian surface >20 times faster than HiRISE has done [*McEwen et al.*, 2011]. Four visible/NIR filters are planned, enabling finer mineralogic discrimination than is possible with the three HiRISE filters—for example, the ~0.86 μm absorption in crystalline hematite gives it a very distinct appearance (even relative to other ferric oxides) in the anticipated HiSCI filter set (Fig. 6.7). HiSCI's four-color and stereo

imaging capabilities will make it an ideal tool for future orbital studies of compositional stratigraphy on Mars.

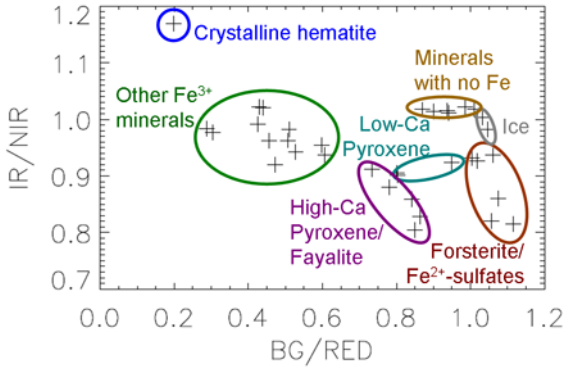

Fig. 6.7: Mineralogic discrimination using color filters currently planned for the HiSCI camera on the 2016 ExoMars Trace Gas Orbiter. Spectra from CRISM and USGS libraries were convolved to nominal HiSCI bandpasses to compute I/F ratios. NIR, RED, and BG are identical to HiRISE filters; the IR filter is new.

Nevertheless, as has been emphasized previously, many key measurements desired from Martian aqueous deposits can only be made with landed instruments. Whereas recent Mars missions (e.g., MER, MRO, Phoenix) have been driven by the theme of "Following the Water," the recently endorsed theme for surface missions after MSL wil be "Seeking the Signs of Life" [*MEPAG MRR-SAG*, 2010]. The Viking landers pursued a similar objective, and their negative results demonstrate the importance of careful landing site selection to maximize the potential for accessing materials that might preserve organic matter or other biomarkers.

Fortunately, the results of chapter 3 indicate that Mars has hosted widespread and diverse aqueous environments, many of which may be promising locations to seek signs of life. Synthesizing results from a number of early CRISM studies, *Murchie et al.* [2009b] defined 9–10 distinct classes of aqueous deposits based on orbital data; this list would grow slightly after accounting for some of the new deposits described in previous chapters, such as the hydrated sulfates in the Sisyphi Montes and the crater-exposed Fe/Ca-carbonates. Each class of deposit is inferred to reflect a distinct

environment of formation. Their mineralogies allow some inferences to be made about the relative suitability of these environments for the evolution, persistence, and preservation of life (e.g., based on water activity limits for terrestrial biology [*Tosca et al.*, 2008a]), but to state such evaluations with great confidence seems hubristic. Instead, a type location for each class of aqueous deposit should eventually be studied with landed instruments; viewing each site with the same payload would facilitate direct comparisons, as has been possible with Spirit and Opportunity. Ideally these new landings would occur before selection of the single site for costly return of Martian samples to the Earth, but it is possible that only two sites will be explored prior to sample return—that of MSL and that of the Mars Astrobiology Explorer-Cacher (MAX-C) concept rover envisioned for launch in 2018 [*MEPAG 2R-iSAG*, 2010].

For MAX-C and beyond, a minimal rover payload should include a near-infrared spectrometer for direct linkage of the materials examined *in situ* with the remotely sensed mineralogy that will likely drive landing site selection. Outcrop-scale spectroscopy is most critical, but substantial further insight could be gained from microscale mineralogy, resolving the grain-scale distribution of minerals of interest. The latter may be possible using active IR reflectance [*Anderson et al.*, 2005; *Hand et al.*, 2005; *Leroi et al.*, 2009; *Nuñez et al.*, 2009, 2010] or Raman spectroscopy [e.g., *Wang et al.*, 2003], or possibly polarizing microscopy [*Dreyer et al.*, 2010]. Other key payload capabilities include remote and microscale optical imaging for examining rock textures, and elemental chemistry (e.g., from an APXS-like instrument) to further constrain compositions. Finally, to seriously pursue signs of life, an organic detection capability must be included. As an alternative to the resource-intensive pyrolysis/mass spectroscopic approaches pursued by previous landed missions [e.g., *Mahaffy*, 2008], active mid-IR spectroscopy could detect a range of organic

compounds in addition to mineralogy [*Anderson et al.*, 2005; *Hand et al.*, 2005]. *MEPAG MRR-SAG* [2010] describe other alternative methods of detecting organics.

Beyond Mars, the insights gained from CRISM strongly motivate the use of similar instruments to investigate the mineralogy of other planetary surfaces. For example, ground-based observations of the dwarf planet Ceres suggest an alteration assemblage of Fe-rich phyllosilicate (serpentine) and Mg-rich carbonate and hydroxide [*Milliken and Rivkin*, 2009], with apparent spectral variations across the surface [*Rivkin and Volquardsen*, 2010]. These variations can be explored in much greater detail with the Visible and Infrared Mapping Spectrometer on board the Dawn mission when it reaches Ceres in 2015 [*Russell et al.*, 2008]. On Jupiter's moon Europa, Galileo's Near Infrared Mapping Spectrometer (NIMS) detected spatially varying non-ice component(s) interpreted as sulfuric acid hydrate and/or hydrated salts (e.g., Mg/Na-sulfates) or flash-frozen brines; *Carlson et al.* [2009] provide a thorough review. Similar materials may also be present on Ganymede [*McCord et al.*, 2001]. If these precipitated from salty water upwelling from subsurface oceans, then they may provide the best opportunities for studying the composition and habitability of these putative oceans in the near term. A radiation-hardened NIR spectrometer could observe Europa from orbit or during flybys at higher SNR and higher spatial resolution than was possible with NIMS. Such observations would yield insights into the composition and variability of Europan hydrates and would help identify the most promising locations for future landed astrobiology missions, as OMEGA and CRISM have done for Mars.

REFERENCES

Albee, A. L., R. E. Arvidson, and F. D. Palluconi (1992), Mars Observer Mission, *J. Geophys. Res.*, *97*(E5), 7665–7680.

Altheide, T. S., V. F. Chevrier, E. G. Rivera-Valentin, and J. J. Wray (2010a), Geochemical Modeling of the Evaporation of an Ancient Paleolake in Columbus Crater, Terra Sirenum, Mars, *Lunar Planet. Sci., XLI*, Abstract 2479.

Altheide, T. S., V. F. Chevrier, and E. Noe Dobrea (2010b), Mineralogical Characterization of Acid Weathered Phyllosilicates with Implications for Secondary Martian Deposits, *Geochim. Cosmochim. Acta, 74*, 6232–6248, doi:10.1016/j.gca.2010.08.005.

Anderson, J. H., Jr., and K. A. Wickersheim (1964), Near infrared characterization of water and hydroxyl groups on silica surfaces, *Surface Science, 2*, 252–260.

Anderson, M. S., et al. (2005), Fourier transform infrared spectroscopy for Mars science, *Rev. Sci. Instrum., 76*, 034101.

Anderson, R. C., J. M. Dohm, M. P. Golombek, A. F. C. Haldemann, B. J. Franklin, K. L. Tanaka, J. Lias, and B. Peer (2001), Primary centers and secondary concentrations of tectonic activity through time in the western hemisphere of Mars, *J. Geophys. Res.*, *106*(E9), 20,563–20,585, doi:10.1029/2000JE001278.

Andrews-Hanna, and K. W. Lewis (2011), Early Mars hydrology: Hydrological evolution in the Noachian and Hesperian epochs, *J. Geophys. Res.*, doi:10.1029/2010JE003709, in press.

Andrews-Hanna, J. C., R. J. Phillips, and M. T. Zuber (2007), Meridiani Planum and the global hydrology of Mars, *Nature*, *446*(7132), 163–166, doi:10.1038/nature05594.

Andrews-Hanna, J. C., M. T. Zuber, R. E. Arvidson, and S. J. Wiseman (2010), Early Mars hydrology: Meridiani playa deposits and the sedimentary record of Arabia Terra, *J. Geophys. Res.*, *115*, E06002, doi:10.1029/2009JE003485.

Ansan, V., et al., Stratigraphy, mineralogy, and origin of layered deposits inside Terby crater, Mars, *Icarus*, doi:10.1016/j.icarus.2010.09.011, in press.

Arvidson, R. E., F. P. Seelos IV, K. S. Deal, W. C. Koeppen, N. O. Snider, J. M. Kieniewicz, B. M. Hynek, M. T. Mellon, and J. B. Garvin (2003), Mantled and exhumed terrains in Terra Meridiani, Mars, *J. Geophys. Res.*, *108*(E12), 8073, doi:10.1029/2002JE001982.

Arvidson, R. E., F. Poulet, J.-P. Bibring, M. Wolff, A. Gendrin, R. V. Morris, J. J. Freeman, Y. Langevin, N. Mangold, and G. Bellucci (2005), Spectral reflectance and morphologic correlations in eastern Terra Meridiani, Mars, *Science*, *307*, 1591–1594, doi:10.1126/science.1109087.

Arvidson, R. E., et al. (2006), Nature and origin of the hematite-bearing plains of Terra Meridiani based on analyses of orbital and Mars Exploration rover data sets, *J. Geophys. Res.*, *111*, E12S08, doi:10.1029/2006JE002728.

Arvidson, R. E., et al. (2011), Opportunity Mars Rover Mission: Overview and selected results from Purgatory Ripple to traverses to Endeavour Crater, *J. Geophys. Res.*, doi:10.1029/2010JE003746, in press.

Baker, V. R. (1982), *The Channels of Mars*, Univ. of Texas Press, Austin.

Baldridge, A. M., and P. R. Christensen (2006), Detection of the Hydration Phase of Martian Sulfates Using Emission Spectroscopy of Magnesium and Calcium Sulfates, *Lunar and Planetary Institute Contributions*, *1331*, Abstract 7041.

Baldridge, A. M., J. D. Farmer, and J. E. Moersch (2004), Mars remote-sensing analog studies in the Badwater Basin, Death Valley, California, *J. Geophys. Res.*, *109*, E12006, doi:10.1029/2004JE002315.

Baldridge, A. M., S. J. Hook, J. K. Crowley, G. M. Marion, J. S. Kargel, J. L. Michalski, B. J. Thomson, C. R. de Souza Filho, N. T. Bridges, and A. J. Brown (2009), Contemporaneous deposition of phyllosilicates and sulfates: Using Australian acidic saline lake deposits to describe geochemical variability on Mars, *Geophys. Res. Lett., 36*, L19201, doi:10.1029/2009GL040069.

Bandfield, J. L., V. E. Hamilton, and P. R. Christensen (2000), A Global View of Martian Surface Compositions from MGS-TES, *Science, 287*, 1626–1630, doi:10.1126/science.287.5458.1626.

Bandfield, J. L., T. D. Glotch, and P. R. Christensen (2003), Spectroscopic Identification of Carbonate Minerals in the Martian Dust, *Science, 301*, 1084–1087.

Barlow, N. G., and C. B. Perez (2003), Martian impact crater ejecta morphologies as indicators of the distribution of subsurface volatiles, *J. Geophys. Res., 108*(E8), 5085, doi:10.1029/2002JE002036.

Bell, J. F., III, and D. Crisp (1993), Groundbased Imaging Spectroscopy of Mars in the Near-Infrared: Preliminary Results, *Icarus, 104*, 2–19.

Bell, J. F., III, and T. B. McCord (1989), Mars: Near-Infrared Comparative Spectroscopy during the 1986 Opposition, *Icarus, 77*, 21–34.

Bell, J. F., III, W. H. Farrand, J. R. Johnson, and R. V. Morris (2002), Low Abundance Materials at the Mars Pathfinder Landing Site: An Investigation Using Spectral Mixture Analysis and Related Techniques, *Icarus, 158*, 56–71, doi:10.1006/icar.2002.6865.

Benison, K. C., B. Beitler Bowen, F. E. Oboh-Ikuenobe, E. A. Jagniecki, D. A. LaClair, S. L. Story, M. R. Mormile, and B.-Y. Hong (2007), Sedimentology of acid saline lakes in southern Western Australia: Newly described processes and products of an extreme environment, *J. Sed. Res., 77*, 366–388,

doi:10.2110/jsr.2007.038.

Benison, K. C., E. A. Jagniecki, T. B. Edwards, M. R. Mormile, and M. C. Storrie-Lombardi (2008), "Hairy Blobs:" Microbial Suspects Preserved in Modern and Ancient Extremely Acid Lake Evaporites, *Astrobiology, 8*(4), 807–821, doi:10.1089/ast.2006.0034.

Bhattacharya, J. P., T. H. D. Payenberg, S. C. Lang, and M. Bourke (2005), Dynamic river channels suggest a long-lived Noachian crater lake on Mars, *Geophys. Res. Lett., 32*, L10201, doi:10.1029/2005GL022747.

Bibring, J.-P., et al. (1989), Results from the ISM experiment, *Nature, 341*, 591–593.

Bibring, J.-P., et al. (2004), OMEGA: Observatoire pour la Minéralogie, l'Eau, les Glaces et l'Activité, in *Mars Express: The Scientific Payload*, edited by A. Wilson, *Eur. Space Agency Spec. Publ., ESA SP-1240*, 37–49.

Bibring, J.-P., et al. (2005), Mars Surface Diversity as Revealed by the OMEGA/Mars Express Observations, *Science, 307*(5715), 1576–1581, doi:10.1126/science.1108806.

Bibring, J.-P., et al. (2006a), Global Mineralogical and Aqueous Mars History Derived from OMEGA/Mars Express Data, *Science, 312*, 400–404, doi:10.1126/science.1122659.

Bibring, J.-P., S. W. Squyres, and R. E. Arvidson (2006b), Merging Views on Mars, *Science, 313*, 1899–1901, doi:10.1126/science.1132311.

Bibring, J.-P., et al. (2007), Coupled Ferric Oxides and Sulfates on the Martian Surface, *Science, 317*, 1206–1210, doi:10.1126/science.1144174.

Biddanda, B. A., D. F. Coleman, T. H. Johengen, S. A. Ruberg, G. A. Meadows, H. W. Van Sumerem, R. R. Rediske, and S. T. Kendall (2006), Exploration of a Submerged Sinkhole Ecosystem in Lake Huron, *Ecosystems, 9*, 828–842, doi:10.1007/s10021-005-0057-y.

Bigham, J. M., U. Schwertmann, S. J. Traina, R. L. Winland, and M. Wolf (1996), Schwertmannite and the chemical modeling of iron in acid sulfate waters, *Geochim. Cosmochim. Acta, 60*(12), 2111–2121, doi:10.1016/0016-7037(96)00091-9.

Bishop, J. L., and E. Murad (2002), Spectroscopic and geochemical analyses of ferrihydrite from springs in Iceland and applications to Mars, in *Volcano-Ice Interactions on Earth and Mars*, edited by J. L. Smellie and M. G. Chapman, pp. 357–370, Geological Society, Special Publication No. 202, London.

Bishop, J. L., and E. Murad (2005), The visible and infrared spectral properties of jarosite and alunite, *Am. Mineral., 90*, 1100–1107, doi:10.2138/am.2005.1700.

Bishop, J. L., and C. M. Pieters (1995), Low-temperature and low atmospheric pressure infrared reflectance spectroscopy of Mars soil analog materials, *J. Geophys. Res., 100*, 5369–5379, doi:10.1029/94JE03331.

Bishop, J. L., C. M. Pieters, and R. G. Burns (1993), Reflectance and Mössbauer spectroscopy of ferrihydrite-montmorillonite assemblages as Mars soil analog materials, *Geochim. Cosmochim. Acta, 57*, 4583–4595.

Bishop, J. L., A. Banin, R. L. Mancinelli, and M. R. Klovstad (2002a), Detection of soluble and fixed NH_4^+ in clay minerals by DTA and IR reflectance spectroscopy: A potential tool for planetary surface exploration, *Planet. Space Sci., 50*, 11–19.

Bishop, J. L., E. Murad, and M. D. Dyar (2002b), The influence of octahedral and tetrahedral cation substitution on the structure of smectites and serpentines as observed through infrared spectroscopy, *Clay Miner., 37*, 617–628.

Bishop, J. L., M. D. Dyar, M. D. Lane, and J. F. Banfield (2005), Spectral identification of hydrated sulfates on Mars and comparison with acidic environments on Earth, *Int. J. Astrobiol., 3*(4), 275–285,

doi:10.1017/S1473550405002259.

Bishop, J. L., P. Schiffman, E. Murad, M. D. Dyar, A. Drief, and M. D. Lane (2007), Characterization of alteration products in tephra from Haleakala, Maui: A visible-infrared spectroscopy, Mössbauer spectroscopy, XRD, EMPA and TEM study, *Clays Clay Min., 55*, 1–17, doi:10.1346/CCMN.2007.0550101.

Bishop, J. L., M. D. Lane, M. D. Dyar, and A. J. Brown (2008a), Reflectance and emission spectroscopy of four groups of phyllosilicates: Smectites, kaolinite-serpentines, chlorites, and micas, *Clay Miner., 43*, 35–54, doi:10.1180/claymin.2008.043.1.03.

Bishop, J. L., et al. (2008b), Phyllosilicate diversity and past aqueous activity revealed at Mawrth Vallis, Mars, *Science, 321*, 830–833, doi:10.1126/science.1159699.

Bishop, J. L., et al. (2009a), Mineralogy of Juventae Chasma: Sulfates in the light-toned mounds, mafic minerals in the bedrock, and hydrated silica and hydroxylated ferric sulfate on the plateau, *J. Geophys. Res., 114*, E00D09, doi:10.1029/2009JE003352.

Bishop, J. L., N. K. McKeown, M. Parente, H. D. Makarewicz, R. L. Mancinelli, D. J. Des Marais, S. L. Murchie, and J. F. Mustard (2009b), Potential for biomarkers in phyllosilicate-bearing rocks at Mawrth Vallis, Mars, *Eos Trans. AGU, 90*(52), Fall Meet. Suppl., Abstract P41B-05.

Bishop, J. L., H. D. Makarewicz, W. P. Gates, N. K. McKeown, and T. Hiroi (2010), Beidellites: spectral properties and importance for Mars, *Lunar Planet. Sci., XLI*, Abstract 2080.

Blaney, D. L., and T. B. McCord (1995), Indications of sulfate minerals in the Martian soil from Earth-based spectroscopy, *J. Geophys. Res., 100*(E7), 14,433–14,441.

Bourke, M. C., R. Ewing, D. Finnegan, and H. A. McGowan (2008), Migration rates of niveo-aeolian dunes in Antarctica: Implications for Martian dunes, *Lunar*

Planet. Sci., XXXIX, Abstract 2166.

Boynton, W. V., et al. (2009), Evidence for Calcium Carbonate at the Mars Phoenix Landing Site, *Science, 325*, 61–64, doi:10.1126/science.1172768.

Bridges, J. C., D. C. Catling, J. M. Saxton, T. D. Swindle, I. C. Lyon, and M. M. Grady (2001), Alteration assemblages in Martian meteorites: Implications for near-surface processes, *Space Sci. Rev., 96*, 365–392.

Bridges, N. T., et al. (2010), Aeolian bedforms, yardangs, and indurated surfaces in the Tharsis Montes as seen by the HiRISE Camera: Evidence for dust aggregates, *Icarus, 205*, 165–182, doi:10.1016/j.icarus.2009.05.017.

Buczkowski, D. L., S. Murchie, R. N. Clark, K. Seelos, F. Seelos, E. Malaret, and C. Hash, Investigation of an Argyre Basin ring structure using MRO/CRISM, *J. Geophys. Res.*, doi:10.1029/2009JE003508, in press.

Bullock, M. A., and J. M. Moore (2004), Aqueous alteration of Mars-analog rocks under an acidic atmosphere, *Geophys. Res. Lett., 31*, L14701, doi:10.1029/2004GL019980.

Burns, R. G. (1993a), *Mineralogical Applications of Crystal Field Theory*, 2nd ed., 551 pp., Cambridge Univ. Press, Cambridge, UK.

Burns, R. G. (1993b), Rates and mechanisms of chemical weathering of ferromagnesium silicate minerals on Mars, *Geochim. Cosmochim. Acta, 57*, 4555–4574, doi:10.1016/0016-7037(93)90182-V.

Cabrol, N. A., and E. A. Grin (1999), Distribution, Classification, and Ages of Martian Impact Crater Lakes, *Icarus, 142*, 160–172.

Calvin, W. M., and J. F. Bell III (2008), Historical context: the pre-MGS view of Mars' surface composition, in *The Martian Surface: Composition, Mineralogy, and Physical Properties*, edited by J. Bell, pp. 20–30, Cambridge University Press, Cambridge.

Calvin, W. M., T. V. V. King, and R. N. Clark (1994), Hydrous carbonates on Mars?: Evidence from Mariner 6/7 infrared spectrometer and ground-based telescopic spectra, *J. Geophys. Res., 99*(E7), 14,659–14,675.

Campbell, J. L., R. Gellert, M. Lee, C. L. Mallett, J. A. Maxwell, and J. M. O'Meara (2008), Qualitative in situ determination of hydration of bright high-sulfate Martian soils, *J. Geophys. Res., 113*, E06S11, doi:10.1029/2007JE002959.

Carlson, R. W., W. M. Calvin, J. B. Dalton, G. B. Hansen, R. L. Hudson, R. E. Johnson, T. B. McCord, and M. H. Moore (2009), Europa's Surface Composition, in *Europa*, edited by R. T. Pappalardo, W. B. McKinnon, and K. K. Khurana, pp. 283–327, The University of Arizona Press, Tucson.

Carr, M. H. (1995), The Martian drainage system and the origin of valley networks and fretted channels, *J. Geophys. Res., 100*(E4), 7479–7507, doi:10.1029/95JE00260.

Carr, M. H., and J. W. Head III (2010), Geologic history of Mars, *Earth Planet. Sci. Lett., 294*, 185–203, doi:10.1016/j.epsl.2009.06.042.

Carter, J., F. Poulet, J.-P. Bibring, S. Murchie, Y. Langevin, J. F. Mustard, and B. Gondet (2009), Phyllosilicates and other hydrated minerals on Mars: 1. Global distribution as seen by MEx/OMEGA, *Lunar Planet. Sci., XL*, Abstract 2028.

Carter, J., F. Poulet, J.-P. Bibring, and S. Murchie (2010), Detection of Hydrated Silicates in Crustal Outcrops in the Northern Plains of Mars, *Science, 328*, 1682–1686, doi:10.1126/science.1189013.

Chan, M. A., W. A. Yonkee, D. I. Netoff, W. M. Seiler, and R. L. Ford (2008), Polygonal cracks in bedrock on Earth and Mars: Implications for weathering, *Icarus, 194*, 65–71, doi:10.1016/j.icarus.2007.09.026.

Chavdarian, G. V., and D. Y. Sumner (2008), Crack geometry and morphology in hydrous sulfate sands, *Lunar Planet. Sci., XXXIX*, Abstract 2285.

Chevrier, V., and T. S. Altheide (2008), Low temperature aqueous ferric sulfate solutions on the surface of Mars, *Geophys. Res. Lett., 35*, L22101, doi:10.1029/2008GL035489.

Chevrier, V., F. Poulet, and J.-P. Bibring (2007), Early geochemical environment of Mars as determined from thermodynamics of phyllosilicates, *Nature, 448*, 60–63, doi:10.1038/nature05961.

Chojnacki, M., and B. M. Hynek (2008), Geological context of water-altered minerals in Valles Marineris, Mars, *J. Geophys. Res., 113*, E12005, doi:10.1029/2007JE003070.

Christensen, P. R., et al. (1992), Thermal Emission Spectrometer Experiment: Mars Observer Mission, *J. Geophys. Res., 97*(E5), 7719–7734.

Christensen, P. R., et al. (2000), Detection of crystalline hematite mineralization on Mars by the Thermal Emission Spectrometer: Evidence for near-surface water, *J. Geophys. Res., 105*, 9632–9642, doi:10.1029/1999JE001093.

Christensen, P. R., et al. (2001a), Mars Global Surveyor Thermal Emission Spectrometer experiment: Investigation description and surface science results, *J. Geophys. Res., 106*(E10), 23,823–23,871, doi:10.1029/2000JE001370.

Christensen, P. R., R. V. Morris, M. D. Lane, J. L. Bandfield, and M. C. Malin (2001b), Global mapping of Martian hematite mineral deposits: Remnants of water-driven processes on early Mars, *J. Geophys. Res., 106*(E10), 23,873–23,885, doi:10.1029/2000JE001415.

Christensen, P. R., et al. (2004a), The Thermal Emission Imaging System (THEMIS) for the Mars 2001 Odyssey Mission, *Space Sci. Rev., 110*, 85–130.

Christensen, P. R., et al. (2004b), Initial Results from the Mini-TES Experiment in Gusev Crater from the Spirit Rover, *Science, 305*, 837–842.

Christensen, P. R., et al. (2004c), Mineralogy at Meridiani Planum from the Mini-TES

Experiment on the Opportunity Rover, *Science, 306*, 1733–1739.

Clark, B. C. (1993), Geochemical components in Martian soil, *Geochim. Cosmochim. Acta, 57*, 4575–4581.

Clark, B. C., and D. C. Van Hart (1981), The Salts of Mars, *Icarus, 45*, 370–378.

Clark, B. C., et al. (2005), Chemistry and mineralogy of outcrops at Meridiani Planum, *Earth Planet. Sci. Lett., 240*, 73–94, doi:10.1016/j.epsl.2005.09.040.

Clark, B. C., et al. (2007), Evidence for montmorillonite or its compositional equivalent in Columbia Hills, Mars, *J. Geophys. Res., 112*, E06S01, doi:10.1029/2006JE002756.

Clark, R. N. (1999), Spectroscopy of Rocks and Minerals, and Principles of Spectroscopy, in *Manual of Remote Sensing, Volume 3, Remote Sensing for the Earth Sciences*, edited by A. N. Rencz, pp. 3–58, John Wiley and Sons, New York.

Clark, R. N., T. V. V. King, M. Klejwa, G. A. Swayze, and N. Vergo (1990), High spectral resolution reflectance spectroscopy of minerals, *J. Geophys. Res., 95*, 12,653–12,680, doi:10.1029/JB095iB08p12653.

Clark, R. N., G. A. Swayze, K. E. Livo, R. F. Kokaly, S. J. Sutley, J. B. Dalton, R. R. McDougal, and C. A. Gent (2003), Imaging spectroscopy: Earth and planetary remote sensing with the USGS Tetracorder and expert systems, *J. Geophys. Res., 108*(E12), 5131, doi:10.1029/2002JE001847.

Clark, R. N., G. A. Swayze, R. A. Wise, K. E. Livo, T. M. Hoefen, R. F. Kokaly, and S. J. Sutley (2007), USGS digital spectral library splib06a, U.S. Geological Survey, Digital Data Series 231.

Cloutis, E. A., and J. F. Bell III (2000), Diaspores and related hydroxides: Spectral-compositional properties and implications for Mars, *J. Geophys. Res., 105*(E3), 7053–7070.

Cloutis, E. A., P. M. Asher, and S. A. Mertzman (2002), Spectral reflectance properties of zeolites and remote sensing implications, *J. Geophys. Res., 107*(E9), 5067, doi:10.1029/2000JE001467.

Cloutis, E. A., et al. (2006), Detection and discrimination of sulfate minerals using reflectance spectroscopy, *Icarus, 184*, 121–157, doi:10.1016/j.icarus.2006.04.003.

Cloutis, E. A., M. S. Rice, J. F. Bell III, S. A. Mertzman, D. L. Bish, and R. Renaut (2009), Spectral Reflectance Diversity of Silica-Rich Materials: Insights into Structure and Petrogenesis and Implications for Mars, *Lunar and Planetary Institute Contributions, 1482*, Abstract 4002.

Craddock, R. A., and A. D. Howard (2002), The case for rainfall on a warm, wet early Mars, *J. Geophys. Res., 107*(E11), 5111, doi:10.1029/2001JE001505.

Craddock, R. A., and T. A. Maxwell (1993), Geomorphic Evolution of the Martian Highlands Through Ancient Fluvial Processes, *J. Geophys. Res., 98*(E2), 3453–3468, doi:10.1029/92JE02508.

Crowley, J. K. (1991), Visible and near-infrared (0.4–2.5 μm) reflectance spectra of playa evaporite minerals, *J. Geophys. Res., 96*, 16,231–16,240.

Crowley, J. K., D. E. Williams, J. M. Hammarstrom, N. Piatak, I.-M. Chou, and J. C. Mars (2003), Spectral reflectance properties (0.4–2.5 μm) of secondary Fe-oxide, Fe-hydroxide, and Fe-sulphate-hydrate minerals associated with sulphide-bearing mine wastes, *Geochemistry: Explor. Environ. Anal., 3*, 219–228.

Crumpler, L. (2003), Physical Characteristics, Geologic Setting, and Possible Formation Processes of Spring Deposits on Mars Based on Terrestrial Analogs, *Sixth Int. Conf. on Mars*, Abstract 3228.

Dehouck, E., N. Mangold, S. Le Mouélic, V. Ansan, and F. Poulet (2010), Ismenius

Cavus, Mars: A deep paleolake with phyllosilicate deposits, *Planet. Space Sci., 58*, 941–946, doi:10.1016/j.pss.2010.02.005.

Delamere, W. A., et al. (2010), Color imaging of Mars by the High Resolution Imaging Science Experiment (HiRISE), *Icarus, 205*, 38–52, doi:10.1016/j.icarus.2009.03.012.

DeVries, R. J., and N. G. Barlow (2009), Central pit craters in the southern hemisphere of Mars, *Lunar Planet. Sci., XL*, Abstract 1929.

Di Achille, G., G. G. Ori, and D. Reiss (2007), Evidence for late Hesperian lacustrine activity in Shalbatana Vallis, Mars, *J. Geophys. Res., 112*, E07007, doi:10.1029/2006JE002858.

Di Achille, G., B. M. Hynek, and M. L. Searls (2009), Positive identification of lake strandlines in Shalbatana Vallis, Mars, *Geophys. Res. Lett., 36*, L14201, doi:10.1029/2009GL038854.

Dickson, J. L., and J. W. Head (2009), The formation and evolution of youthful gullies on Mars, *Icarus, 204*, 63–86, doi:10.1016/j.icarus.2009.06.018.

Dreyer, C. B., K. Zacny, R. C. Anderson, J. Skok, J. Steele, G. Paulsen, M. Szczesiak, and J. Schwendeman (2010), A rock thin section device for space exploration, *Lunar Planet. Sci., XLI*, Abstract 2573.

Dumke, A., M. Spiegel, R. Schmidt, and G. Neukum (2008), High-resolution digital terrain models and ortho-image mosaics of Mars: Generation on the basis of Mars-Express HRSC data, *Lunar Planet. Sci., XXXIX*, Abstract 1910.

Dundas, C. M., A. S. McEwen, S. Diniega, and S. Byrne (2010), New and Recent Gully Activity on Mars as Seen by HiRISE, *Geophys. Res. Lett., 37*, L07202, doi:10.1029/2009GL041351.

Dyar, M. D., and M. W. Schaefer (2008), Discriminating among layer silicates using remote Mössbauer spectroscopy, *Lunar and Planetary Institute Contributions,*

1441, Abstract 7034.

Dyar, M. D., M. W. Schaeffer, E. C. Sklute, and J. L. Bishop (2008), Mössbauer spectroscopy of phyllosilicates: effects of fitting models on recoil-free fractions and redox ratios, *Clay Miner., 43*, 3–33.

Eberl, D. D. (1984), Clay mineral formation and transformation in rocks and soils, *Phil. Trans. R. Soc. Lond. A, 311*, 241–257, doi:10.1098/rsta.1984.0026.

Edgett, K. S., and T. J. Parker (1997), Water on early Mars: Possible subaqueous sedimentary deposits covering ancient cratered terrain in western Arabia and Sinus Meridiani, *Geophys. Res. Lett., 24*(22), 2897–2900.

Edgett, K. S., and M. C. Malin (2002), Martian sedimentary rock stratigraphy: Outcrops and interbedded craters of northwest Sinus Meridiani and southwest Arabia Terra, *Geophys. Res. Lett., 29*(24), 2179, doi:10.1029/2002GL016515.

Ehlmann, B. L., J. F. Mustard, C. I. Fassett, S. C. Schon, J. W. Head, D. J. Des Marais, J. A. Grant, and S. L. Murchie (2008a), Clay minerals in delta deposits and organic preservation potential on Mars, *Nature Geosci., 1*, 355–358, doi:10.1038/ngeo207.

Ehlmann, B. L., et al. (2008b), Orbital Identification of Carbonate-Bearing Rocks on Mars, *Science, 322*, 1828–1832, doi:10.1126/science.1164759.

Ehlmann, B. L., et al. (2009), Identification of hydrated silicate minerals on Mars using MRO-CRISM: Geologic context near Nili Fossae and implications for aqueous alteration, *J. Geophys. Res., 114*, E00D08, doi:10.1029/2009JE003339.

El Maarry, M. R., W. J. Markiewicz, M. T. Mellon, W. Goetz, J. M. Dohm, and A. Pack (2010), Crater floor polygons: Desiccation patterns of ancient lakes on Mars?, *J. Geophys. Res., 115*, E10006, doi:10.1029/2010JE003609.

Farmer, J. D., and D. J. Des Marais (1999), Exploring for a record of ancient Martian

life, *J. Geophys. Res., 104*(E11), 26,977–26,995.

Farrand, W. H., T. D. Glotch, J. W. Rice Jr., J. A. Hurowitz, and G. A. Swayze (2009), Discovery of jarosite within the Mawrth Vallis region of Mars: Implications for the geologic history of the region, *Icarus, 204*, 478–488, doi:10.1016/j.icarus.2009.07.014.

Fassett, C. I., and J. W. Head III (2005), Fluvial sedimentary deposits on Mars: Ancient deltas in a crater lake in the Nili Fossae region, *Geophys. Res. Lett., 32*, L14201, doi:10.1029/2005GL023456.

Fassett, C. I., and J. W. Head III (2008a), The timing of martian valley network activity: Constraints from buffered crater counting, *Icarus, 195*(1), 61–89, doi:10.1016/j.icarus.2007.12.009.

Fassett, C. I., and J. W. Head III (2008b), Valley network-fed, open-basin lakes on Mars: Distribution and implications for Noachian surface and subsurface hydrology, *Icarus, 198*, 37–56, doi:10.1016/j.icarus.2008.06.016.

Fedorova, A. A., E. Lellouch, D. V. Titov, T. de Graauw, and H. Feuchtgruber (2002), Remote sounding of the Martian dust from ISO spectroscopy in the 2.7 μm CO_2 bands, *Planet. Space Sci., 50*, 3–9.

Feely, K. C., and P. R. Christensen (1999), Quantitative compositional analysis using thermal emission spectroscopy: Application to igneous and metamorphic rocks, *J. Geophys. Res., 104*(E10), 24,195–24,210, doi:10.1029/1999JE001034.

Fergason, R. L., P. R. Christensen, and H. H. Kieffer (2006), High-resolution thermal inertia derived from the Thermal Emission Imaging System (THEMIS): Thermal model and applications, *J. Geophys. Res., 111*, E12004, doi:10.1029/2006JE002735.

Fernández-Remolar, D. C., R. V. Morris, J. E. Gruener, R. Amils, and A. H. Knoll

(2005), The Río Tinto Basin, Spain: Mineralogy, sedimentary geobiology, and implications for interpretation of outcrop rocks at Meridiani Planum, Mars, *Earth Planet. Sci. Lett., 240*, 149–167, doi:10.1016/j.epsl.2005.09.043.

Ford, T. D., and H. M. Pedley (1996), A review of tufa and travertine deposits of the world, *Earth-Sci. Rev., 41*, 117–175.

Forsythe, R. D., and C. R. Blackwelder (1998), Closed drainage basins of the Martian highlands: Constraints on the early Martian hydrologic cycle, *J. Geophys. Res., 103*(E13), 31,421–31,431.

Foster, I. S., P. L. King, B. C. Hyde, and G. Southam (2010), Characterization of halophiles in natural $MgSO_4$ salts and laboratory enrichment samples: Astrobiological implications for Mars, *Planet. Space Sci., 58*, 599–615, doi:10.1016/j.pss.2009.08.009.

Fouke, B. W., J. D. Farmer, D. J. Des Marais, L. Pratt, N. C. Sturchio, P. C. Burns, and M. K. Discipulo (2000), Depositional Facies and Aqueous-Solid Geochemistry of Travertine-Depositing Hot Springs (Angel Terrace, Mammoth Hot Springs, Yellowstone National Park, U.S.A.), *J. Sed. Res., 70*, 565–585.

Freeman, J. J., A. Wang, and B. L. Jolliff (2007), Pathways to form kieserite from epsomite at mid to low temperatures, with relevance to Mars, *Lunar Planet. Sci., XXXVIII*, Abstract 1298.

Garvin, J. B., S. E. H. Sakimoto, and J. J. Frawley (2003), Craters on Mars: Global geometric properties from gridded MOLA topography, *Sixth Int. Conf. on Mars*, Abstract 3277.

Gendrin, A., et al. (2005), Sulfates in Martian Layered Terrains: The OMEGA/Mars Express View, *Science, 307*, 1587–1591, doi:10.1126/science.1109087.

Ghatan, G. J., and J. W. Head (2002), Candidate subglacial volcanoes in the south polar region of Mars: Morphology, morphometry, and eruption conditions, *J. Geophys. Res., 107*, 5048, doi:10.1029/2001JE001519.

Gilbert, G. K. (1890), Lake Bonneville, *U.S. Geol. Surv. Monogr., 1*, 438 pp.

Glotch, T. D., J. L. Bandfield, P. R. Christensen, W. M. Calvin, S. M. McLennan, B. C. Clark, A. D. Rogers, and S. W. Squyres (2006), Mineralogy of the light-toned outcrop at Meridiani Planum as seen by the Miniature Thermal Emission Spectrometer and implications for its formation, *J. Geophys. Res., 111*, E12S03, doi:10.1029/2005JE002672.

Glotch, T. D., J. L. Bandfield, L. L. Tornabene, H. B. Jensen, and F. P. Seelos (2010), Distribution and formation of chlorides and phyllosilicates in Terra Sirenum, Mars, *Geophys. Res. Lett., 37*, L16202, doi:10.1029/2010GL044557.

Goldspiel, J. M., and S. W. Squyres (1991), Ancient Aqueous Sedimentation on Mars, *Icarus, 89*, 392–410.

Golombek, M. P., et al. (2003), Selection of the Mars Exploration Rover landing sites, *J. Geophys. Res., 108*, 8072, doi:10.1029/2003JE002074.

Golombek, M., K. Robinson, A. McEwen, N. Bridges, B. Ivanov, L. Tornabene, and R. Sullivan (2010), Constraints on ripple migration at Meridiani Planum from Opportunity and HiRISE observations of fresh craters, *J. Geophys. Res., 115*, E00F08, doi:10.1029/2010JE003628.

Goodman, B. A., J. D. Russell, A. R. Fraser, and F. W. D. Woodhams (1976), A Mössbauer and I.R. spectroscopy study of the structure of nontronite, *Clays Clay Min., 24*, 53–59.

Grant, J. A., R. P. Irwin III, J. P. Grotzinger, R. E. Milliken, L. L. Tornabene, A. S. McEwen, C. M. Weitz, S. W. Squyres, T. D. Glotch, and B. J. Thomson (2008), HiRISE imaging of impact megabreccia and sub-meter aqueous strata

in Holden Crater, Mars, *Geology, 36,* 195–198, doi:10.1130/G24340A.1.

Grant, J. A., S. A. Wilson, E. Noe Dobrea, R. L. Fergason, J. L. Griffes, J. M. Moore, and A. D. Howard (2010), HiRISE views enigmatic deposits in the Sirenum Fossae region of Mars, *Icarus, 205*, 53–63, doi:10.1016/j.icarus.2009.04.009.

Grant, J. A., M. P. Golombek, J. P. Grotzinger, S. A. Wilson, M. M. Watkins, A. R. Vasavada, J. L. Griffes, and T. J. Parker, The science process for selecting the landing site for the 2011 Mars Science Laboratory, *Planet. Space Sci.*, doi:10.1016/j.pss.2010.06.016, in press.

Greeley, R., and J. E. Guest (1987), Geologic map of the eastern equatorial region of Mars, *U.S. Geol. Surv. Misc. Invest. Map, I-1802-B.*

Greeley, R., and P. D. Spudis (1981), Volcanism on Mars, *Rev. Geophys. Space Phys.*, *19*(1), 13–41.

Griffes, J. L., R. E. Arvidson, F. Poulet, and A. Gendrin (2007), Geologic and spectral mapping of etched terrain deposits in northern Meridiani Planum, *J. Geophys. Res.*, *112*, E08S09, doi:10.1029/2006JE002811.

Grotzinger, J. (2009), Beyond water on Mars, *Nature Geosci.*, *2*, 231–233, doi:10.1038/ngeo480.

Guidry, S. A., and H. S. Chafetz (2003), Anatomy of siliceous hot springs: examples from Yellowstone National Park, Wyoming, USA, *Sed. Geol., 157*, 71–106, doi:10.1016/S0037-0738(02)00195-1.

Hagerty, J. J., and H. E. Newsom (2003), Hydrothermal alteration at the Lonar Lake impact structure, India: Implications for impact cratering on Mars, *Meteor. Planet. Sci., 38*(3), 365–381.

Hamilton, V. E., and P. R. Christensen (2005), Evidence for extensive, olivine-rich bedrock on Mars, *Geology, 33*, 433–436, doi:10.1130/G21258.1.

Hand, K. P., R. W. Carlson, H. Sun, M. Anderson, W. Wadsworth, and R. Levy

(2005), Utilizing active mid-infrared microspectrometry for in-situ analysis of cryptoendolithic microbial communities of Battleship Promontory, Dry Valleys, Antarctica, in *Proc. of SPIE, 5906*, 590610.

Handford, C. R. (1991), Marginal marine halite: Sabkhas and salinas, in *Evaporites, Petroleum, and Mineral Resources*, edited by J. L. Melvin, Elsevier, New York.

Hanley, J., V. F. Chevrier, B. L. Davis, T. S. Altheide, and A. Francis (2010), Reflectance spectra of low-temperature chloride and perchlorate hydrates and their relevance to the Martian surface, *Lunar Planet. Sci., XLI*, Abstract 1953.

Hartmann, W. K., and G. Neukum (2001), Cratering chronology and the evolution of Mars, *Space Sci. Rev., 96*, 165–194.

Hausrath, E. M., A. K. Navarre-Sitchler, P. B. Sak, C. I. Steefel, and S. L. Brantley (2008), Basalt weathering rates on Earth and the duration of liquid water on the plains of Gusev Crater, Mars, *Geology, 36*(1), 67–70, doi:10.1130/G24238A.1.

Hoke, M. R. T., and B. M. Hynek (2009), Roaming zones of precipitation on ancient Mars as recorded in valley networks, *J. Geophys. Res., 114*, E08002, doi:10.1029/2008JE003247.

Horgan, B., J. F. Bell III, and M. C. Bourke (2010), Dry flow, surface cementation, and ice induration features on dunes in the north polar region of Mars, *Lunar Planet. Sci., XLI*, Abstract 1325.

Howard, A. D., and J. H. Moore (2007), The Light-toned Sediments in and near Lower Mawrth Vallis May be a Drape Deposit, *Lunar Planet. Sci., XXXVIII*, 1339.

Howard, A. D., J. M. Moore, and R. P. Irwin III (2005), An intense terminal epoch of widespread fluvial activity on early Mars: 1. Valley network incision and associated deposits, *J. Geophys. Res., 110*, E12S14, doi:10.1029/2005JE002459.

Hurowitz, J. A., and S. M. McLennan (2007), A ~3.5 Ga record of water-limited, acidic weathering conditions on Mars, *Earth Planet. Sci. Lett., 260*, 432–443, doi:10.1016/j.epsl.2007.05.043.

Hurowitz, J. A., W. W. Fischer, N. J. Tosca, and R. E. Milliken (2010), Origin of acidic surface waters and the evolution of atmospheric chemistry on early Mars, *Nature Geosci., 3*, 323–326, doi:10.1038/ngeo831.

Hynek, B. M., and R. J. Phillips (2001), Evidence for extensive denudation of the Martian highlands, *Geology*, 29, 407–410.

Hynek, B. M., R. E. Arvidson, and R. J. Phillips (2002), Geologic setting and origin of Terra Meridiani hematite deposit on Mars, *J. Geophys. Res., 107*(E10), 5088, doi:10.1029/2002JE001891.

Hynek, B. M., M. Beach, and M. R. T. Hoke (2010), Updated global map of Martian valley networks and implications for climate and hydrologic processes, *J. Geophys. Res., 115*, E09008, doi:10.1029/2009JE003548.

Irwin, R. P., III, T. A. Maxwell, A. D. Howard, R. A. Craddock, and D. W. Leverington (2002), A Large Paleolake Basin at the Head of Ma'adim Vallis, Mars, *Science, 296*, 2209–2212.

Irwin, R. P., III, A. D. Howard, R. A. Craddock, and J. M. Moore (2005), An intense terminal epoch of widespread fluvial activity on early Mars: 2. Increased runoff and paleolake development, *J. Geophys. Res., 110*, E12S15, doi:10.1029/2005JE002460.

Irwin, R. P., III, R. A. Craddock, A. D. Howard, and H. L. Flemming (2011), Topographic influences on development of Martian valley networks, *J. Geophys. Res.*, doi:10.1029/2010JE003620, in press.

Ivanov, M. A., and J. W. Head (2001), Chryse Planitia, Mars: Topographic configuration, outflow channel continuity and sequence, and tests for

hypothesized ancient bodies of water using Mars Orbiter Laser Altimeter (MOLA) data, *J. Geophys. Res.*, *106*(E2), 3275–3296, doi:10.1029/2000JE001257.

Jakosky, B. M., and R. J. Phillips (2001), Mars' volatile and climate history, *Nature*, *412*, 237–244.

Johnson, J. R., J. F. Bell, E. Cloutis, M. Staid, W. H. Farrand, T. McCoy, M. Rice, A. Wang, and A. Yen (2007), Mineralogic constraints on sulfur-rich soils from Pancam spectra at Gusev crater, Mars, *Geophys. Res. Lett.*, *34*, L13202, doi:10.1029/2007GL029894.

Johnson, S. S., M. A. Mischna, T. L. Grove, and M. T. Zuber (2008), Sulfur-induced greenhouse warming on early Mars, *J. Geophys. Res.*, *113*, E08005, doi:10.1029/2007JE002962.

Jouglet, D., F. Poulet, R. E. Milliken, J. F. Mustard, J.-P. Bibring, Y. Langevin, B. Gondet, and C. Gomez (2007), Hydration state of the Martian surface as seen by Mars Express OMEGA: 1. Analysis of the 3 μm hydration feature, *J. Geophys. Res.*, *112*, E08S06, doi:10.1029/2006JE002846.

Kahn, R. (1985), The Evolution of CO_2 on Mars, *Icarus*, *62*, 175–190.

Karunatillake, S., J. J. Wray, S. W. Squyres, G. J. Taylor, O. Gasnault, S. M. McLennan, W. Boynton, M. R. El Maarry, and J. M. Dohm (2009), Chemically striking regions on Mars and Stealth revisited, *J. Geophys. Res.*, *114*, E12001, doi:10.1029/2008JE003303.

Kasting, J. F. (1997), Warming Early Earth and Mars, *Science*, *276*, 1213–1215.

Kirk, R. L., et al. (2008), Ultrahigh resolution topographic mapping of Mars with MRO HiRISE stereo images: Meter-scale slopes of candidate Phoenix landing sites, *J. Geophys. Res.*, *113*, E00A24, doi:10.1029/2007JE003000.

Kirkland, L. E., K. C. Herr, and P. M. Adams (2003), Infrared stealthy surfaces: Why

TES and THEMIS may miss some substantial mineral deposits on Mars and implications for remote sensing of planetary surfaces, *J. Geophys. Res.*, *108*(E12), 5137, doi:10.1029/2003JE002105.

Klingelhöfer, G., et al. (2004), Jarosite and Hematite at Meridiani Planum from Opportunity's Mössbauer Spectrometer, *Science, 306*, 1740–1745, doi:10.1126/science.1104653.

Kloprogge, J. T. (2006), Spectroscopic studies of synthetic and natural beidellites: A review, *Appl. Clay Sci.*, *31*, 165–179, doi:10.1016/j.clay.2005.10.003.

Kolb, K. J., A. S. McEwen, V. C. Gulick, and the HiRISE Team (2007), Gullies potentially formed by water from the subsurface, *Lunar Planet. Sci.*, *XXXVIII*, Abstract 1391.

Kounaves, S. P., et al. (2010), Soluble sulfate in the martian soil at the Phoenix landing site, *Geophys. Res. Lett., 37*, L09201, doi:10.1029/2010GL042613.

Kraal, E. R., E. Asphaug, J. M. Moore, and R. D. Lorenz (2006), Quantitative geomorphic modeling of Martian bedrock shorelines, *J. Geophys. Res., 111*, E03001, doi:10.1029/2005JE002567.

Kreslavsky, M. A., and J. W. Head (2002), Fate of outflow channel effluents in the northern lowlands of Mars: The Vastitas Borealis Formation as a sublimation residue from frozen ponded bodies of water, *J. Geophys. Res., 107*(E12), 5121, doi:10.1029/2001JE001831.

Kuzmin, R. O., M. V. Mironenko, and N. A. Evdokimova (2009), Spectral and thermodynamic constraints on the existence of gypsum at the Juventae Chasma on Mars, *Planet. Space Sci., 57*, 975–981, doi:10.1016/j.pss.2008.12.008.

Lane, M. D., M. D. Dyar, and J. L. Bishop (2004), Spectroscopic evidence for hydrous iron sulfate in the Martian soil, *Geophys. Res. Lett., 31*, L19702, doi:10.1029/2004GL021231.

Lane, M. D. (2007), Mid-infrared emission spectroscopy of sulfate and sulfate-bearing minerals, *Am. Mineral., 92,* 1–18, doi:10.2138/am.2007.2170.

Lane, M. D., J. L. Bishop, M. D. Dyar, P. L. King, M. Parente, and B. C. Hyde (2008), Mineralogy of the Paso Robles soils on Mars, *Am. Mineral., 93,* 728–739, doi:10.2138/am.2008.2757.

Langevin, Y., F. Poulet, J.-P. Bibring, and B. Gondet (2005), Sulfates in the North Polar Region of Mars Detected by OMEGA/Mars Express, *Science, 307,* 1584–1586, doi:10.1126/science.1109091.

Le Deit, L., S. Le Mouélic, O. Bourgeois, J.-P. Combe, D. Mège, C. Sotin, A. Gendrin, E. Hauber, N. Mangold, and J.-P. Bibring (2008), Ferric oxides in East Candor Chasma, Valles Marineris (Mars) inferred from analysis of OMEGA/Mars Express data: Identification and geological interpretation, *J. Geophys. Res., 113,* E07001, doi:10.1029/2007JE002950.

Lellouch, E., T. Encrenaz, T. de Graauw, S. Erard, P. Morris, J. Crovisier, H. Feuchtgruber, T. Girard, and M. Burgdorf (2000), The 2.4–45 μm spectrum of Mars observed with the Infrared Space Observatory, *Planet. Space Sci., 48,* 1393–1405.

Leroi, V., J.-P. Bibring, and M. Berthe (2009), Micromega/IR: Design and status of a near-infrared spectral microscope for in situ analysis of Mars samples, *Planet. Space Sci., 57,* 1068–1075, doi:10.1016/j.pss.2008.12.014.

Leverington, D. W., and T. A. Maxwell (2004), An igneous origin for features of a candidate crater-lake system in western Memnonia, Mars, *J. Geophys. Res., 109,* E06006, doi:10.1029/2004JE002237.

Lewis, K. W., and O. Aharonson (2006), Stratigraphic analysis of the distributary fan in Eberswalde crater using stereo imagery, *J. Geophys. Res., 111,* E06001, doi:10.1029/2005JE002558.

Lichtenberg, K. A., et al. (2010), Stratigraphy of hydrated sulfates in the sedimentary deposits of Aram Chaos, Mars, *J. Geophys. Res., 115*, E00D17, doi:10.1029/2009JE003353.

Loizeau, D., et al. (2007), Phyllosilicates in the Mawrth Vallis region of Mars, *J. Geophys. Res., 112*, E08S08, doi:10.1029/2006JE002877.

Loizeau, D., et al. (2010), Stratigraphy in the Mawrth Vallis region through OMEGA, HRSC color imagery and DTM, *Icarus, 205*, 396–418, doi:10.1016/j.icarus.2009.04.018.

Longhi, J., E. Knittle, J. R. Holloway, and H. Wänke (1992), The bulk composition, mineralogy and internal structure of Mars, in *Mars*, edited by H. H. Kieffer, B. M. Jakosky, C. W. Snyder, and M. S. Matthews, pp. 184–208, The University of Arizona Press, Tucson.

Lorenz, R. D., E. R. Kraal, E. E. Eddlemon, J. Cheney, and R. Greeley (2005), Sea-surface wave growth under extraterrestrial atmospheres: Preliminary wind tunnel experiments with application to Mars and Titan, *Icarus, 175*, 556–560, doi:10.1016/j.icarus.2004.11.019.

Madejová, J., M. Pentrák, H. Pálková, and P. Komadel (2009), Near-infrared spectroscopy: A powerful tool in studies of acid-treated clay minerals, *Vibrational Spectroscopy, 49*, 211–218, doi:10.1016/j.vibspec.2008.08.001.

Mahaffy, P. (2008), Exploration of the Habitability of Mars: Development of Analytical Protocols for Measurement of Organic Carbon on the 2009 Mars Science Laboratory, *Space Sci. Rev., 135*, 255–268, doi:10.1007/s11214-007-9223-1.

Mal, D., S. Sinha, T. Dutta, S. Mitra, and S. Tarafdar (2007), Formation of Crack Patterns in Clay Films: Desiccation and Relaxation, *J. Phys. Soc. Jap., 76*(1), 014801, doi:10.1143/jpsj.76.014801.

Malin, M. C., and K. S. Edgett (1999), Oceans or seas in the Martian northern lowlands: High resolution imaging tests of proposed coastlines, *Geophys. Res. Lett., 26*(19), 3049–3052.

Malin, M. C., and K. S. Edgett (2000), Sedimentary Rocks of Early Mars, *Science, 290*, 1927–1937.

Malin, M. C., and K. S. Edgett (2001), Mars Global Surveyor Mars Orbiter Camera: Interplanetary cruise through primary mission, *J. Geophys. Res., 106*(E10), 23,429–23,570.

Malin, M. C., and K. S. Edgett (2003), Evidence for Persistent Flow and Aqueous Sedimentation on Early Mars, *Science, 302*, 1931–1934, doi:10.1126/science.1090544.

Malin, M. C., G. E. Danielson, A. P. Ingersoll, H. Masursky, J. Veverka, M. A. Ravine, and T. A. Soulanille (1992), Mars Observer Camera, *J. Geophys. Res., 97*(E5), 7699–7718.

Malin, M. C., K. S. Edgett, L. V. Posiolova, S. M. McColley, and E. Z. Noe Dobrea (2006), Present-Day Impact Cratering Rate and Contemporary Gully Activity on Mars, *Science, 314*, 1573–1577, doi:10.1126/science.1135156.

Malin, M. C., et al. (2007), Context Camera Investigation on board the Mars Reconnaissance Orbiter, *J. Geophys. Res., 112*, E05S04, doi:10.1029/2006JE002808.

Mangold, N., A. Gendrin, B. Gondet, S. LeMouelic, C. Quantin, V. Ansan, J.-P. Bibring, Y. Langevin, P. Masson, and G. Neukum (2008), Spectral and geological study of the sulfate-rich region of West Candor Chasma, Mars, *Icarus, 194*, 519–543, doi:10.1016/j.icarus.2007.10.021.

Mangold, N., L. Roach, R. Milliken, S. Le Mouélic, V. Ansan, J.-P. Bibring, Ph. Masson, J. F. Mustard, S. Murchie, and G. Neukum (2010), A Late Amazonian

alteration layer related to local volcanism on Mars, *Icarus, 207*, 265–276, doi:10.1016/j.icarus.2009.10.015.

Marzo, G. A., T. L. Roush, N. L. Lanza, P. C. McGuire, H. E. Newsom, A. M. Ollila, and S. M. Wiseman (2009), Association of phyllosilicates and the inverted channel in Miyamoto crater, Mars, *Geophys. Res. Lett., 36*, L11204, doi:10.1029/2009GL038703.

McCauley, J. F. (1973), Mariner 9 Evidence for Wind Erosion in the Equatorial and Mid-Latitude Regions of Mars, *J. Geophys. Res., 78*(20), 4123–4137.

McCord, T. B., R. N. Clark, and R. B. Singer (1982), Mars: Near-Infrared Spectral Reflectance of Surface Regions and Compositional Implications, *J. Geophys. Res., 87*(B4), 3021–3032.

McCord, T. B., G. B. Hansen, and C. A. Hibbitts (2001), Hydrated Salt Minerals on Ganymede's Surface: Evidence of an Ocean Below, *Science*, *292*, 1523–1525.

McEwen, A. S., B. S. Preblich, E. P. Turtle, N. A. Artemieva, M. P. Golombek, M. Hurst, R. L. Kirk, D. M. Burr, and P. R. Christensen (2005), The rayed crater Zunil and interpretations of small impact craters on Mars, *Icarus, 176*, 351–381, doi:10.1016/j.icarus.2005.02.009.

McEwen, A. S., et al. (2007), Mars Reconnaissance Orbiter's High Resolution Imaging Science Experiment (HiRISE), *J. Geophys. Res., 112*, E05S02, doi:10.1029/2005JE002605.

McEwen, A. S., L. Tornabene, J. Grant, J. Wray, and J. Mustard (2008), Noachian Megabreccia on Mars, *Eos Trans. AGU, 89*(53), Fall Meet. Suppl., Abstract P43D-03.

McEwen, A. S., et al. (2010), The High Resolution Imaging Science Experiment (HiRISE) during MRO's Primary Science Phase (PSP), *Icarus, 205*, 2–37, doi:10.1016/j.icarus.2009.04.023.

McEwen, A., et al. (2011), HiSCI Experiment on ExoMars Trace Gas Orbiter, *Fourth International Workshop on the Mars Atmosphere: Modeling and Observations*, Paris, France, February 8–11, 2011.

McGuire, P. C., et al. (2009), An improvement to the volcano-scan algorithm for atmospheric correction of CRISM and OMEGA spectral data, *Planet. Space Sci., 57*, 809–815, doi:10.1016/j.pss.2009.03.007.

McKay, C. P., G. D. Clow, R. A. Wharton Jr., and S. W. Squyres (1985), Thickness of ice on perennially frozen lakes, *Nature, 313*, 561–562.

McKeown, N. K., J. L. Bishop, E. Z. Noe Dobrea, B. L. Ehlmann, M. Parente, J. F. Mustard, S. L. Murchie, G. A. Swayze, J.-P. Bibring, and E. A. Silver (2009), Characterization of phyllosilicates observed in the central Mawrth Vallis region, Mars, their potential formational processes, and implications for past climate, *J. Geophys. Res., 114*, E00D10, doi:10.1029/2008JE003301.

McKeown, N. K., J. L. Bishop, E. Amador, J. Cuadros, S. Hillier, H. D. Makarewicz, M. Parente, and E. A. Silver (2010), Spectral mixtures of clays and their impact on CRISM mineral identifications, *Lunar Planet. Sci., XLI*, Abstract 2510.

McLennan, S. M., et al. (2005), Provenance and diagenesis of the evaporite-bearing Burns formation, Meridiani Planum, Mars, *Earth Planet. Sci. Lett., 240*, 95–121, doi:10.1016/j.epsl.2005.09.041.

Mellon, M. T., R. E. Arvidson, J. J. Marlow, R. J. Phillips, and E. Asphaug (2008), Periglacial landforms at the Phoenix landing site and the northern plains of Mars, *J. Geophys. Res., 113*, E00A23, doi:10.1029/2007JE003039.

Melosh, H. J. (1989), Impact Cratering: A Geologic Process, 245 pp., Oxford Univ. Press, New York.

MEPAG 2R-iSAG (2010), Two Rovers to the Same Site on Mars, 2018: Possibilities

for Cooperative Science, *Astrobiology, 10*(7), 663–685, doi:10.1089/ast.2010.0526.

MEPAG MRR-SAG (2010), The Mars Astrobiology Explorer-Cacher (MAX-C): A Potential Rover Mission for 2018, *Astrobiology, 10*(2), 127–163, doi:10.1089/ast.2010.0462.

Metz, J. M., J. P. Grotzinger, D. Mohrig, R. Milliken, B. Prather, C. Pirmez, A. S. McEwen, and C. M. Weitz (2009), Sublacustrine depositional fans in southwest Melas Chasma, *J. Geophys. Res., 114*, E10002, doi:10.1029/2009JE003365.

Metz, J., J. Grotzinger, C. Okubo, and R. Milliken (2010), Thin-skinned deformation of sedimentary rocks in Valles Marineris, Mars, *J. Geophys. Res., 115*, E11004, doi:10.1029/2010JE003593.

Michalski, J.R., and R. L. Fergason (2009), Composition and thermal inertia of the Mawrth Vallis region of Mars from TES and THEMIS data, *Icarus, 199*, 25–48, doi:10.1016/j.icarus.2008.08.016.

Michalski, J. R., and P. B. Niles (2010), Deep crustal carbonate rocks exposed by meteor impact on Mars, *Nature Geosci., 3*, 751–755, doi:10.1038/ngeo971.

Michalski, J. R., and E. Z. Noe Dobrea (2007), Evidence for a sedimentary origin of clay minerals in the Mawrth Vallis region, Mars, *Geology, 35*(10), 951-954, doi:10.1130/G23854A.

Michalski, J. R., M. D. Kraft, T. G. Sharp, L. B. Williams, and P. R. Christensen (2006), Emission spectroscopy of clay minerals and evidence for poorly crystalline aluminosilicates on Mars from Thermal Emission Spectrometer data, *J. Geophys. Res., 111*, E03004, doi:10.1029/2005JE002438.

Michalski, J. R., et al. (2010), The Mawrth Vallis Region of Mars: A Potential Landing Site for the Mars Science Laboratory (MSL) Mission, *Astrobiology,*

10(7), 687–703, doi:10.1089/ast.2010.0491.

Milliken, R. E. (2006), Estimating the water content of geologic materials using near-infrared reflectance spectroscopy: Applications to laboratory and spacecraft data, Ph.D. Thesis, Brown University, Providence, RI, 404 pp.

Milliken, R. E. (2008), Which clays are really present on Mars and how did they form?, *Lunar and Planetary Institute Contributions, 1441*, Abstract 7009.

Milliken, R. E., and D. L. Bish (2010), Sources and sinks of clay minerals on Mars, *Philos. Mag., 90*, 2293–2308, doi:10.1080/14786430903575132.

Milliken, R. E., and J. F. Mustard (2005), Quantifying absolute water content of minerals using near-infrared reflectance spectroscopy, *J. Geophys. Res., 110*, E12001, doi:10.1029/2005JE002534.

Milliken, R. E., and A. S. Rivkin (2009), Brucite and carbonate assemblages from altered olivine-rich materials on Ceres, *Nature Geosci., 2*, 258–261, doi:10.1038/ngeo478.

Milliken, R. E., J. F. Mustard, F. Poulet, D. Jouglet, J.-P. Bibring, B. Gondet, Y. Langevin, and the OMEGA team (2007), Hydration state of the Martian surface as seen by Mars Express OMEGA II: H_2O content of the surface, *J. Geophys. Res.*, 112(E8), doi:10.1029/2006JE002853.

Milliken, R. E., et al. (2008), Opaline silica in young deposits on Mars, *Geology, 36*, 847–850, doi:10.1130/G24967A.1.

Milliken, R. E., W. W. Fischer, and J. A. Hurowitz (2009), Missing salts on early Mars, *Geophys. Res. Lett., 36*, L11202, doi:10.1029/2009GL038558.

Milliken, R. E., J. P. Grotzinger, and B. J. Thomson (2010), The paleoclimate of Mars as captured by the stratigraphic record in Gale Crater, *Geophys. Res. Lett., 37*, L04201, doi:10.1029/2009GL041870.

Moller, P., et al. (1997), Paleofluids and recent fluids in the upper continental crust:

Results from the German Continental Deep Drilling Program (KTB), *J. Geophys. Res.*, *102*, 18,233–18,254.

Moore, J. M., and A. D. Howard (2005), Large alluvial fans on Mars, *J. Geophys. Res.*, *110*, E04005, doi:10.1029/2004JE002352.

Moore, J. M., G. D. Clow, W. L. Davis, V. C. Gulick, D. R. Janke, C. P. McKay, C. R. Stoker, and A. P. Zent (1995), The circum-Chryse region as a possible example of a hydrologic cycle on Mars: Geologic observations and theoretical evaluation, *J. Geophys. Res.*, *100*(E3), 5433–5447.

Moore, J. M., A. D. Howard, W. E. Dietrich, and P. M. Schenk (2003), Martian Layered Fluvial Deposits: Implications for Noachian Climate Scenarios, *Geophys. Res. Lett.*, *30*, 2292, doi:10.1029/2003GL019002.

Moore, J. M., M. A. Bullock, H. Newsom, and M. Nelson (2010), Laboratory simulations of Mars evaporite geochemistry, *J. Geophys. Res.*, *115*, E06009, doi:10.1029/2008JE003208.

Morgan, G. A., J. W. Head, F. Forget, J.-B. Madeleine, and A. Spiga (2010), Gully formation on Mars: Two recent phases of formation suggested by links between morphology, slope orientation and insolation history, *Icarus*, *208*, 658–666, doi:10.1016/j.icarus.2010.02.019.

Mormile, M. R., B.-Y. Hong, and K. C. Benison (2009), Molecular Analysis of the Microbial Communities of Mars Analog Lakes in Western Australia, *Astrobiology*, *9*(10), 919–930, doi:10.1089/ast.2008.0293.

Morris, R. V., and G. Klingelhöfer (2008), Iron mineralogy and aqueous alteration on Mars from the MER Mössbauer spectrometers, in *The Martian Surface: Composition, Mineralogy, and Physical Properties*, edited by J. Bell, pp. 339–365, Cambridge University Press, Cambridge.

Morris, R. V., et al. (2000), Mineralogy, composition, and alteration of Mars

Pathfinder rocks and soils: Evidence from multispectral, elemental, and magnetic data on terrestrial analogue, SNC meteorite, and Pathfinder samples, *J. Geophys. Res., 105*(E1), 1757–1817, doi:10.1029/1999JE001059.

Morris, R. V., et al. (2006a), Mössbauer mineralogy of rock, soil, and dust at Gusev crater, Mars: Spirit's journey through weakly altered olivine basalt on the plains and pervasively altered basalt in the Columbia Hills, *J. Geophys. Res., 111*, E02S13, doi:10.1029/2005JE002584.

Morris, R. V., et al. (2006b), Mössbauer mineralogy of rock, soil, and dust at Meridiani Planum, Mars: Opportunity's journey across sulfate-rich outcrop, basaltic sand and dust, and hematite lag deposits, *J. Geophys. Res., 111*, E12S15, doi:10.1029/2006JE002791.

Morris, R. V., et al. (2008), Iron mineralogy and aqueous alteration from Husband Hill through Home Plate at Gusev Crater, Mars: Results from the Mössbauer instrument on the Spirit Mars Exploration Rover, *J. Geophys. Res., 113*, E12S42, doi:10.1029/2008JE003201.

Morris, R. V., D. C. Golden, D. W. Ming, T. G. Graff, R. E. Arvidson, S. M. Wiseman, K. A. Lichtenberg, and S. Cull (2009), Visible and near-IR reflectance spectra for smectite, sulfate and perchlorate under dry conditions for interpretation of Martian surface mineralogy. *Lunar Planet. Sci., XL*, Abstract 2317.

Morris, R. V., et al. (2010), Identification of Carbonate-Rich Outcrops on Mars by the Spirit Rover, *Science, 329*, 421–424, doi:10.1126/science.1189667.

Mueller, K., and M. Golombek (2004), Compressional Structures on Mars, *Annu. Rev. Earth Planet. Sci., 32*, 435–464, doi:10.1146/annurev.earth.32.101802.120553.

Müller, G. (1998), Starch columns: Analog model for basalt columns, *J. Geophys. Res., 103*(B7), 15,239–15,253.

Murad, E., and U. Wagner (1989), Pure and impure clays and their firing products, *Hyperfine Interactions, 45*, 161–177.

Murchie, S., J. Mustard, J. Bishop, J. Head, and C. Pieters (1993), Spatial Variations in the Spectral Properties of Bright Regions on Mars, *Icarus, 105*, 454–468.

Murchie, S., L. Kirkland, S. Erard, J. Mustard, and M. Robinson (2000), Near-Infrared Spectral Variations of Martian Surface Materials from ISM Imaging Spectrometer Data, *Icarus, 147*, 444–471.

Murchie, S., et al. (2007), Compact Reconnaissance Imaging Spectrometer for Mars (CRISM) on Mars Reconnaissance Orbiter (MRO), *J. Geophys. Res., 112*, E05S03, doi:10.1029/2006JE002682.

Murchie, S., et al. (2009a), Evidence for the origin of layered deposits in Candor Chasma, Mars, from mineral composition and hydrologic modeling, *J. Geophys. Res., 114*, E00D05, doi:10.1029/2009JE003343.

Murchie, S. L., et al. (2009b), A synthesis of Martian aqueous mineralogy after 1 Mars year of observations from the Mars Reconnaissance Orbiter, *J. Geophys. Res., 114*, E00D06, doi:10.1029/2009JE003342.

Murchie, S. L., et al. (2009c), Compact Reconnaissance Imaging Spectrometer for Mars investigation and data set from the Mars Reconnaissance Orbiter's primary science phase, *J. Geophys. Res., 114*, E00D07, doi:10.1029/2009JE003344.

Mustard, J. F., and J. M. Sunshine (1995), Seeing Through the Dust: Martian Crustal Heterogeneity and Links to the SNC Meteorites, *Science, 267*, 1623–1626.

Mustard, J. F., S. Erard, J.-P. Bibring, J. W. Head, S. Hurtrez, Y. Langevin, C. M. Pieters, and C. J. Sotin (1993), The Surface of Syrtis Major: Composition of the Volcanic Substrate and Mixing With Altered Dust and Soil, *J. Geophys. Res., 98*(E2), 3387–3400.

Mustard, J. F., S. Murchie, S. Erard, and J. Sunshine (1997), In situ compositions of Martian volcanics: Implications for the mantle, *J. Geophys. Res.*, *102*(E11), 25,605–25,615.

Mustard, J. F., C. D. Cooper, and M. K. Rifkin (2001), Evidence for recent climate change on Mars from the identification of youthful near-surface ground ice, *Nature*, *412*, 411–414.

Mustard, J. F., F. Poulet, A. Gendrin, J.-P. Bibring, Y. Langevin, B. Gondet, N. Mangold, G. Bellucci, and F. Altieri (2005), Olivine and Pyroxene Diversity in the Crust of Mars, *Science*, *307*, 1595–1597, doi:10.1126/science.1109098.

Mustard, J. F., et al. (2008), Hydrated silicate minerals on Mars observed by the Mars Reconnaissance Orbiter CRISM instrument, *Nature*, *454*, 305–309, doi:10.1038/nature07097.

Mustard, J. F., B. L. Ehlmann, S. L. Murchie, F. Poulet, N. Mangold, J. W. Head, J.-P. Bibring, and L. H. Roach (2009), Composition, morphology, and stratigraphy of Noachian crust around the Isidis basin, *J. Geophys. Res.*, *114*, E00D12, doi:10.1029/2009JE003349.

Nedell, S. S., D. W. Andersen, S. W. Squyres, and F. G. Love (1987), Sedimentation in ice-covered Lake Hoare, Antarctica, *Sedimentology*, *34*, 1093–1106.

Neukum, G., and R. Jaumann (2004), HRSC: the High Resolution Stereo Camera of Mars Express, in *Mars Express: The Scientific Payload*, edited by A. Wilson, *Eur. Space Agency Spec. Publ., ESA SP-1240*, 17–35.

Newsom, H. E., G. E. Brittelle, C. A. Hibbitts, L. J. Crossey, and A. M. Kudo (1996), Impact crater lakes on Mars, *J. Geophys. Res.*, *101*(E6), 14,951–14,955.

Niederberger, T. D., N. N. Perreault, S. Tille, B. Sherwood Lollar, G. Lacrampe Couloume, D. Andersen, C. W. Greer, W. Pollard, and L. G. Whyte (2010), Microbial characterization of a subzero, hypersaline methane seep in the

Canadian High Arctic, *Int. Soc. Microb. Ecol. J.*, *4*(10), 1326–1339, doi:10.1038/ismej.2010.57.

Noe Dobrea, E. Z., and G. Swayze (2010), Acid Pedogenesis on Mars? Evidence for top-down alteration on Mars from CRISM and HiRISE data, *Lunar Planet. Sci., XLI*, Abstract 2620.

Noe Dobrea, E. Z., F. Poulet, and M. C. Malin (2008a), Correlations between hematite and sulfates in the chaotic terrain east of Valles Marineris, *Icarus, 193*, 516–534, doi:10.1016/j.icarus.2007.06.029.

Noe Dobrea, E. Z., et al. (2008b), Clay Bearing Units in the Region Around Mawrth Vallis: Stratigraphy, Extent, and Possible Alteration Fronts, *Lunar Planet. Sci., XXXIX*, 1077.

Noe Dobrea, E. Z., J. Moore, A. Howard, D. Catling, and J. Grant (2008c), Spectral and Geomorphic Evidence for a Past Inland Sea in Eridania Basin, Mars, *Eos Trans. AGU, 89*(53), Fall Meet. Suppl., Abstract P32B-03.

Noe Dobrea, E. Z., et al. (2010), Mineralogy and stratigraphy of phyllosilicate-bearing and dark mantling units in the greater Mawrth Vallis / west Arabia Terra area: Constraints on geological origin, *J. Geophys. Res., 115*, E00D19, doi:10.1029/2009JE003351.

Nuñez, J. I., J. D. Farmer, R. G. Sellar, and P. B. Gardner (2009), The Multispectral Microscopic Imager (MMI) with Improved Spectral Range and Resolution, *Lunar Planet. Sci., XL*, Abstract 1830.

Nuñez, J. I., J. D. Farmer, R. G. Sellar, and C. C. Allen (2010), The Multispectral Microscopic Imager: Integrating Microimaging with Spectroscopy for the In-Situ Exploration of the Moon, *Lunar Planet. Sci., XLI*, Abstract 1581.

Okubo, C. H., and A. S. McEwen (2007), Fracture-Controlled Paleo-Fluid Flow in Candor Chasma, Mars, *Science, 315*(5814), 983–985,

doi:10.1126/science.1136855.

Okubo, C. H., R. A. Schultz, M. A. Chan, G. Komatsu, and HiRISE Team (2009), Deformation band clusters on Mars and implications for subsurface fluid flow, *Geol. Soc. Am. Bull., 121*, 474–482, doi:10.1130/B26421.1.

Orofino, V., J. Goldspiel, I. Carofalo, A. Blanco, S. Fonti, and G. A. Marzo (2009), Evaluation of carbonate abundance in putative martian paleolake basins, *Icarus, 200*, 426–435, doi:10.1016/j.icarus.2008.11.020.

Osinski, G. R. (2003), Impact glasses in fallout suevites from the Ries impact structure, Germany: An analytical SEM study, *Meteor. Planet. Sci.*, *38*(11), 1641–1667.

Osinski, G. R., J. G. Spray, and P. Lee (2001), Impact-induced hydrothermal activity within the Haughton impact structure, arctic Canada: Generation of a transient, warm, wet oasis, *Meteor. Planet. Sci.*, *36*, 731–745.

Osinski, G. R., R. A. F. Grieve, and J. G. Spray (2004), The nature of the groundmass of surficial suevite from the Ries impact structure, Germany, and constraints on its origin, *Meteor. Planet. Sci.*, *39*(10), 1655–1683.

Osinski, G. R., P. Lee, J. Parnell, J. G. Spray, and M. Baron (2005), A case study of impact-induced hydrothermal activity: The Haughton impact structure, Devon Island, Canadian High Arctic, *Meteor. Planet. Sci., 40*(12), 1859–1877.

Osterloo, M. M., V. E. Hamilton, J. L. Bandfield, T. D. Glotch, A. M. Baldridge, P. R. Christensen, L. L. Tornabene, and F. S. Anderson (2008), Chloride-Bearing Materials in the Southern Highlands of Mars, *Science, 319*, 1651–1654, doi:10.1126/science.1150690.

Osterloo, M. M., F. S. Anderson, V. E. Hamilton, and B. M. Hynek (2010), Geologic context of proposed chloride-bearing materials on Mars, *J. Geophys. Res., 115*, E10012, doi:10.1029/2010JE003613.

Palomba, E., A. Zinzi, E. A. Cloutis, M. D'Amore, D. Grassi, and A. Maturilli (2009), Evidence for Mg-rich carbonates on Mars from a 3.9 μm absorption feature, *Icarus, 203*, 58–65, doi:10.1016/j.icarus.2009.04.013.

Parente, M. (2008), A new approach to denoising CRISM images, *Lunar Planet. Sci., XXXIX*, Abstract 2528.

Pedley, H. M. (1990), Classification and environmental models of cool freshwater tufas, *Sed. Geol., 68*, 143–154.

Pelkey, S. M., et al. (2007), CRISM multispectral summary products: Parameterizing mineral diversity on Mars from reflectance, *J. Geophys. Res., 112*, E08S14, doi:10.1029/2006JE002831.

Phillips, R. J., et al. (2001), Ancient geodynamics and global-scale hydrology on Mars, *Science, 291*(5513), 2587–2591, doi:10.1126/science.1058701.

Pina, P., J. Saraiva, L. Bandeira, and T. Barata (2006), Identification of Martian Polygonal Patterns Using the Dynamics of Watershed Contours, *Lect. Notes Comput. Sci., 4142*, 691–699.

Pina, P., J. Antunes, L. Bandeira, and J. Saraiva (2009), Analyzing the large extension of polygonal terrains in the northern plains of Mars, *Lunar Planet. Sci., XL*, Abstract 2035.

Plescia, J. B., and R. S. Saunders (1982), Tectonic history of the Tharsis region, Mars, *J. Geophys. Res., 87*(B12), 9775–9791, doi:10.1029/JB087iB12p09775.

Pollack, J. B., J. F. Kasting, S. M. Richardson, and K. Poliakoff (1987), The Case for a Warm, Wet Climate on Early Mars, *Icarus, 71*, 203–224.

Pollack, J. B., T. Roush, F. Witteborn, J. Bregman, D. Wooden, C. Stoker, O. B. Toon, D. Rank, B. Dalton, and R. Freedman (1990), Thermal Emission Spectra of Mars (5.4–10.5 μm): Evidence for Sulfates, Carbonates, and Hydrates, *J. Geophys. Res., 95*(B9), 14,595–14,627.

Pollak, H., and J. G. Stevens (1986), Phyllosilicates: A Mössbauer evaluation, *Hyperfine Interactions, 29*, 1153–1156.

Poulet, F., J.-P. Bibring, J. F. Mustard, A. Gendrin, N. Mangold, Y. Langevin, R. E. Arvidson, B. Gondet, C. Gomez, and the Omega Team (2005), Phyllosilicates on Mars and Implications for early martian climate, *Nature, 438*, 623–627, doi:10.1038/nature04274.

Poulet, F., J.-P. Bibring, B. Gondet, Y. Langevin, J. Mustard, N. Mangold, V. Chevrier, and A. Gendrin (2007), Discovery, mapping and mineralogy of phyllosilicates on Mars by MEx-OMEGA: a reappraisal, *Lunar and Planetary Institute Contributions, 1353*, Abstract 3170.

Poulet, F., R. E. Arvidson, C. Gomez, R. V. Morris, J.-P. Bibring, Y. Langevin, B. Gondet, and J. Griffes (2008a), Mineralogy of Terra Meridiani and western Arabia Terra from OMEGA/MEx and implications for their formation, *Icarus, 195*, 106–130, doi:10.1016/j.icarus.2007.11.031.

Poulet, F., N. Mangold, D. Loizeau, J.-P. Bibring, Y. Langevin, J. Michalski, and B. Gondet (2008b), Abundance of minerals in the phyllosilicate-rich units on Mars, *Astron. Astrophys., 487*, L41–L44, doi:10.1051/0004-6361:200810150.

Presley, M. A., and P. R. Christensen (1997), Thermal conductivity measurements of particulate materials: 2. Results, *J. Geophys. Res., 102*(E3), 6551–6556, doi:10.1029/96JE03303.

Price, J. R., M. A. Velbel, and L. C. Patino (2005), Rates and time scales of clay-mineral formation by weathering in saprolitic regoliths of the southern Appalachians from geochemical mass balance, *Geol. Soc. Am. Bull., 117*, 783–794, doi:10.1130/B25547.1.

Putzig, N. E., and M. T. Mellon (2007), Apparent thermal inertia and the surface heterogeneity of Mars, *Icarus, 191*, 68–94, doi:10.1016/j.icarus.2007.05.013.

Putzig, N. E., M. T. Mellon, K. A. Kretke, and R. E. Arvidson (2005), Global thermal inertia and surface properties of Mars from the MGS mapping mission, *Icarus, 173*, 325–341, doi:10.1016/j.icarus.2004.08.017.

Ramsey, M. S., and P. R. Christensen (1998), Mineral abundance determination: Quantitative deconvolution of thermal emission spectra, *J. Geophys. Res., 103*(B1), 577-596, doi:10.1029/97JB02784.

Rancourt, D. G. (1994), Mössbauer Spectroscopy of Minerals: I. Inadequacy of Lorentzian-line Doublets in Fitting Spectra Arising from Quadrupole Splitting Distributions, *Phys. Chem. Minerals, 21*, 244–249.

Rathbun, J. A., and S. W. Squyres (2002), Hydrothermal Systems Associated with Martian Impact Craters, *Icarus, 157*, 362–372, doi:10.1006/icar.2002.6838.

Rennó, N. O., et al. (2009), Possible physical and thermodynamical evidence for liquid water at the Phoenix landing site, *J. Geophys. Res., 114*, E00E03, doi:10.1029/2009JE003362.

Rice, J. W., Jr. (1994), Terrestrial Polar Beach Processes: Martian Paleolake Analogs, *Lunar Planet. Sci., XXV*, 1125–1126.

Rice, M. S., J. F. Bell III, E. A. Cloutis, A. Wang, S. W. Ruff, M. A. Craig, D. T. Bailey, J. R. Johnson, P. A. de Souza Jr., and W. H. Farrand (2010), Silica-rich deposits and hydrated minerals at Gusev Crater, Mars: Vis-NIR spectral characterization and regional mapping, *Icarus, 205*, 375–395, doi:10.1016/j.icarus.2009.03.035.

Rivera-Valentin, E. G., R. Ulrich, V. F. Chevrier, T. S. Altheide, and J. J. Wray (2010), Dynamic Modeling of Martian Paleolake Stability, *Lunar Planet. Sci., XLI*, Abstract 1446.

Rivkin, A. S., and E. L. Volquardsen (2010), Rotationally-resolved spectra of Ceres in the 3-μm region, *Icarus, 206*, 327–333.

Roach, L. H., J. F. Mustard, S. L. Murchie, J.-P. Bibring, F. Forget, K. W. Lewis, O. Aharonson, M. Vincendon, and J. L. Bishop (2009), Testing evidence of recent hydration state change in sulfates on Mars, *J. Geophys. Res.*, *114*, E00D02, doi:10.1029/2008JE003245.

Roach, L. H., J. F. Mustard, G. Swayze, R. E. Milliken, J. L. Bishop, S. L. Murchie, and K. Lichtenberg (2010a), Hydrated mineral stratigraphy of Ius Chasma, Valles Marineris, *Icarus, 206*, 253–268, doi:10.1016/j.icarus.2009.09.003.

Roach, L. H., J. F. Mustard, M. D. Lane, J. L. Bishop, and S. L. Murchie (2010b), Diagenetic hematite and sulfate assemblages in Valles Marineris, *Icarus, 207*, 659–674, doi:10.1016/j.icarus.2009.11.029.

Rogers, A. D., and P. R. Christensen (2007), Surface mineralogy of Martian low-albedo regions from MGS-TES data: Implications for upper crustal evolution and surface alteration, *J. Geophys. Res.*, *112*, E01003, doi:10.1029/2006JE002727.

Rogers, A. D., J. L. Bandfield, and P. R. Christensen (2007), Global spectral classification of Martian low-albedo regions with Mars Global Surveyor Thermal Emission Spectrometer (TES) data, *J. Geophys. Res.*, *112*, E02004, doi:10.1029/2006JE002726.

Rossi, A. P., G. Neukum, M. Pondrelli, S. van Gasselt, T. Zegers, E. Hauber, A. Chicarro, and B. Foing (2008), Large-scale spring deposits on Mars?, *J. Geophys. Res.*, *113*, E08016, doi:10.1029/2007JE003062.

Ruff, S. W. (2009), Gusev-style alteration: unique or ubiquitous on Mars?, *Lunar and Planetary Institute Contributions, 1482*, Abstract 4027.

Ruff, S. W., and P. R. Christensen (2002), Bright and dark regions on Mars: Particle size and mineralogical characteristics based on Thermal Emission Spectrometer data, *J. Geophys. Res.*, *107*(E12), 5127,

doi:10.1029/2001JE001580.

Ruff, S. W., P. R. Christensen, R. N. Clark, H. H. Kieffer, M. C. Malin, J. L. Bandfield, B. M. Jakosky, M. D. Lane, M. T. Mellon, and M. A. Presley (2001), Mars' "White Rock" feature lacks evidence of an aqueous origin: Results from Mars Global Surveyor, *J. Geophys. Res., 106*(E10), 23,921–23,927.

Russell, C. T., et al. (2008), Dawn Mission to Vesta and Ceres: Symbiosis between Terrestrial Observations and Robotic Exploration, *Earth Moon Planet, 101*, 65–91, doi:10.1007/s11038-007-9151-9.

Sagan, C., and C. Chyba (1997), The Early Faint Sun Paradox: Organic Shielding of Ultraviolet-Labile Greenhouse Gases, *Science, 276*, 1217–1221.

Saraiva, J., J. Antunes, L. Bandeira, and P. Pina (2009), Identification and characterization of small-scale polygons around the Phoenix landing site, *Lunar Planet. Sci., XL*, Abstract 1323.

Scott, D. H., and M. H. Carr (1978), Geologic map of Mars, *U.S. Geol. Surv. Misc. Invest. Map, I-1083.*

Scott, D. H., and K. L. Tanaka (1986), Geologic map of the western equatorial region of Mars, *U.S. Geol. Surv. Misc. Invest. Map, I-1802-A.*

Seelos, F.P., O. S. Barnouin-Jha, and S. L. Murchie (2008), MRO CRISM systematic investigation of the MSL candidate landing sites, *Lunar Planet. Sci., XXXIX*, Abstract 2041.

Seelos, K. D., R. E. Arvidson, B. L. Jolliff, S. M. Chemtob, R. V. Morris, D. W. Ming, and G. A. Swayze (2010), Silica in a Mars analog environment: Ka'u Desert, Kilauea Volcano, Hawaii, *J. Geophys. Res., 115*, E00D15, doi:10.1029/2009JE003347.

Segura, T. S., O. B. Toon, A. Colaprete, and K. Zahnle (2002), Environmental Effects

of Large Impacts on Mars, *Science, 298*, 1977–1980, doi:10.1126/science.1073586.

Seibert, N. M., and J. S. Kargel (2001), Small-Scale Martian Polygonal Terrain: Implications for Liquid Surface Water, *Geophys. Res. Lett., 28*(5), 899–902.

Shorlin, K. A., J. R. de Bruyn, M. Graham, and S. W. Morris (2000), Development and geometry of isotropic and directional shrinkage-crack patterns, *Phys. Rev. E, 61*(6), 6950–6957.

Skok, J. R., J. F. Mustard, B. L. Ehlmann, R. E. Milliken, and S. L. Murchie (2010), Silica deposits in the Nili Patera caldera on the Syrtis Major volcanic complex on Mars, *Nature Geosci., 3*(12), 838–841, doi:10.1038/ngeo990.

Smith, D. E., et al. (1999), The Global Topography of Mars and Implications for Surface Evolution, *Science, 284*, 1495–1503, doi:10.1126/science.284.5419.1495.

Soderblom, L. A., et al. (2004), Soils of Eagle Crater and Meridiani Planum at the Opportunity Rover Landing Site, *Science, 306*, 1723–1726.

Squyres, S. W. (1989), Urey Prize Lecture: Water on Mars, *Icarus, 79*, 229–288.

Squyres, S. W., D. E. Wilhelms, and A. C. Moosman (1987), Large-Scale Volcano-Ground Ice Interactions on Mars, *Icarus, 70*, 385–408.

Squyres, S. W., et al. (2003), Athena Mars rover science investigation, *J. Geophys. Res., 108*, 8062, doi:10.1029/2003JE002121.

Squyres, S. W., et al. (2004a), The Spirit Rover's Athena Science Investigation at Gusev Crater, Mars, *Science, 305*, 794–799, doi:10.1126/science.3050794.

Squyres, S. W., et al. (2004b), In Situ Evidence for an Ancient Aqueous Environment at Meridiani Planum, Mars, *Science, 306*, 1709–1714, doi:10.1126/science.1104559.

Squyres, S. W., et al. (2006a), Rocks of the Columbia Hills, *J. Geophys. Res., 111*,

E02S11, doi:10.1029/2005JE002562.

Squyres, S. W., et al. (2006b), Overview of the Opportunity Mars Exploration Rover Mission to Meridiani Planum: Eagle Crater to Purgatory Ripple, *J. Geophys. Res.*, *111*, E12S12, doi:10.1029/2006JE002771.

Squyres, S. W., et al. (2008), Detection of Silica-Rich Deposits on Mars, *Science*, *320*, 1063–1067, doi:10.1126/science.1155429.

Squyres, S. W., et al. (2009), Exploration of Victoria Crater by the Mars Rover Opportunity, *Science*, *324*, 1058–1061, doi:10.1126/science.1170355.

Steefel, C. I., D. J. DePaolo, and P. C. Lichtner (2005), Reactive transport modeling: An essential tool and a new research approach for the Earth sciences, *Earth Planet. Sci. Lett.*, *240*, 539–558, doi:10.1016/j.epsl.2005.09.017.

Stockstill, K. R., J. E. Moersch, S. W. Ruff, A. Baldridge, and J. Farmer (2005), Thermal Emission Spectrometer hyperspectral analyses of proposed paleolake basins on Mars: No evidence for in-place carbonates, *J. Geophys. Res.*, *110*, E10004, doi:10.1029/2004JE002353.

Stockstill, K. R., J. E. Moersch, H. Y. McSween Jr., J. Piatek, and P. R. Christensen (2007), TES and THEMIS study of proposed paleolake basins within the Aeolis quadrangle of Mars, *J. Geophys. Res.*, *112*, E01001, doi:10.1029/2005JE002517.

Story, S., B. Beitler Bowen, K. C. Benison, and D. G. Schulze (2010), Authigenic phyllosilicates in modern acid saline lake sediments and implications for Mars, *J. Geophys. Res.*, doi:10.1029/2010JE003687, in press.

Swayze, G. A. (2004), Using reflectance spectroscopy to evaluate minerals of environmental concern, in *Infrared Spectroscopy in Geochemistry, Exploration Geochemistry, and Remote Sensing*, edited by P. L. King, M. S. Ramsey, and G. A. Swayze, pp. 181–196, Mineral. Assoc. Can., London, Ontario, Canada.

Swayze, G. A., R. N. Clark, S. J. Sutley, C. A. Gent, B. W. Rockwell, D. L. Blaney, J. L. Post, and B. P. Farm (2002), Mineral mapping Mauna Kea and Mauna Loa shield volcanos on Hawaii using AVIRIS data and the USGS Tetracorder spectral identification system: Lessons applicable to the search for relict Martian hydrothermal systems, in *Proceedings of the 11th JPL Airborne Earth Science Workshop*, edited by R. O. Green, *JPL Publication 03-4*, pp. 373–387.

Swayze, G. A., G. A. Desborough, K. S. Smith, H. A. Lowers, J. M. Hammarstrom, S. F. Diehl, R. W. Leinz, and R. L. Driscoll (2008a), Understanding jarosite—from mine waste to Mars, in *Understanding Contaminants Associated with Mineral Deposits*, edited by P. L. Verplanck, U.S. Geological Survey Circular 1328, pp. 8–13.

Swayze, G. A., et al. (2008b), Discovery of the Acid-Sulfate Mineral Alunite in Terra Sirenum, Mars, Using MRO CRISM: Possible Evidence for Acid-Saline Lacustrine Deposits?, *Eos Trans. AGU, 89*(53), Fall Meet. Suppl., Abstract P44A-04.

Szynkiewicz, A., R. C. Ewing, K. E. Fishbaugh, M. C. Bourke, D. Bustos, and L. M. Pratt (2009), Geomorphological evidence of plausible water activity and evaporitic deposition in interdune areas of the gypsum-rich Olympia Undae dune field, *Lunar Planet. Sci., XL*, Abstract 2038.

Szynkiewicz, A., R. C. Ewing, C. H. Moore, M. Glamoclija, D. Bustos, and L. M. Pratt (2010), Origin of terrestrial gypsum dunes—Implications for Martian gypsum-rich dunes of Olympia Undae, *Geomorphology*, *121*, 69–83, doi:10.1016/j.geomorph.2009.02.017.

Tanaka, K. L. (1986), The stratigraphy of Mars, *J. Geophys. Res., 91*, E139–E158, doi:10.1029/JB091iB13p0E139.

Tian, F., J. F. Kasting, and S. C. Solomon (2009), Thermal escape of carbon from the early Martian atmosphere, *Geophys. Res. Lett., 36*, L02205, doi:10.1029/2008GL036513.

Tornabene, L. L., A. S. McEwen, G. R. Osinski, P. J. Mouginis-Mark, J. M. Boyce, R. M. E. Williams, J. J. Wray, J. A. Grant, and the HiRISE Team (2007), Impact melting and the role of subsurface volatiles: Implications for the formation of valley networks and phyllosilicate-rich lithologies on early Mars, *Lunar and Planetary Institute Contributions, 1353*, Abstract 3288.

Tornabene, L. L., J. E. Moersch, H. Y. McSween Jr., V. E. Hamilton, J. L. Piatek, and P. R. Christensen (2008), Surface and crater-exposed lithologic units of the Isidis Basin as mapped by coanalysis of THEMIS and TES derived data products, *J. Geophys. Res., 113*, E10001, doi:10.1029/2007JE002988.

Tornabene, L. L., A. S. McEwen, C. Caudill, G. R. Osinski, J. J. Wray, G. A. Marzo, J. F. Mustard, J. R. Skok, J. A. Grant, and S. Mattson (2010), A crater-exposed bedrock database for Mars with applications for determining the composition and structure of the upper crust, *Lunar Planet. Sci., XLI*, Abstract 1737.

Tosca, N. J., and S. M. McLennan (2009), Experimental constraints on the evaporation of partially oxidized acid-sulfate waters at the martian surface, *Geochim. Cosmochim. Acta, 73*, 1205–1222, doi:10.1016/j.gca.2008.11.015.

Tosca, N. J., S. M. McLennan, D. H. Lindsley, and M. A. A. Schoonen (2004), Acid-sulfate weathering of synthetic Martian basalt: The acid fog model revisited, *J. Geophys. Res., 109*, E05003, doi:10.1029/2003JE002218.

Tosca, N. J., S. M. McLennan, B. C. Clark, J. P. Grotzinger, J. A. Hurowitz, A. H. Knoll, C. Schröder, and S. W. Squyres (2005), Geochemical modeling of evaporation processes on Mars: Insight from the sedimentary record at Meridiani Planum, *Earth Planet. Sci. Lett., 240*, 122–148,

doi:10.1016/j.epsl.2005.09.042.

Tosca, N. J., A. H. Knoll, and S. M. McLennan (2008a), Water Activity and the Challenge for Life on Early Mars, *Science, 320*, 1204–1207, doi:10.1126/science.1155432.

Tosca, N. J., R. E. Milliken, and F. M. Michel (2008b), Smectite formation on early Mars: Experimental constraints, *Lunar and Planetary Institute Contributions, 1441*, Abstract 7030.

Vaniman, D. T., D. L. Bish, S. J. Chipera, C. I. Fialips, J. W. Carey, and W. C. Feldman (2004), Magnesium sulphate salts and the history of water on Mars, *Nature, 431*, 663–665, doi:10.1038/nature.02973.

Vaniman, D.T., D. L. Bish, and S. J. Chipera (2008), Calcium sulfate hydration, stability, and transformation on Mars, *Lunar Planet. Sci., XXXIX*, Abstract 1816.

Vaniman, D.T., D. L. Bish, and S. J. Chipera (2009), Bassanite on Mars, *Lunar Planet. Sci., XL*, Abstract 1654.

Wang, A., L. A. Haskin, A. L. Lane, T. J. Wdowiak, S. W. Squyres, R. J. Wilson, L. E. Hovland, K. S. Manatt, N. Raouf, and C. D. Smith (2003), Development of the Mars microbeam Raman spectrometer (MMRS), *J. Geophys. Res., 108*(E1), 5005, doi:10.1029/2002JE001902.

Wang, A., et al. (2006), Evidence of phyllosilicates in Wooly Patch, an altered rock encountered at West Spur, Columbia Hills, by the Spirit rover in Gusev crater, Mars, *J. Geophys. Res., 111*, E02S16, doi:10.1029/2005JE002516.

Wänke, H., J. Brückner, G. Dreibus, R. Rieder, and I Ryabchikov (2001), Chemical composition of rocks and soils at the Pathfinder site, *Space Sci. Rev., 96*, 317–330.

Watters, W. A., and S. W. Squyres (2009), Mechanisms for shrinkage fracturing at

Meridiani Planum, *Eos Trans. AGU, 90*(52), Fall Meet. Suppl., Abstract P22A-04.

Weitz, C. M., M. D. Lane, M. Staid, and E. Noe Dobrea (2008), Gray hematite distribution and formation in Ophir and Candor chasmata, *J. Geophys. Res., 113*, E02016, doi:10.1029/2007JE002930.

Weitz, C. M., R. E. Milliken, J. A. Grant, A. S. McEwen, R. M. E. Williams, J. L. Bishop, and B. J. Thomson (2010a), Mars Reconnaissance Orbiter observations of light-toned layered deposits and associated fluvial landforms on the plateaus adjacent to Valles Marineris, *Icarus, 205*, 73–102, doi:10.1016/j.icarus.2009.04.017.

Weitz, C.M., J. L. Bishop, L. Roach, R. E. Milliken, and J. A. Rodriguez (2010b), Mineralogy and morphology of light-toned deposits in Noctis Labyrinthus, *Lunar Planet. Sci., XLI*, Abstract 2240.

Werner, S. C. (2008), The early martian evolution—Constraints from basin formation ages, *Icarus, 195*, 45–60, doi:10.1016/j.icarus.2007.12.008.

Williams, R. M. E., and M. C. Malin (2008), Sub-kilometer fans in Mojave Crater, Mars, *Icarus, 198*, 365–383, doi:10.1016/j.icarus.2008.07.013.

Wilson, S. A., A. D. Howard, J. M. Moore, and J. A. Grant (2007), Geomorphic and stratigraphic analysis of Crater Terby and layered deposits north of Hellas basin, Mars, *J. Geophys. Res., 112*, E08009, doi:10.1029/2006JE002830.

Wiseman, S. M., et al. (2008), Phyllosilicate and sulfate-hematite deposits within Miyamoto crater in southern Sinus Meridiani, Mars, *Geophys. Res. Lett., 35*, L19204, doi:10.1029/2008GL035363.

Wiseman, S. M., R. E. Arvidson, R. V. Morris, F. Poulet, J. C. Andrews-Hanna, J. L. Bishop, S. L. Murchie, F. P. Seelos, D. Des Marais, and J. L. Griffes (2010), Spectral and stratigraphic mapping of hydrated sulfate and phyllosilicate-

bearing deposits in northern Sinus Meridiani, Mars, *J. Geophys. Res., 115*, E00D18, doi:10.1029/2009JE003354.

Yen, A. S., et al. (2008), Hydrothermal processes at Gusev Crater: An evaluation of Paso Robles class soils, *J. Geophys. Res., 113*, E06S10, doi:10.1029/2007JE002978.

Zimbelman, J. R., W. B. Garry, and R. P. Irwin III (2009), Precision Topography of Pluvial Features in Western Nevada as Analogs for Possible Pluvial Landforms on Mars, *Lunar Planet. Sci., XL*, Abstract 1370.

Zolotov, M. Y., and M. V. Mironenko (2007a), Timing of acid weathering on Mars: A kinetic-thermodynamic assessment, *J. Geophys. Res., 112*, E07006, doi:10.1029/2006JE002882.

Zolotov, M. Y., and M. V. Mironenko (2007b), Formation and Fate of Phyllosilicates on the Surface of Mars: Geochemical Modeling of Aqueous Weathering, *Lunar and Planetary Institute Contributions, 1353*, Abstract 3365.

Zurek, R. W., A. Chicarro, M. A. Allen, J.-L. Bertaux, R. T. Clancy, F. Daerden, V. Formisano, J. B. Garvin, G. Neukum, and M. D. Smith, Assessment of a 2016 Mission Concept: The Search for Trace Gases in the Atmosphere of Mars, *Planet. Space Sci.*, doi:10.1016/j.pss.2010.07.007, in press.